V for Venous Pressure

by

Alex T. Jaffe

S.B., Massachusetts Institute of Technology, USA (2016)

M.Eng., Massachusetts Institute of Technology, USA (2018)

Submitted to the

Department of Electrical Engineering and Computer Science

in partial fulfillment of requirements for the degree of

Doctor of Philosophy

at the

MASSACHUSETTS INSTITUTE OF TECHNOLOGY

February 2023

Author . . . . . .

Department of Electrical Engineering and Computer Science

September 30, 2022

Certified by . . . . . .

Brian W. Anthony

Principle Research Scientist of Mechanical Engineering

Thesis Supervisor

Accepted by . . . . . .

Leslie A. Kolodziejski

Professor of Electrical Engineering and Computer Science

Chair, Department Committee on Graduate Students

V for Venous Pressure

by

Alex T. Jaffe

Submitted to the Department of Electrical Engineering and Computer Science
on September 30, 2022, in partial fulfillment of requirements
for the degree of Doctor of Philosophy

Abstract

Cardiovascular disease is the world's leading cause of death. Striving to decrease cardiovascular related deaths and improve quality of life, medical treatments have advanced, and society has become better informed on leading a healthy lifestyle. In parallel, our ability to monitor patients with cardiovascular disease has progressed substantially. Yet, many measurements still require invasive means for clinically acceptable accuracy. Medical ultrasound imaging noninvasively provides images of the heart and major blood vessels in real-time while emitting no harmful radiation and costing relatively little to operate. In this thesis, force-coupled ultrasound imaging techniques are developed to create accurate and noninvasive methods to measure central venous pressure and central arterial pressure.

Force-coupled ultrasound imaging of blood vessels is a process which outputs ultrasound images containing at least one segmented blood vessel of interest and assigns a force to each image. Data is acquired with a force-coupled ultrasound probe – an ultrasound probe which measures force applied. To analyze, three data processing steps proceed automatically in order: (1) ultrasound images are synchronized with force data, (2) the blood vessel of interest is detected within the force-coupled ultrasound images, and (3) the blood vessel is segmented in each relevant image. Central arterial pressure is estimated calibration-free through force-coupled ultrasound imaging of the carotid artery combined with inverse finite element modeling ($\mathrm{n} = 20, |\bar{\Delta}|_{\mathrm{dia}} = 6.2\ \mathrm{mmHg}, |\bar{\Delta}|_{\mathrm{sys}} = 5.6\ \mathrm{mmHg}$). Collapse force – the force necessary to completely occlude a vein in a particular anatomical location – of the internal jugular vein is shown to predict central venous pressure with high accuracy at MIT ($n = 26$, $r^2 = 0.89$, $|\bar{\Delta}| = 0.23\ \mathrm{mmHg}$) with a limited range of venous pressures with healthy subjects and at Massachusetts General Hospital ($n = 11$, $r^2 = 0.82$, $|\bar{\Delta}| = 1.08\ \mathrm{mmHg}$) with a more vast range of venous pressures and heart failure intensive care unit patients. Additionally, central arterial and central venous pressure are simultaneously estimated through force-coupled ultrasound imaging and inverse finite element modeling of the carotid artery and internal jugular vein in the same image ultrasound viewing window.

The proposed force-coupled ultrasound imaging techniques are well-suited to improve how central venous pressure is measured in patients with decompensated heart failure. These methods also have potential to provide a more accurate and facile central venous pressure measurement for compensated and early stage heart failure and a more informed central arterial pressure measurement for cardiovascular disease in general.

Thesis Supervisor: Brian W. Anthony

Title: Principal Research Scientist, Department of Mechanical Engineering

Acknowledgements

I'd like to start off by thanking my advisor, Dr. Brian Anthony. He made it possible for me to reach this point and, in the process, gave me broad lee way to make significant research decisions. That said, he also provided sound advising whenever necessary throughout my Ph.D. His administrative assistant, Samantha Young, has also been a great help to me. She has been an excellent resource for scheduling, orders, and overall lab organization.

Regarding my committee members, they were valuable and complementary in their roles advising me. Prof. Luca Daniel, with his expertise in numerical methods, was instrumental in inverse modeling and uncertainty quantification. Prof. Thomas Heldt, with his mastery of human physiology and physiological modeling and his clinical wherewithal, helped me shape my research to most effectively address congestive heart failure.

I have two additional research advisors. Prof. Charles Sodini, my co-advisor, has provided me with consistent and dependable advising for the entirety of my Ph.D. with respect to electrical engineering for cardiology in general. He has helped me focus on distilling information in an understandable way when communicating. Dr. Aaron Aguirre, while acting as the most essential part of our most impactful venous pressure study at Massachusetts General Hospital, has given me both a cardiologist's and an engineer's perspective when considering the applicability of my research.

Next, I'd like to acknowledge those who've helped me navigate MIT for the past 10 years (undergrad through graduate school). My academic advisor throughout undergrad was Prof. Rafael Reif, whom, despite his busy schedule, made time to guide me through the decision to become an engineer for medicine instead of a medical doctor. Dr. Julie Greenberg aptly advised me during my M.Eng. and helped me make the decision to pursue a Ph.D. During the second half of undergrad and M.Eng., my research advisor was Prof. Joel Voldman. Aside from teaching me what independent research entails, he also was immense help in my navigation of Ph.D. applications, after he already knew that I would be leaving his lab for Ph.D. I'll always be grateful for the kindness this guides to MIT have shown me.

Part of the conception for my Ph.D. project originated in an MIT project class 2.75/6.525 Medical Device Design in Fall 2016, run by Dr. Nevan Hanumara and Prof. Alex Slocum. In this class, clinical advisor Dr. Maulik Majmudar, and group members Dr. Galit Frydman and Dr. Robin Singh helped develop a prototype which served as the impetus for collapse force of the internal jugular vein predicting central venous pressure, in my view, the most impactful work of this thesis. Prof. Collin Stultz provided motivation for me to further explore the idea, leading me to decide to continue on for a Ph.D.

I'd now like to acknowledge the fellow researchers who've played a key role in helping my research which produced this thesis. Dr. Anne Tresansky acted as a student advisor to me when I first started and urged me to keep a good balance between technical research and data collection. Dr. Alex Benjamin was consistently willing to brainstorm my research and explain concepts to me with which he was familiar. Melinda Chen consistently asked the best questions to me during group meetings, often causing me to alter my approach for a more optimal path. Rebecca Zubajlo introduced me to force-coupled ultrasound imaging conceptually and in practice. Ivan Goryachev, is fully responsible for the construction of the force-coupling which has been used primarily for venous pressure estimation. Dr. Anand Chandrasekhar and Dr. Syed (Imad) Immaduddin provided excellent insights and suggestions for my research despite not being in the same lab.

Next, I'd like to thank my parents, Suzan and Gary. On top of always being there for me, each of them had a career in medicine as a sleep doctor (Mom) and ophthalmologist (Dad). Growing up in that

household greatly influenced my choice in career, but they never pressured me to pursue a career in medicine. They've consistently cheered me on at every point in my time at MIT, something I'm incredibly thankful for.

Thank you to my close friends and extended family for giving me a life outside of research and occasionally providing valuable advice for my research, especially in the past two years. I'm fortunate enough to have several friends who've gone through a Ph.D. before and each of them has given me perspective on the thesis process.

Penultimately, I'd like to thank Philips Healthcare and their liaison Dr. Jonathan Sutton for funding the bulk of the research that led to producing this thesis.

Finally, I'd like to thank *you* for reading this thesis. It takes a village to raise a…doctor of philosophy.

List of Figures

List of Tables

Contents

Chapter 1 – Introduction

1.1 Motivation

When I enrolled as an undergraduate at MIT, I was convinced I wanted to be a medical doctor. My parents were doctors and in addition to having heard them discuss cases with me, I was fortunate to shadow them and their colleagues on several occasions. What gravitated me to the medical field was my desire to improve or even save lives by fixing problems that arose within the human body. In my view, becoming a physician was a profession that could prioritize helping people without other incentives getting in the way. However, my thoughts changed after discovering engineering. I majored in electrical engineering as an undergraduate and noticed the type of research in the department that could be applied to medicine. Observing the acceleration of technological development in the world, I realized I was more attracted to inventing a solution (engineering/modeling) than discovering one (science/biology).

The idea of this project was first introduced to me in fall 2016 when I was taking Medical Device Design (MIT course numbers 2.75/6.525) as a first semester master's in engineering student. Our group came up with a single element force-coupled ultrasound device to be able to sense relative changes in venous pressure through compression of the internal jugular vein. The translational impact on congestive heart failure seemed palpable at the time and Brian Anthony, principle investigator of the lab at MIT which did force-coupled ultrasound research, expressed interest in exploring force-coupled ultrasound imaging for a more ambitious purpose of an absolute venous pressure estimate with an ultrasound array. It was not until late spring 2017 when I decided I'd like to pursue a Ph.D. with this as my project. What kept me motivated throughout the Ph.D. and what still keeps me motivated is the potential of force-coupled ultrasound imaging to positively impact the lives of patients. This could be through a milder, noninvasive way of accurately measuring venous pressure or possibly even early detection of heart failure leading to better outcomes.

"All we have to decide is what to do with the time that is given us," (J. R. R. Tolkien, 1954).

1.2 Foundation

It is imperative to note what I consider to be foundational work for this thesis in the area of force-coupled ultrasound blood vessel pressure estimation, which I see as the central topic of this thesis. The history is actually quite extensive and far reaching, but I hope to highlight key inventions and discoveries without which, it would be difficult to imagine my research taking place.

- 1905 – Nikolai Korotkoff invents the auscultatory method of arterial blood pressure measurement. By measuring the pressure applied and observing a collapse of an artery with a stethoscope when enough pressure is applied, Korotkoff provided the method from which the compression of a blood vessel with force-coupled ultrasound is derived.
- 1942 – Karl Dussik, a neurologist, uses ultrasound to attempt to detect brain tumors in a human.
- 1949 – Brightness mode (B-mode) ultrasound images are first created by Douglas Howry and Joseph Holmes of the University of Colorado.
- 2005 – The simultaneous measurement of contact force and ultrasound is first accomplished by M. R. Burcher et al. of Oxford.
- 2010 – Brian Anthony's lab at MIT begins force-coupled ultrasound based research with graduate student Matthew Gilbertson. In the years immediately preceding the beginning of my Ph.D., calibrated arterial pressure estimation with force-coupled ultrasound imaging was accomplished by graduate student Aaron Zakrzewski.

These inventions and discoveries, among countless others, are excellent prior work from which to build my own research.

"If I have seen further, it is by standing on the shoulders of giants," (Isaac Newton, 1675).

1.3 Approach

The research in force-coupled ultrasound imaging of large superficial blood vessels seeks to observe compressible blood vessels large enough to be observed visually in real time with ultrasound imaging. The compressibility of a blood vessel depends on whether there is anything fixed and rigid between the ultrasound probe contacting the skin and the blood vessel. Although arteries require more force for compression to be observed, they are still compressible. On the other hand, the inferior vena

cava, enveloped by the rib cage is not compressible as there will not be transmission of force from the skin to the blood vessel which travels past the ribs. Furthermore, blood vessels must be superficial, which we define to be within 5 centimeters of depth from the surface of the skin to the anterior wall of the blood vessel. This is imperative in order to prevent the attenuation of the compression force within the tissue and other blood vessels in between the skin and the blood vessel of interest. Although leg veins are also studied in this thesis, the utmost attention is paid to the carotid artery and internal jugular vein, which run anti-parallel to each other and have short-axis cross-sections nearly always visible in the same ultrasound image.

Data acquisition of force-coupled ultrasound images requires creating artifacts which will be visible in the force signal and ultrasound images, so the force can be synchronized with the ultrasound imaging in post-processing. Also, during data acquisition, the blood vessel of interest should be as horizontally centered as possible, so a reasonably symmetric force can be applied to it. In the analysis, the approach is to have a modular, automated processing of force-coupled ultrasound images to arrive at a segmented blood vessel in a set of relevant force-coupled ultrasound images. At this point, the approach varies depending on which blood vessel is being analyzed, as we will cover later in this thesis.

The central intent of this research is to make significant improvements in noninvasive venous pressure measurement and arterial pressure measurement, with more emphasis on venous pressure measurement. This approach has not been researched with respect to force-coupled ultrasound, nor even with respect to all technologies, nearly as much as arterial pressure.

1.4 Contributions

The major contributions of this thesis are:

- The automation of force-coupled ultrasound post-processing: Synchronization of force and ultrasound images is executed reliably with peak detection in the force signal and a derived optical flow based signal from tracking the vertical movement of pixels in the ultrasound images from one frame to the next. Detection of the blood vessel of interest relies on an object detection convolutional neural network trained on segmented images of the blood vessel of interest in several different subjects. Segmentation employs a region-growing and point optimization approach to automatically segment the blood vessel of interest from frame to frame.

    - Relevant publication: “Automated force-coupled ultrasound method for calibration-free carotid artery blood pressure estimation” (Jaffe, Zubajlo, Daniel, Anthony; Ultrasound in Medicine and Biology; 2022)
- The development of the carotid arterial pressure measurement into a stand-alone method: With improvements in the finite element modeling to make it more physiologically accurate, no calibration is necessary to provide moderately accurate central blood pressure prediction with force-coupled ultrasound imaging of the carotid artery.
    - Relevant publication: “Automated force-coupled ultrasound method for calibration-free carotid artery blood pressure estimation” (Jaffe, Zubajlo, Daniel, Anthony; Ultrasound in Medicine and Biology; 2022)
- The novel collapse force measurement of the internal jugular vein: This measurement demonstrates an accurate and simple methodology for noninvasive central venous pressure measurement which has the potential to be assessed in real-time. It is automatically detected at the force at which cross-sectional area of the vein, calculated from segmentation, is first below a threshold to be considered collapsed. This collapse force measurement is verified against a direct central venous pressure measurement with invasive catheterization at Massachusetts General Hospital.
    - Relevant paper in review: “Central Venous Pressure Estimation with Force-coupled Ultrasound of the Internal Jugular Vein” (Jaffe, Goryachev, Sodini, Anthony; Scientific Reports; 2022)
    - Relevant study: “Noninvasive Assessment of Venous Pressure with Force-coupled Ultrasound” (Jaffe, Aguirre; Massachusetts General Hospital; 2022)
- Arterial and venous pressure wave measurement based on force-coupled ultrasound imaging observations and analysis and inverse finite element modeling: From previous diastolic and systolic pressure estimates in the case of the carotid and average central venous pressure estimates in the case of the internal jugular vein, a sampled pressure wave can be predicted for each through one stand-alone force-coupled ultrasound probe.
    - Relevant publication: “Automated force-coupled ultrasound method for calibration-free carotid artery blood pressure estimation” (Jaffe, Zubajlo, Daniel, Anthony; Ultrasound in Medicine and Biology; 2022)

- Relevant paper in review: “Central Venous Pressure Estimation with Force-coupled Ultrasound of the Internal Jugular Vein” (Jaffe, Goryachev, Sodini, Anthony; Scientific Reports; 2022)

1.5 Ethics

Given the translational medicine aspect of this research, an ethical discussion is merited. The stakeholders are the researchers, the advisors, those funding the research, and those seeking to apply the research, be that through technology licensing and/or clinical adoption. At this point, the research is purely academic. Hence, no stakeholder stands to directly benefit financially or suffer from results related to this research. Yet, there remains some inherent risk due to the fact the technology discussed in this thesis does make meaningful contact with the human body. Ultrasound is radiation free and does not emit enough acoustic power to damage the human body. That said, the force application is still of concern. Steps must be taken when using force-coupled ultrasound on patients to ensure their safety. This must be addressed through simulation and in vitro modeling if the technology is to be marketed as a medical device. Finally, the decision to order the use of said medical device must be scrutinized to be in the best interest of the patient and not mainly for the purpose of charging a billing code. For now, this ethical discussion remains mostly hypothetical, but the circumstances surrounding this research could change eventually.

1.6 Structure

This thesis can be divided into background information, methods, and studies. Regarding background information, chapter 2 is technical background, covering topics important to the understanding of study results from a science and engineering standpoint. Chapter 3 is clinical background, providing a basis and significance in medicine for the research being done. The methods section of this thesis has only one chapter solely dedicated to it. Chapter 4 seeks to explain in detail everything created in order to process the force-coupled ultrasound images of the studies in the proceeding chapters. Chapters 5 through 9 all refer to specific and isolated studies. Chapter 5 covers a carotid artery study where central arterial pressure is estimated. Chapter 6 covers a leg vein study which looks at collapse force in different orthostatic positions of different leg veins. Chapter 7 covers an internal jugular vein study where central venous pressure is estimated and compared to the noninvasive

standard. Chapter 8 covers an internal jugular vein study where central venous pressure is estimated and compared to the invasive standard. Chapter 9 covers a study of the carotid artery and internal jugular vein where both central arterial pressure and central venous pressure are estimated and compared to noninvasive standards. Chapter 10 is the conclusion and future work chapter where final thoughts on the research and suggestions for future relevant research directions are expressed. What follows are appendices which do not fit cleanly into any of the chapters but are relevant research which occurred while striving toward a Ph.D. and build on information provided in earlier chapters.

Chapter 2 – Background – Signal Processing, Ultrasound, Force Measurement, and Structural Modeling

This thesis uses several fundamental concepts within the broad fields of mathematics, science, and engineering. The goal of this chapter is to provide enough background information and formulation to understand technical concepts presented in the remainder of this thesis. First, we cover fundamental concepts in signal processing with respect to 1-D signals and 2-D images. Second, we cover the physics and the signal processing involved in producing medical ultrasound images. Third, we cover the engineering involved in measuring force applied which allows us to capture the force-applied to a specific ultrasound image. Last, we cover the mechanical modeling of structures which allows us to compare these models to physiological observations from force-coupled ultrasound images.

2.1 Signal and Image Processing

Signal processing is the concept of using mathematics to interpret, modify, and synthesize scientific measurements. It's a very broad field, but here we strive to explain the concepts repetitively used in subsequent chapters when processing signals related to force-coupled ultrasound imaging. These concepts are sampling, filtering, peak detection, and optical flow. Sampling and filtering are two of the broadest concepts in signal processing while peak detection and optical flow are quite specific and build on both concepts of sampling and filtering. In explaining these concepts, we attempt to work in useful examples from the field of force-coupled ultrasound imaging.

2.1.1 Sampling

Sampling is the process of capturing an analog (real world) signal and converting it to a digital signal at a certain capture frequency. This capture frequency is called the sampling rate. Conceptually, we can think about the analog signal as having an infinite sampling rate in that it always exists. Hence, it is continuous in time. The sampled, or digitized, signal only has a value at the exact time it is sampled. From one sample to the next, there is no value. Hence, it is discrete in time [1].

The simplest form of sampling captures a single scalar value at a given time, such as when an analog voltage signal representing the force applied by an ultrasound probe at a given time is captured at a specific time. This single sample can be thought of as a zero-dimensional signal. In sampling a signal

ultrasound element to observe a signal received at a specific time, such as in M-mode ultrasound imaging where we only want to observe one vertical line of the image, a one-dimensional signal or vector is captured. The rate at which this line is captured is called the line rate. When we consider a B-mode ultrasound frame and the capture of that entire frame at a given time, that is called the frame rate, as it is referred to with a video camera [1], [2].

It is important to distinguish the minimum sampling frequency necessary to capture a certain phenomenon of a specific frequency in an analog signal. This is called the Nyquist rate, which is twice the frequency of the highest frequency we intend to capture in a signal. We have the formula:

$$f_s = 2N \tag{2.1}$$

which dictates that the Nyquist frequency N is the maximum frequency one can capture with a given sample rate f_s. To aid our understanding of this concept, we can use the concept of a sinusoid such as:

$$F = cos(2\pi t) \tag{2.2}$$

where F is force in Newtons (N) and t is time in seconds (s). This signal has a single frequency of 1 cycle per second, or 1 Hertz (Hz), as we can see that it returns to its maximum position once per second. If we were to imagine sampling the signal at 2 samples per second, we would note that in order to capture the full signal, we would have to sample exactly at each half and whole second mark. If we were to sample at each quarter and three-quarter second mark but not at any half or whole second mark, even at 2 samples per second, we would have a digitized signal with a value of zero at all time points. If we were to decrease the sampling frequency to 1 sample per second, we would have a digitized signal with a constant value at all time points [3].

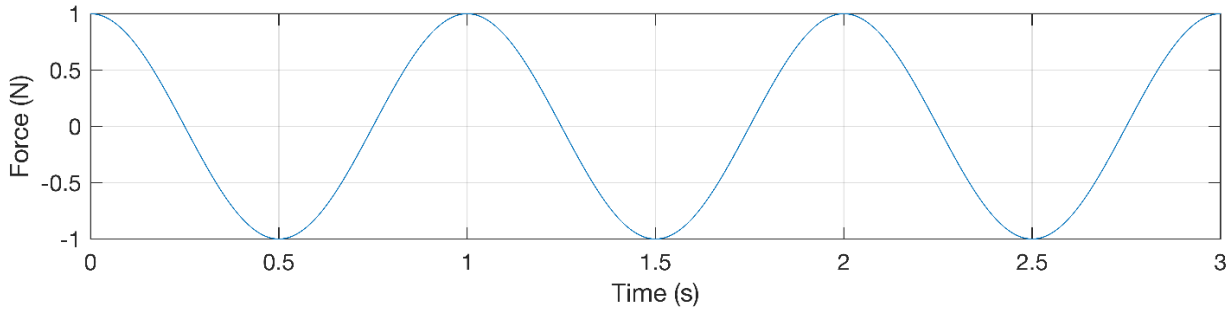

Figure 2-1: Cosine force signal in time with frequency 1 Hz.

2.1.2 Filtering

Filtering is the process of modifying a signal in order to eliminate irrelevant information, or noise, from the signal. Some of these filters occur before a signal is sampled (continuous time analog filters) while a larger portion happen after a signal is sampled (discrete time digital filters). We will further subdivide this section into an analog subsection and a larger digital subsection with more emphasis on the digital subsection as digital filtering is more relevant to this thesis.

2.1.2.1 Continuous Time Analog Filtering

When any analog signal is propagating through space, it could come into contact with something that causes it to lose certain frequency components. For instance, when light travels from the sun to the earth, ultraviolet wavelengths are attenuated in the earth's ozone layer. More specifically considering electrical circuits, there are certain arrangements of lump components which filter out high frequencies, low frequencies, or a specific band of frequencies. In the case of force-coupled ultrasound, noise is usually constrained to higher frequencies than the signal. In terms of cardiovascular physiology, blood vessel compliance can be represented as a capacitor circuit component when making physiological circuit models. Therefore, we will discuss the capacitive low-pass filter, which lets low frequencies through and stops high frequencies. Basic electrical circuit knowledge is helpful to know when reading through the remainder of this section.

The simplest capacitive low-pass filter is a resistor-capacitor circuit (RC circuit). It has a resistor in series and a capacitor to ground with an input and output voltage on either side of the circuit. In this arrangement of the resistor and capacitor, it is always a low-pass filter. The voltage across the capacitor is represented by the differential equation:

$$\frac{dv_C}{dt} = \frac{i_C}{C} \tag{2.3}$$

which has the following step response in response to the input voltage step:

$$v_C = v_{in}\left(1 - e^{\frac{-t}{RC}}\right) \tag{2.4}$$

This equation is in the time domain. In order to understand why this circuit is a low pass filter, we look at the equation in the frequency domain. To convert from the time domain to the frequency domain, we look at the continuous time Fourier transform (CTFT):

$$X(\omega) = \int_{-\infty}^{\infty} x(t)e^{-j\omega t}dt \tag{2.5}$$

In this equation, ω is the angular frequency which is equivalent to cyclic frequency f multiplied by 2π radians, $x(t)$ represents some time domain equation, $X(\omega)$ represents the frequency domain conversion of that equation, and j is an imaginary number such that $j^2 = -1$. With analog signals we use parenthesis to index. Viewing the RC circuit equation in the frequency domain, we have:

$$v_C = v_{in}\left(\frac{1}{1+j\omega RC}\right) \tag{2.6}$$

We see from this equation that at low frequencies, v_{in} is conserved in v_C or v_{out}, while at high frequencies, it is attenuated. The phase of the signal, or rather how many degrees off of the beginning of the cycle the signal is at an arbitrary point in time, is shifted in response to an analog low pass filter.

Another type of filter is a differential filter, which takes two signals and subtracts one from the other. This type of filter is often useful because there is often deterministic information we would like to filter out which is common to both signals. When the signals are subtracted, this common mode information is filtered out.

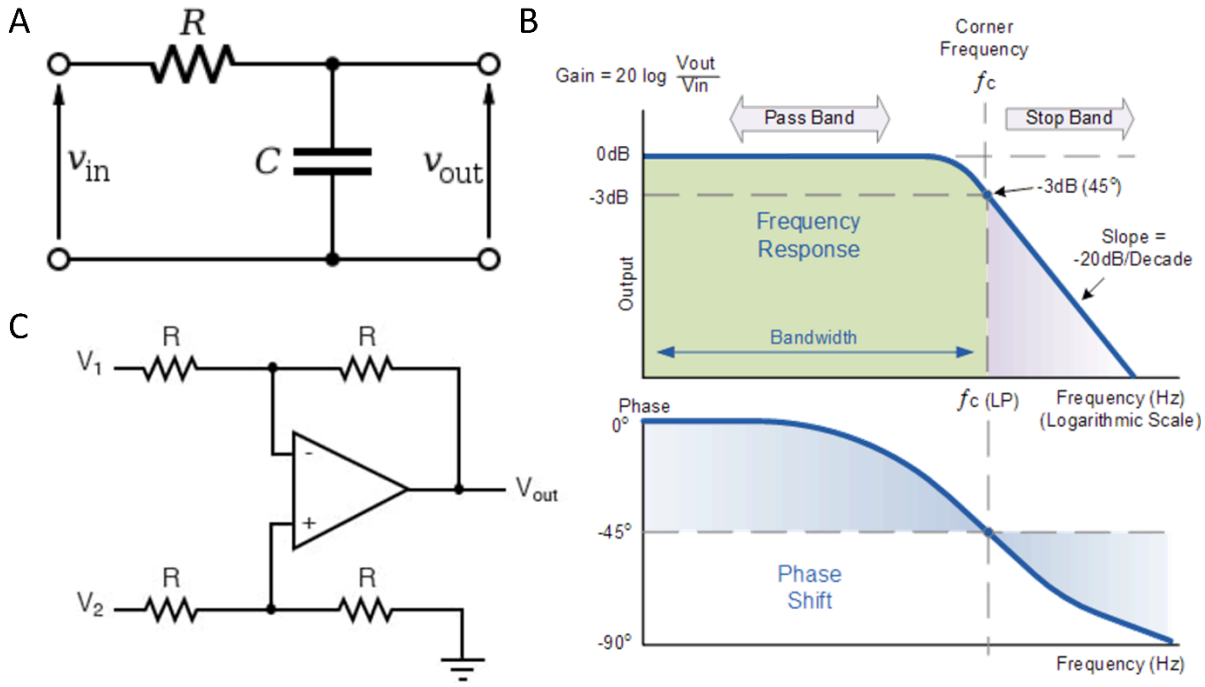

Figure 2-2: (A) Series RC circuit model [4]. (B) Frequency response of the passive series RC circuit as a low pass filter [5]. (C) Circuit model of a simplified differential amplifier [6].

There are plenty of other frequency domain filter configurations one can construct with analog circuit components, such as high pass, band pass, and notch filters. However, the work in this thesis does not utilize them in favor of using them post digitization.

2.1.2.2 Discrete Time Digital Filtering

An analog signal is converted to a discrete time digital signal (digitized) by being sampled and quantized. Sampling a signal captures the signal's value at a certain point in time. Quantizing the signal defines the decimal precision of that value to be finite. Digital signals have quantized values at sampled times and are undefined at other times while analog signals always have a value and have infinitesimal decimal precision. Regarding filtering in digital space, only math and computational power is required. Furthermore, virtually every digital filter imaginable has already been created and is freely available for public use. Therefore, there is quite a lot of flexibility in the filters one can construct with little mental effort. In this thesis, we employ digital filters in the time domain, frequency domain, and two-dimensional spatial domain.

Time domain filters look at signals in the time domain and adjust them by multiplying them by another function in the time domain. These filters are generally called finite impulse response (FIR) filters because they have a finite number of elements in the time domain. For instance, the moving average filter is a type of low pass time domain filter which averages each point with a certain number of proceeding and succeeding points. It is described by:

$$x[n] = \frac{x[n-N]+\cdots+x[n-1]+x[n]+x[n+1]+\cdots+x[n+N]}{2N+1} \tag{2.7}$$

where x is a discrete time signal, n is the current index, and $2N + 1$ is the number of neighboring elements in the signal to average. With digital signals we use brackets to index. The moving average filter is the most common time-domain digital filter used in the analysis code which produced this thesis.

Frequency domain filters look at signals in the frequency domain and adjust them by multiplying them by another function in the frequency domain. These filters are referred to as infinite impulse response (IIR) filters because they have an infinite number of elements in the time domain. In digital filtering, an actual infinite impulse response is not possible, but filters with a large number of points do well to approximate an infinite response and decrease side lobes. In order to convert a digital signal to the frequency domain from the time domain, we use the discrete Fourier transform (DFT):

$$X[k] = \sum_{n=0}^{N-1} x[n] e^{\frac{-j2\pi kn}{N}} \quad (2.8)$$

In this equation, k is the discrete frequency, $x[n]$ represents a point in the time domain signal, $X[k]$ is a point in the frequency domain signal, and N is the number of points in the signal. Unlike with analog filters, digital filters are able to completely negate all frequencies within a specified range through the use of the DFT. We note that the low-pass filter has an infinitely steep drop off at the cutoff frequency, which we can contrast with the analog low-pass filter's finite slope. The complement to the low pass filter is the high pass filter which passes all frequencies above the cutoff frequency and stops all below. Slightly more intricate are the band-pass and band-stop filters which exclusively pass or stop a particular range of frequencies, respectively.

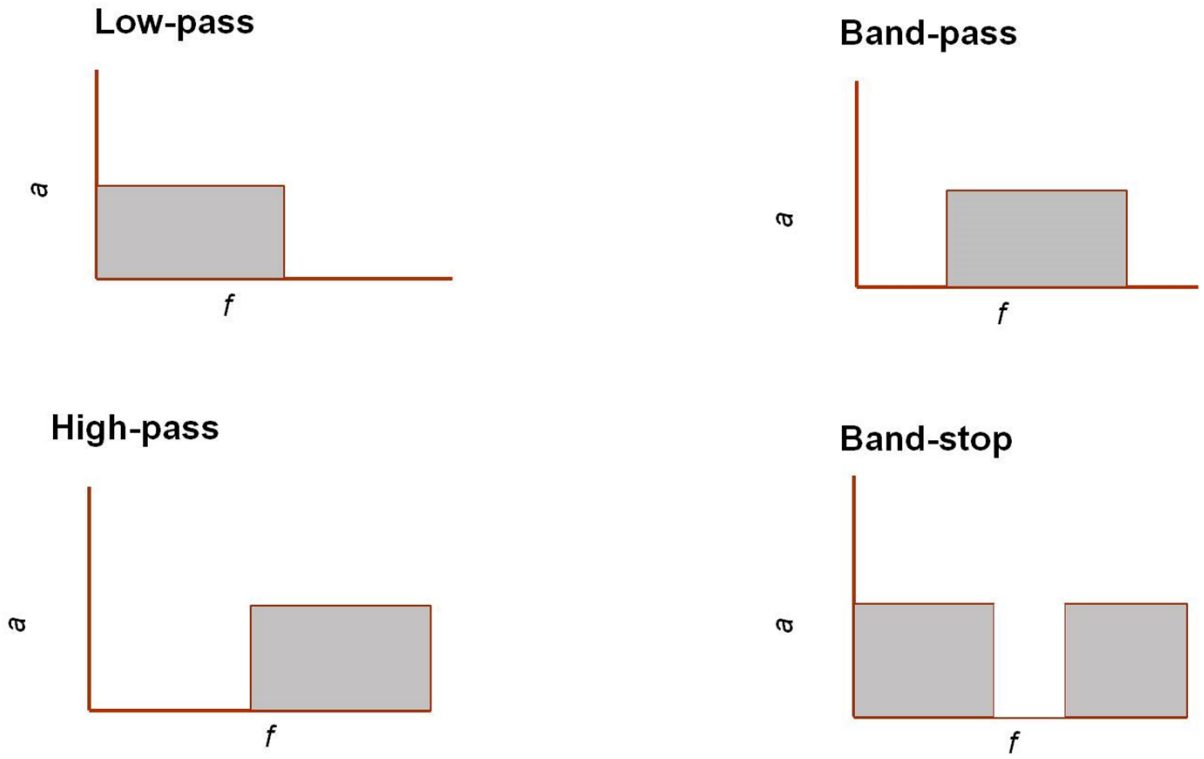

Figure 2-3: Examples of simple digital filters in the frequency domain. Frequency is on the x-axis while magnitude (a) is on the y-axis [7].

Spatial image filters modify the intensity of pixels in images in two-dimensional space. Here, we will briefly go over three types of image filters: thresholds, median filters, and Gaussian filters.

- Thresholding a pixel will typically negate or maximize its intensity if it is above or below a threshold intensity. This technique is useful to label certain pixels of interest and to amplify features in images.
- Median filters are one way to remove noise from an image. A median filter of a certain size will modify a pixel's intensity to be the median intensity of its original value and the values of its neighbors.
- Gaussian filters are another way to remove noise from an image. With a Gaussian filter of a certain standard deviation, a pixel intensity will be modified to be a weighted average of its intensity and the intensities of its neighbors according to the following Gaussian distribution:

$$I[m,n] = \sum_{x=0}^{M} \sum_{y=0}^{N} \frac{1}{2\pi\sigma^2} e^{\frac{-((m-x)^2+(n-y)^2)}{2\sigma^2}} \quad (2.9)$$

  where I is pixel intensity, m and n are the horizontal and vertical indices, respectively, M and N are the horizontal and vertical image dimensions, respectively, and σ is the standard deviation of the Gaussian distribution.

We mainly use these three types of filters in the signal and image processing sections of this thesis when we discuss automated post-processing of force-coupled ultrasound images.

2.1.3 Peak Detection

In the most general form, we define a peak in n-dimensional discrete space to be a point with higher amplitude than all of its neighbors. In one dimension, the following inequalities will apply to a peak at n:

$$x[n] > x[n-1], x[n] > x[n+1] \quad (2.10)$$

In this thesis, we create peak detection algorithms with more specificity to identify relevant signal features to the formation of force-coupled ultrasound images by assigning a force to an ultrasound image. We qualify what constitutes a peak with several conditions, such as a minimum peak distance from one peak to the next, a minimum peak height, and a minimum peak prominence. Sometimes it is useful to find troughs of signals as opposed to peaks which works by performing peak detection on the negative of a signal. Aside from synchronization of force and ultrasound, we also utilize peak detections to identify certain points on arterial pressure and venous pressure waves.

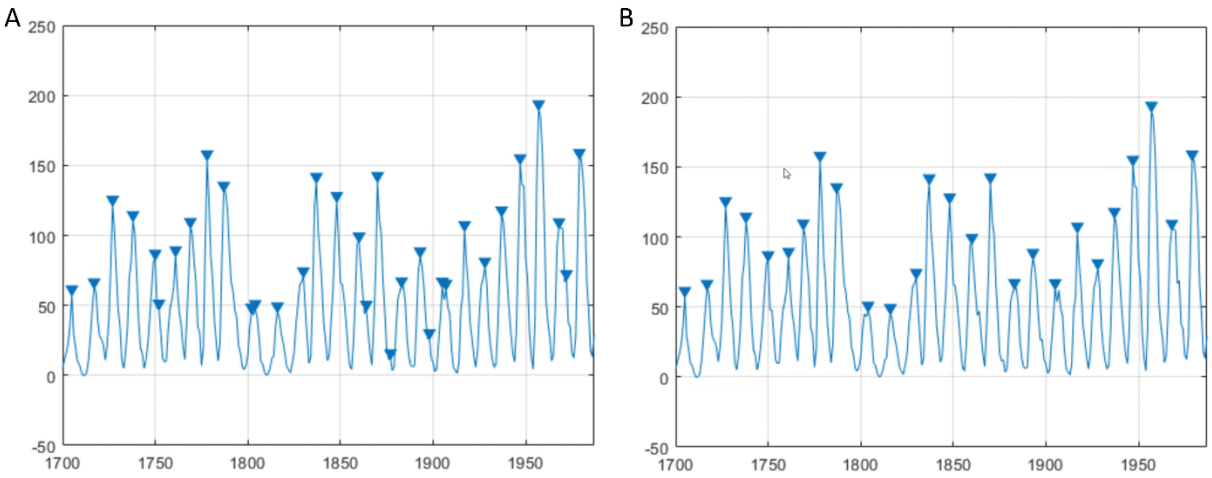

Figure 2-4: (A) MATLAB peak detection run on number of sunspots (vertical axis) by year (horizontal axis) without a minimum peak distance restriction [8]. (B) Peak detection on the same dataset with a minimum peak distance restriction of six years [8].

2.1.4 Optical Flow

Optical flow measures the velocity of certain pixel intensity signals in a set of sequential images from frame to frame. Developed at MIT by Horn and Schunck in 1981, the algorithm assumes smooth pixel distributions in images and is able to capture a higher percentage of movement from frame to frame if the true total movement of all the pixels from frame to frame is small [9].

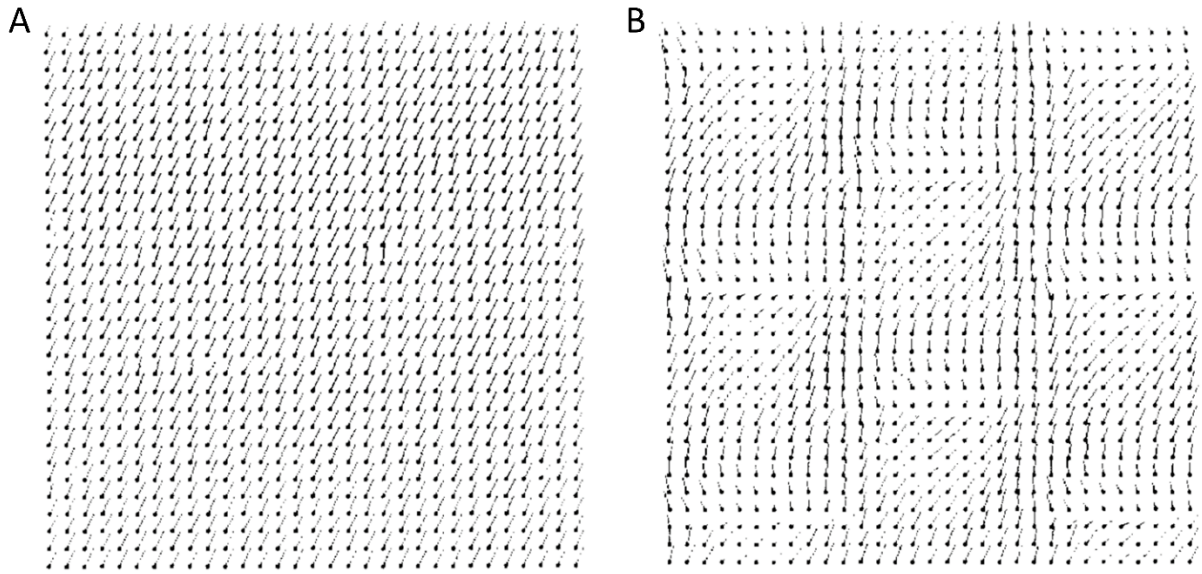

Figure 2-5: (A) Optical flow pixel velocity map with relatively translational movement [9]. (B) Optical flow pixel velocity map with relatively chaotic rotational movement [9].

In this thesis, optical flow ties in with peak detection through integration of the vertical components of the velocity of each pixel over time. Peak detection on that signal is then used to synchronize with the peak detection on the force signal.

2.1.5 Convolutional Neural Networks

An artificial neural network is a powerful tool in applied statistics, machine learning, and artificial intelligence which seeks to simulate the interaction of neurons in the human central nervous system. Each neuron is typically some nonlinear function and the output of the network is usually some classification. A convolutional neural network is a type of neural network, usually applied to images, which has convolutional layers. Each neuron in a convolutional layer convolves its input. Convolution is the operation of pointwise multiplication of every directionally and orderly consistent orientation of a signal with respect to another signal and is represented in one-dimension by the equation:

$$(f * g)[n] = \sum_{m=-M}^{M} f[m]g[n-m] \tag{2.11}$$

where f and g are two discrete functions of finite length. Here g is shifted over f in every arrangement of the two signals with respect to one another [10], [11].

2.1.5.1 Object Detection

An object detection convolutional neural network is used to automatically find certain objects within images. It proposes regions and outputs a probability that a region is an object it has been trained to detect. In this thesis, we train an object detection convolutional neural network called Faster R-CNN to detect blood vessels, specifically the carotid artery and the internal jugular vein [11], [12].

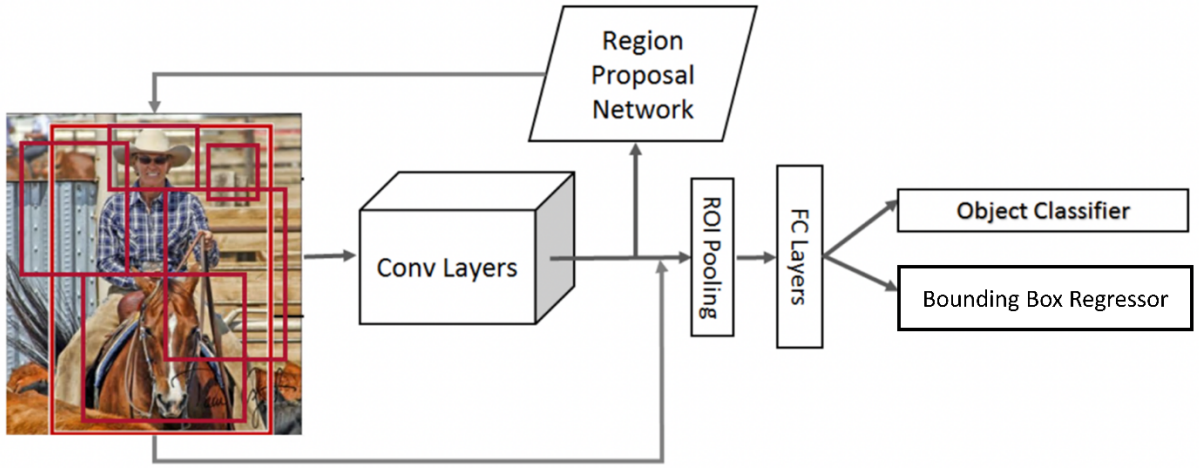

Figure 2-6: Diagram of Faster RCNN object detection convolutional neural network used for carotid artery detection in ultrasound images [13].

2.2 Ultrasound Imaging

Ultrasound imaging generates sound waves at higher than audible frequencies and measures their reflections at certain points in time. The magnitude of these reflections help form an image in a short enough time span that the images can be thought of to be live. Medical ultrasound imaging is perhaps most well-known for imaging a fetus in-utero. Among other medical subspecialties besides obstetrics, cardiology has benefitted greatly by medical ultrasound allowing live images of the heart to be taken with the echocardiogram and vascular imaging. In this thesis we will focus only on ultrasound imaging of large, superficial blood vessels to form force-coupled ultrasound images. In this section, we will go over the fundamental principles of ultrasound imaging necessary to understand the root of the ultrasound images obtained in later chapters [2].

2.2.1 Acoustic Wave Propagation

Most people, knowingly or not, are familiar with the concept of electromagnetic waves, such as visible light, radio waves, and X-rays. These waves propagate at a maximum speed of 300,000,000 m/s and slow down depending on how dense the media is. Acoustic waves, ultrasound waves included, are fundamentally pressure waves which travel from atom to atom within a medium. We have the following formula for the speed of sound in a particular medium:

$$v = \sqrt{\frac{\mathrm{K}}{\rho}} \tag{2.12}$$

where K is the bulk modulus and ρ is the density of the medium. K is substituted for Y, or Young's modulus, when considering a solid as opposed to a fluid. Both numerator terms are quantifications of stiffness. The stiffer the medium, the faster sound will propagate through it. Stiffnesses change more drastically than densities between states of matter, such as solid, liquid, and gas. Therefore, speed of sound tends to be faster in solids than in liquids and faster in liquids than in gases. For example, the speed of sound in air is 331 m/s, the speed of sound in water is 1493 m/s, and the speed of sound in ice is around 3900 m/s [14]–[16].

Another thing to consider in acoustic wave propagation is attenuation. Certain materials, such as highly viscous materials, tend to attenuate sound waves as they propagate more than others by absorbing more energy from the sound waves. Additionally, higher frequency acoustic waves attenuate faster than low frequency waves. We can observe the propagation of an acoustic wave while considering attenuation with the following one-dimensional (z) wave equation:

$$A(z,t) = A_0 e^{j(\omega t - kz)} e^{-\alpha z} \tag{2.13}$$

where A is amplitude, A_0 is unattenuated amplitude, ω is angular frequency, k is special wavenumber and α is the attenuation coefficient. The lower the attenuation coefficient, the deeper an ultrasound probe can image. There is much variance in attenuation coefficients in different human tissues and organs. For example, $\alpha_{blood} \approx 0.18$, $\alpha_{fat} \approx 0.63$, $\alpha_{cardiac\_muscle} \approx 1.8$, $\alpha_{skeletal\_muscle} \approx 3.3$, $\alpha_{bone} \approx 20$, and $\alpha_{lung} \approx 41$. These attenuation coefficients make it prohibitively difficult to image through bones or lungs, which informs placement of an ultrasound probe [2], [17], [18].

Time-gain-compensation accounts for an estimated level of attenuation, depending on the body part for which an ultrasound probe is optimized. This is accomplished by increasing the amplitude of the ultrasound signal more when the ultrasound reflection occurs deeper [2].

2.2.2 Pulse-Echo Ultrasound

A conventional ultrasound image is constructed by having an array of piezoelectric ultrasound transducers emit a pulse through a medium and then receive reflections of the pulse back. To do this, the array is first in transmit mode for a small fraction of the cycle and then in receive mode for the longer rest of the cycle. In transmit mode, the acoustic pulse is transmitted by an ultrasound element which is excited by an electrical signal. In the receive mode, the reflected acoustic pulses are sensed by

that same ultrasound element, converting them to electrical signals. No sensing happens in transmit mode and no pulsing happens in receive mode, hence the term “pulse-echo”. The magnitude of the echo depends on the difference of acoustic impedance at an interface described by:

$$R = \left(\frac{Z_2 - Z_1}{Z_1 + Z_2}\right)^2 \tag{2.14}$$

Where R is the reflection coefficient, Z_1 is the acoustic impedance of the anterior reflector, and Z_2 is the acoustic impedance of the posterior reflector. A reflector is any substance that reflects an acoustic wave. Furthermore, the maximum resolution of the received signal depends on the wavelength of the transmitted signal. A lower wavelength (higher frequency) will provide a higher resolution signal [2], [19].

A key assumption made in conventional commercial medical ultrasound imaging is that the speed of sound is constant throughout the area of the body being imaged. For different types of human tissue which are commonly imaged, therefore excluding bone and lungs, the speed of sound ranges from about 1450 to 1640 m/s. However, the assumption of constant speed of sound is useful because it provides an estimate for the depth of a certain reflected ultrasound pulse based on the time it takes to return to the ultrasound probe. This simple formulation is as follows:

$$d = \frac{T}{2c_{s,t}} \tag{2.15}$$

Where d is the estimated depth of the reflection, T is the time between the pulse occurring and the sensed reflection, and $c_{s,t}$ is the speed of sound estimate for the given tissue being imaged. The coefficient of 2 in the denominator signifies that we are interested in the amount of time it takes for the ultrasound to travel to the point of reflection to give us the distance while T gives the round-trip time. Speed of sound ultrasound imaging does not impose a constant speed of sound, but rather derives the speed of sound through a computational inversion technique [2], [20], [21].

One can imagine a one-dimensional array of ultrasound elements which can produce an image by each element emitting a pulse and then receiving reflections of that pulse. One could digitize reflections coming back to each element in the line of elements as pixels. One element over would be one pixel over horizontally. This would produce a low resolution and unfocused ultrasound image. In 2.2.3 and 2.2.4, we will complete the simplified explanation of forming a conventional B-mode ultrasound image.

2.2.3 Focal Point and Focal Zone Determination

Any emitted plane wave will have a focal point which is dependent on the lens or aperture from which the wave is emitted and the wavelength of the wave. For an acoustic plane wave, the simplest formula to determine the focal point is for a circular aperture with diameter D is:

$$Z_{minF} = \frac{D^2}{4\lambda} \tag{2.16}$$

where $\lambda = v/f$ is the wavelength determined by speed of sound v and frequency f and Z_{minF} is the focal point. In reality, the apertures used are not circular; they are rectangular. However, it is still useful to digest from this formula that increasing aperture size will increase focal point depth. Increasing frequency should also increase focal point depth, but with higher frequency comes steeper attenuation, as mentioned in section 2.2.1. Therefore, manipulating aperture size by turning on an off specific elements in, say, a linear array of elements as with a vascular ultrasound probe, is the method of choice when attempting to adjust focal point depth [2].

Depth-of-field is the zone where the beam width of the acoustic wave is at most twice the beam width of the focal point. Specifically in ultrasound, this is called the focal Fraunhofer zone. It is crucial when imaging blood vessels that the blood vessel to be segmented is within the focal Fraunhofer zone to acquire crisp blood vessel cross-sections for optimal segmentation. If a blood vessel is outside of this zone, more distortion will occur. However, in modern commercial ultrasound systems with linear arrays of elements, dynamic focusing can provide adequate focus throughout the scan depth. Also, apodization, which is a weighting of signal amplitudes in elements when transmitting and receiving a signal, is able to increase depth-of-field such that less dynamic focusing with fewer focal points needs to be provided to produce focus throughout scan depth. That said, a focal depth is still provided and the most focused objects will occur at that focal depth [2].

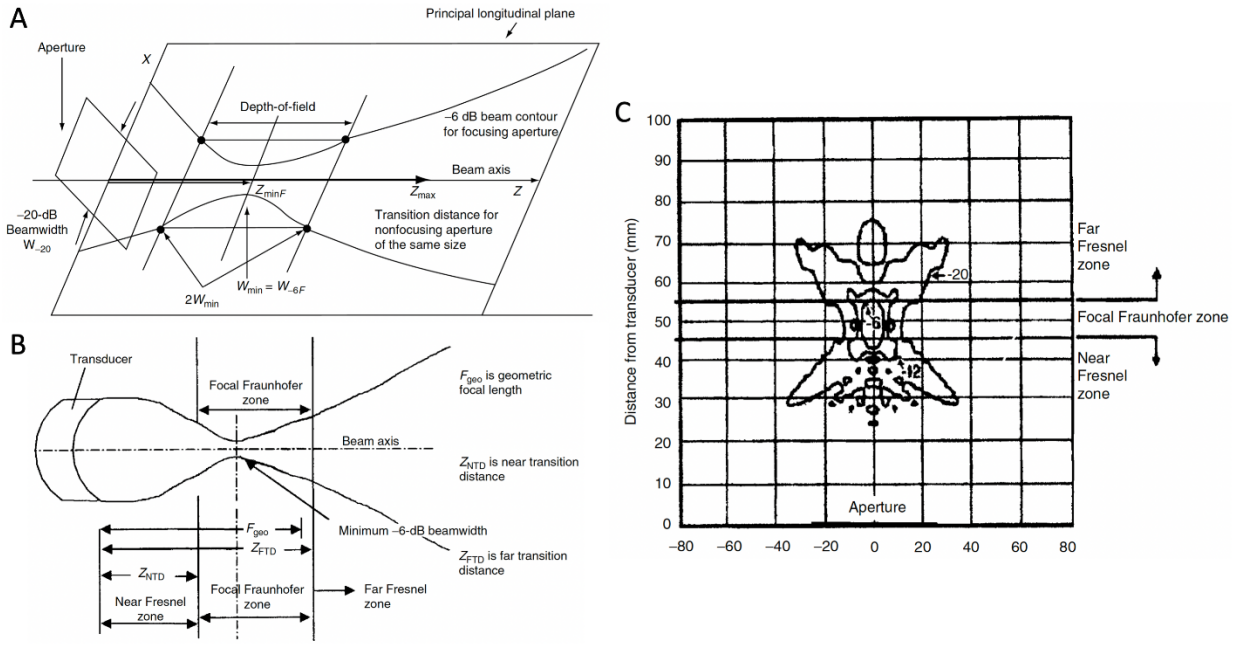

Figure 2-7: Three ways of showing focal points and depth-of-field in ultrasound imaging. (A) Generalized focusing for a beam in a plane [2]. (B) Less generalized beam with a specified transducer as an aperture showing a near zone, a focused zone, and a far zone [2]. (C) Two-dimensional layout of beam contours [2].

2.2.4 B-mode Image Construction

When acoustic reflections are received by an array of ultrasound transducers, certain techniques are employed to maximize image quality. A conventional ultrasound image is called a brightness mode (or B-mode) image. Here we will cover the basics of two essential techniques of B-mode ultrasound imaging called beamforming and logarithmic compression.

2.2.4.1 Beamforming

Beamforming is a general term for methodology regarding delaying, weighting, and summing received signals from an array of ultrasound elements to form a powerful and succinct reflected signal from an object. We note that beamforming cannot be accomplished with a single element as can a focal point because no delays can be provided. In the example below, we see that waves received from elements not completely in-line with an object, or scatterer, will take longer to reach those elements by a predictable margin given speed of sound is constant throughout the region being imaged. To reverse those delays, a complement of delays is applied to each reflection after they are received such that all received signals from the scatterer are in line. Then an apodization is applied to the signals in order to

decrease sidelobe reflections which result from the aperture having a finite size. The apodization will generally increase the signals received near the center of the aperture and decrease the signals received close to the edge of the aperture. The final step is when each of these signals is summed together to form a single reflected signal. Beamforming is an essential component of dynamic focusing, mentioned in section 2.2.3 [2], [22], [23].

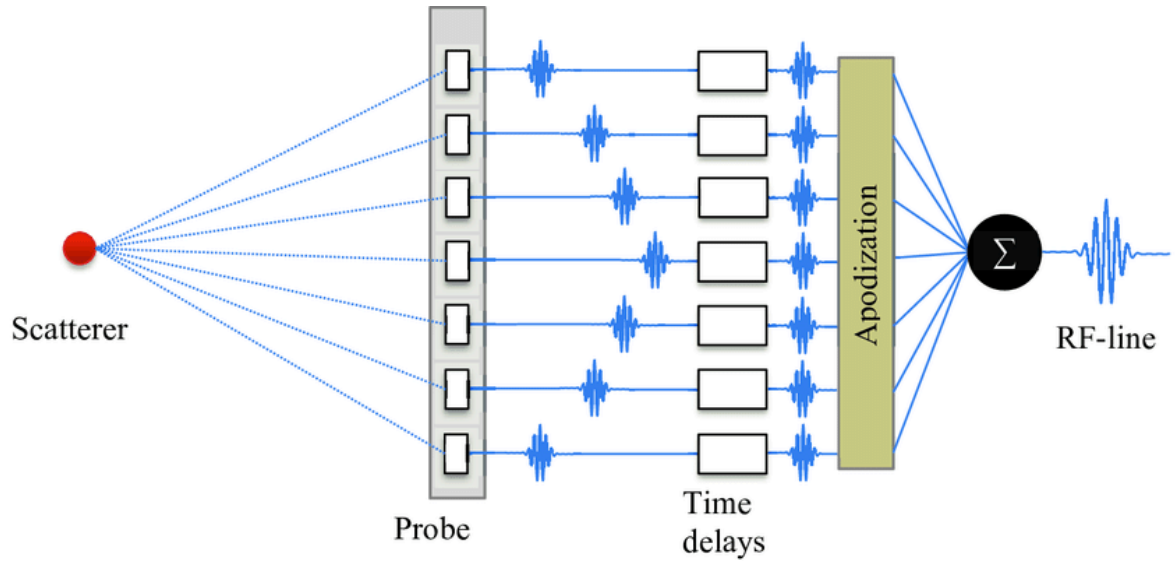

Figure 2-8: Beamforming processing conceptual diagram [23].

2.2.4.2 Log-compression

After beamforming and dynamic focusing, ultrasound images come out focused and crisp. However, if a human were to observe these images, as they often do with ultrasound images in real time, only extremely highly reflective areas, such as bone, would be clearly observed. This is because if one were to observe pixel intensity values on scale with actual magnitude of reflections, most reflections would be close to invisible. To combat this and make ultrasound images more observable, a compression is applied with a logarithmic function to the pixels of the image which will intentionally reduce the dynamic range of pixel values and center the pixel intensities around half of the maximum possible pixel intensity. However, when the average pixel intensity as high as half the maximum possible, say 0.5 if the maximum is 1, the reflections appear brighter than ideal. Thus, a decrease in this average pixel intensity can make images easier to observe as we see from the example in **Figure 2-9** where the decrease is by 13 decibels or by a factor of 4.5 [2], [24].

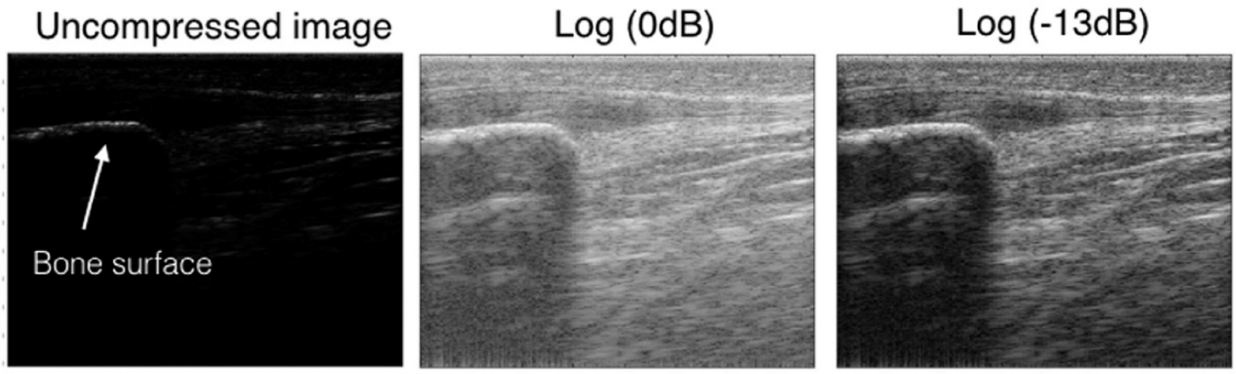

Figure 2-9: Comparison of an ultrasound image without any logarithmic compression (left) to the same ultrasound images with logarithmic compression centered at half maximum pixel intensity (center) and at 13 decibels below half maximum pixel intensity [24].

2.2.5 Shear Wave Elastography

A more recent development in ultrasound imaging is shear wave imaging. In this methodology, an acoustic radiation force is briefly applied in a focused area overlaid on a conventional B-mode ultrasound image. This force emits transverse shear waves in the defined focused area which can be observed in lateral positions in order to derive the speed of the shear wave through the specific tissue. Assuming an isotropic material, which implies consistent material properties independent of the direction of perturbation, one can relate shear speed to the shear modulus via the following formula:

$$G = \rho c_s^2 \tag{2.17}$$

where G is the shear modulus, ρ is density, and c_s is the measured shear speed. The shear modulus is a metric for stiffness itself, but it can be related to the more commonly used Young's modulus via the following equation assuming isotropic and homogeneous material:

$$E = 2G(1 + \upsilon) \tag{2.18}$$

Where E is the elastic modulus (or Young's modulus) and υ is the Poisson ratio describing how compressible the material is. It's worth noting that human tissue is almost never entirely isotropic and homogenous in any given area. We must not assume exceptional accuracy when attempting to convert a measured shear speed to a Young's modulus. Rather, we assume directional accuracy such as interpreting a positive change in the shear speed to correspond to positive changes in the shear modulus and Young's modulus [2], [25], [26].

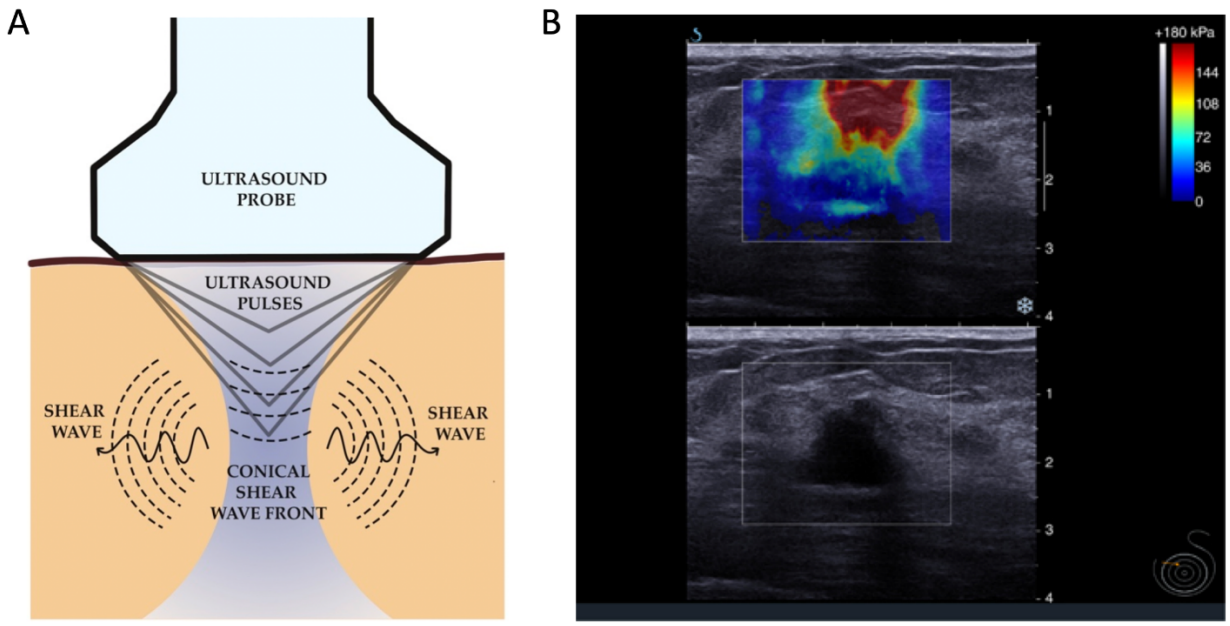

Figure 2-10: (A) Conceptual diagram of shear wave generation from an ultrasound probe [27]. (B) Example of a shear wave elastography image of a breast tumor [28].

2.3 Force Measurement

Mechanical force is the product of a mass and an acceleration of that mass. Perhaps the most common measurement of force can be found in the act of weighing something or someone. Hence, the weight of something is its mass multiplied by the acceleration of Earth's gravity (about 9.8 m/s^2 at sea level). Some weight scales – or balances – are digital in that they convert an applied force to an electrical signal nearly perfectly proportional to that applied force. This type of force measurement is highly relevant to force-coupled ultrasound, the application we will focus on for the rest of this section. In force-coupled ultrasound, we use a load cell, comprised of strain gauges to measure force applied by an ultrasound probe while accounting for the weight of the probe using an accelerometer [29].

2.3.1 The Strain Gauge and Load Cell

A strain gauge is a type of electrical resistor whose resistance changes depending on how much mechanical strain it experiences, which is linear with stress – in other words, linearly elastic. A constant current can be passed through a strain gauge to measure the voltage across the strain gauge. A load cell is merely a combination of strain gauges best arranged to produce an accurate and large range of force measurements. Often some strain gauges are specialized to compress and have lower resistance due to

being wider while others are specialized to extend and have a higher resistance due to being narrower. The formula for resistance R of a cylinder explains this phenomenon:

$$R = \frac{rl}{A} \tag{2.19}$$

where r is the intrinsic resistivity of the cylinder material, l is its length, and A is its cross-sectional area. Strain gauges can alter length and cross-sectional area. The Wheatstone bridge is a common arrangement of strain gauges in a load cell which has the measurement capabilities of tension and compression, which correspond to negative and positive force, respectively, in force-coupled ultrasound. In terms of voltage measurement, it is the opposite. Load cells usually have an active end and fixed end along with an inactive remainder of body to provide good constraint of measurement [30]–[32].

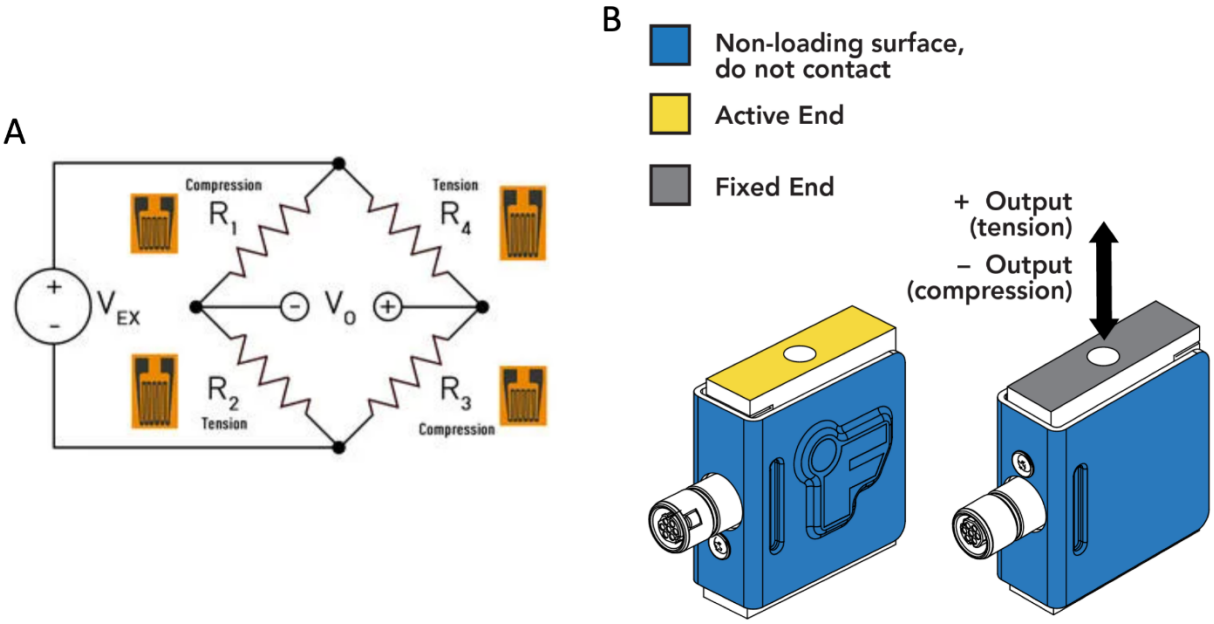

Figure 2-11: (A) Wheatstone bridge circuit configuration of strain gauges [31]. LSB205 load cell diagram [30].

2.3.2 Angle Calculation with Accelerometer

Many accelerometers have three axes on which acceleration can be measured to account for physical space. Through rotation matrices and the assumption of gravity being the only acceleration present when the accelerometer is fixed, we can derive two angles of orientation of a structure. For a

force-coupled ultrasound probe, these angles are sufficient to determine the weight from the probe pushing or pulling on the load cell. We start from the system of equations:

$$\begin{bmatrix} a_x \\ a_y \\ a_z \end{bmatrix} = \boldsymbol{R} \begin{bmatrix} 0 \\ 0 \\ g \end{bmatrix} \tag{2.20}$$

with the components of acceleration on the left and the rotation matrix $\boldsymbol{R}$ multiplied by the acceleration of gravity g on the right. We end up with yaw ϕ and pitch θ angles for the structure:

$$\phi = \tan^{-1}\left(\frac{a_y}{a_z}\right) \tag{2.21}$$

$$\theta = \tan^{-1}\frac{-a_x}{\sqrt{a_y^2 + a_z^2}} \tag{2.22}$$

Being able to calculate the orientation of the structure on which a load cell resides, such as a force-coupled ultrasound probe, accounts for weight experienced by the load cell due to the structure of what it is mounted on. These angle measurements can also provide reference points for orthogonality of blood vessels as we will cover in chapter 4 [33].

2.4 Structural Modeling

Direct signal and image processing of force-coupled ultrasound imaging are inherently observations wherein one observes real physiology occurring in the force-coupled ultrasound images. In order to predict measurements which cannot be measured via direct observation, some sort of model must be applied which abstracts away real physiology for pure mathematics and aims to intelligently predict that measurement. Definitionally, the model prediction can never be quite as accurate as a direct measurement if one exists. That said, models are often far more convenient. In the case of this thesis less costly and safer to apply than direct measurements. Therefore, “all models are wrong, but some are useful” [34].

In this thesis our modeling is mostly of the carotid artery, internal jugular vein, and their surrounding tissue. We call these *structural* models as they seek to emulate real structures. We will now cover finite difference modeling which is seldom used in this thesis as a lead-in for finite element modeling which is used often. We will then conclude this technical background chapter with an

explanation of inverse modeling which allows us to effectively compare our structural models with observations made in reality.

2.4.1 Finite Difference Modeling

As mentioned earlier in this chapter discretizing reality is often mathematically beneficial as it offers a high flexibility of computation. A finite difference model lumps continuous structures into discrete, volume-less points at a specific place in space and time. An electrical circuit model is a commonly applied finite difference model as it contains discrete electrical potentials which may be time-dependent but does not contain information for electrical potentials anywhere in space. An example of a finite difference written out is the derivative formula for discrete mathematics:

$$\frac{dx}{dt} \approx \frac{x(t+\Delta t) - x(t)}{\Delta t} \tag{2.23}$$

Here, the function x is only defined at times t and $t + \Delta t$ and nowhere in between. Therefore, to approximate its derivative in time, one must take a finite difference in the function and divide it by the time in between the two points defined by the function.

2.4.2 Finite Element Modeling

Unlike a finite difference model, a finite element model has elements which have a finite size and are directly connected to each other via a mesh, as shown in **Figure 2-12**A. This mesh can be perturbed by some boundary condition acting on it, yielding various stress, strain, and displacement for each element, with stress depicted in **Figure 2-12**B [35].

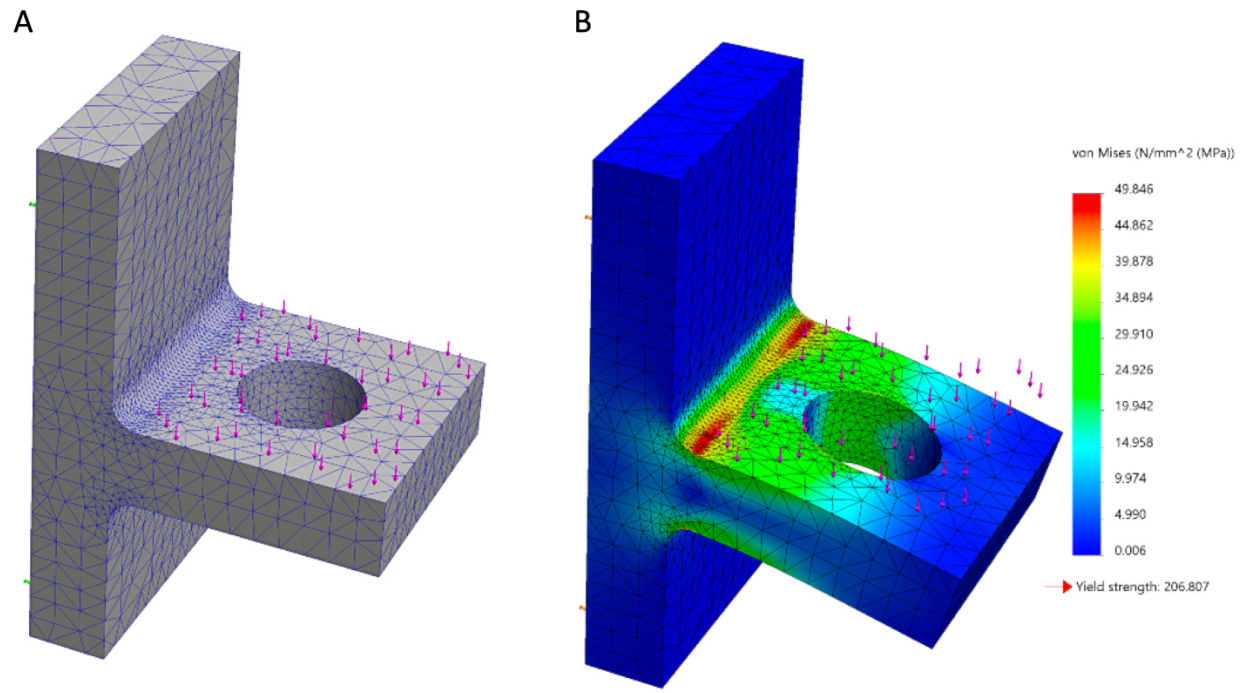

Figure 2-12: (A) Triangular mesh of a finite element model of a hinge [36]. (B) Color-coded stress map of the hinge finite element model in response to a downward force [36].

In structural finite element modeling, each element will have its own stiffness matrix which must be derived through solving various partial differential equations (PDEs). Direct solving of these PDEs with given boundary conditions is called the strong formulation. However, many partial differential equations either don't have a known analytical solution or require costly computation to produce an analytical solution. Most finite element software instead use numerical approximations for the solutions to the PDEs called weak formulations. The Galerkin method of weighted residuals, which uses a linear combination of trial functions with unknown coefficients (weights) to formulate a solution to a given PDE with residual error, is a commonly used weak formulation. We have:

$$y(x) = \sum_{j=1}^{n} w_j f_j(x) \tag{2.24}$$

with $y(x)$ the solution, w_j a weight, and $f_j(x)$ a trial function. In this method, the solution is found by solving for the weights which minimize the residual error from plugging the solution back into the PDE [35].

Solving finite element models are computationally expensive, often with tens of thousands, if not hundreds of thousands, of degrees of freedom which depend on the number of elements in the model. It is useful to have a large number of small elements in areas of the model in which

measurement is sensitive because it leads to higher accuracy. Hence, the finite element modeling software COMSOL is used to produce and solve the finite element models of this thesis.

2.4.3 Inverse Modeling

In this thesis, finite element models are nested into inverse models which allow one to iteratively solve for parameters such as the lumen pressure and stiffness of a blood vessel. We use the finite element model to predict measurements we can observe in real life. We use the inverse model to measure the error between the predicted measurements and the real observations and provide new informed guesses to plug into the finite element model. How we provide those new informed guesses is where inverse optimization comes into play [37].

Gradient descent is an umbrella term for describing how an optimization decides what to guess next. Every optimization has a cost which it aims to minimize. In gradient descent, a cost function which most likely doesn't have an analytical formula solution is numerically and locally linearized to estimate its derivative. Then the optimization "descends" the cost function by adjusting its input variables in the direction of the derivative (gradient). There are three main flavors of gradient descent: batch, mini batch, and stochastic. Batch gradient descent calculates the gradient with respect to all parameters and updates all parameters in the same iteration. Mini-batch gradient descent does so with a smaller subset of parameters chosen at random for each iteration. Stochastic gradient descent does so with only one parameter chosen at random for each iteration. In each of these versions, the learning rate, the magnitude of the adjustment in any or all input variables, can be altered within the gradient descent. Convergence criteria are usually specified based on the cost function and/or derivative of the cost function falling below a specified value and/or the learning rate for the input variables falling below a specified value [37].

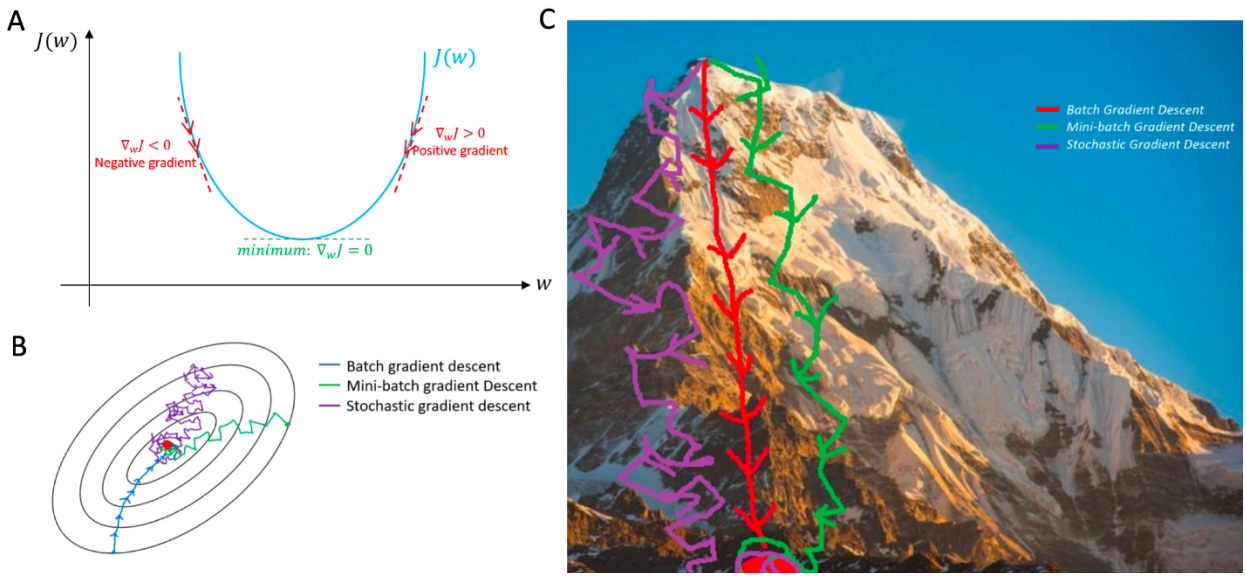

Figure 2-13: (A) Simplified model of a general gradient descent algorithm [38]. (B) Two-dimensional comparison of the three basic gradient descent algorithms [38]. Using an image of the 8000-meter altitude Annapurna in Nepal to provide a rendered three-dimensional example of the three basic gradient descent algorithms [38].

In this thesis, the optimization algorithm employed most often is the Nelder-Mead (downhill simplex) algorithm. This algorithm still descends a cost function in a variety of ways but does not calculate a gradient or use randomness when doing so. Throughout the optimization, there is a structure called a working simplex which can be thought of as a shape with n+1 vertices in n-dimensional space, with each dimension representing a parameter. Vertices x_1 to x_n are generated off of an initial point x_0 in the following way:

$$x_i = x_0 + \eta_i e_i \tag{2.25}$$

where η_i is a step size or learning rate and e_i is an orthogonal unit vector in n-dimensional space. The simplex is then transformed until it meets the convergence criteria [39], [40].

Each transformation starts with ordering the vertices of the simplex from lowest to highest cost. A centroid is calculated from all vertices except the one with the highest cost. Then a variety of different transformations can ensue depending on the relationships among the vertices with the highest, lowest, and second lowest costs $J(x_n)$, $J(x_1)$, and $J(x_2)$, respectively:

- **Reflect:** Find x_r, the reflection of x_h across the hyperplane not including x_h. If $J(x_2) > J(x_r) > J(x_1)$, replace x_n with x_r. This requires one cost function calculation (run of the forward model).

- **Expand:** If $J(x_1) > J(x_r)$, replace x_n with x_e, the further expansion of x_r in the same direction as reflection. Together with reflection, this requires two cost function calculations.
- **Contract inside:** If $J(x_r) > J(x_n)$, find x_{ci}, a point between the centroid and x_h not contained in the hyperplane from which the centroid is calculated. If $J(x_{ci}) < J(x_n)$, replace x_n with x_{co}. Together with reflection, this requires two cost function calculations.
- **Contract outside:** If $J(x_n) > J(x_r) > J(x_2)$, find x_{co}, a point between the centroid and x_r not contained in the hyperplane from which the centroid is calculated. If $J(x_{co}) \leq J(x_r)$, replace x_n with x_{co}. Together with reflection, this requires two cost function calculations.
- **Shrink:** If $J(x_{co}) > J(x_r)$ or if $J(x_{ci}) \geq J(x_h)$, replace every point in the simplex except x_1 with points closer to x_1. Together with reflection and contraction, this requires n+2 cost function calculations.

The convergence criteria of the Nelder-Mead method is that both the cost function range and parameter range of the simplex must be below specified thresholds. It is possible for the method to converge to non-stationary points if parameters are not well-conditioned [37], [39], [40].

Chapter 3 – Background – The Cardiovascular System and its Pressures

The cardiovascular system provides the body's organs with the oxygen they need to function properly. Within the cardiovascular system there are pressure gradients which dictate the proper direction of blood flow, the filling and emptying of both the right heart and the left heart, and the diffusion of oxygen from blood vessels to tissue. The two ventricles of the heart are responsible for providing increases in pressure as blood flows through it while everywhere else decreases pressure as blood flows through. The pumping action of the ventricles is reflected in the pressure wave which generally attenuates down the system and pulmonary arterial trees. Given arterial pressure and venous pressure are at the center of this thesis, we will discuss the cardiovascular system in the context of pressure [41].

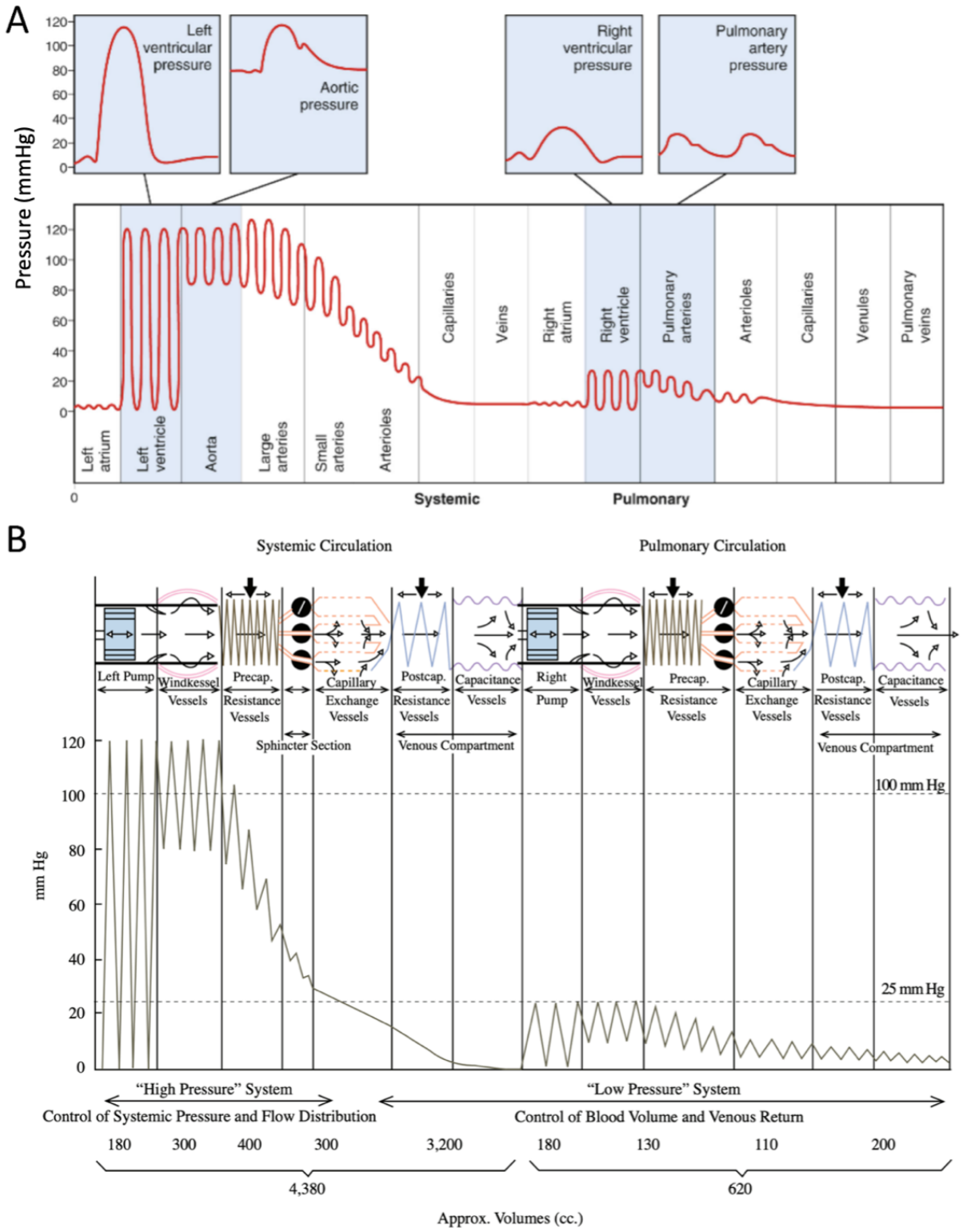

Figure 3-1: (A) Illustration of pressure in (mmHg) throughout the cardiovascular system [41]. (B) Hybrid circuit model of cardiovascular system with pressure shown throughout. The graph lines are spatially dependent and conceptual [42], [43].

3.1 Cardiovascular Physiology

The high-level path of blood through the cardiovascular system is as follows. Oxygen-rich blood is pumped from the left atrium into the left ventricle through the mitral valve, where it is pumped out of the left ventricle through the aortic valve. The blood travels through the systemic arterial tree through smaller arterioles and then even smaller capillaries. The deoxygenated blood then travels through the venules and then the veins until reaching the right atrium of the heart. The right atrium then pumps into the right ventricle through the tricuspid valve, where it is pumped out of the right ventricle through the pulmonary artery valve. The pulmonary circulation is a miniaturized version of the systemic network where blood is oxygenated. This oxygenated blood finally enters the left atrium [41].

At any given time, about 7 percent of the blood is in the heart, 9 percent is in the pulmonary circulation, and 84 percent in the systemic circulation. We note that the low pressure and very compliant systemic venous system by itself holds 64 percent of the blood on average [41], [44], [45].

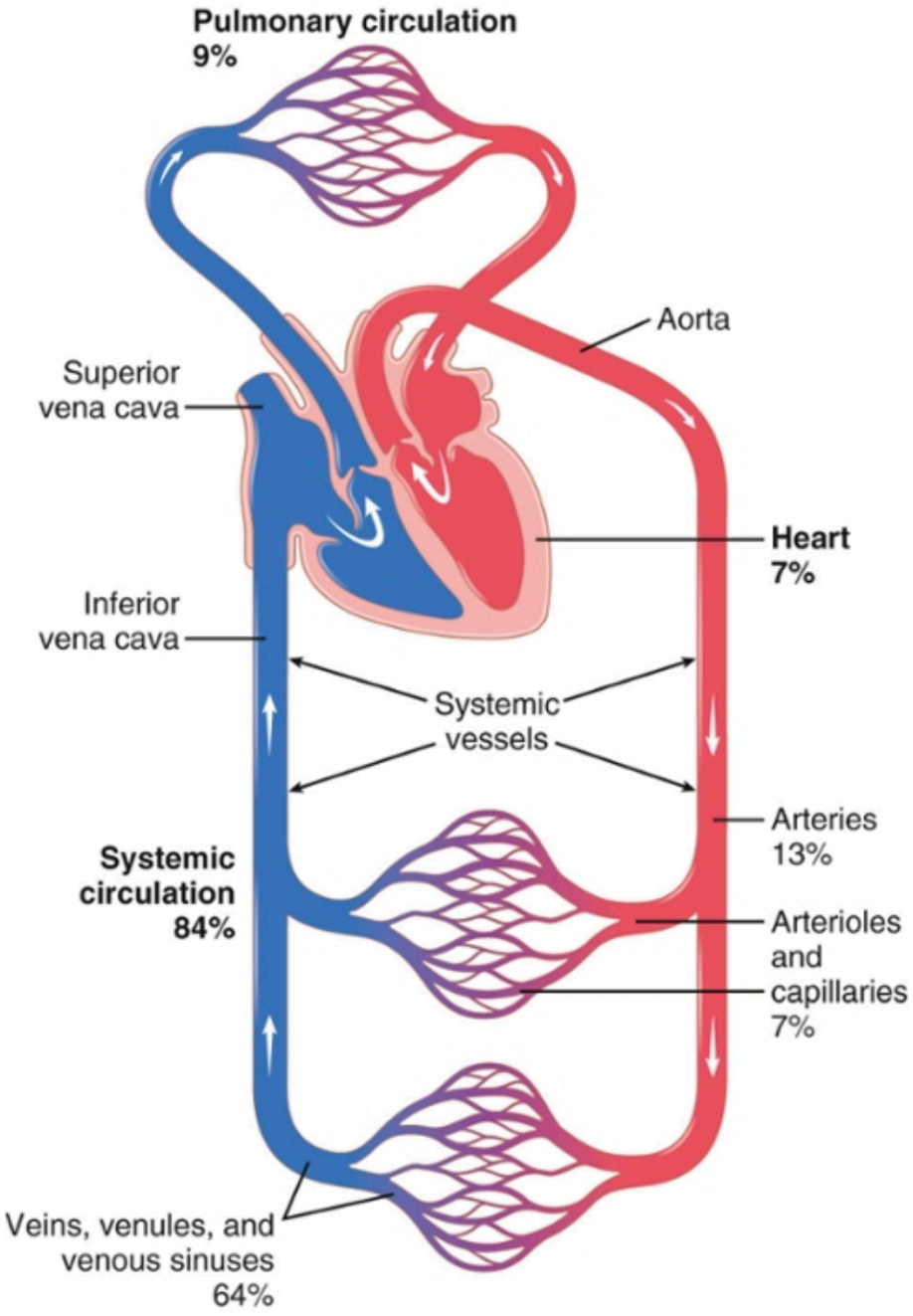

Figure 3-2: Simplified diagram of the cardiovascular system blood volume distribution. Adapted from [41].

Within the systemic circulation, blood goes to various organs and muscle. Certain organs are highly prioritized. For instance, despite its small mass of about 1.3 kg, the brain receives 14 percent of cardiac output. This is due to the heart's high prioritization of supplying blood to the brain. The kidneys, which perform the function of filtering the blood, receive 22 percent of cardiac output [44], [45].

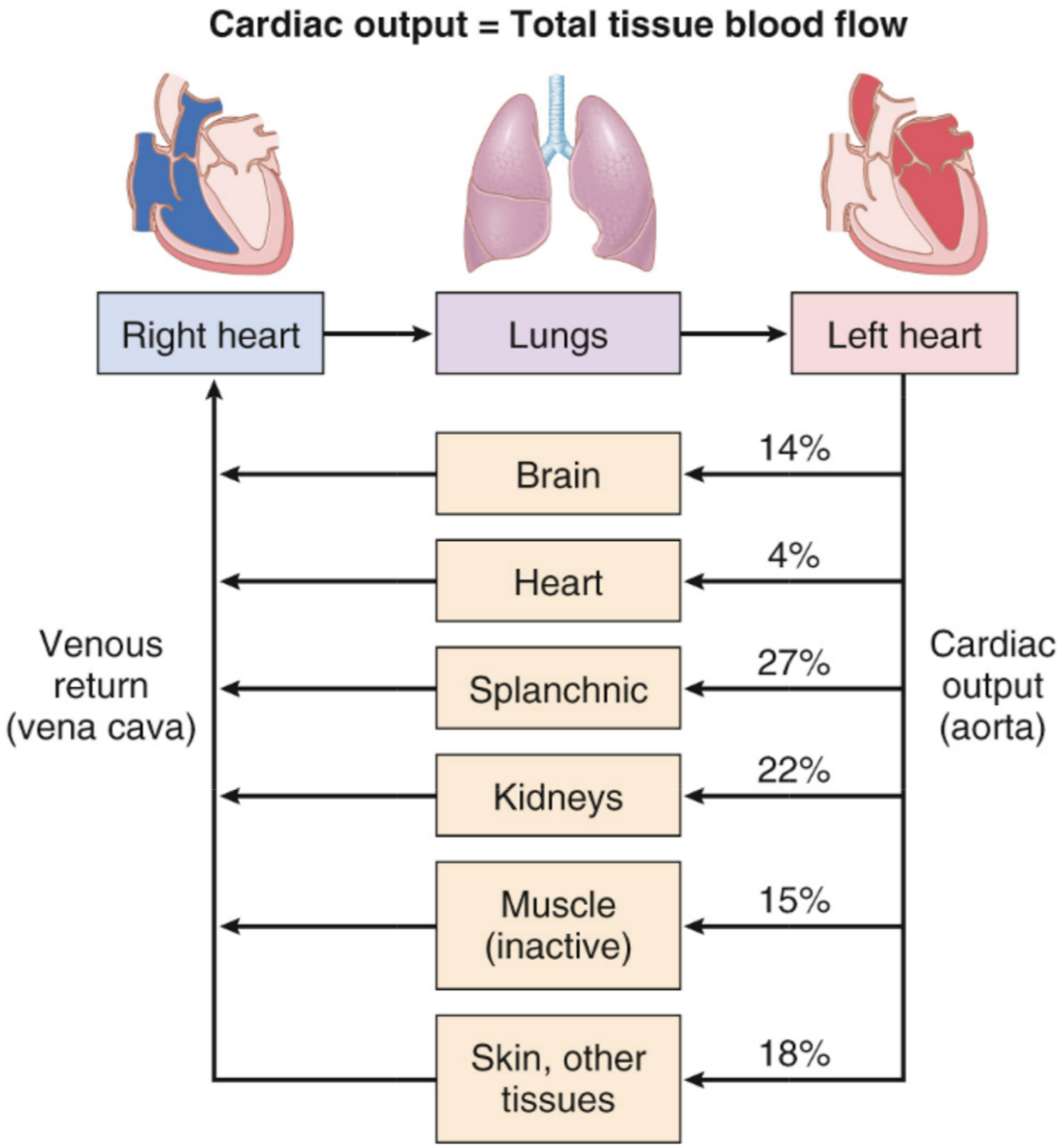

Figure 3-3: Diagram of cardiac distribution among organs. Adapted from [41].

Next, we discuss how enough pressure gradient is generated to distribute blood throughout the systemic circulation and pulmonary circulation via the heart.

3.1.1 The Heart

The heart is the muscular organ which pumps blood to the rest of the body. In order to synchronously pump blood from the atria to the ventricles and then from the ventricles to the pulmonary and systemic circulation, an electrical signal propagates through the heart's Purkinje fibers. This propagation signals a contraction (depolarization) to pump blood out of a chamber and then a relaxation (repolarization) to refill the chamber with blood [41].

The electrical path is as follows. The signal originates in the sinoatrial (S-A) node, which has cells which automatically depolarize and repolarize with a frequency of the heart rate. The signal propagates through the atria to get to the atrioventricular (A-V) node. After spending about a tenth of a second in the A-V node, the signal propagates through the ventricles via the bundle branches located in the intraventricular septum [41].

The electrocardiogram (ECG) shows a projection of the heart electrical signal onto an electrical lead on the surface of the skin. There are three typical components to the ECG morphology for each heart beat: the P-wave, the QRS-complex, and the T-wave. The P-wave signals the depolarization of the atria. The QRS-complex signals the depolarization of the ventricles and the repolarization of the atria. The T-wave signals the repolarization of the ventricles. We note that after, and not during, each depolarization is when the contraction occurs, pumping blood out of each chamber [41], [46].

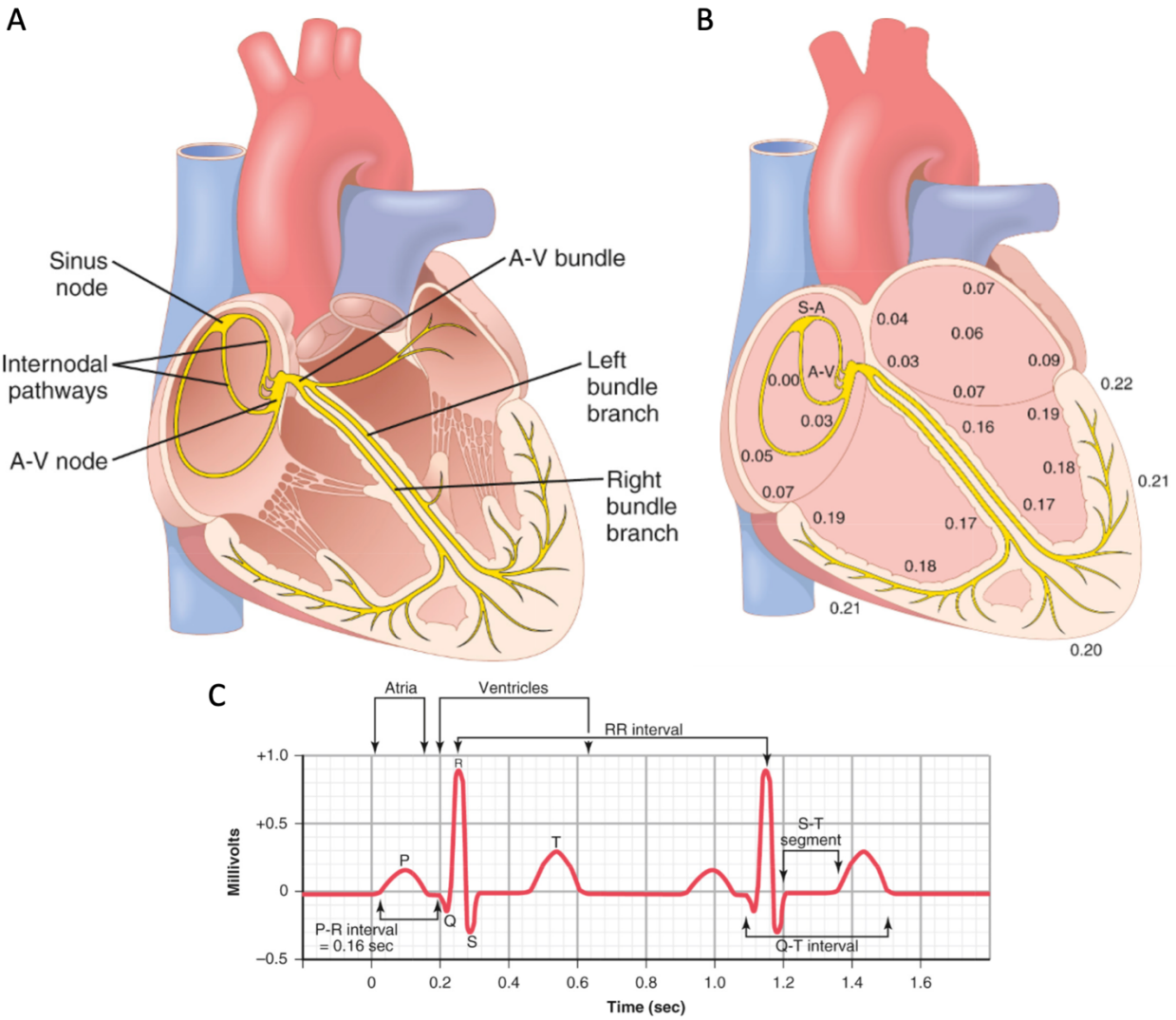

Figure 3-4: (A) Electrical pathway diagram of the heart which shows the structure of the Purkinje fibers. (B) Shows the time (in seconds) that the electrical signal takes to reach different sections of the electrical fibers. (C) Two heart beats from an electrocardiogram signal (ECG), labeling key intervals and where atria and ventricles are reflected in the signal. Adapted from [41].

The heart is divided into two pumps: the right ventricle which delivers blood to the pulmonary circulation to be oxygenated and the left ventricle which delivers oxygenated blood to the systemic circulation to be metabolized. The left ventricle is required to pump blood much farther in the body than the right ventricle. Therefore, it is much more powerful – by a factor of ten – and generates a much higher pressure. The left and right ventricle are electrically synchronized in that they fill and contract at the same time. Additionally, the right ventricle largely mirrors the left ventricle, just at lower power [41], [47].

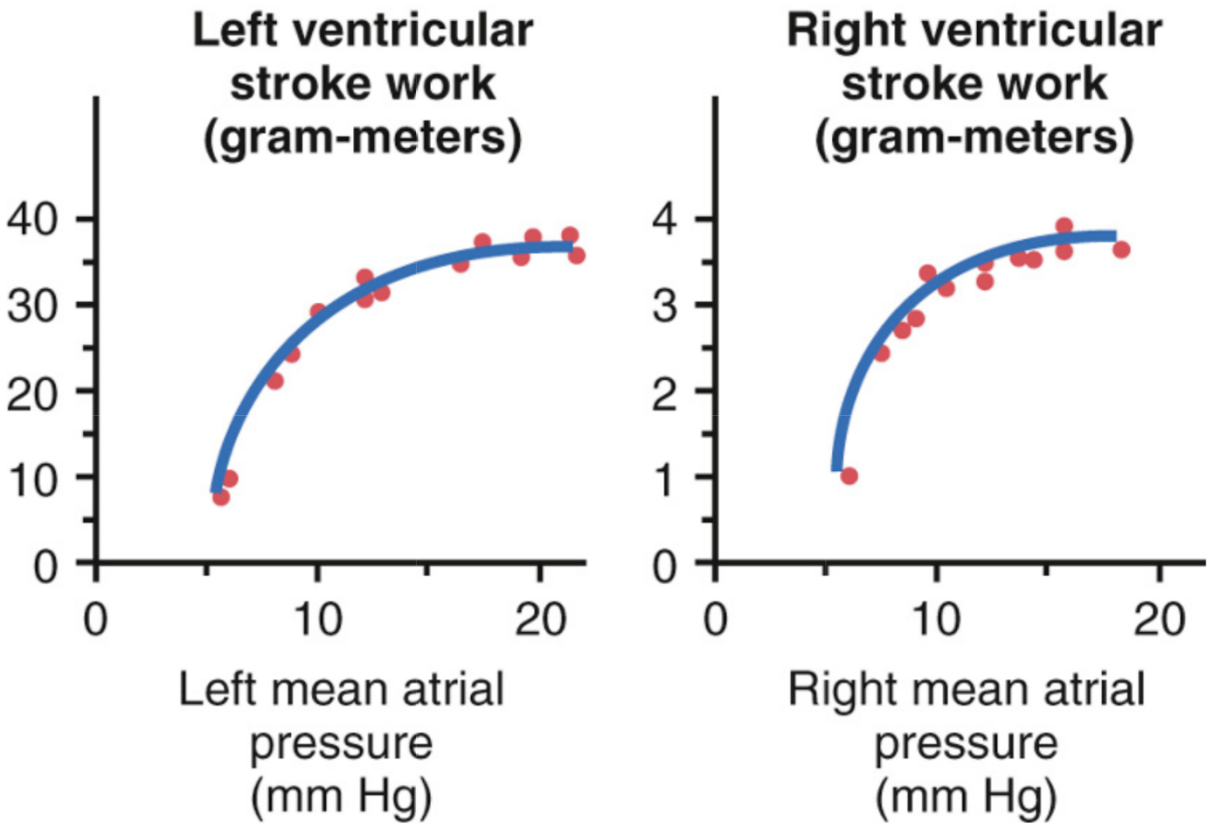

Figure 3-5: Showing work done per stroke of each ventricle as a function of respective atrial pressure. Adapted from [41].

The left ventricle has four phases: (I) Filling, (II) Isovolumetric Contraction, (III) Ejection, and (IV) Isovolumetric relaxation. In filling, the mitral valve opens, letting in blood from the left atrium to fill the left ventricle. Isovolumetric contraction occurs when the mitral valve closes and pressure rises to the diastolic arterial pressure. At this point, the aortic valve opens, commencing the period of ejection where blood is pumped into the systemic circulation until the pressure in the left ventricle goes below the pressure in the aorta, causing the aortic valve to close. Isovolumetric relaxation occurs until left ventricle pressure reaches left atrium pressure, allowing the mitral valve to open [41].

One quantity evident in left ventricular pressure volume loops is the stroke volume which is the subtraction of the isovolumetric relaxation volume from the isovolumetric contraction volume. Cardiac output is calculated by multiplying the stroke volume from the heart rate. Left ventricular ejection fraction is the amount of blood expelled from the left ventricle divided by the end-diastolic volume of the left ventricle [41], [48].

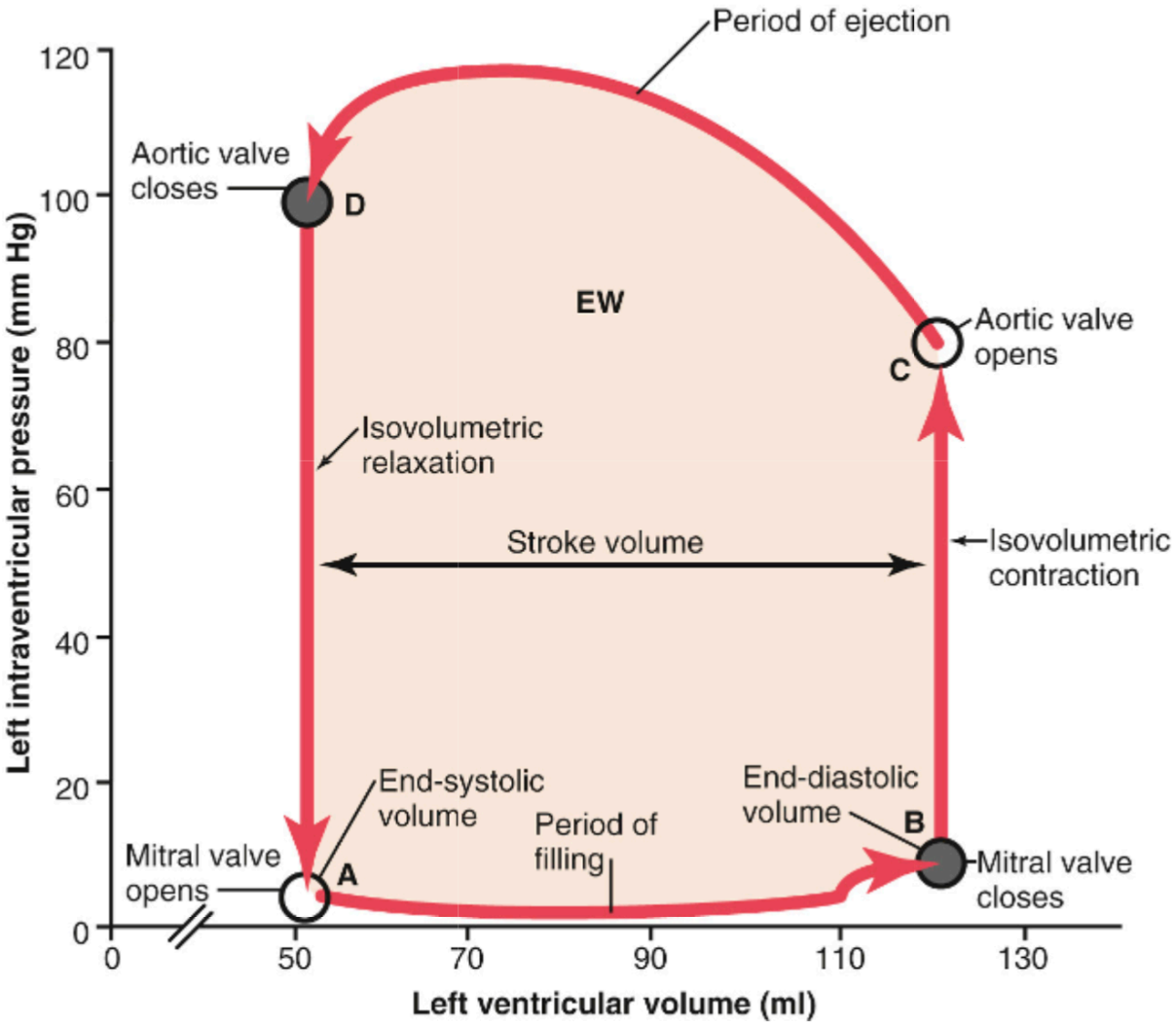

Figure 3-6: Labeled left ventricular pressure-volume loop. Adapted from [41].

It is also common to track left ventricular volume and pressure in the time domain along with the ECG and the phonocardiogram (PCG). The time domain affords one the ability to observe the dependence of one signal on the other. In the span of one cardiac cycle, we first note the P-wave of the ECG signifying the electrical depolarization of the atria leading to contraction of the atria, pumping blood into the ventricles, seen in the left ventricular volume (LVV) and pressure (LVP) curves. The closing of the mitral and tricuspid valves (A-V valves) causes the first heart sound. Next, the QRS-complex signifies the depolarization of the ventricles leading on the contraction of the ventricles, seen in the LVV remaining constant and then rapidly descending and the LVP ascending and descending. The closing of the aortic and pulmonary valves causes the second heart sound. Finally, the T-wave signifies the electrical repolarization of the ventricles, which leads to the relaxation and filling of the ventricles, seen in the LVV constant and then increasing and LVP rapidly decreasing and then constant. The mitral and

tricuspid valves opening allows for the filling of the ventricles. We also observe pressure signals from the atrium and the aorta which illustrates what causes the opening and closing of heart valves [41], [47].

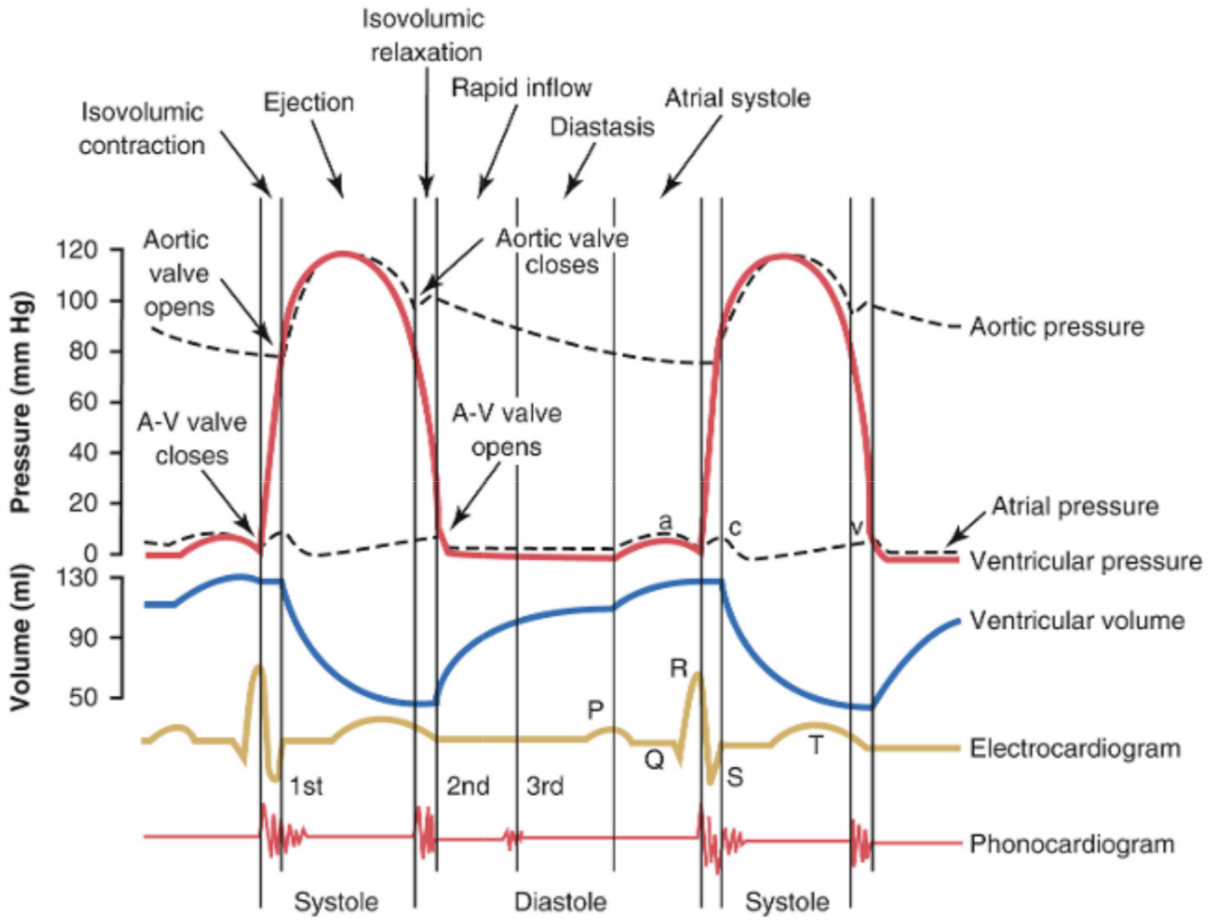

Figure 3-7: Time-domain plot of multiple modality heart signals. Adapted from [41].

We now turn to the input of blood to the heart's right atrium, the venous return, and the output of blood from the left ventricle of the heart, the cardiac output. For completeness, we note that the amount of blood entering the right atrium and left atrium should be about equal and the amount of blood leaving the right ventricle and left ventricle should be equal. This is because the heart's left and right side should be have conserved blood flow [41].

Cardiac output and venous return curves are usually expressed as monotonic functions of right atrial pressure. Cardiac output is increasing while venous return is decreasing. Their intersection point acts as an operating point at a specific right atrial pressure and cardiac output / venous return. The sympathetic nervous system can increase cardiac output and venous return by means of increasing heart rate, increasing cardiac contractility, and vasodilation. The nonzero baseline sympathetic

stimulation means that when it is removed, such as with spinal anesthesia, cardiac output and venous return decrease [41], [44], [49].

Also displayed in the shifted cardiac output and venous return curves is the cardiac reserve. The cardiac reserve is the difference between a person's normal cardiac output and the maximum attainable cardiac output. Sympathetic stimulation can cause cardiac reserve to rise to 400% of cardiac output in a normal healthy individual, as shown by the maximum of the green plot compared to point A in **Figure 3-8**A. This allows the heart to pump adequate blood to the muscles of the body during heavy exertion [50].

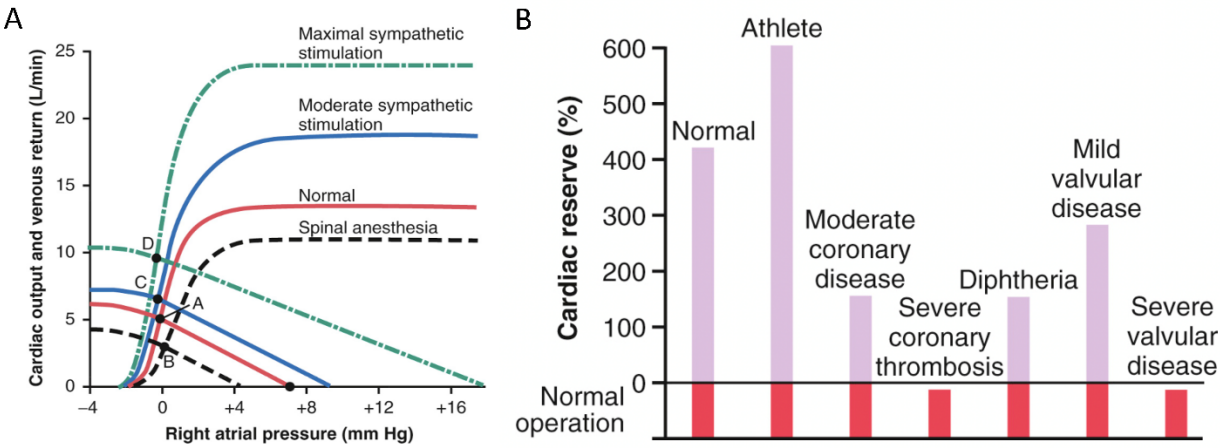

Figure 3-8: (A) Cardiac output and venous return curves in response to different levels of sympathetic stimulation. Adapted from [41]. (B) Cardiac reserve given various physiologies and pathologies. Adapted from [41].

3.1.2. The Blood Vessels

Various blood vessels transport blood throughout the pulmonary and systemic circulation. The heart pumps blood through arteries at high pressure. The pressure drops significantly after passing through high resistance arterioles. Capillaries are where the vast majority of nutrient and fluid exchange takes place. This exchange is largely dictated by the expression:

$$P_c - P_{if} + \pi_{if} - \pi_c \tag{3.1}$$

where P_c is capillary fluid pressure, P_{if} is interstitial fluid pressure, π_{if} is interstitial osmotic pressure, and π_c is capillary osmotic pressure. The sign of this equation dictates which direction the fluid exchange occurs: positive is out of the capillaries and negative is into the capillaries. Capillaries then lead to venules, which then lead to veins [41], [51].

Arteries and veins are the two largest types of blood vessels and are therefore easiest to observe individually. Stiff and thick-walled arteries are designed for high pressure, pumping transport of blood while compliant and thin-walled veins are designed for low pressure, passive transport of blood. The pumping of the heart anterior to the arteries and the valves within the veins keep blood flowing in the correct direction. One key difference between arteries and veins is the thickness of their walls as the structural layers of their walls are similar. Thick walls contribute to less compliance but also sturdier structures which are built to withstand high blood pressure without losing any fluid through them. In the arteries, the stiffness of these walls and the narrowing of individual artery diameters along the arterial tree causes a sizeable increase in pulse pressure compared to the aortic pulse pressure, mainly manifesting in increased systolic pressure. Another difference, as mentioned before, is that veins have valves. These valves work with muscle to push blood back to the heart, ensuring blood does not flow backwards, especially in the legs [41], [52]–[55].

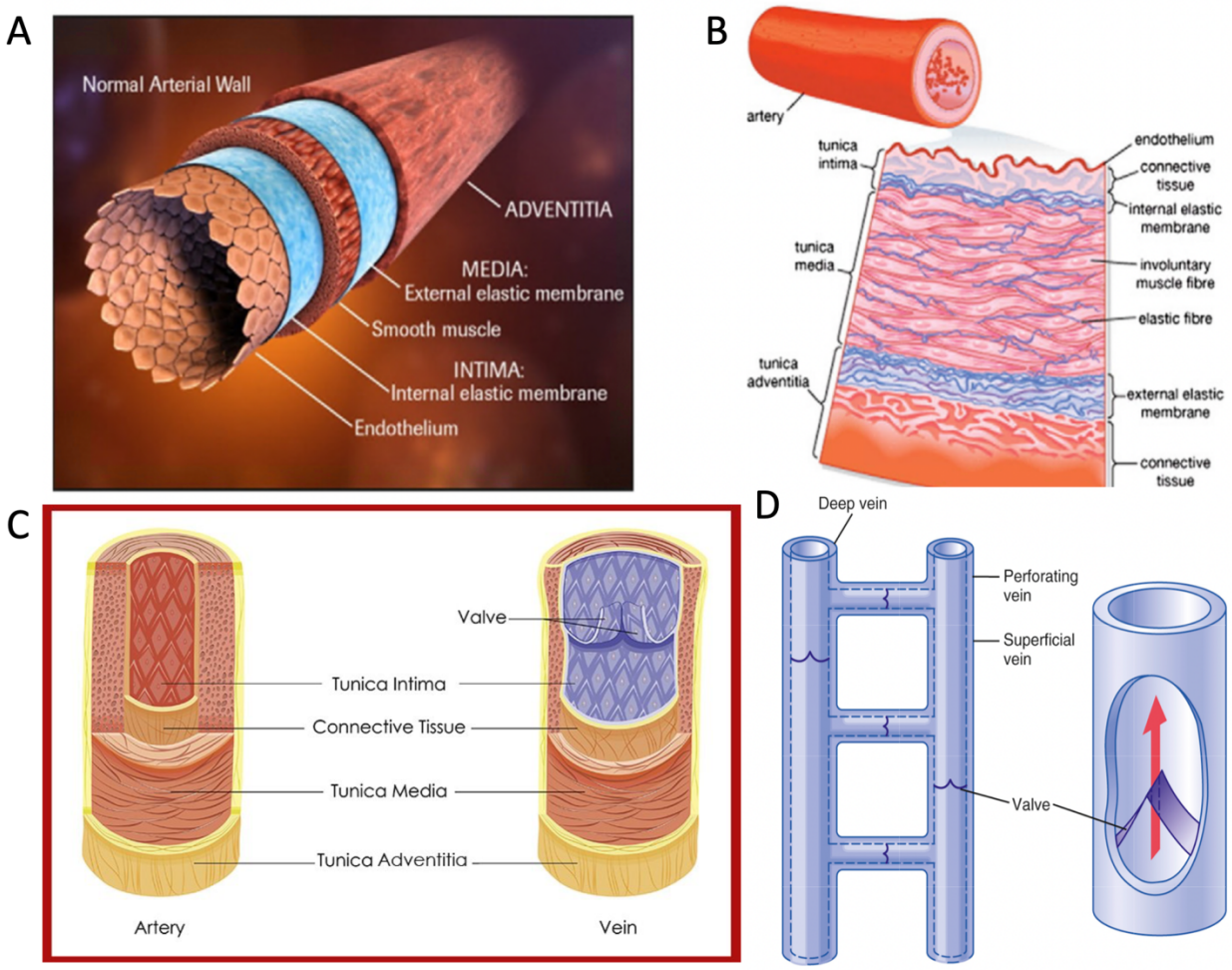

Figure 3-9: (A) Artery wall layer structure, 3-D artistic rendering, adapted from [53]. (B) Artery wall layer structure, 3-D pathology artistic rendering, adapted from [53]. (C) Comparing and contrasting artery and veins [56]. (D) Diagram of valves' directionality in deep and superficial veins, adapted from [41].

Hydrostatic pressure is given by the expression $\rho g h$, where ρ is the density of blood, g is the acceleration of gravity, and h is the height difference between the heart and the anatomical landmark. If the vein pump system in the legs is inactive, venous pressures can attain their hydrostatic values as blood will struggle to travel upward. This pooling of blood in the legs can sometimes cause fainting. However, even small movements of calf muscles typical of a person standing, sitting, and especially walking, will keep venous pressure in the legs below 20 mmHg no matter the orthostatic position [57], [58].

Other factors besides the venous pump and valves are responsible for moving venous pressures away from their hydrostatic values at certain anatomical landmarks. For instance, the internal jugular vein (IJV) is exposed to atmospheric pressure, causing it to collapse if pressure dips below atmospheric

pressure, clamping the minimum IJV pressure at zero even when traveling up and decreasing hydrostatic pressure. However, once atmospheric pressure exposure is taken away, such as in the subdural sagittal sinus, the clamp is removed [41], [57].

Another example of a factor responsible in manipulating venous pressure is the downstream pressure exerted by the squeezing of the subclavian vein by the top rib and the clavicle. This phenomenon adds about 6 mmHg of venous pressure to any vein upstream of the subclavian vein, such as the basilic vein in the upper arm or the radial vein in the lower arm [41].

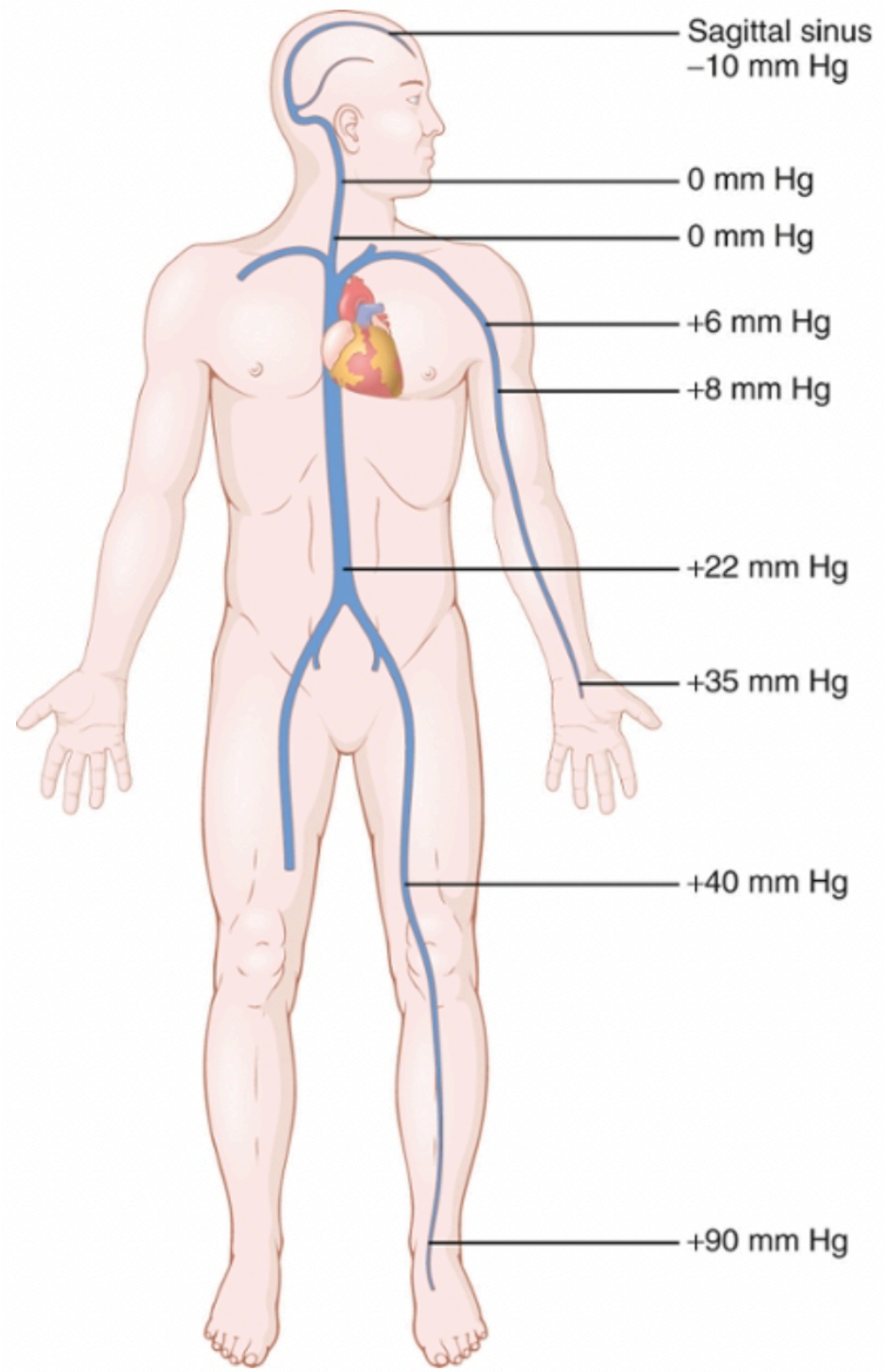

Figure 3-10: Map of venous pressures in an adult male standing completely still for hydrostatic pressure equilibration [41].

3.2 Cardiovascular Pathophysiology

Cardiovascular pathophysiology refers to any abnormal, adverse, or diseased alteration of state from normal cardiovascular physiology which is discussed in the previous section of this chapter. With respect to cardiovascular pressures, there will often be a tradeoff of higher venous pressure (right atrial pressure) for lower arterial pressure (mean aortic pressure). We note that as the pressure difference (gradient) between arterial and venous pressure decreases, cardiac output also decreases, which is often the root cause of the pressure gradient decrease. The decrease of this pressure gradient also decreases organ perfusion, which can lead to hypoxia in the organs, which can cause them to go into failure [41], [59].

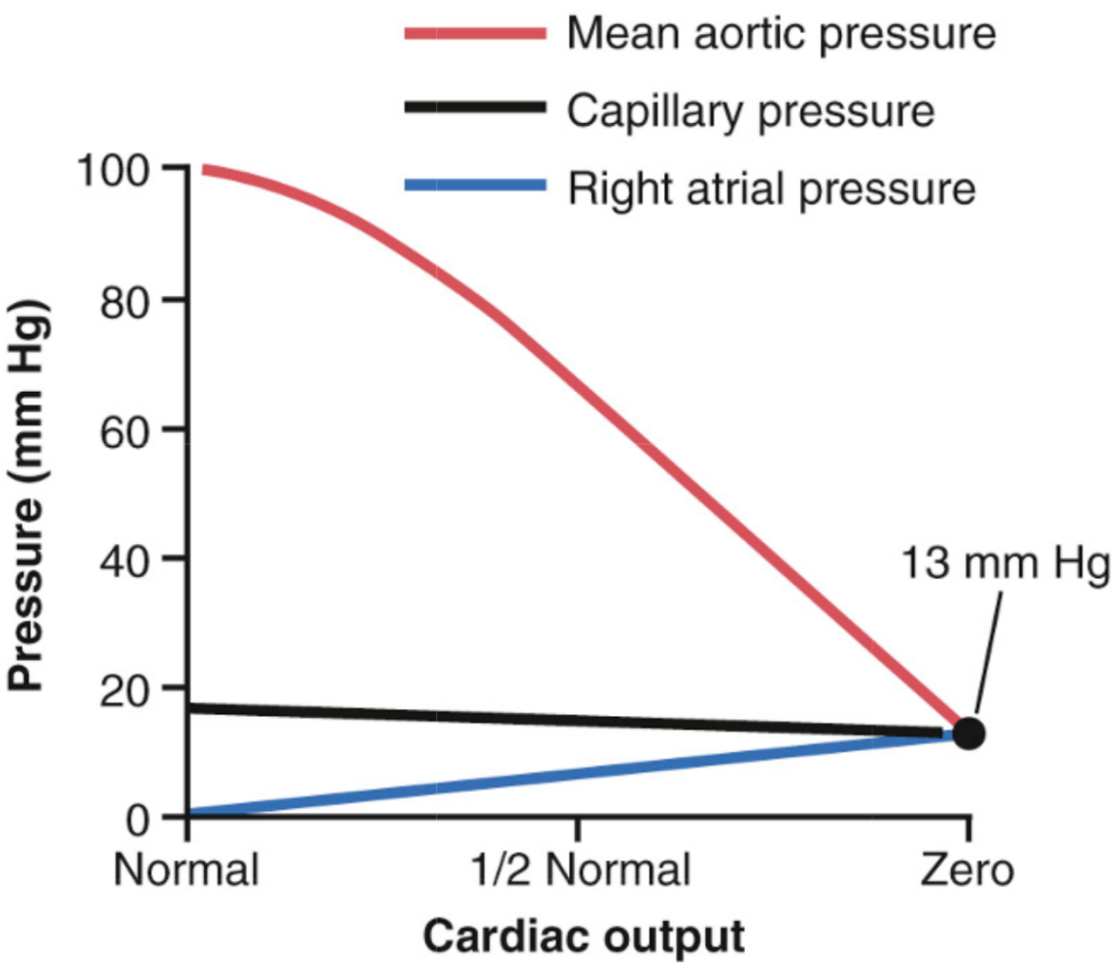

Figure 3-11: Plot of arterial (mean aortic) pressure, peripheral capillary pressure, and venous (right atrial) pressure in relation to each other and in relation to cardiac output [41].

Cardiovascular pathophysiology is a broad field with several disease states, many of which are interdependent. Given the emphasis of this thesis on cardiovascular pressures, we will focus our descriptions of cardiovascular pathophysiology to those affecting pressures. We will first describe pathological alterations to arterial pressures and then focus on what congestive heart failure (CHF) does to venous pressures.

3.2.1 Hypertension and Hypotension

Hypertension is defined to be a pathological cardiovascular state of consistently elevated arterial pressure. This consistently elevated pressure causes arterial walls to stiffen, increasing systemic vascular resistance, which allows blood flow to return to more normal levels. Hypertension puts one at higher risk for myocardial infarction (heart attack), heart failure, stroke, and kidney disease. Hypertension is classified as either Stage 1 with either a systolic blood pressure of over 130 mmHg or a diastolic blood pressure of over 80 mmHg or Stage 2 with either a systolic pressure of over 140 mmHg or a diastolic pressure of over 90 mmHg. About 116 million Americans have at least Stage 1 Hypertension while about 52 million Americans have Stage 2 Hypertension [60]–[64].

Hypotension is defined to be a pathological cardiovascular state of reduced arterial pressure. It is a less common problem than hypertension, especially in the United States, but can still cause inadequate organ perfusion. Ease of fainting can be a symptom of hypotension. Extreme hypotension can lead to inadequate brain perfusion. Hypotension is classified as either absolute hypotension (systolic < 90 mmHg, diastolic < 60 mmHg when resting), which affects people of all ages and tends to be asymptomatic, or orthostatic hypotension, when blood pressure drops by at least 20 mmHg for systolic and 10 mmHg for diastolic within three minutes of going from the sitting position to the standing position. About 22 percent of the population above age 65 has orthostatic hypotension [59], [65], [66].

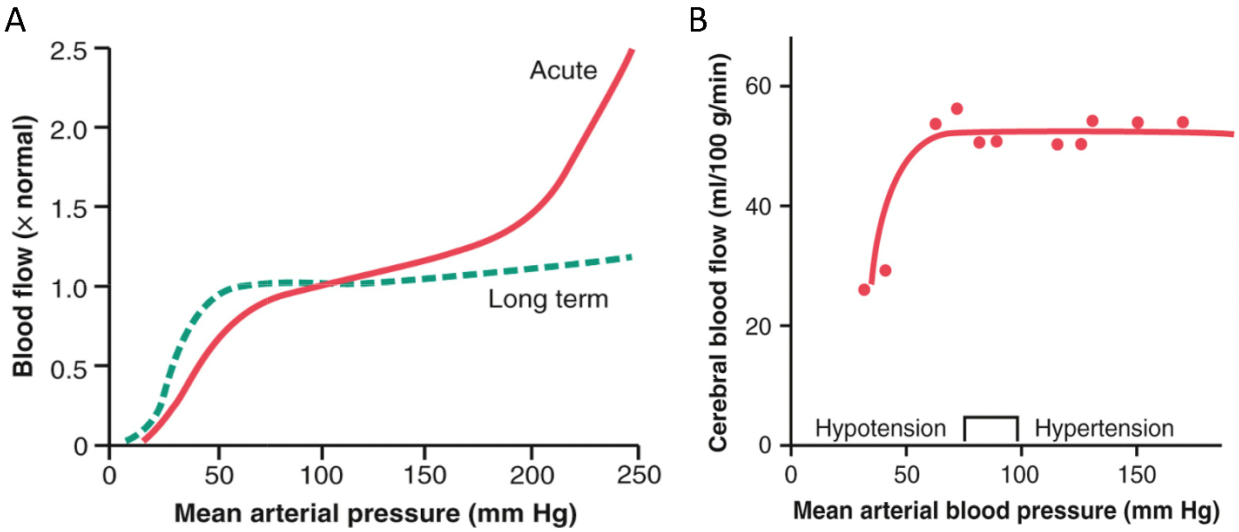

Figure 3-12: (A) Plot of cardiac output as a function of arterial pressure with the normal range of arterial pressure is highlighted [41]. Effect of severe hypotension on cerebral blood flow [41].

3.2.2 Congestive Heart Failure

Heart failure is a syndrome which describes when the heart is unable to adequately pump blood to meet the demands of the body's organs. Congestive heart failure (CHF) refers to the fluid buildup that occurs in the cardiovascular system due to the heart's decreased pumping ability. CHF is categorized into diastolic and systolic types. Diastolic heart failure is also known as heart failure with preserved ejection fraction (HFPEF) and is defined by difficulty in filling the ventricles with blood to be pumped. Systolic heart failure is also known as heart failure with reduced ejection fraction (HFREF) and is defined by difficulty in expelling blood from the filled ventricles. Here, we focus mainly on the pathophysiology, diagnostics, and treatment of HFREF [41], [67]–[69].

CHF can be in one of two modes: compensated or decompensated. In compensated heart failure, other organs, and even the myocardium (heart muscle) itself, adjust such that adequate cardiac output is maintained to perfuse the organs. The most central non-heart organ in compensated heart failure is the kidneys, including the adrenal glands. In the kidneys, reduced blood flow increases renin secretion, which allows angiotensin II to form from angiotensinogen (secreted by the liver) and angiotensin converting enzyme (ACE). Angiotensin II will increase water and salt reabsorption in the kidneys and increase aldosterone secretion from the adrenal glands. Aldosterone will directly further increase salt retention, which increases water retention by causing water to exit the kidney tubules into the blood and antidiuretic hormone secretion due to overall high extracellular osmolality. This cycle is called the renin-angiotensin-aldosterone (RAAS) cycle [70]–[72].

The RAAS cycle combined with sympathetic nervous system stimulation and myocardium recovery from any damage, such as collateral coronary supply creation, combine to bring cardiac output up to a high enough level for adequate organ perfusion with oxygen, but also for the kidneys to excrete enough salt and water to equal intake. Decompensated heart failure usually occurs when the kidneys fail to excrete enough salt and water. Atrial natriuretic peptide (ANP), released by atrial walls when they are stretched, can help the kidneys excrete more salt and water and delay decompensated heart failure. In decompensated heart failure, compensatory bodily effects initiated are insufficient to restore cardiac output to necessary levels for the kidneys to excrete enough salt and water and will continue until death if no intervention occurs [41], [71], [73].

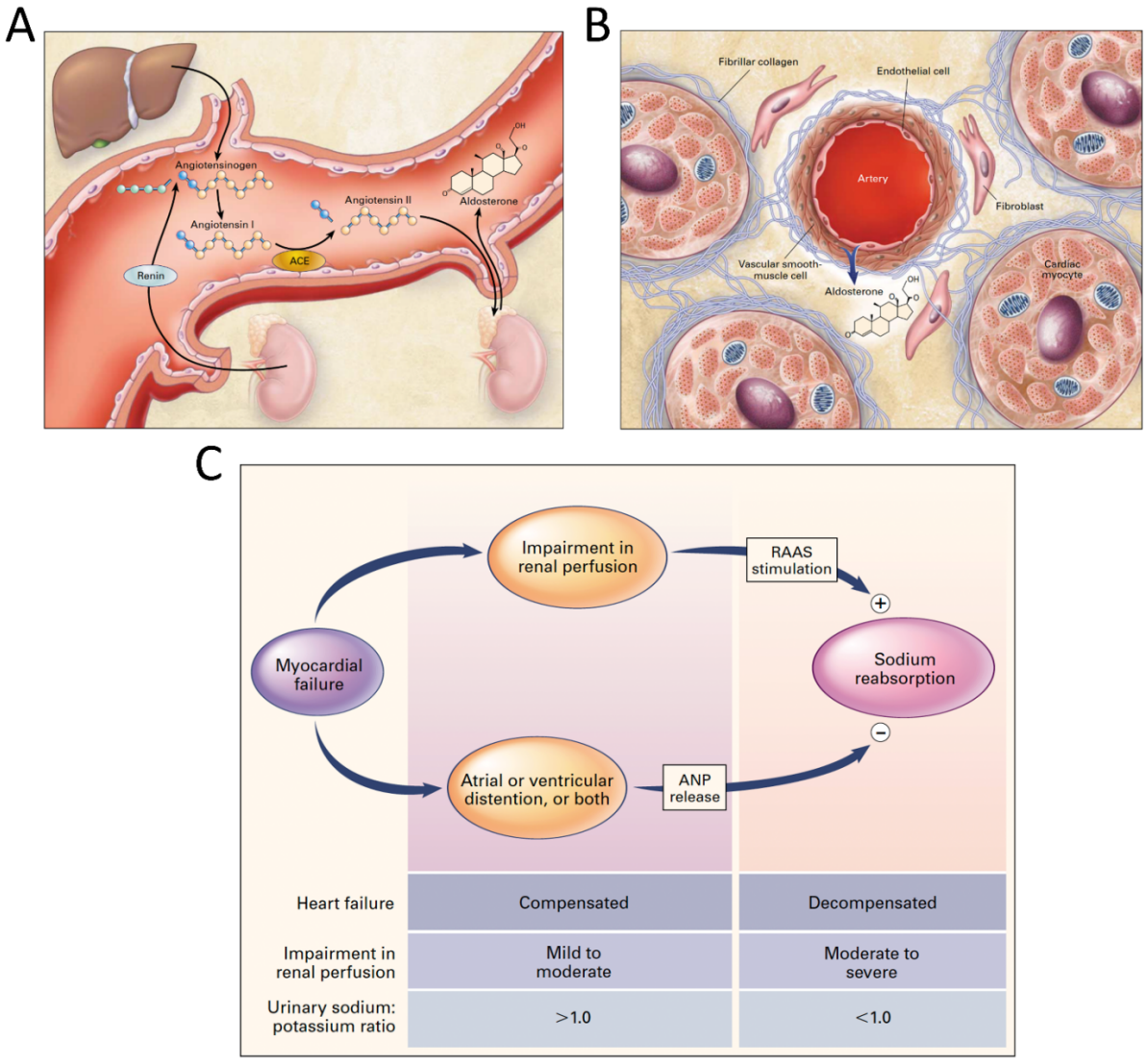

Figure 3-13: (A) The renin-angiotensin-aldosterone system (RAAS) [71]. (B) Coronary artery endothelial and vascular smooth muscle cells' production of aldosterone [71]. Diagram of kidney status in compensated versus decompensated heart failure [71].

It is useful to compare and contrast compensated and decompensated heart failure given a singular event which damages the myocardium, causing its pumping ability to decrease. Given compensated heart failure, an event such as a myocardial infarction could severely decrease cardiac output to less the half of its equilibrium resting value in only a few seconds. Sympathetic stimulation and parasympathetic suppression will increase both the cardiac output curve and venous return curve within one minute. In the next several weeks, collateral myocardial blood supply to increase pumping ability and the RAAS cycle to increase blood volume will increase cardiac output and venous return curves such that cardiac output is back to its original resting value. However, right atrial pressure (and central venous pressure) will equilibrate to a higher intravascular volume state. Often damage to the myocardium happens slowly over time with multiple events [41], [50], [67].

Given decompensated heart failure, the same event would decrease cardiac output and still induce sympathetic and parasympathetic responses. Without intervention, the RAAS cycle and collateral blood supply will not be enough to return cardiac output to its original resting state. Therefore, intravascular volume (often measured with right atrial pressure) will continue to increase. Edema will occur such that excess fluid moves from the vasculature to the interstitium. There will come a point at a high enough right atrial pressure where detrimental effects to cardiac output will occur, such as the overstretching of ventricular walls (mechanical pumping ability). If this condition persists, pulmonary edema will occur, preventing the gas exchange of oxygen and carbon dioxide at the alveoli and the pulmonary capillaries (i.e. decreased energy for ventricular contraction). It is vitally necessary for intervention to happen at this critical juncture to save the life of the patient. [41], [71], [74], [75].

3.2.2.1 Treatments and Interventions

For compensated heart failure, specifically with left ventricular dysfunction, the most promising treatment utilizes angiotensin-converting enzyme (ACE) inhibitors. ACE inhibitors prevent the conversion of angiotensin I to angiotensin II. These drugs ultimately decrease the compensatory efforts of the RAAS system such that intravascular volume increases only modestly in response to the weakening of the heart muscle. Cardiac output is still able to increase because ACE inhibitors also decrease systemic vascular resistance such that a weaker heart could still pump sufficient blood to perfuse the organs [76], [77].

For decompensated heart failure, interventions consist of diuretics which decrease intravascular volume and cardiotonic drugs which increase cardiac output. Many of the diuretic options act on the nephron of the kidney, specifically the thick ascending loop of Henle, where they prevent salt from being reabsorbed by the blood, which allows eventual flow into the urine. Cardiotonic drugs give strength to the heart, first causing an increase in cardiac output which allows a downward shift of venous return after several days [41], [78]–[80].

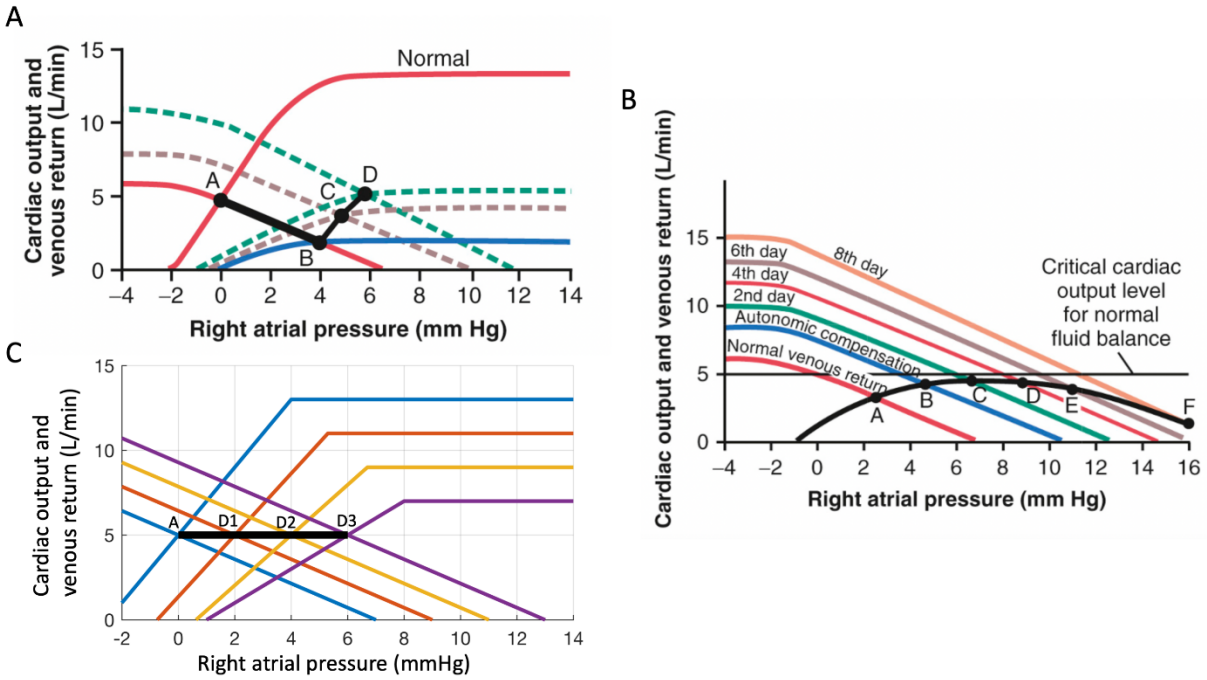

Figure 3-14: (A) Cardiac output and venous return curves progressing from a healthy state ('A') to a low cardiac output state immediately after damaging event 'B' to a sympathetic and parasympathetic influenced state about 1 minute after the damaging event 'C' to a state of fully compensated heart failure 'D' [41]. (B) Cardiac output and venous return in decompensated heart failure. The cardiac output curve is that of a severely damaged heart and is unable to attain adequate cardiac output [41]. (C) A simplified simulation of cardiac output and venous return with multiple more minorly damaging events in compensated heart failure. The first event is 'A' to 'D1'. The second event is 'D1' to 'D2'. The third event is 'D2' to 'D3'. Less extreme versions of points 'B' and 'C' are implied but not shown.

3.3 Arterial Pressure Measurement

A given method to measure the pressure in a specific artery is either invasive or noninvasive. The noninvasive methods are much more desirable as they present a low-risk, low-cost, and easy-to-execute alternative to the invasive methods. Some noninvasive methods, when combined and calibrated, can even produce a full arterial blood pressure waveform given ample effort. However, the invasive methods have higher accuracy and readily inform about the arterial pressure waveform without

any additional effort. The most common noninvasive method is the brachial artery blood pressure cuff and the most common invasive method is the radial artery fluidic pressure measurement [41], [81], [82].

There are two main types of blood pressure cuffs. The first is the auscultatory cuff, also known as the Korotkoff blood pressure cuff, combines the use of the cuff with a stethoscope on the artery of interest distal to the cuff. The cuff is inflated to a pressure surely above the systolic pressure of the artery. Then it is slowly deflated from that pressure to below the diastolic pressure. The systolic pressure is first identified by noticing at what pressure sounds, known as Korotkoff sounds, are first audible in the stethoscope. The diastolic pressure is identified to be the pressure where the Korotkoff sounds become inaudible. The second type is the oscillometric cuff, which automatically performs the same procedure of increasing the cuff pressure above systolic pressure and slowly lowering the blood pressure to below diastolic pressure. However, this cuff senses the pressure signal reflected by the artery which peaks around the mean arterial pressure and significantly diminishes but doesn't fully disappear on the high side of systolic pressure and low side of diastolic pressure. Given they are properly sized, these blood pressure cuffs can be used on any of the four limbs in multiple sites on each limb [83]–[86].

Unlike the noninvasive, cuff-based methods of measuring arterial pressure, the invasive fluidic catheter-based methods capture full arterial blood pressure waveforms. There are a few variations to this methodology but the basic principle for each of these variations is that the fluidic pressure in the chamber aims to mirror the pressure exposed to the catheter's needle which is connected to the chamber. The pressure is transduced to an electrical signal and sampled. The sample rate of this pressure measurement can be driven up to 0.5 kHz, which is far past the Nyquist frequency of the arterial pressure wave. Similar blood pressure cuffs, arterial line placement is limited to major arteries in limbs [87], [88].

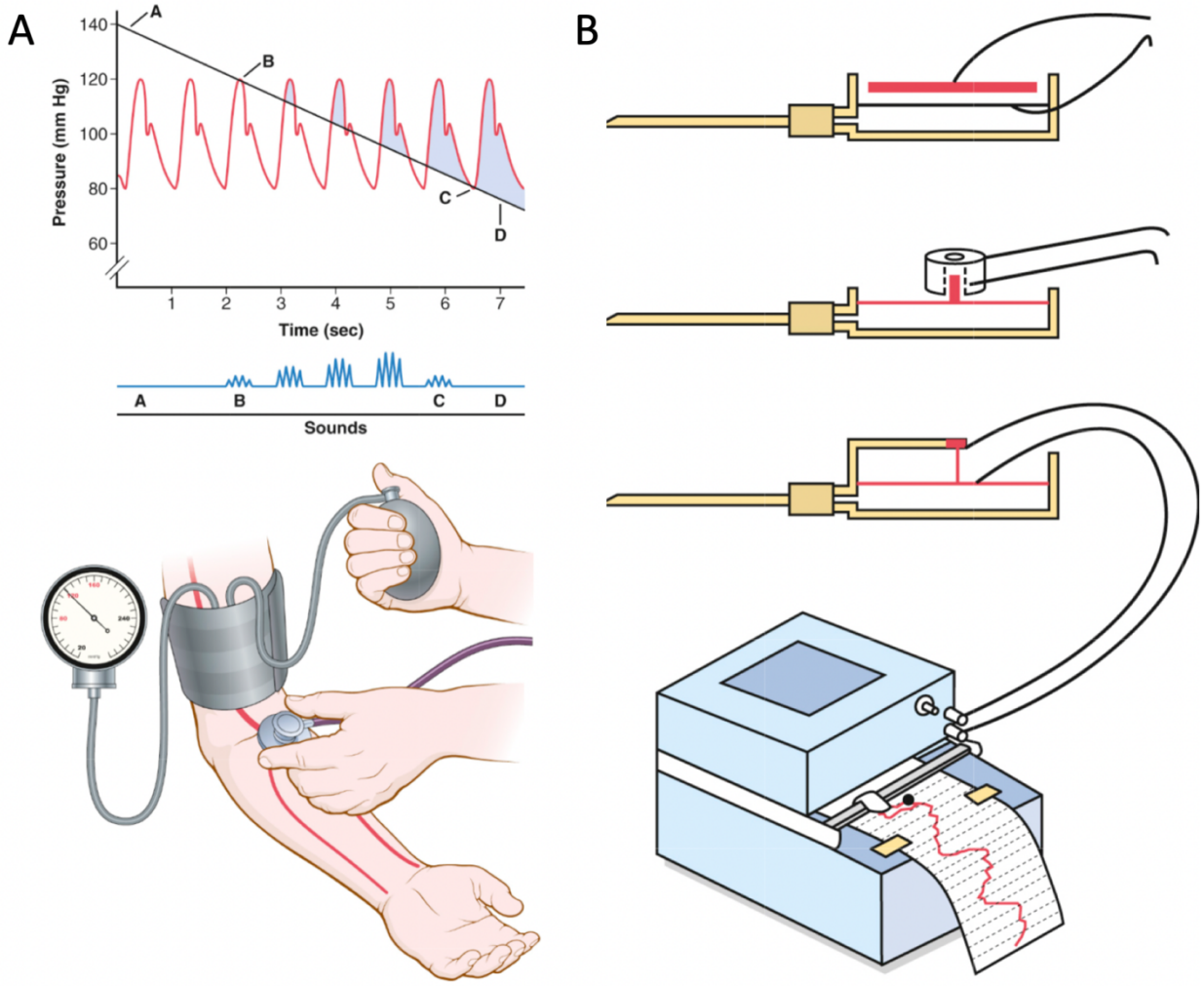

Figure 3-15: (A) Auscultatory brachial blood pressure cuff functional diagram [41]. (B) Three similar pressure transduction techniques using fluid chambers in arterial lines [41].

3.3.1 Force-based Arterial Pressure Measurement

Force-based approaches to arterial pressure measurements have been explored in the past with notable success but fall short of the blood pressure cuff in terms of accuracy and ease of use. Arterial applanation tonometry seeks to sense how much force is necessary to partially flatten an artery, most often the radial artery, noninvasively. Modern applanation tonometry techniques can output blood pressure estimates which include full waveforms with estimates of systolic and diastolic pressure. The dicrotic notch should also be visible in the waveform. Furthermore, the systolic and diastolic pressure estimates are usually within 5 mmHg of the blood pressure cuff and arterial line measurements when calibrated to them or invasive central blood pressure measurements. However, the fact that these

measurements are calibrated is a weakness of the method because it cannot stand alone as an independent measurement [89]–[91].

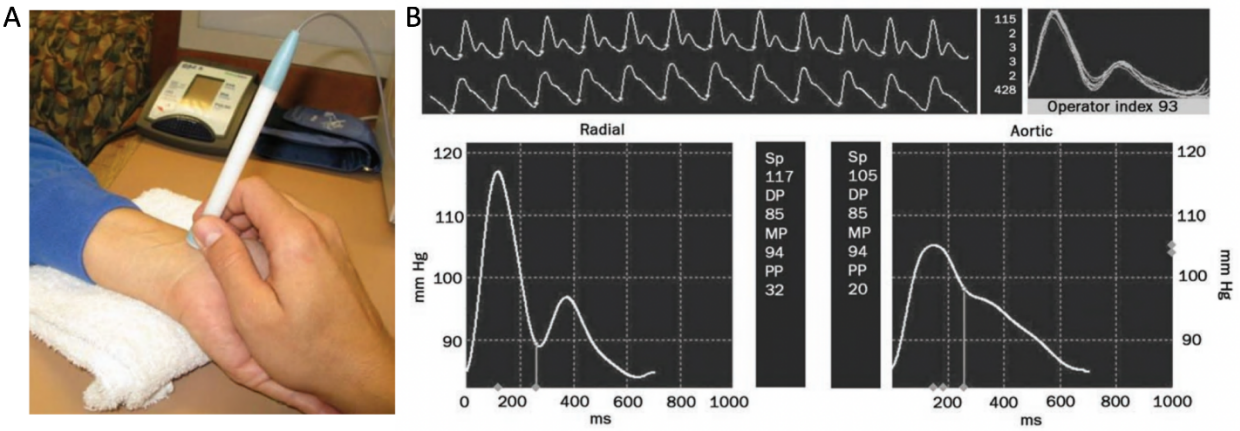

Figure 3-16: (A) Picture of applanation tonometer of the radial artery [89]. (B) Applanation tonometer pressure estimation in the radial artery and the aorta via transfer function and calibration [89].

3.4 Venous Pressure Measurement

Unlike arterial blood pressure measurement, where the blood pressure cuff – auscultatory or oscillometric, has become the noninvasive standard of care and is employed as a standard vital sign, venous pressure measurement is far less established and is considered to be a more specialized measurement for patients already diagnosed with a cardiovascular disease, most commonly heart failure [92], [93].

The methodology which could best be described as the noninvasive standard for venous pressure measurement is the jugular venous pulsation height measurement (JVP). In this measurement, a clinician asks the patient to recline in order to observe the height of the highest visible pulsation of the jugular venous pulse waveform on the neck. This point on the neck is thought to be where the pressure is equal to zero. The hydrostatic pressure difference between this point and the middle of the right atrium is made by measuring the height of the highest pulsation above the sternal angle. The sternal angle refers to the top of the sternum, assumed to be 5 cm above the middle of the right atrium, independent of angle of recline. There are several issues with this measurement which prevent it from being a fully satisfactory analog to the arterial blood pressure cuff. The two most central are:

- Difficulty in spotting the highest jugular venous pulsation and differentiating from the nearby and different carotid pulsation

- Actual variation in sternal angle height above the right atrium across a population given a constant angle and across a range of angles given the same person

For these reasons, the accuracy in the binary decision in deciding if CVP is above or below 10 mmHg is only about 70% combined among medical students, medical residents, and cardiology fellows [92]–[96].

The invasive standard for venous pressure measurement is to pass a central line in either the superior vena cava or the right atrium and directly measure the pressure, making sure the pressure transducer, which is outside the body and usually on an intravenous cart beside the patient, is at the same height as the tip of the catheter. This method is accurate, however, like arterial lines, it is not a routine procedure due to risk, invasiveness, and cost [97]–[99].

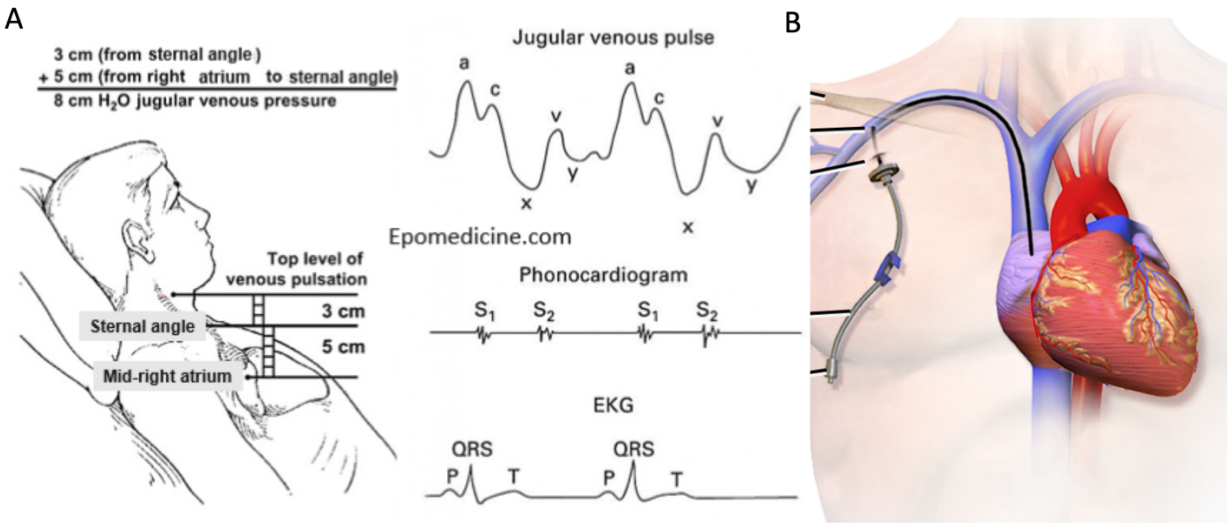

Figure 3-17: (A) Diagram of JVP height measurement with aligned jugular venous pulse, heart sounds, and electrocardiogram measurements [100]. (B) Diagram of central line placement for invasive right atrial pressure measurement [101].

3.4.1 Ultrasound-based Venous Pressure Measurements

Ultrasound-based venous pressure estimations have shown promise in recent years in creating a more accurate noninvasive standard of venous pressure measurement but have either fallen short of accuracy requirements or are quite difficult to execute. The inferior vena cava (IVC) is the vein which leads into the right atrium from below the right atrium. Although it is quite deep and has ribs in between it and the ultrasound probe, ultrasound measurements of the IVC are possible with ample skill. When measuring the diameter of the IVC at end-inspiration, a correlation of $r^2 \approx 0.25$ has been observed with invasive CVP measurement. An alteration to this methodology has been presented by

measuring both end-inspiratory and end-expiratory IVC diameters, with a quick sniff as the inspiration, to formulate a “caval index” (CI).

$$CI = \frac{D_{IVC,end-exp} - D_{IVC,end-insp}}{D_{IVC,end-exp}} \tag{3.2}$$

This method adds difficulty to the measurement and requires post-processing of data. However, it has been shown to be quite accurate when compared to the invasive CVP measurement with a correlation of $r^2 \approx 0.88$ and sensitivity and specificity each over 0.8 when predicting whether CVP is above or below 10 mmHg by noting if CI is below or above 0.5. The difficulty of IVC ultrasound measurements and the lack of empirical accuracy at lower CVP values – 10 mmHg is already very high – are what have most likely prevented this methodology from becoming more prominent [93], [102]–[105].

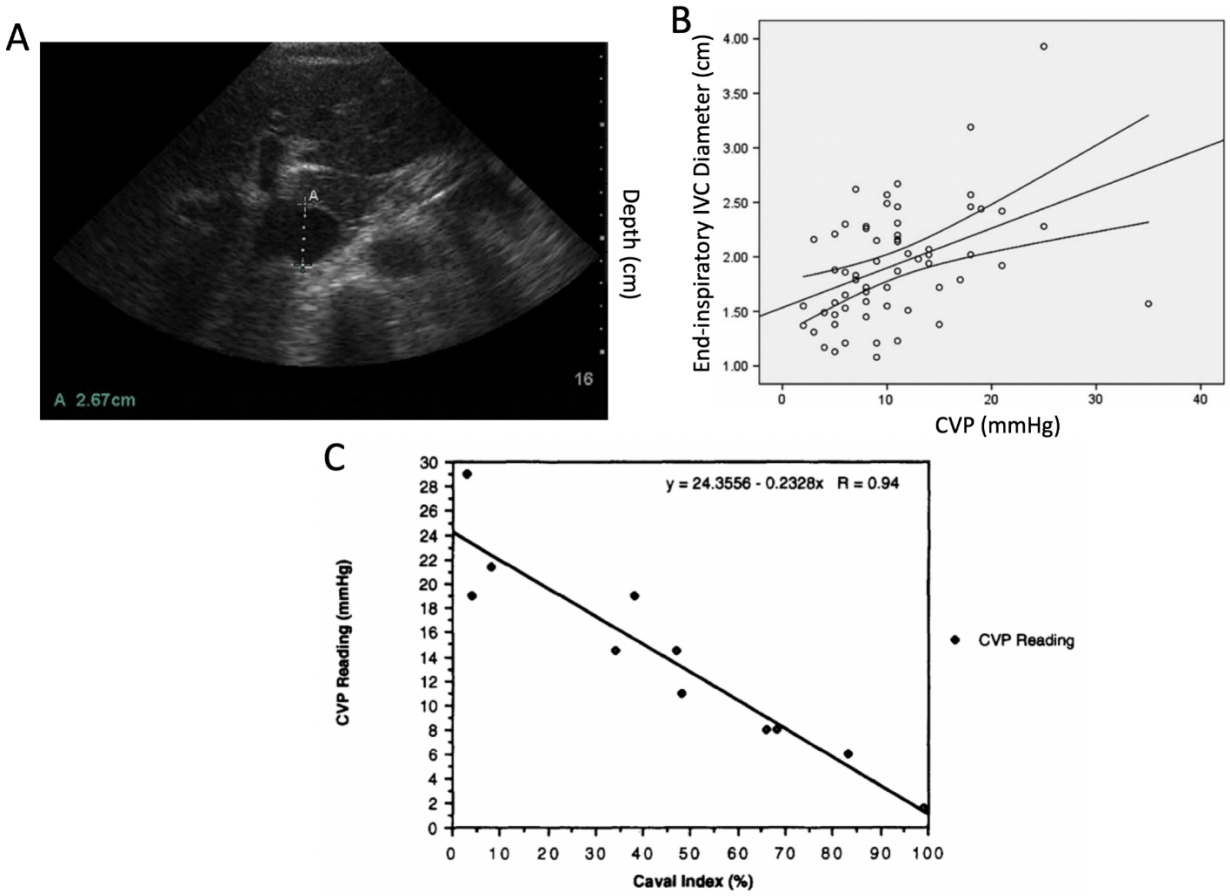

Figure 3-18: (A) Annotated ultrasound image of IVC with diameter labeled [102]. (B) Correlation of end-inspiratory IVC diameter with invasive CVP measurements [102]. (C) Correlation of caval index with invasive CVP measurements [103].

Chapter 4 – Force-coupled Ultrasound of Large Superficial Blood Vessels

In this chapter we introduce the idea of using an ultrasound probe attachment called a force-coupling, which measures force as ultrasound images are being captured by a commercial ultrasound probe and system. We first go over the hardware used for the force-coupled ultrasound data collection and processing. We then walk through the process of starting with B-mode images of a large superficial blood vessel and its surroundings and a force signal, (1) assigning a force to each ultrasound image we seek to analyze through synchronization, (2) detecting the blood vessel of interest to be segmented, and (3) segmenting the blood vessel of interest. The blood vessel of interest in this chapter will be either the carotid artery or the internal jugular vein. At the end of this process, we have a segmented blood vessel with known force applied to it for each ultrasound frame to be further analyzed. We stress that all three steps in this process are automated.

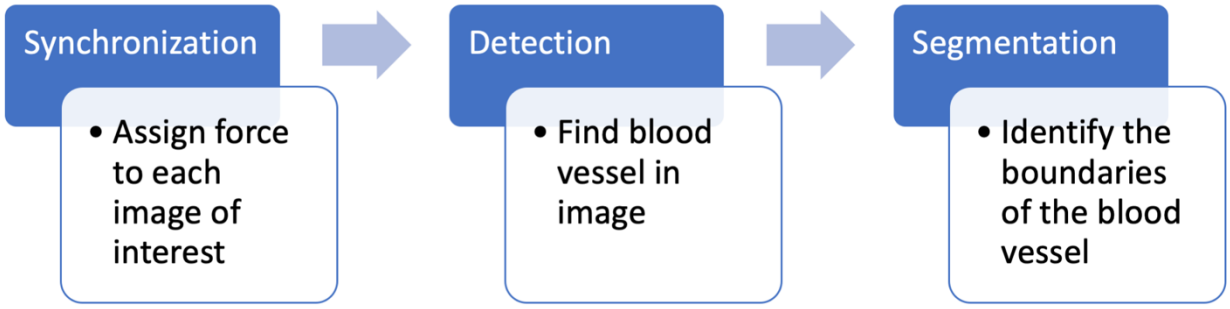

Figure 4-1: Force-coupled ultrasound automated data processing flow chart.

4.1 Force-coupling Hardware

We have developed a force-coupled ultrasound probe attachment, providing the ability to measure the force applied to the surface of the skin by an ultrasound probe for each ultrasound image obtained. We combine this probe attachment with a commercial ultrasound probe and system. The components of the attachment connect to an electronics box via wire bundle and then to a display tablet or laptop via USB. In this section, we cover the ultrasound transducers and systems used, the force-coupled ultrasound casings used, and the electronics hardware used upstream from our signal and image processing in software.

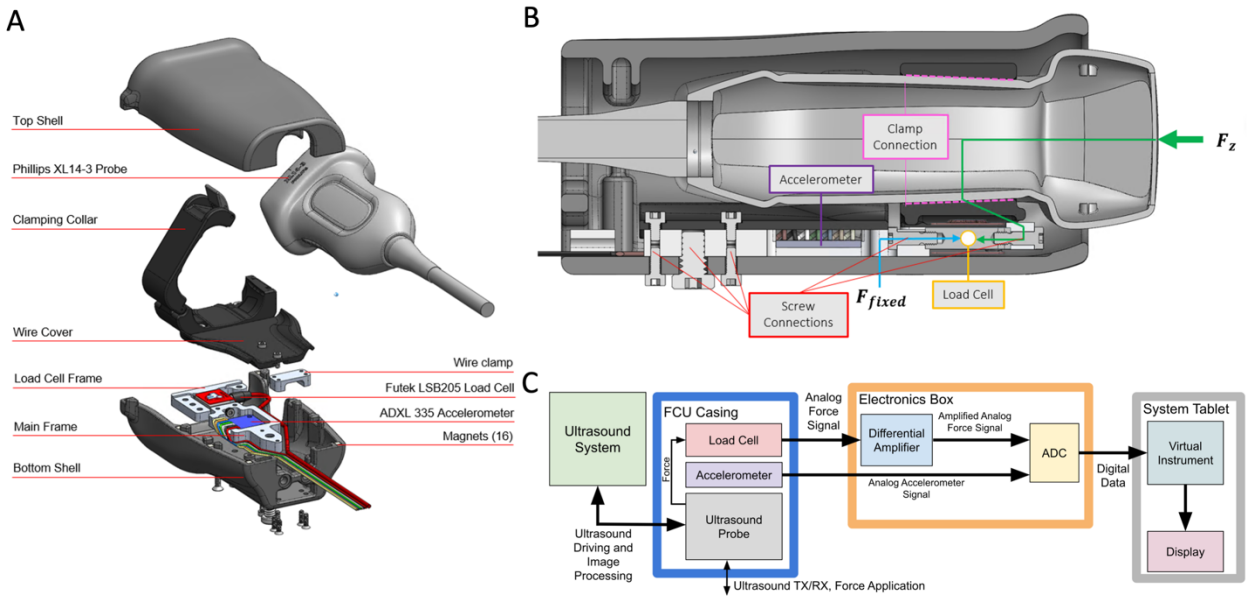

Figure 4-2: Philips force-coupled ultrasound hardware summary. (A) CAD diagram of force-coupled ultrasound probe to show individual components. (B)) CAD diagram of force-coupled ultrasound probe longitudinal cross-section. The force transmission is shown in green from the imaging surface of the ultrasound probe to the clamp connection to the load cell. (C) Force-coupled ultrasound data collection block diagram.

4.1.1 Ultrasound Transducers and Systems

The commercial ultrasound probes used are the Philips XL14-3 xMATRIX vascular ultrasound transducer and the GE 9L linear vascular ultrasound probe (Philips Inc., Amsterdam, Netherlands; General Electric Co., Boston, MA, USA). The commercial ultrasound systems used are the Philips Ultrasound EPIQ system and the GE Logiq E9 ultrasound system (Philips Inc., Amsterdam, Netherlands; General Electric Co., Boston, MA, USA).

The Philips transducer is a 2-D array of piezoelectric elements and has the ability to acquire 3-D images as well as 2-D images. The ultrasound system used is the commercial Philips Ultrasound EPIQ system to display relevant ultrasound images to the data being acquired and save the images to later be combined with the data from the force-coupled ultrasound casing. Neither of these components to the overall system are experimental. The GE transducer is merely a 1-D array which has the ability to acquire 2-D images. 1-D M-mode imaging, which is presented a similar way to a photo finish in a track and field race as a 2-D image with time on the horizontal axis and depth on the vertical axis, is also utilized in the GE transducer for this thesis.

The primary safety concern for the ultrasound transducer and system is thermal-acoustic safety. The ultrasound system and probe are only designed for imaging and are incapable of high enough

acoustic intensities to thermally damage tissues. The Food and Drug Administration (FDA) has approved both systems and transducers for clinical use. The ultrasound probe contacts the patient's skin just as a normal ultrasound probe would make contact. The guidelines by the FDA and the AIUM (American Institute of Ultrasound in Medicine) provide quantitative guidelines in order to prevent any adverse effects.

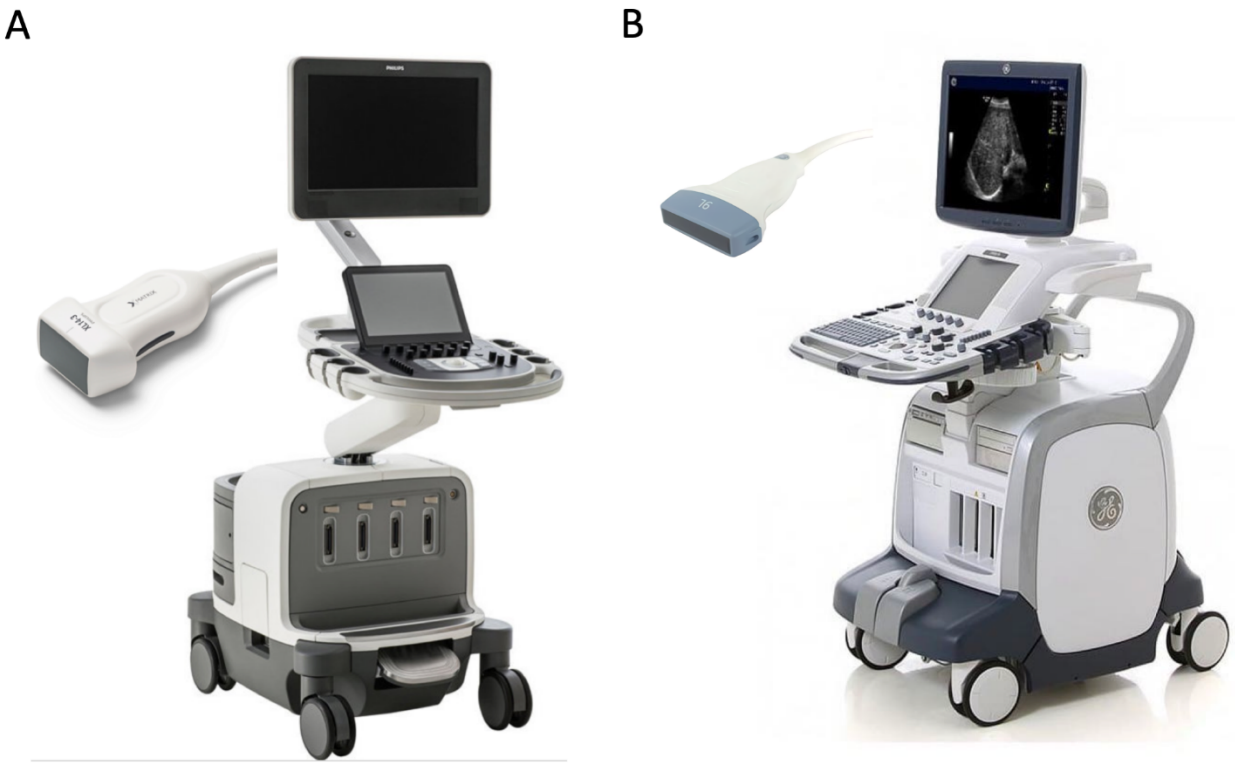

Figure 4-3: (A) Philips ultrasound transducer and system used in this thesis. (B) GE ultrasound transducer and system used in this thesis.

4.1.2 Force-coupled Ultrasound Casings

The casing is equipped with a load cell and an accelerometer, both powered by an external power source. The load cell measures force. For the Philips setup, the load cell is a Futek Miniature S-beam with a 25 lb capacity and an excitation (power) voltage of +- 10 V (model number LSB205). For the GE setup, the load cell is a Futek Miniature S-beam with a 5 lb capacity (model number LSB200). The difference in capacities of the load cells is due to the fact that the Philips probe has about four times the contact area as the GE probe has since the external pressure applied is a function of external force and cross-sectional area. The accelerometer (ADXL 335, Analog Devices, Wilmington, MA, USA) measures acceleration in principle, but can provide an estimate for two angles of orientation, pitch and yaw, for

the force-coupled ultrasound probe as well. This is because the accelerometer has three axles with rigidly known positions relatively to each other.

The casing is made with stainless steel and ABS plastic. The casing is grounded, has no electrical current going through its exterior where someone would grip it, and is thermally insulated. The casing is held together with metal wiring and magnets.

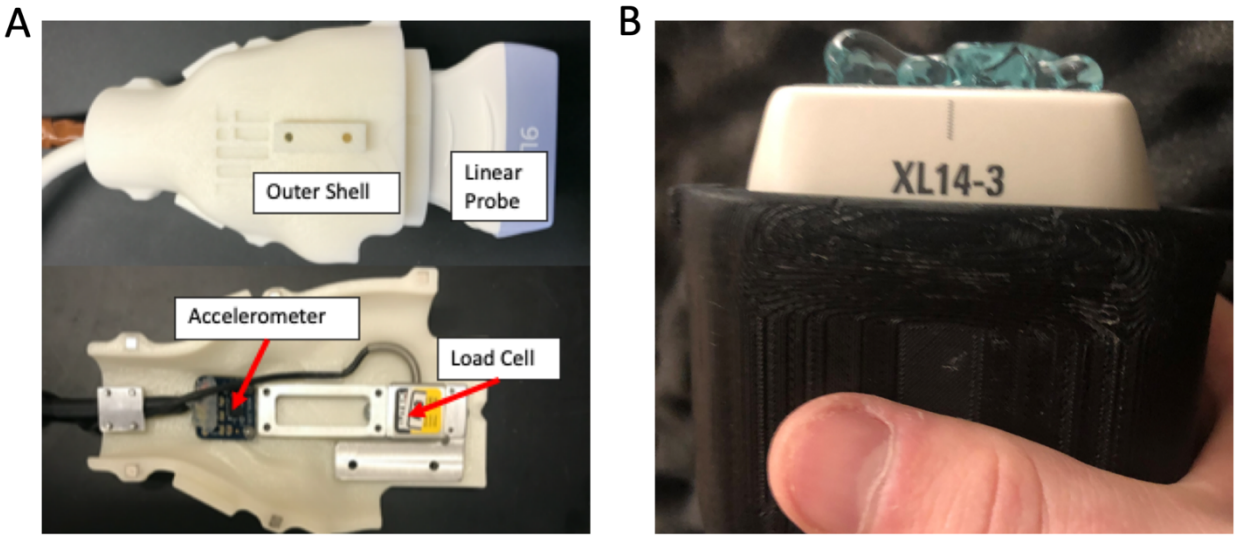

Figure 4-4: (A) GE Force-coupled ultrasound probe separated to show components. This force-coupled ultrasound probe is used for all studies involved in chapters 5, 6, and 9. (B) Picture Philips of handheld probe with ultrasound gel on it. This force-coupled ultrasound probe is used for all studies involved in chapter 7 and 8.

For the Philips setup, the accelerometer's ability to estimate the angle of orientation of the force-coupled ultrasound probe has additional functionality. Given the ability of the Philips setup to produce 3-D ultrasound images, we are able to record the angles which are orthogonal to the long-axis of the blood vessel in the orientation we attend to compress that blood vessel in. This functionality is fruitful as it helps ensure that the minimum amount of force necessary compresses the blood vessel of interest. For the GE setup, it is also possible to record an angle of orthogonality to the long-axis of the blood vessel of interest. However, the probe would not be in the correct (short-axis) orientation for compression.

The primary safety concern of the force-coupled ultrasound casing is mechanical. This concern is minor as the casing is quite light, yet quite sturdy. Magnetic failure could cause part of the casing desired entirely for grip ergonomics to fall off, but not part of the casing attached the load cell, so no damage of equipment would occur. The weight of what could fall is less than 2 ounces and made of light

plastic, so no injury should occur should it fall on a foot. There should be no contact of the force-coupled ultrasound casing with the patient given no mechanical failure.

4.1.3 Force-coupled Ultrasound Electronics and Displays

The National Instruments data acquisition (NIDAQ) system (model numbers: PXI-6363 for A/D conversion, PXIe-1071 for power circuitry) acts as the analog to digital conversion and force-calculation by means of a LabVIEW virtual instrument on either a tablet or laptop. This program is usually run on a tablet but could be run on any Windows system. Full use is made of the force data while the accelerometer data is used for angle of orientation measurement for the force-coupled ultrasound probe. The NIDAQ is powered via USB by a computer or tablet. For the Philips setup, the load cell output goes into a differential amplifier (model number IAA100), which is a low noise differential amplifier designed to make the force signal clear. It is powered with two 9V batteries in series. For the GE setup, the load cell output goes into a differential amplifier (model number CSG110) which is powered by wall power. The display could either be a laptop or a tablet and functions much as a display for an ultrasound system works in that it gives feedback to the operator to guide the data acquisition. Unlike the ultrasound system, this display lets the operator know how much force is being applied.

Electronic safety is the priority concerning the electronics box and associated wiring. All wires and cables outside the electronics box are properly insulated. The electronics box is grounded. No electrical connection whatsoever is exposed at any accessible point in the system. The electronics box is closed and fastened with four separate screws. The electronics box typically resides within the larger plastic casing used to transport the electronics box and the force-coupled ultrasound casing.

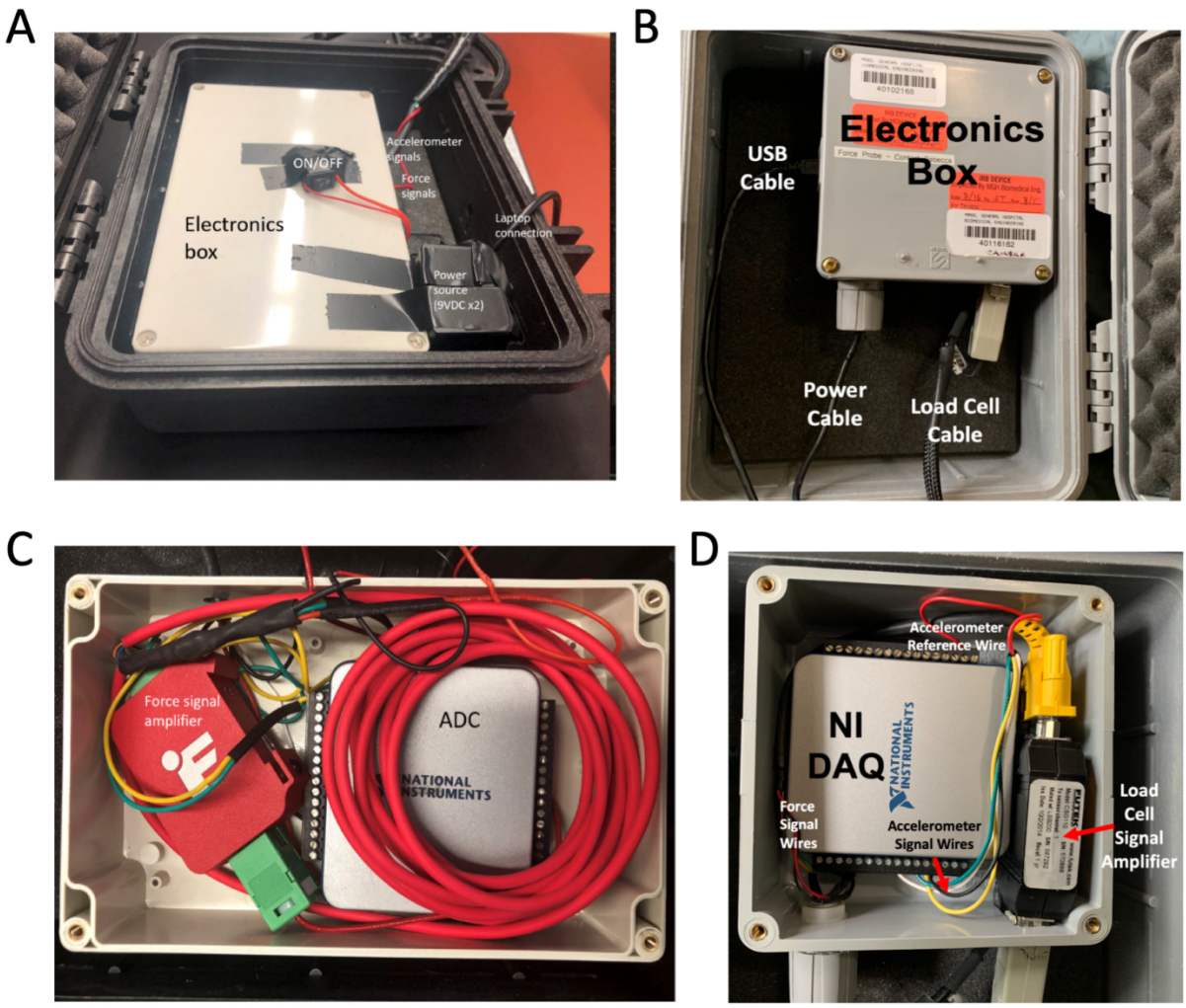

Figure 4-5: (A) Open carrying case for Philips force-coupled ultrasound powered by two 9V batteries in series. (B) Open carrying case for GE force-coupled ultrasound powered by AC wall power. (C) Open electronics box for Philips force-coupled ultrasound with Futek IAA100 differential amplifier. (D) Open electronics box for GE force-coupled ultrasound with Futek CSG110 differential amplifier.

4.2 Synchronization

Synchronization of force and ultrasound is necessary as the force signal and ultrasound images are recorded by two systems with independent clocks by the force-coupled ultrasound probe depicted in **Figure 4-4**A. Our approach to automated synchronization is to apply a series of quick transient compressions, before and after the smooth force sweep, which are unique patterns in the force signal and in a derived signal from the ultrasound frames [106]. Specifically, three quick compressions before the force sweep (1-3), the peak of the force sweep (4), and one quick compression after the force sweep

(5) are signatures in the force signal shown in **Figure 4-6**C. Recordings which do not follow this synchronization protocol are discarded before automated post-processing begins.

When tissue is compressed as it is when force is increased (**Figure 4-6**A,B), the tissue moves closer to the ultrasound probe causing it to move up in the image. The signal derived from the ultrasound images is the frame region integration of axial optical flow [107]. Optical flow estimates the velocity of pixels in a sequence of image-to-image transitions. We use the Horn-Schunck method (MATLAB function: opticalflowHS within its Computer Vision Toolbox) to acquire frame-to-frame pixel velocities [9], which yields vertical and horizontal components of velocity for each pixel coordinate for all image transitions [107]. For each image transition, we sum all the vertical velocity components for all image pixels. Horizontal movement of the carotid to the left is not quantified for the purpose of synchronization. We sum across all image transitions over time to obtain an aggregate pixel vertical position signal as a function of discrete time $P[t]$. We have

$$P[t] = \sum_0^t \sum_i \sum_j v_{y\,(i,j,t)} \tag{4.1}$$

where t is the discrete time, $v_{y,(i,j,t)}$ is the vertical component of optical flow velocity for a given pixel at a given time, and i and j are the respective vertical and horizontal image spatial coordinates. This optical flow-derived signal and the raw force signal, seen in **Figure 4-6**C both present the patterns before and after a force sweep. The force signal is synchronized with the optical flow-derived signal; a force is then assigned to each ultrasound image.

4.2.1 Primary Synchronization

The force signal is sampled at 25 Hz (samples per second) to avoid lag in displaying real-time force during data acquisition while sampling fast enough to capture systole and diastole with high resolution. The ultrasound frame rate is slightly faster than the force sample rate at 33 Hz (frames per second), as shown by the wider peak spread in **Figure 4-6**C. However, this frame rate is imprecise and is subject to slight variations from frame to frame. Therefore, the reference time axis we use after interpolation is that of the force measurement. The synchronization algorithm as follows:

1. The 5 most prominent peaks in the force signal and in the optical flow signal are detected.

2. The peaks are aligned such that there are just as many samples between the first and last peaks in the force signal as there are between the first and last peaks in the optical flow signal. The data are interpolated into a common time axis.
3. We assess the accuracy of the synchronization by checking the alignment of the three middle peak pairs (**Figure 4-6**D), placed as a result of the alignment of the first and last peak pairs in the signals. These are the remaining peak pairs which are not guaranteed to have perfect alignment after interpolation. The first two middle peaks are the second and third quick compressions before the force sweep and the third is the peak of the force sweep. The synchronization passes if the sum of the absolute values of the peak pair differences between the force and optical flow peaks is less than 20 samples or about 0.7 seconds. This criterion is chosen to guarantee an offset of less than one cardiac cycle during normal sinus rhythm. Given the slow and linear force ramp applied, disagreement between true force and assigned force should remain low. Written in inequality form, we use

$$\sum_{i=2}^{4}\left|t_{F,i} - t_{OF,i}\right| < 20 \tag{4.2}$$

   where $t_{F,i}$ is the sample number of a force peak, $t_{OF,i}$ is the sample number of an optical flow peak, and the summation is indexed from 2 to 4 to indicate the three middle peaks originally detected as depicted in **Figure 4-6**D.

4. Once the synchronization check passes, we assign a force to each ultrasound frame.

For synchronizations that fail the check in step 3, a more exhaustive peak detection method which chooses up to 30 peaks in each signal is performed. The methodology for this secondary synchronization is described in more detail in section 4.2.2 Secondary Synchronization.

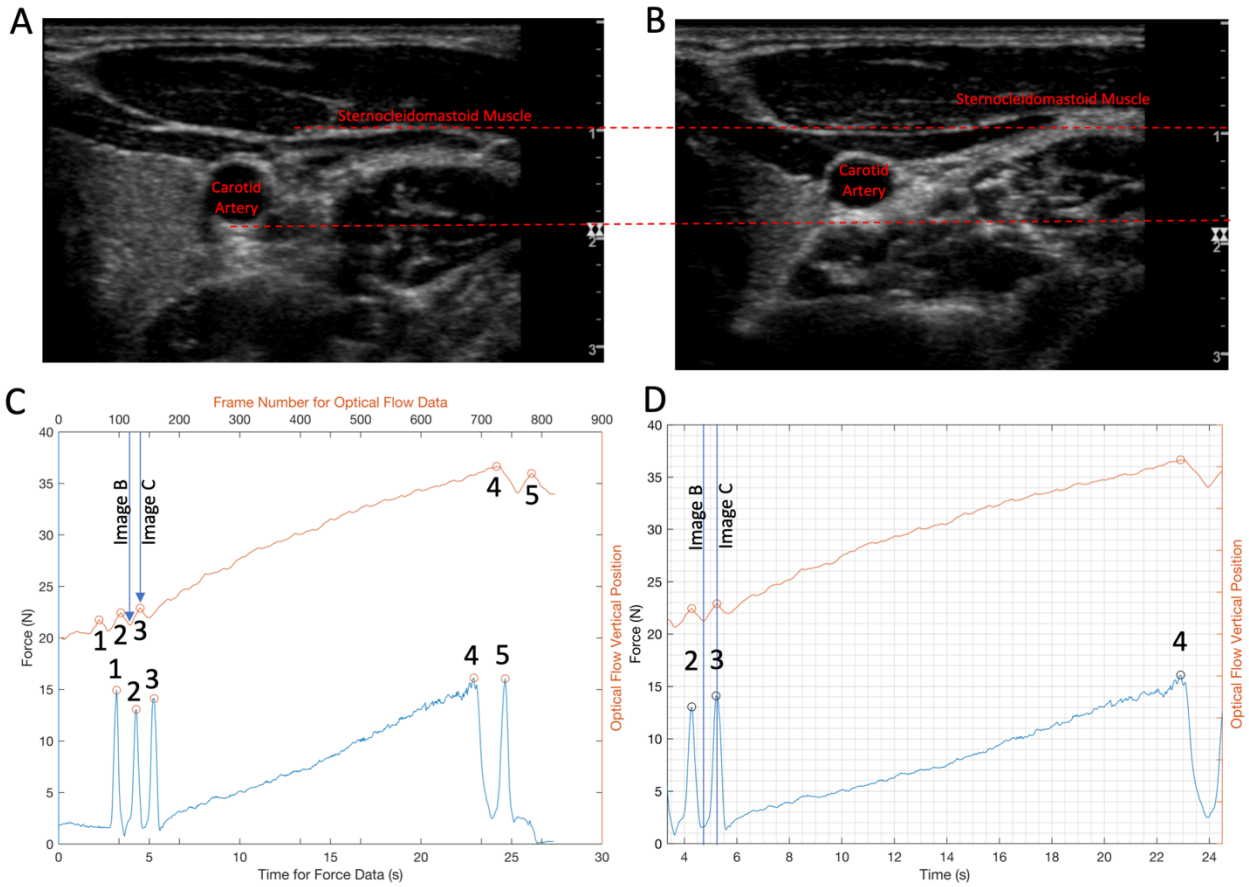

Figure 4-6: (A) Ultrasound image of the carotid artery in the trough of a synchronization compression. (B) Ultrasound image of the carotid artery at the peak of a synchronization compression. (A,B) Red, dashed horizontal lines drawn to signify changes in position of two labeled anatomical landmarks from trough (A) to peak (B). (C,D) Force signal (blue, left y-axis) and optical flow integration signal (orange, right y-axis). with the synchronization peaks for force and optical flow integration (orange) marked as circles. Associated peaks are numbered. (C) Pre-synchronization, force peaks marked as orange circles. (D) Post-synchronization, force peaks marked as black circles.

For the internal jugular vein, the synchronization methodology is identical. The five most prominent peaks are detected in force and optical flow and the first and fifth peaks are aligned. The synchronization check is also the same. This is because the synchronization is independent of what blood vessel is being imaged. It is merely dependent on the presence of a force signal and ultrasound images subject to the same synchronization technique.

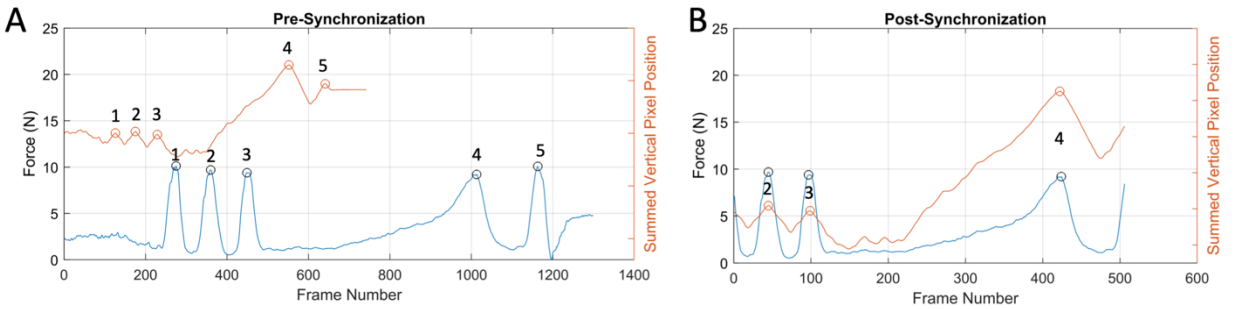

Figure 4-7: Synchronization used on the internal jugular vein. (A) Force and optical flow overlay pre-synchronization . Force is in blue while optical flow is in orange. Synchronization-relevant peaks are marked. (B) Force and optical flow overlay post-synchronization. Force is in blue while optical flow is in orange. Synchronization-relevant peaks are marked.

4.2.2 Secondary Synchronization

Some initial synchronizations are not fully described in the four-step process outlined in section II-A. About 25% of those synchronizations which eventually pass initially fail by not satisfying equation 1.2. For those synchronizations, a more exhaustive synchronization is executed where up to the 30 most prominent peaks are selected in the optical flow signal and up to the 12 most prominent peaks are selected in the force signal. Different combinations of five-peak pairs in optical flow and force are tested via steps two and three of the process in the Materials and Methods Synchronization subsection. If at least one combination passes, the previously failed synchronization now passes. If more than one combination passes, the combination chosen to complete step four of the process is the lowest total error defined on the left side of equation 1.2.

Table 4-1: Summary of automated synchronization evaluation.

Total		Primary Passed	Primary Pass Percentage (%)	Secondary Passed	Secondary Pass Percentage (%)	Total Failed	Total Pass Percentage (%)	Total Incorrect
191		141	73.8	47	94.0	3	98.4	0

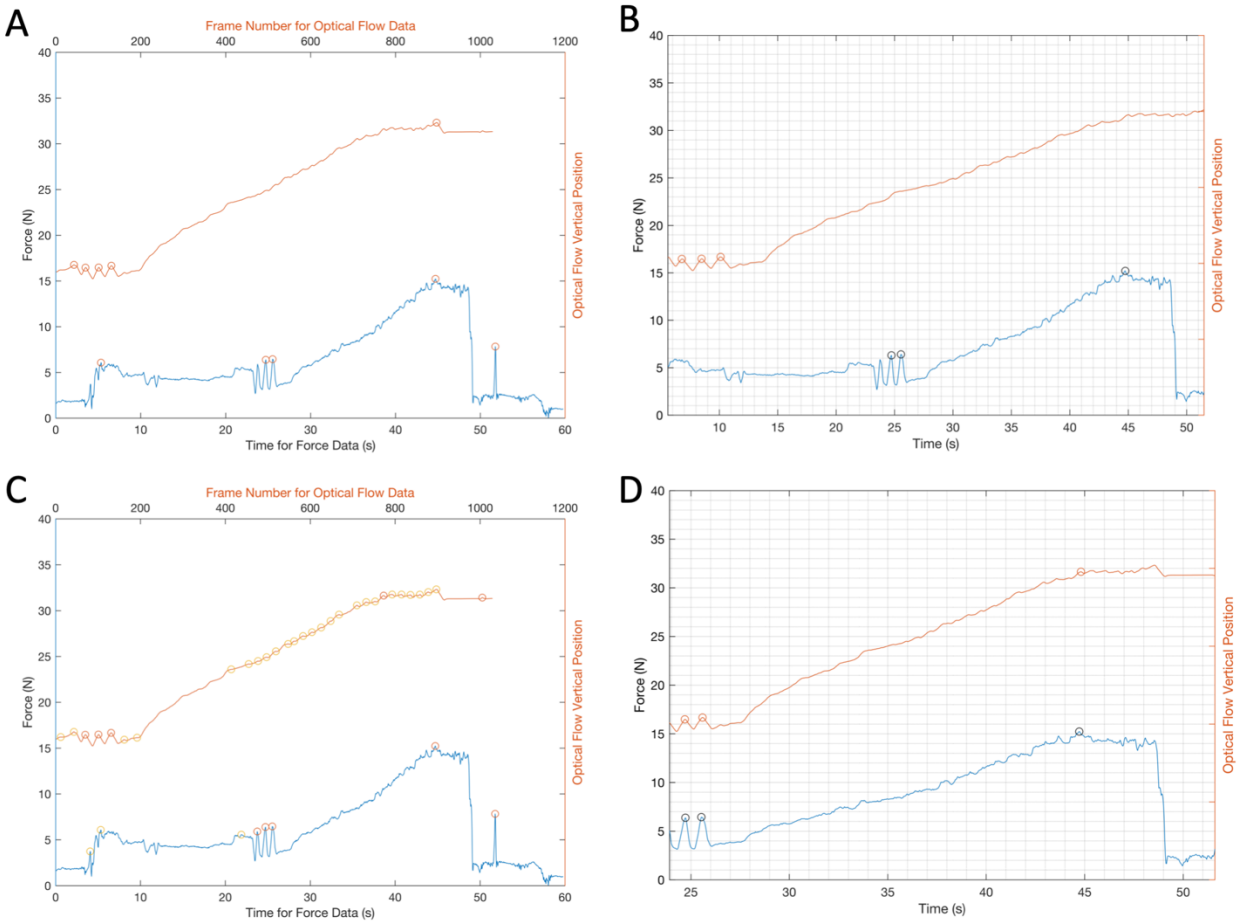

Figure 4-8: (A) Primary synchronization, pre-synchronization. (B) Primary synchronization, post-synchronization. (C) Secondary synchronization, pre-synchronization. The correct peaks are marked with orange circles and the incorrect peaks are marked with yellow circles. (D) Secondary synchronization, post-synchronization.

4.3 Detection

After synchronization, the frames in the slow force sweep which have forces between 2 N and 15 N are segmented. We choose 2 N as the minimum because this is the lowest external force we find to consistently produce a high-quality ultrasound image of the carotid artery. To initialize the carotid artery in the sequence of images, we utilize a convolutional neural network for object detection called a region-based convolutional neural network (R-CNN), which proposes regions via bounding boxes [108]. Specifically, we train Faster R-CNN to identify the carotid artery in 1500 raw ultrasound images [12], [13]. This trained detector finds a supposed carotid and assigns a probability of detection, as seen in the example in **Figure 4-9**A. From the bounding box, the center of the carotid is approximated and used as a seed point. After seed selection, the segmentation of the carotid begins.

Once a force is assigned to each ultrasound image, we must detect the carotid artery in one of the ultrasound images which occur during the force sweep. For this, we use the object detection convolutional neural network Faster R-CNN, trained with 1500 previously segmented images of the carotid artery, to create a detector. The detector outputs a probability that an object is the carotid artery. In evaluating this detector, we find that when we set a confidence threshold value of 0.7, the default, our precision is at about 0.95 for most values of recall.

When we assess this detector's ability to accurately find the carotid and initiate segmentation, it succeeds about 99 percent of the time. This increase to near perfect accuracy is due to the increase of the confidence threshold to 0.95 and the segmentation's ability to test whether or not a detected carotid is correct and tell the detector to try again if necessary. This is what we describe as our secondary detection.

Table 4-2: Summary of automated carotid detection evaluation.

Total	Primary Passed	Primary Pass Percentage (%)	Secondary Passed	Secondary Pass Percentage (%)	Total Failed	Total Pass Percentage (%)	Total Incorrect
188	174	92.6	12	85.7	2	98.9	0

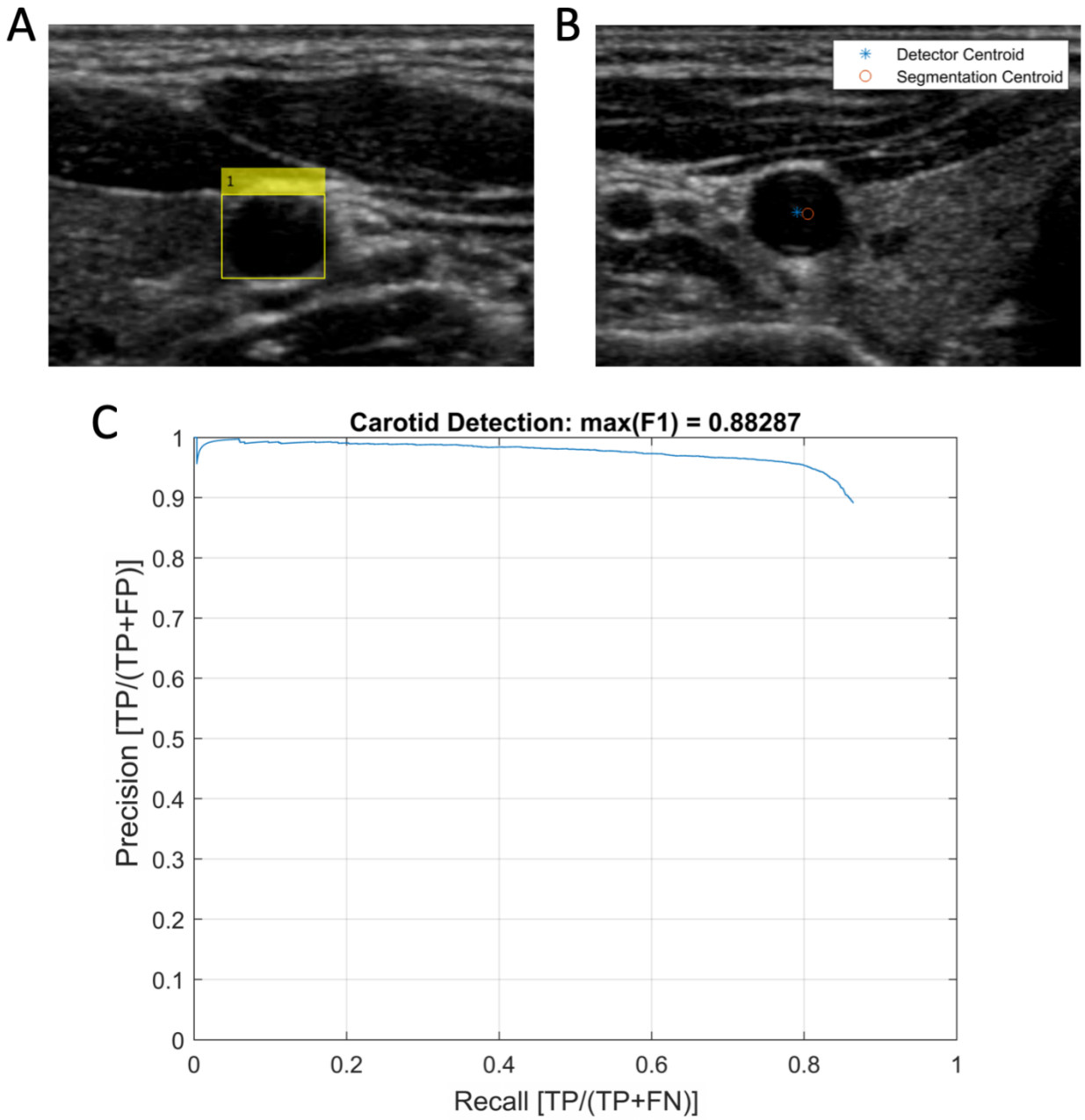

Figure 4-9: (A) Example of the Faster R-CNN detector being used for carotid detection. The labeled boxes highlight the carotid in each image with the probability of (B) Comparing a carotid centroid detected by the carotid detector (blue asterisk) with a centroid derived from the carotid segmentation points (red circle). (C) Precision/recall plot for holdout set of carotid detection training data.

In order to initiate segmentation of the IJV in the force-coupled ultrasound images, the IJV must be detected and a seed point must be provided near the center of the IJV. The IJV is primarily detected via Faster RCNN an object detector neural network, trained on 3000 IJV ultrasound images in a similar manner to the automatic detection of the carotid artery [109]. To avoid the small risk of failure to detect the IJV, the user can click in the IJV when presented with a synchronized force-coupled ultrasound image

to initiate segmentation. All IJV detection is done in MATLAB 2021b (The MathWorks, Inc.; Natick, Massachusetts, United States).

Table 4-3: Summary of automated IJV detection evaluation.

Total	Primary Passed	Primary Pass Percentage (%)	Secondary Passed	Secondary Pass Percentage (%)	Total Failed	Total Pass Percentage (%)	Total Incorrect
128	82	64.1	35	76.1	11	91.4	0

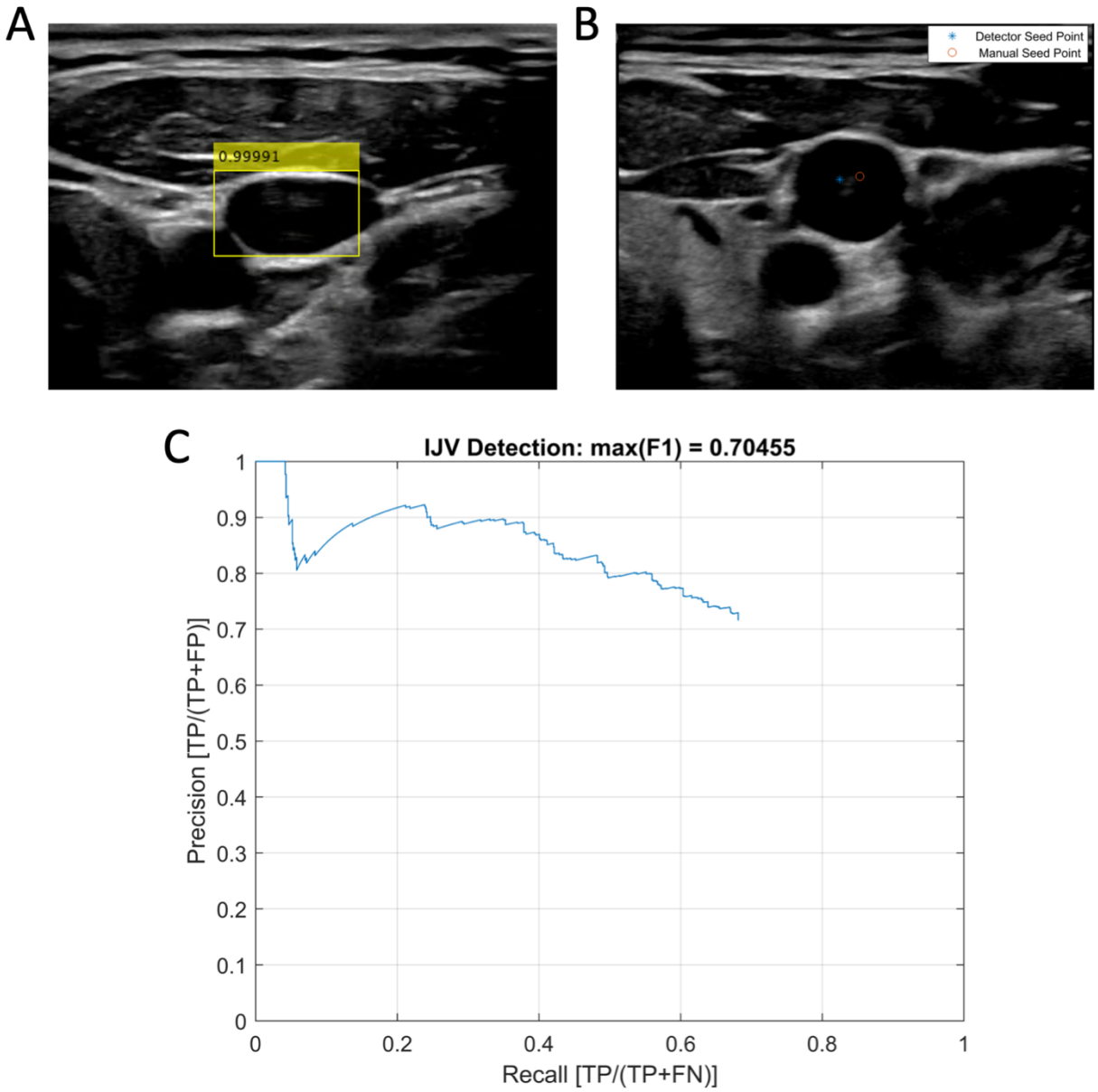

Figure 4-10: (A) Detector bounding box drawn in the vicinity of the IJV with high confidence during detector training. (B) Comparing an IJV seed point detected by the carotid detector (blue asterisk) with a centroid derived from the carotid segmentation points (red circle). (C) Precision/recall plot for holdout set of carotid detection training data. TP is true positives. FP is false positives. FN is false negatives.

4.4 Segmentation

Segmentation provides dimensions of blood vessels for each frame of interest so we can observe the compression and/or pulsation of the blood vessel of interest

4.4.1 Carotid Segmentation

The segmentation of the carotid, in each image starting with the seed point, is a modified version of the region growing (connected components) method for short-axis internal jugular vein cross-sections described in previous research [110]. The method is modified to better optimize for segmenting the more elliptical shape of the carotid. The segmentation methodology within each frame is as follows:

A 2-D median filter of size 20 by 20 (14 mm by 14 mm) and then a Gaussian filter with a standard deviation of 0.5 are applied to the image.

Region growing is executed from a seed point to expand the region in vertical, horizontal, and diagonal directions given candidate pixels have intensities below a threshold from [110]

$$I_{pixel} - I_{mean} < 0.05(I_{max} - I_{min}) \tag{4.3}$$

where I_{max}, I_{mean}, I_{min} are, respectively, the maximum, average, and minimum pixel intensities of the entire image, and I_{pixel} is the intensity of the candidate pixel [110]. The seed point and outline are shown in the magenta scattered point tracing in **Figure 4-11**A.

16 radial lines originating from the calculated centroid from the region growing step are generated. Along each line, a 3-point moving average is applied; the maximum intensity increase is found and selected. This intermediate result is shown in the green asterisks in **Figure 4-11**A. These points are adjusted until a cost function is minimized to the point where the cost decrease from one iteration to the next is less than 10^{-6}. This simple optimization is described by the following cost function equations:

$$C = \frac{\nabla I_0}{D_{c,0} + D_{nn,0}} \tag{4.4}$$

$$Cost = C(D_c + D_{nn}) - \nabla I \tag{4.5}$$

where ∇I is the sum of the radial pixel intensity gradients for each of the points, D_c is the sum of the distances to the centroid for each of the points, D_{nn} is the sum of the distances to the two nearest neighbor points of each of the points, and the subscript 0 indicates the value of these quantities before the optimization starts. This penultimate result is represented as the red circles in **Figure 4-11**A.

An ellipse fit (MATLAB function fitellipse created by Richard Brown, The MathWorks, Inc.) of these points is performed, as shown in the teal solid curve tracing in **Figure 4-11**A.

The centroid coordinates and the vertical and horizontal radii (the minor and major axes of the ellipse fit) are recorded. The coordinates of this centroid are used as a seed point for the next frame in the force sweep. We assume that during the force sweep, displacement of the carotid due to force is gradual in that the carotid will never move more than half its vertical radius from one frame to the next, or over about 30 milliseconds, which ensures the carotid is not lost between frames. This process continues until the end of the relevant sequence of frames in the force sweep. Given the centroid of the carotid remains in the center horizontal third of the ultrasound images for the frames in the force sweep, the segmentation data can subsequently be used in the iterative inverse model to estimate carotid pressure and stiffness parameters. We have this qualification so that the carotid horizontal position in the segmentation approximately matches the horizontally centered position of the carotid in the finite element model without edge effects coming into play.

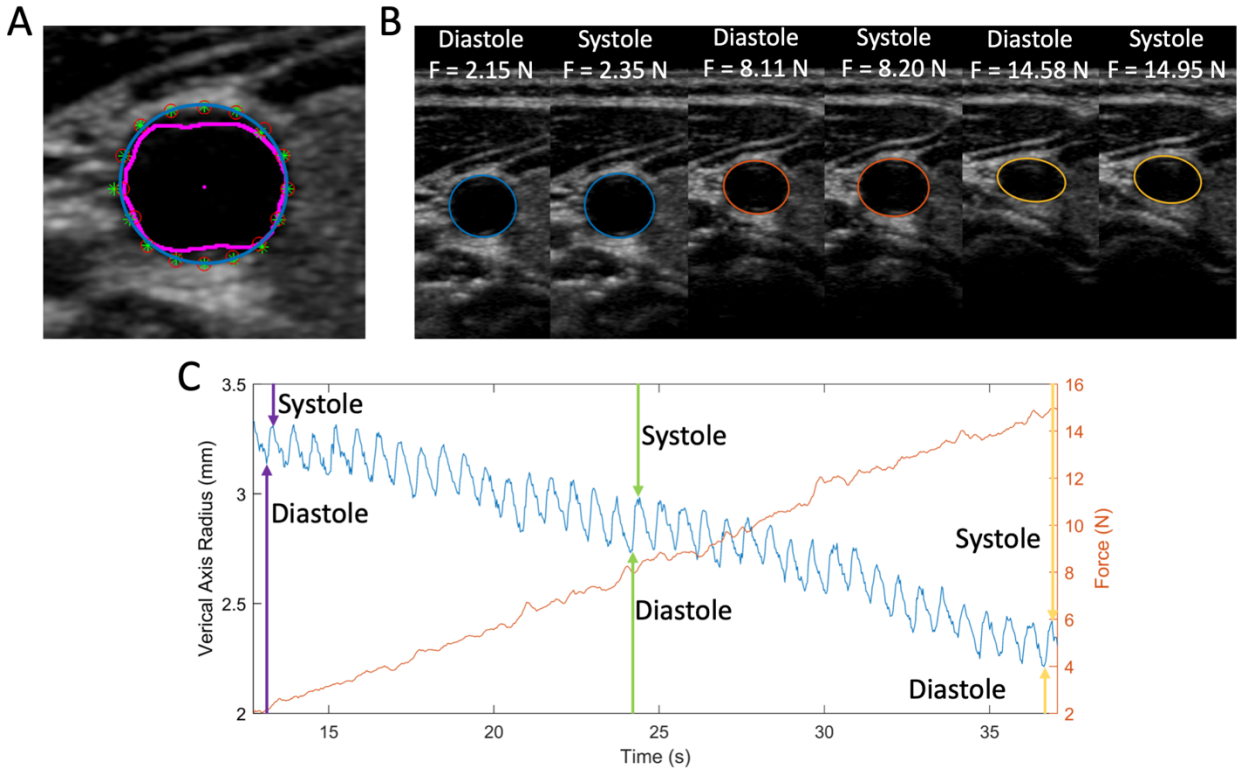

Figure 4-11: (A) Seed point and region growing output in magenta, intensity gradient maximization output as green asterisks, shape and intensity gradient optimization output as red circles, and ellipse fit as teal ellipse. (B) Diastolic and systolic segmentations at different forces, outlined in purple for low force, green for intermediate force, and yellow for high force. (C) Vertical axis radius plot as a function of time with force as a function of time overlaid. Color-corresponding vertical arrows (upward for diastolic, downward for systolic) are drawn to denote where each image is taken in time and how much force is being applied.

4.4.1.1 Average Filtering

When the carotid artery is fully in the far field of the ultrasound image, which decreases image resolution, a noisy carotid area waveform is likely to result. An in-band filter is developed in an effort to decrease in-band noise to produce a carotid area waveform of a more typical and consistent morphology. First, each beat is isolated from the rest of the signal, balanced such that the y-value of the first point in the beat is equal to the y-value in the last point in the beat, interpolated such that the number of samples in the beat is equal to the number of samples in the beat with the most samples, and normalized such that the mean and standard deviation of the beat are zero and one, respectively. At this point, an arithmetically averaged beat is produced (**Figure 4-12**A,B). Then, each isolated beat is filtered by comparing each sample of the beat to the analogous sample in the average beat. If the difference is larger than the standard deviation (**Figure 4-12**C) among the sample at each of the nine

beats, the sample in the beat under examination is replaced with the average sample. **Figure 4-12**D shows an overlay of the raw carotid area waveform and the “average” filtered carotid area waveform.

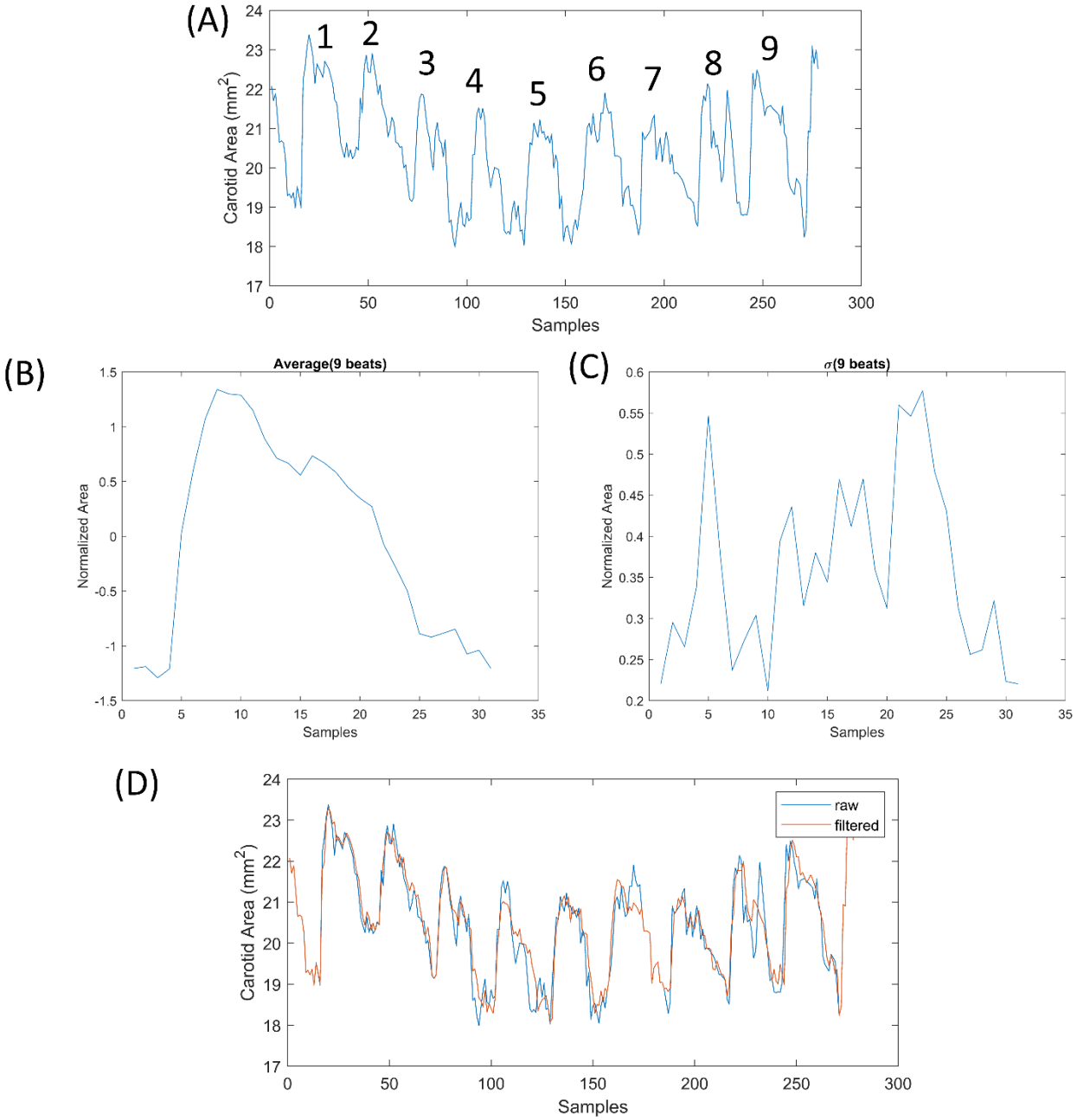

Figure 4-12: (A) Raw carotid area waveform with beats numbered. (B) Average beat, normalized in y with a mean of 0 and a standard deviation of 1 and interpolated in x. (C) Standard deviation at each normalized and interpolated beat sample. (D) Overlay of raw carotid area and carotid area after going through “average” filter.

4.4.2 IJV Segmentation

When the IJV is not near collapse, region growing from a seed point is followed by a radial line intensity difference maximization, intensity difference and shape optimization, and finally a 2000-point third-order interpolation. The differences from carotid segmentation are that 32 radial lines are drawn after region growing instead of 16 and a 2000-point interpolation replaces the ellipse fit at the end of segmentation [109]. Furthermore, when the IJV is near collapse (area of previous image IJV is less than 5 mm^2), only region growing occurs because IJV wall pixels tend to be high-intensity when near collapse such that the region does not grow outside of the walls. Area measurement occurs after the segmentation for a frame is complete by creating a binary image differentiating what is outside the segmentation boundary from what is inside and counting the pixels which are inside.

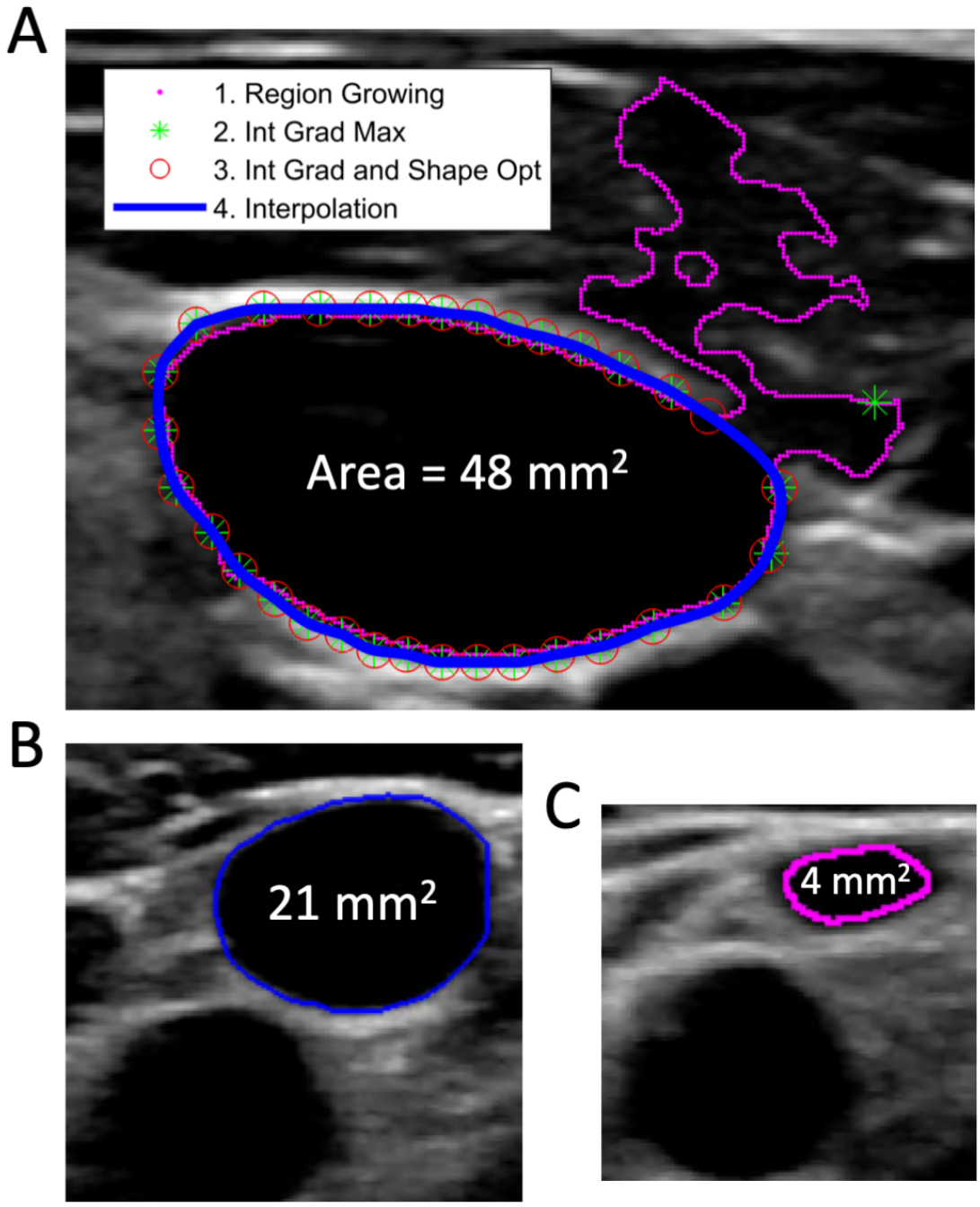

Figure 4-13: (A) Segmentation of an open IJV with all intermediate steps included in subject 2. The pink indicates the first stage region growing output. The green asterisks represent the second stage radial line intensity gradient maximization output. The red circles represent the third stage intensity gradient and shape optimization. The blue tracing represents the final 2000-point interpolation stage. (B) Segmentation of an open IJV in subject 21. The full segmentation algorithm is used. (C) Segmentation of an almost collapsed IJV in subject 21. Only the first region growing step is used.

4.4.3 Trade-offs Between Full and Partial Vessel Segmentations

For the carotid artery and the internal jugular vein, there are slightly different versions of the segmentation executed for each force-coupled ultrasound image in order to optimize for speed and accuracy. As mentioned in the last section, when the IJV is close to collapse the first step of the segmentation (region growing) is sufficient and preferable to execute by itself because the reflections of the IJV walls tend to be strong when close to collapse, yielding high accuracy of the region growing method. Also, the execution time of the region growing step is linearly proportional to the area measured, yielding a tenth the execution time for an IJV a tenth as large. Besides the specific situation of the IJV being near collapse, there are often two options to choose from when segmenting a vessel via the methodology explained earlier in this chapter section: the fast small adjustment and the slow generalized adjustment.

The slow generalized adjustment is exactly the full segmentation for the IJV and the carotid with all steps executed. The fast small adjustment removed the region growing step entirely and bases first boundary estimates of the boundary points from the previous frame's segmentation. The slow generalized adjustment can take anywhere from 0.5 seconds to 5 seconds depending on the size of the vessel while the fast small adjustment reliably takes 0.1 seconds to execute. The fast small adjustment thrives when the vessel is stable positionally and isn't expanding or contracting dramatically. Therefore, this version is preferable for constant force application. This version also has the benefit of not looking towards the center of the vessel where there could be noise which could actually cause the slow generalized adjustment to error due to the region growing mistaking noise for a true vessel boundary near the center of the vessel. However, one can easily lose track of the vessel if something beyond a small change occurs from one frame to the next. In this case, the segmentation can be alerted to these large changes and shift back to the slow generalized adjustment. The fast small adjustment is more reliable for the carotid artery than the IJV because the irregular shape of the IJV is more conducive to region growing for accurate boundary detection and the changes in vessel area for the IJV tend to be about an order of magnitude larger than when the carotid is compressed.

4.5 Manual Failsafes

Despite the automation of force-coupled ultrasound data processing, there are very occasional instances where one can predict failure of each of the automated methodologies of synchronization,

detection, and segmentation. Therefore, we must mention the manual failsafe implemented for each of these automated methods. For the synchronization method the failsafe is to look for synchronization peaks in the B-mode ultrasound images by paying attention to see which frames have the most compression in each of the three initial quick compressions and one final quick compression. This process is quite tedious but has never had to be employed because the synchronization of the force and optical flow signals is so reliable. For the blood vessel detection, the failsafe is to manually click inside the blood vessel of interest. This process is quick and has been employed more for the IJV than for the carotid and most for the leg veins. For the blood vessel segmentation, the failsafe is to automatically draw lines at evenly spread angles which will intersect with the boundary of the blood vessel and to manually click at each of those intersections. Due to the highly regular elliptical shape of the carotid, 16 points are used while 32 points are used for the IJV. This failsafe has never been used for the leg veins as it is only used when high quality segmentation is needed on specific frames and the automatic segmentation makes major errors. These major errors are most often due to noise in the ultrasound images.

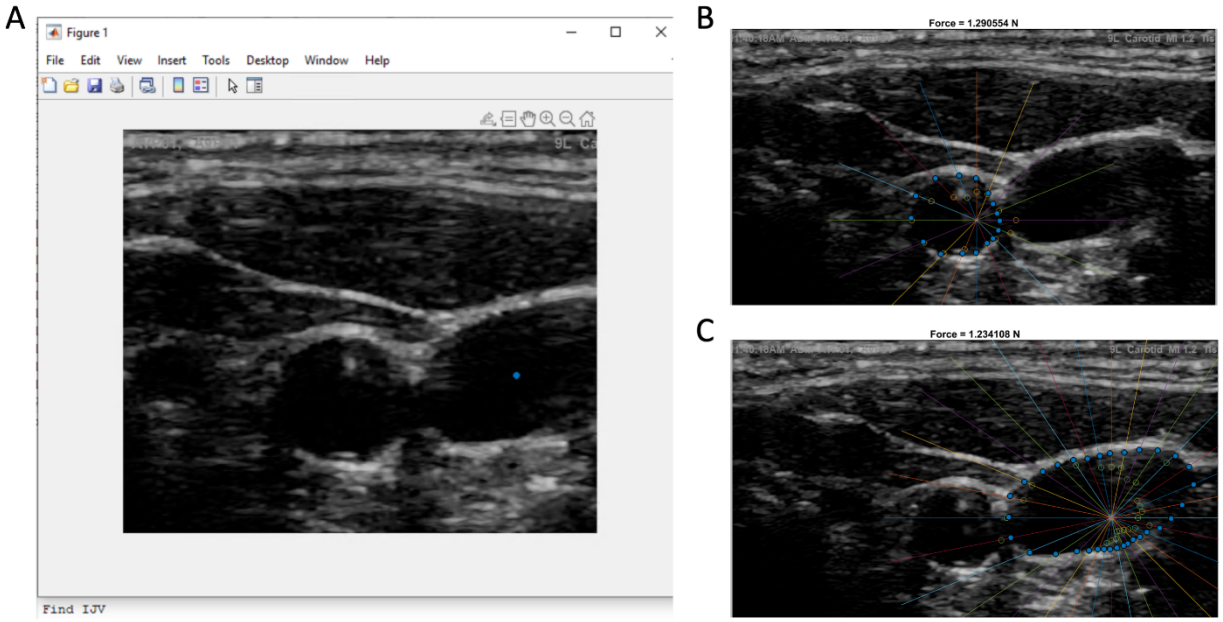

Figure 4-14: (A) Screenshot of manual failsafe of clicking in the IJV with printed direction to do so at the bottom in the MATLAB command window. (B) Manual failsafe for carotid segmentation. (C) Manual failsafe for IJV segmentation.

4.6 Summary

In this chapter, we describe in detail force-coupled ultrasound hardware and software relevant to obtaining segmented force-coupled ultrasound images of large superficial blood vessels in a general sense. We first discuss the hardware necessary to acquire B-mode ultrasound images of the short-axis cross-sections of the blood vessels and their accompanying force signals. Second, we detail the process of automatic synchronization of force and ultrasound to assign each force to an ultrasound image. Third, we describe the object detection convolutional neural network-based approach to automatic detection of the carotid artery and the IJV. Fourth, we describe the automated segmentation of the short axis view of the carotid artery and IJV. Last, we briefly discuss seldom used manual failsafes for synchronization, detection, and segmentation.

Chapter 5 – Central Arterial Pressure Estimation from Force-coupled Ultrasound Imaging of the Common Carotid Artery

We develop, automate, and evaluate a calibration-free technique to estimate human carotid artery blood pressure from force-coupled ultrasound images. After acquiring images and force, we use peak detection to align the raw force signal with an optical flow signal derived from the images. A trained convolutional neural network selects a seed point within the carotid in a single image. We then employ a region-growing algorithm to segment and track the carotid in subsequent images. A finite element deformation model is fit to the observed segmentation and force via a two-stage iterative nonlinear optimization. The first-stage optimization estimates carotid artery wall stiffness parameters along with systolic and diastolic carotid pressures. The second-stage optimization takes the output parameters from the first optimization and estimates the carotid blood pressure waveform. Diastolic and systolic measurements are compared to those of an oscillometric brachial blood pressure cuff. In 20 subjects, average absolute diastolic and systolic errors are 6.2 and 5.6 mmHg, respectively, while correlation coefficients are r = 0.7 and r = 0.8, respectively. Force-coupled ultrasound imaging presents an automated, stand-alone ultrasound-based technique for carotid blood pressure estimation. We propose that this finding inspires its further development and expansion of its applications.

5.1 Introduction

Ultrasound imaging is a prominent and growing modality in many fields of medicine. Force-coupled ultrasound combines medical ultrasound imaging with force-measurement capabilities. A force measuring load cell is coupled to an ultrasound probe by means of an external handheld casing, allowing the user to know the force exerted by the ultrasound probe surface while capturing ultrasound images. This technology can be utilized to help ultrasound sonographers obtain quality B-mode images while knowing the force applied to the image. Applications of force-coupled ultrasound include quantitative strain elastography for Duchenne muscular dystrophy, shear wave elastography of the thyroid under varied preload force, and arterial blood pressure estimation for a litany of cardiovascular-related diseases. Force-coupled ultrasound imaging of an artery typically involves measuring force while observing the partial compression of the artery with ultrasound images. This method applied to blood pressure estimation has a key advantage over the standard blood pressure cuff in that it does not

require complete occlusion of the artery at any point in the measurement. This quality allows it to be used on any artery which can be compressed by an ultrasound probe pressing on the surface of the body without needing to be wrapped around a body part and does not limit measurement to peripheral arteries. The carotid artery is clinically important; it pumps oxygenated blood from the aorta to the brain and regulates blood pressure via its baroreceptors. Previous force-coupled ultrasound research focused on the carotid[106], [111], [112] [2], [25], [119]–[121], [41], [112]–[118].

Other approaches for estimating blood pressure in a noninvasive, calibration-free manor utilize ultrasound and/or photoplethysmography (PPG) signals. One method combines ultrasound and PPG sensing in a single novel device over the carotid to estimate blood pressure by measuring pulse wave velocity and vessel wall distension. This method is significantly less accurate than a blood pressure cuff and is prone to user error from poor placement over the carotid artery. Another method combines PPG with biometric measurements, such as body mass index (BMI), to arrive at a brachial blood pressure estimate with a modified pulse oximeter, but is likely to experience absolute errors of over 10 mmHg [122], [123].

The established workflow of force-coupled ultrasound estimation of arterial blood pressure consists of the following steps:

- Asynchronous ultrasound and force data acquisition
- Synchronization of ultrasound images and force readings
- Segmentation of the artery for each force-coupled ultrasound image in the force sweep
- Blood pressure estimation derived from the segmentation data and computational modeling

We aim to refine each of the analysis modules of this methodology. Previously, synchronization involved a manual selection of synchronization frames and time points in the ultrasound image stack and force signal, respectively. We automate the synchronization process with an algorithm based on optical flow peak detection. The previous method segmented a relatively circular short-axis cross-section of the carotid artery given a B-mode image but was manually initiated by user selection and was occasionally prone to large errors, especially if given a more compressed, elliptical carotid cross-section. The improved segmentation method accurately segments short-axis blood vessel cross-sections of all convex shapes. We automated the start of carotid segmentation by using a trained object detection convolutional neural network (CNN) detector to seed carotid selection. The carotid blood pressure

estimation step established agreement within 10% of standard blood pressure cuff measurements but required calibration. We create an iterative inverse finite element modeling approach with material properties reflective of physiology to achieve strong positive correlation and small disagreement compared with blood pressure cuff measurements without calibration. We validate these multiple improvements to the force-coupled ultrasound methodology by evaluating the synchronization and segmentation accuracy and by comparing the carotid blood pressure estimation to brachial blood pressure cuff measurements [112], [120], [124], [125].

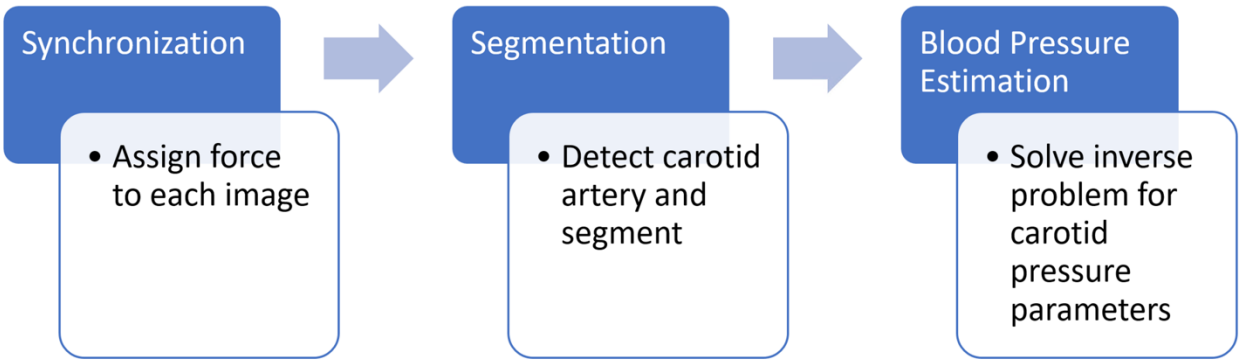

Figure 5-1: Conceptual schematic for postprocessing of force-coupled ultrasound images of the carotid artery short-axis cross-section to estimate carotid blood pressure.

5.2 Data Collection

We collect data on healthy adult subjects without serious cardiovascular disease or hospitalization within six months of data collection. We acquire force and ultrasound data of the short-axis cross-section of the carotid artery and surrounding tissue with the force-coupled ultrasound probe [126]. While sitting upright, the subjects use the device on themselves while the researcher instructs and operates the ultrasound and force data collection user interfaces. They perform a linear force sweep from near 0 N to 15 N with the probe centered over the carotid at the base of the neck. 15 N is chosen to avoid subject discomfort and to stay far away from complete carotid occlusion while still capturing a wide force range.

It is imperative that good acoustic impedance matching and image clarity are confirmed. Regarding acoustic impedance matching, before starting a recording and while the ultrasound probe is contacting the skin in the same location as the recording, we confirm adequate ultrasound gel is present at the contact pair of probe and skin and high intensity reflections are seen throughout the depth and width of the live ultrasound images. Regarding image clarity, after an ultrasound recording is made, it is

played back in its entirety while saving to disk. If blurriness is found during the playback or if the carotid artery is found firmly to be in the far field (e.g. past the depth of the focal point which is shown as the symbol between the bottom red dashed line and the 2-centimeter depth hashmark in **Figure 4-6**A,B), the recording is deleted and a replacement is recorded. For a more quantitative metric of blurriness quantification in ultrasound images please refer to previously published work [127].

Within five minutes after acquisition of the ultrasound and force data, an oscillometric blood pressure cuff is used to capture brachial systolic and diastolic pressures. In postprocessing, given the subject successfully performs the force sweep up to 15 N, a force is assigned to each ultrasound image, the carotid artery in each ultrasound image within the force sweep range of interest is segmented, and finally the carotid blood pressure is estimated by fitting the segmentation data with an iterative finite element model optimization. **Figure 4-1** is a flow chart which highlights the key points of this process through segmentation.

The MIT Institutional Review Board approved this study under protocol number 1601370427. Informed consent was obtained for all subjects of the study. All ultrasound images are acquired with a LOGIQ E9 ultrasound system (General Electric Company; Boston, Massachusetts, United States) with the 9L linear ultrasound probe (General Electric Company; Boston, Massachusetts, United States). The force-coupling casing is a custom designed retrofit to the 9L probe. Force is acquired by a LSB200 load cell (FUTEK Advanced Sensor Technology, Inc.; Irvine, California, United States) and a CSG110 strain gauge amplifier (FUTEK Advanced Sensor Technology, Inc.; Irvine, California, United States), then digitized by the USB-6001 DAQ (National Instruments; Austin, Texas, United States). A LabVIEW (National Instruments; Austin, Texas, United States) virtual instrument was previously designed to display and record the force readings in real time. Brachial artery blood pressure cuff readings for each subject are taken after the force-coupled ultrasound data is acquired with the oscillometric blood pressure cuff model BP3MV1-3W (CVS Pharmacy, Inc.; Woonsocket, Rhode Island, United States). The synchronization and segmentation algorithms are implemented in MATLAB 2018b (The MathWorks, Inc.; Natick, Massachusetts, United States). The iterative inverse finite element modeling algorithms are implemented with the finite element modeling software COMSOL 5.6 (COMSOL Inc.; Burlington, Massachusetts, United States) and MATLAB 2020a (The MathWorks, Inc.; Natick, Massachusetts, United States). The trainings of all convolutional neural networks are implemented in MATLAB 2021b (The MathWorks, Inc.; Natick, Massachusetts, United States) [107].

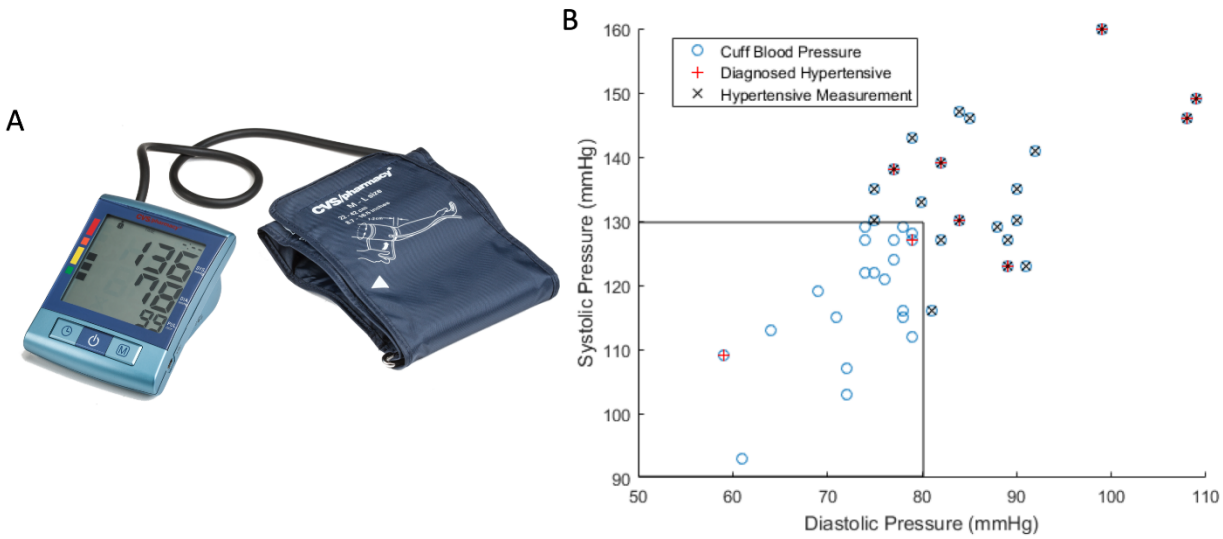

Figure 5-2: (A) Oscillometric brachial blood pressure cuff used as the noninvasive standard for comparison in the carotid blood pressure study. (B) Blood pressure cuff recordings from the oscillometric cuff on the 42 subjects of the carotid blood pressure study. Solid lines are drawn to identify Stage 1 Hypertension.

5.3 Analysis to Obtain Central Blood Pressure Estimate

The physiological parameters of the carotid artery are predicted by comparing observations to a model. The numerical model mirrors what is observed in the ultrasound image. The model is perturbed similarly to the force sweep acquisition and compared to observations. Consistent with previous versions of this method, the forward problem solves a finite element model of a short-axis cross-section for carotid artery deformation. Here, the finite element model is redesigned and expanded to more accurately reflect carotid artery anatomy and physiology by using more inputs from the segmentation over a wider range of forces and nonlinear material elasticities [106], [111].

5.3.1 Finite Element Forward Model

The finite element modeling software COMSOL is used. The model is observed in the COMSOL GUI and then automated with the aid of the LiveLink software (COMSOL, Inc.) in MATLAB. The finite element model design in terms of geometry, meshing, boundary conditions, and parameters is described below.

A 20 cm by 6 cm rectangle with a circular hole and an annulus around the circle, as seen in **Figure 5-3**, represents the nominal geometry. Within this short-axis cross-section, the hole represents the carotid lumen and is placed in reference to the carotid segmentation data. The annulus represents

the carotid wall and is 1 mm thick to reflect literature values. The remainder of the rectangular domain represents the surrounding tissue. The smooth circular carotid lumen assumes the carotid wall to have an unperturbed shape of a circular annulus and no asymmetric plaque distribution lining its interior. The width of the modeled geometry is about 350 percent wider than the width of an ultrasound image to prevent the left and right boundaries of the model from having an edge effect on what is going on at the center [128], [129].

The height of the geometry is about 70 percent greater than the depth of the ultrasound image and accounts for tissue compression that could be going on in deeper tissue. The size of the carotid lumen in the model geometry is referred to as the unperturbed radius r_0 of the carotid, which is a hypothetical estimate of what the carotid radius would be if no forces were acting on the carotid and there was zero transmural pressure between the lumen and the surrounding wall and tissue. The geometry of the model is shown in **Figure 5-3** [130].

The triangular mesh must capture the contact and the interaction between the annulus representing the carotid wall and the rectangle representing the surrounding tissue. To achieve accurate interaction at this contact boundary, the elements representing the carotid wall are at least twice as fine as the elements representing the tissue. Finer elements are used in the vicinity of the carotid, where smaller scale interactions take place and key measurements are made in the model, compared to the surrounding tissue in the model, which are less significant. The meshing is depicted in **Figure 5-3**A [131], [132].

The finite element model has fixed, free, and loaded boundary conditions. The bottom of the model is fixed to anchor the model while the sides of the model are free, preventing unrealistic stress from forming near the side boundaries. The loaded boundary conditions represent (1) the external force of the ultrasound probe compressing from the top of the model for a segment of the length of the ultrasound probe and (2) the blood pressure acting on the inner walls of the carotid artery. To improve convergence of the forward model, both loads are numerically increased from zero to their intended strengths over several steps. In **Figure 5-3**B, a blue line segment at the top of the model represents the external force from the ultrasound probe and the symbol P_l represents the blood pressure in the lumen of the carotid [131], [133].

The model's material parameters approximate the tissue properties of the two distinct uniform materials of the carotid wall and the surrounding tissue. The carotid wall has an exponentially strain-dependent elastic modulus

$$E = E_0 e^{\alpha \varepsilon} \tag{5.1}$$

where E_0 is the base elastic modulus, α is the exponential term, and ε is the absolute radial strain from the unperturbed radius r_0 [130]. The Poisson ratio used for the carotid wall is 0.46. The surrounding tissue is modeled to be a modified version of COMSOL's Ogden hyperelastic material based on success of previous efforts to model soft tissue. COMSOL's input parameters for an Ogden hyperelastic material are the bulk modulus K and the shear modulus. To simplify the tissue model and allow the tissue to reliably stiffen in response to compression as seen in previous works, while also accounting for the tissue stiffness values found in literature [134], the shear modulus is set equal to the bulk modulus. Additionally, an external force-dependent linear adjuster to K is applied

$$\mathrm{K} = \mathrm{K}_0 + F_{ext}\mathrm{K}_1 \tag{5.2}$$

where K_0 is the base bulk modulus, F_{ext} is the external force applied to the top of the model, and K_1 is the linear dependency term. The two tissue stiffness parameters are assumed constant ($K_0 = 75\ kPa, K_1 = 4 * 10^{-5}\ Pa/N$) across all optimizations to avoid overfitting and because tissue displacement is difficult to quantify given the tissue uniformity simplification in our forward model. A sensitivity analysis to deviation from these assumptions can be found in **Figure 5-4**. The material parameter terms are labeled in **Figure 5-3**B. The finite element model is summarized by the equation

$$f(P_l, E, \mathrm{K}, F_{ext}) = [d_y] \tag{5.3}$$

where f symbolizes the finite element model and $[d_y]$ is a vector of vertical displacement of all the elements of the model [124], [134]–[137].

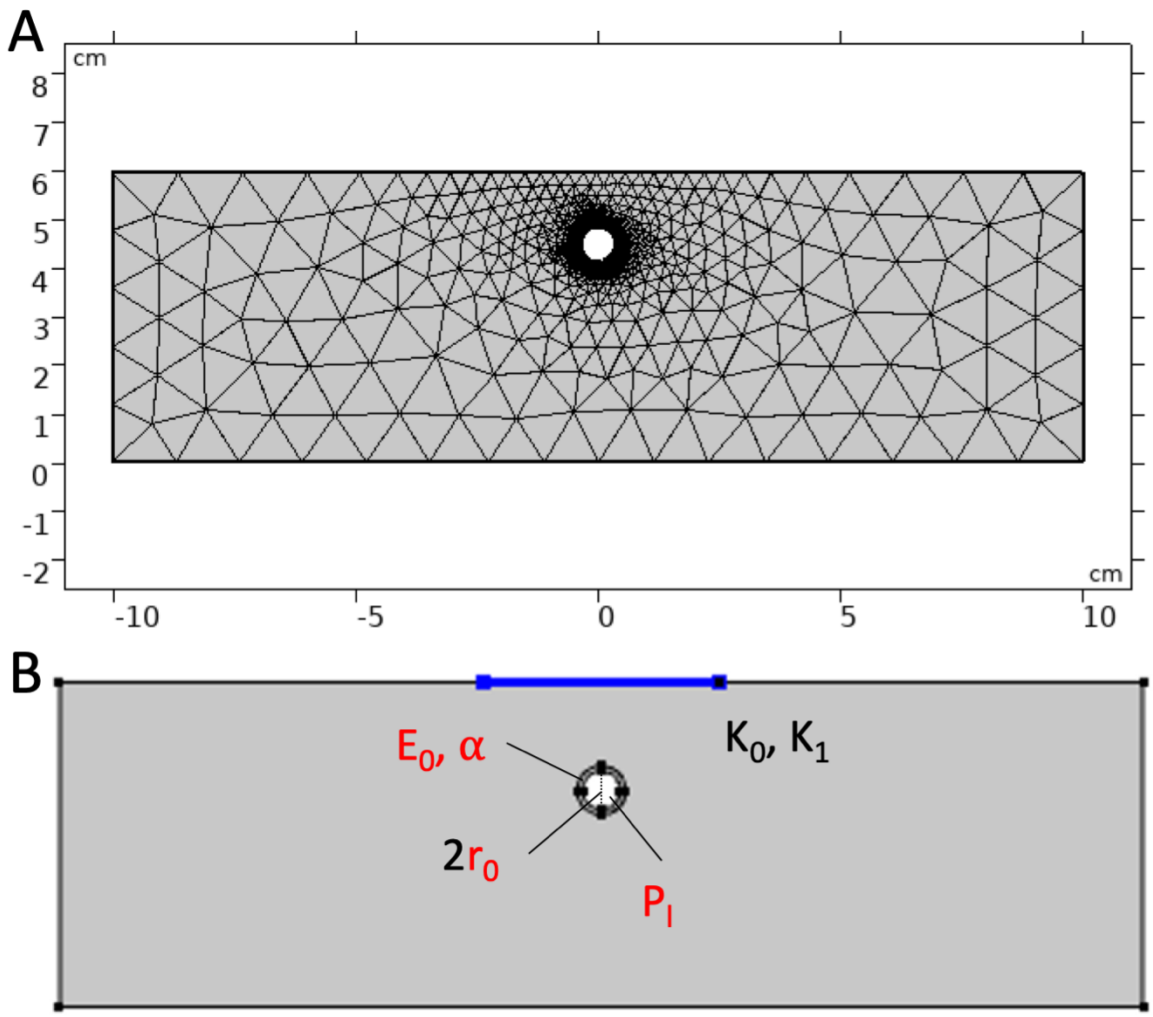

Figure 5-3: COMSOL generated triangular finite element mesh of carotid artery short-axis cross-section. (B) The external force boundary condition is at the top of the model in blue. The tissue stiffness parameters (K0, K1), the carotid wall stiffness parameters (E0, α), the carotid unperturbed radius (r0), and the carotid lumen pressure (Pl) are labeled. Optimization parameters are labeled in red while constants are labeled in black.

5.3.1.1 Forward Model Input Parameter Sensitivity

We assess the estimation sensitivity to parameter perturbation for each of the parameters in the iterative inverse finite element method. We allow -30% to +30% deviation from selected values near initial guess values of each parameter. In **Figure 5-4**, each individual parameter is perturbed while holding all other parameters constant. We observe that the estimation is most sensitive to r_0 while P_l is moderately sensitive and α and K_1 are the least sensitive parameters. Moreover, K_0 and K_1 are least verifiable because surrounding tissue deformation is least indicated by minor (vertical) axis radius, which

is further reasoning for K_0 and K_1 being held constant across all force sweeps during inverse optimization.

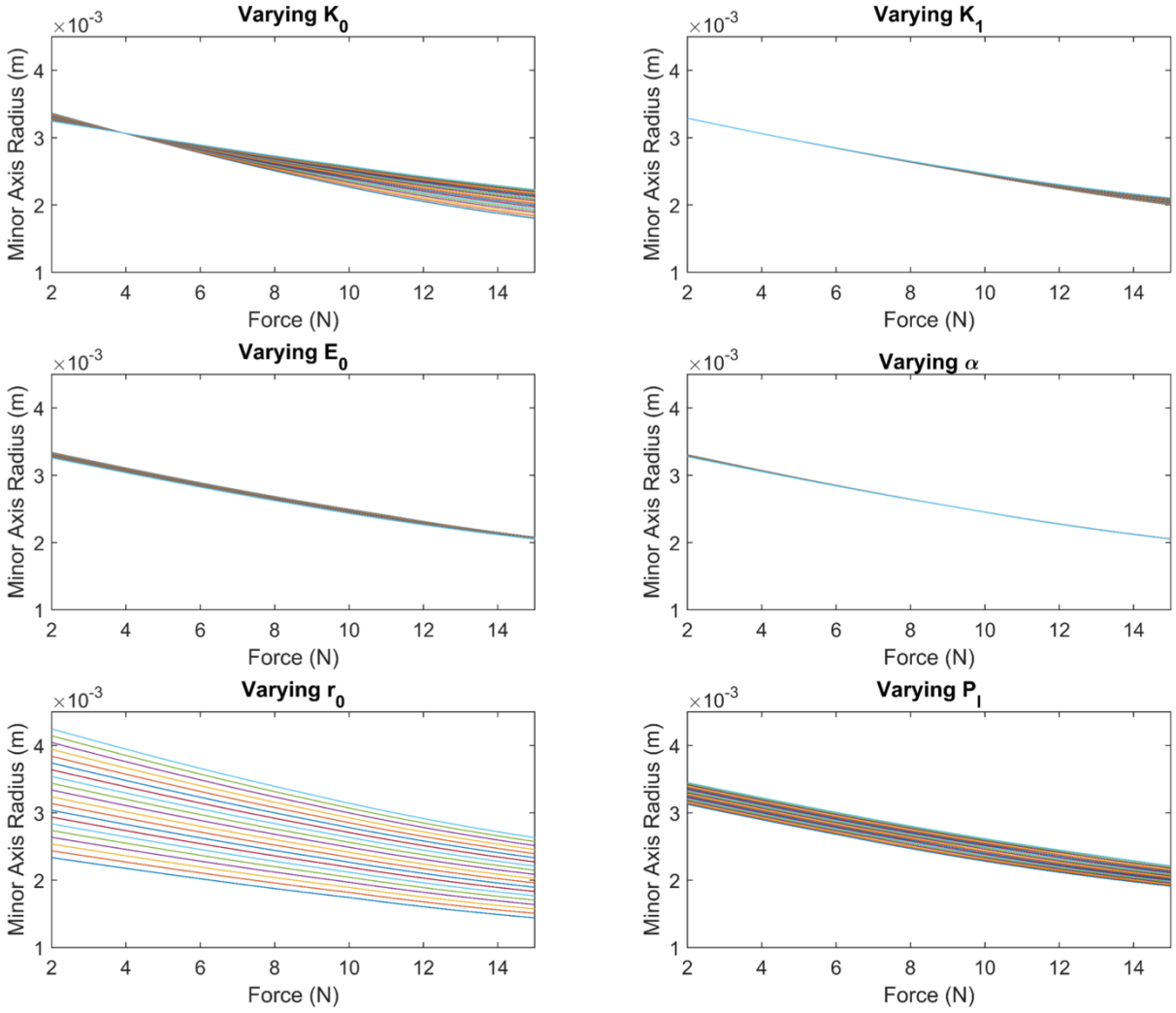

Figure 5-4: A forward model sensitivity analysis for each of the parameters used to run the forward finite element model to determine carotid artery deformation resulting from external force from a force-coupled ultrasound probe. They are varied between -30% and +30% of the initial guess.

5.3.2 Iterative Inverse Model

The finite element model of the short-axis cross-section of the carotid artery is nested in an iterative (inverse model) optimization process to select the pressure parameters of pulse pressure P_p and diastolic pressure P_d, the carotid wall stiffness parameters E_0 and α, and the unperturbed radius parameter r_0. The scalar parameters combine to form a vector of parameters p. A Nelder-Mead simplex

(downhill simplex) method for unconstrained nonlinear optimization from MATLAB's optimization toolbox, called "fminsearch", is used on the force sweep to converge on values for each of these parameters [40].

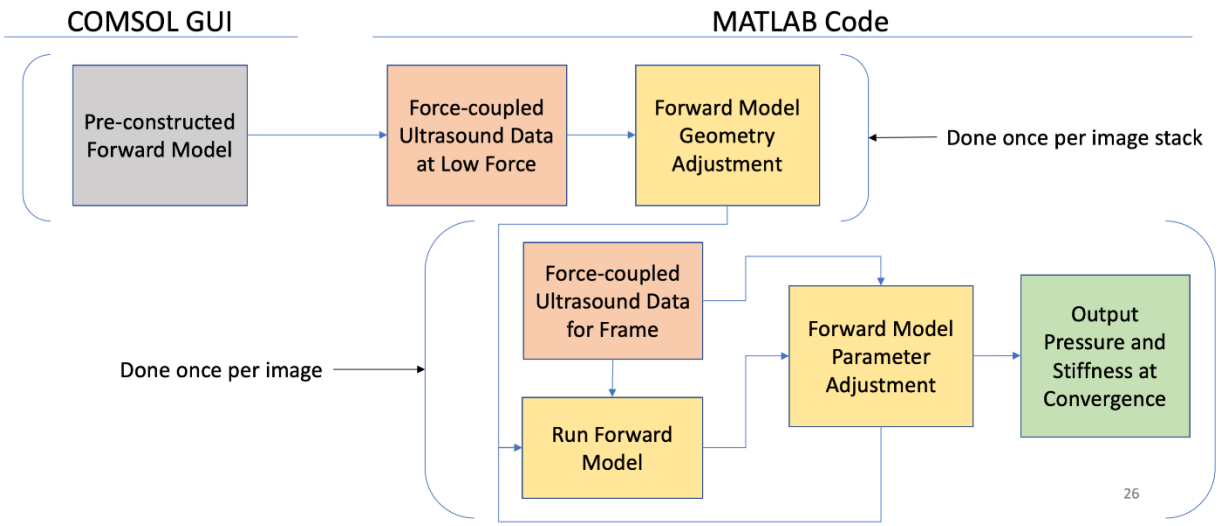

Figure 5-5: Conceptual diagram of force-coupled ultrasound observation guided iterative inverse finite element modeling to produce lumen pressure and wall stiffness parameter estimations

The dimensions of the carotid centroid of the nested forward model are initialized with the segmentation data from the minimum force ultrasound image. Peak detection of the carotid vertical radius signal determines the diastolic and systolic (minimum and maximum) frames of the segmentation and the forces at those frames are used in the parametrized external force sweep. The carotid vertical and horizontal radii in these frames are used to determine radial strain ε used in the carotid wall stiffness while only the vertical radii are used in the optimization's cost function due to the relatively higher accuracy of ultrasound imaging in determining depth compared to determining horizontal position. Representative finite element model solutions and segmentation data are shown in **Figure 5-6**.

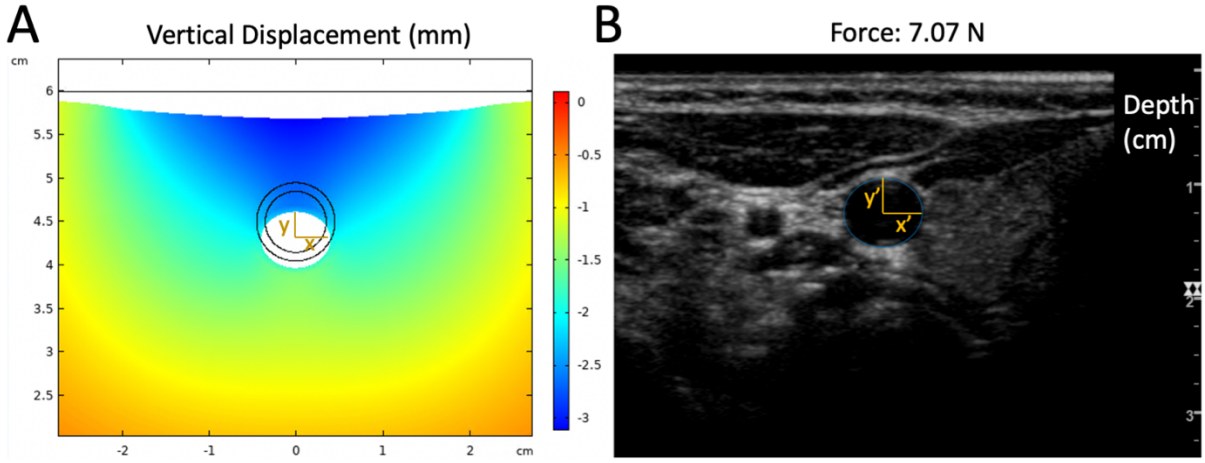

Figure 5-6: (A) Forward model run with vertical axis displacement of elements color coded. The horizontal and vertical carotid radii are labeled by x and y, respectively. (B) Segmented carotid artery in a force-coupled ultrasound image with x' and y' labeling the measured horizontal and vertical carotid radii, respectively.

Each iteration of the forward model uses all the diastolic and systolic points in the force sweep, 25 cycles of each on average, and serves to reduce the difference between the vertical axis radii of the carotid observed in segmentation with what is predicted in the forward model output, as illustrated in **Figure 5-6**. In the nested forward model equations:

$$f_m(P_d, E_0, \alpha, r_0, F_d, S_d) = D_d \tag{5.4}$$

$$f_m(P_p, P_d, E_0, \alpha, r_0, F_s, S_s) = D_s \tag{5.5}$$

f_m symbolizes the nested forward finite element model, F_d and F_s are vectors of the external force by the force coupled ultrasound, S_d and S_s are the observed segmentation data, and D_d and D_s are the diastolic and systolic difference vectors between observed vertical axis radii in the segmentation and the predicted vertical axis radii in the forward model. Due to observation uncertainty in the segmentation of the carotid, any element in either difference vector with a magnitude of less than 0.2 mm is set to zero (additional observation uncertainty notes are found in **Figure 5-7**). The scalar cost function minimized over the optimization is:

$$Cost = D_{d,2}^2 + D_{s,2}^2 + CR_2^2 \tag{5.6}$$

where $D_{d,2}^2$ is the L2 norm squared the vector D_d, $D_{s,2}^2$ is similar but for systole, R_2^2 is the regularization term, and C is a scaling constant of value 10^{-4} to allow the difference terms and the regularization

terms to be at roughly the same order of magnitude. The regularization term is used to penalize parameter ranges that are beyond the physiological ranges expressed in the literature for carotid pressure and wall stiffness [130], [138]. The regularization term equation is:

$$R^2 = \sum_i \left(\frac{\Delta(p_i)}{p_i}\right)^2 \tag{5.7}$$

where i is the parameter index, p_i a parameter, and $\Delta(p_i)$ the distance from the nearest boundary of the parameter's penalty-free range. If all parameter values are within their respective penalty-free ranges, the regularization term is zero. Initial values are within these ranges. The penalty-free bounds for r_0 and tissue stiffness values are determined empirically. r_0 is a theoretical dimension, unobservable in a live subject. The initial guess for r_0, $r_{0,seg}$ in **Table 5-1**, is determined from the segmentation data to be the radius at the point in the force sweep where there is the largest difference in radial strain between diastole and systole. The initial values and regularization penalty free bounds for each parameter are displayed in **Table 5-1**. To account for the hydrostatic pressure difference due to the height above the heart at which the force-coupled ultrasound images are taken at the base of the neck, 8 mmHg, corresponding to about 11 cm of height, is subtracted from the initial guess and regularization bounds and then added back to the converged diastolic pressure [41].

Table 5-1: Iterative inverse model parameter initial guesses and regularization penalty-free bounds.

Parameter	Units	Initial Guess	Regularization Penalty-Free Lower Bound	Regularization Penalty-Free Upper Bound
$\boldsymbol{P_p}$	mmHg	31	18	44
$\boldsymbol{P_d}$	mmHg	75 (67)	64 (56)	94 (86)
$\boldsymbol{E_0}$	kPa	20	15	180
$\boldsymbol{\alpha}$	-	3.0	2.5	4.5
$\boldsymbol{r_0}$	mm	$r_{0,seg}$	2.5	3.5

From this optimization, diastolic and systolic pressure are estimated. Systolic pressure is the sum of diastolic pressure and pulse pressure and can be checked against the blood pressure cuff measurement. A subsequent optimization runs with the converged carotid wall and surrounding tissue stiffness parameters being used as known values while only optimizing over lumen pressure P_l (blood pressure). For each frame the carotid is segmented, the nested forward model and cost equations are

$$f_{m,k}(P_{l,k}) = D_k \tag{5.8}$$

$$Cost = D_k^2 + C\lambda_k^2 \tag{5.9}$$

where subscript k denotes the frame. D_k is the difference between observed and predicted vertical axis radii for the frame. C is the same scaling factor as the antecedent optimization (10^{-4}). λ_k^2 is the regularization term calculated by

$$\lambda_k^2 = \left(\frac{\Delta(P_{l,k})}{P_{l,k}}\right)^2 \tag{5.10}$$

$\Delta(P_{l,k})$ is the distance from the nearest boundary of the penalty-free range $[P_d, P_d + P_p]$ which are the diastolic and systolic converged values from the antecedent optimization. The output of this optimization is a sampled carotid blood pressure wave with a sample rate equal to the frame rate of the ultrasound image sequence.

5.3.3 Uncertainty Quantification

In solving for the pulse pressure, diastolic pressure, and other optimization parameters, one must solve an inverse model where a forward finite element model predicts deformation of the carotid artery based on the parameter inputs and an external force. The model adjusts according to distance differences between this deformation and what is observed at the same force from segmentation of force-coupled ultrasound images. In determining these differences, we note that there is inherent uncertainty in the segmentation methodology due to the pixel resolution of the image and the range of pixel intensities where our segmentation algorithm draws the ellipse boundaries signifying the carotid wall. This range has been found to be between 0.30 and 0.55 of grayscale pixel intensity where zero is black and one is white. We have deduced that this transition usually takes place over 3 pixels or 0.2 mm. Therefore, when measuring differences between the deformed carotid radius in the forward model output and those measured in the segmentation data, differences of less than 0.2 mm are set to zero when calculating the cost function for a given iteration of the inverse model.

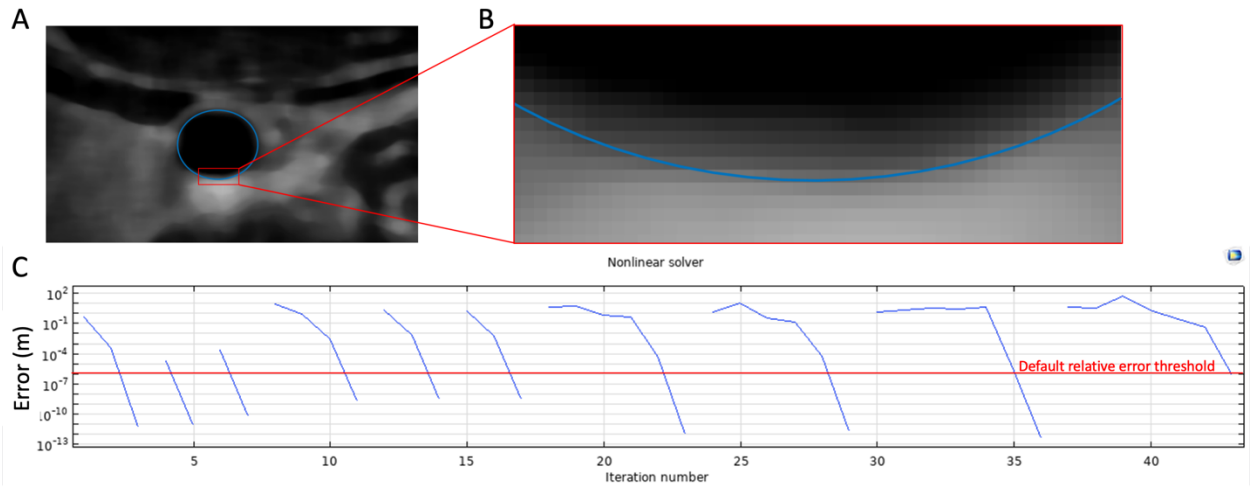

Figure 5-7: (A) Processed and segmented carotid artery in the same image. (B) Zoomed in section of segmented carotid artery highlighting the uncertainty range between pixel intensities 0.30 and 0.55 on a zero to 1 grayscale. (C) Finite element forward model convergences showing relative error threshold. The units for the y-axis is meters.

5.4 Central Blood Pressure Estimation Results

20 relatively high-quality segmentations, each from a different subject, are chosen to go through the optimization. Their converged parameters are recorded in **Table 5-2** along with the initial guesses for the optimization. We note that only force and ultrasound data is used to produce the converged parameters, including systolic and diastolic pressure, despite known positive correlation between age and blood pressure. On the other hand, to assess the accuracy of the carotid blood pressure estimates relative to the blood pressure cuff measurements, we first estimate carotid systolic blood pressure based on the brachial systolic blood pressure cuff value and age. Diastolic pressure is assumed equal in the carotid and the brachial arteries in the same individual. We use the systolic cuff value and the age of each of the volunteers to generate the cuff-derived carotid systolic pressure from a lookup table from a previous study which derives a carotid blood pressure wave via a diastolic brachial blood pressure cuff measurement, ultrasound measurements at the carotid artery and an assumption of constant compliance of the carotid artery wall [138]–[140].

Table 5-2: Initial guess and converged parameter values for 20 volunteers' force sweeps

#	Age Range (yrs)	E_0 (kPa)	α	r_0 (mm)	P_d (mmHg)	$P_{d,cuff}$ (mmHg)	$\lvert\Delta\rvert_d$ (mmHg)	P_s (mmHg)	$P_{s,cuff,adj}$ (mmHg)	$\lvert\Delta\rvert_s$ (mmHg)
1	20-29	20	4.5	2.5	73	75	2	117	110	7
2	20-29	31	2.5	3.0	66	78	12	103	103	0
3	20-29	19	4.1	3.5	83	77	6	116	126	10
4	70-79	15	3.6	3.9	95	108	13	129	129	0
5	40-49	33	2.9	3.5	93	91	2	121	109	12
6	20-29	29	2.5	3.1	70	82	8	109	115	6
7	20-29	29	2.9	2.7	65	71	6	102	103	1
8	60-69	32	3.1	3.5	74	78	4	105	113	8
9	20-29	34	3.2	2.5	80	81	1	111	104	7
10	20-29	28	2.5	2.7	74	74	0	118	115	3
11	70-79	15	2.5	4.5	96	84	12	129	130	1
12	20-29	27	3.0	2.5	66	76	10	101	109	8
13	20-29	29	2.8	3.1	76	88	12	111	117	6
14	20-29	30	3.0	2.9	74	79	5	108	116	8
15	60-69	15	3.5	3.6	94	92	2	134	125	9
16	60-69	30	3.0	3.1	75	76	1	106	105	1
17	20-29	19	3.4	2.9	76	75	1	120	123	3
18	20-29	23	2.6	3.0	95	79	16	130	131	1
19	20-29	32	3.2	3.0	64	61	3	98	81	17
20	20-29	31	3.1	2.9	80	77	3	116	112	4

We observe strong positive correlations and average absolute errors within 10% of the blood pressure cuff-derived values for both diastolic and systolic estimates in **Figure 5-8**. For diastolic estimates in **Figure 5-8**A,B, a correlation coefficient $r = 0.70$, an average error of -1.6 mmHg, and an average absolute error of 6.4 mmHg are found. For systolic estimates in **Figure 5-8**C,D, a correlation coefficient $r = 0.80$, an average error of 0.4 mmHg, and an average absolute error of 5.6 mmHg are found. We note that these average absolute errors are slightly greater than the American Medical Association standard of 5 mmHg [141].

We perform a simple sensitivity analysis on r_0 for all 20 force sweeps which went through the optimization. We find for a perturbation of plus or minus 0.1 mm in the r_0 initial guess, none of the force sweeps experienced changes in their converged parameters. We also find that when the converged value of r_0 is adjusted by one percent (around 0.03 mm) and allow for convergence of the other parameters, all of the converged cost values increased. Finally, when we adjust all converged parameters by one percent, we find the average cost function increase to be 53 percent. This sensitivity analysis indicates our inverse problem is relatively convex and well-conditioned given its inputs. Error bars are drawn in **Figure 5-8**A,C to show how much the diastolic and systolic pressures need to be

changed to display a discernable increase in the cost function without regularization penalties ((0.2 mm)^2 = 0.04 mm^2).

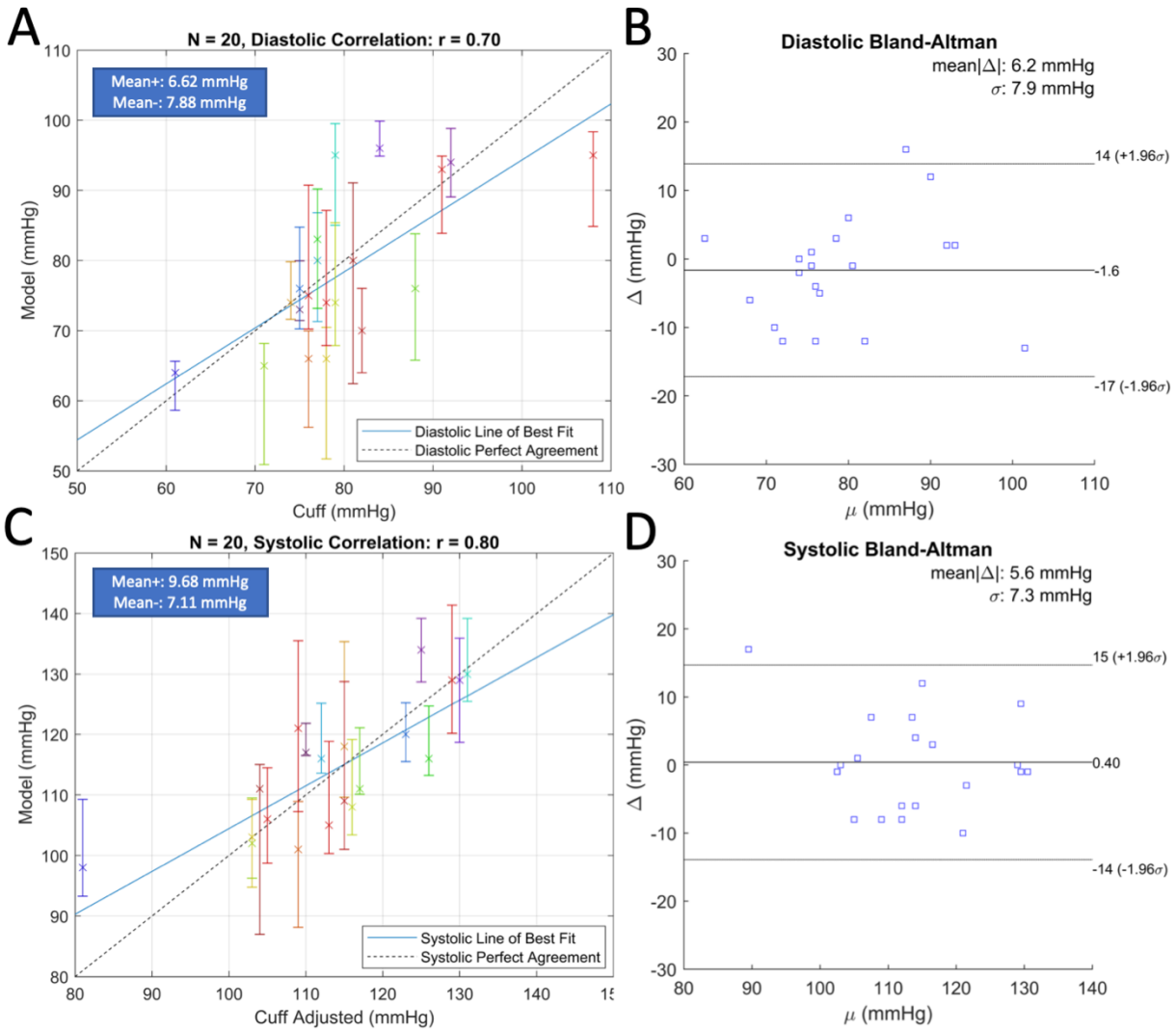

Figure 5-8: (A) Correlation plot comparing brachial cuff diastolic measurements with converged diastolic values from the inverse optimization. (B) Bland-Altman plot comparing brachial cuff diastolic measurements with converged diastolic values from the inverse optimization. (C) Correlation plot comparing adjusted brachial cuff systolic measurements with converged systolic values from the inverse optimization. (D) Bland-Altman plot comparing adjusted brachial cuff systolic measurements with converged systolic values from the inverse optimization.

Figure 5-9 shows a sampled blood pressure wave of one of the volunteers for about 4 cardiac cycles as output by the subsequent optimization to determine a sampled carotid blood pressure wave. Quick expansion and slower relaxation are visible with dicrotic notches somewhat visible on the first, third, and fourth cardiac cycles. The systolic and diastolic estimates from the sample pressure wave are

consistent across the cardiac cycles despite a ramped external force and a further compressed carotid with increasing force between the first cardiac cycle and the last.

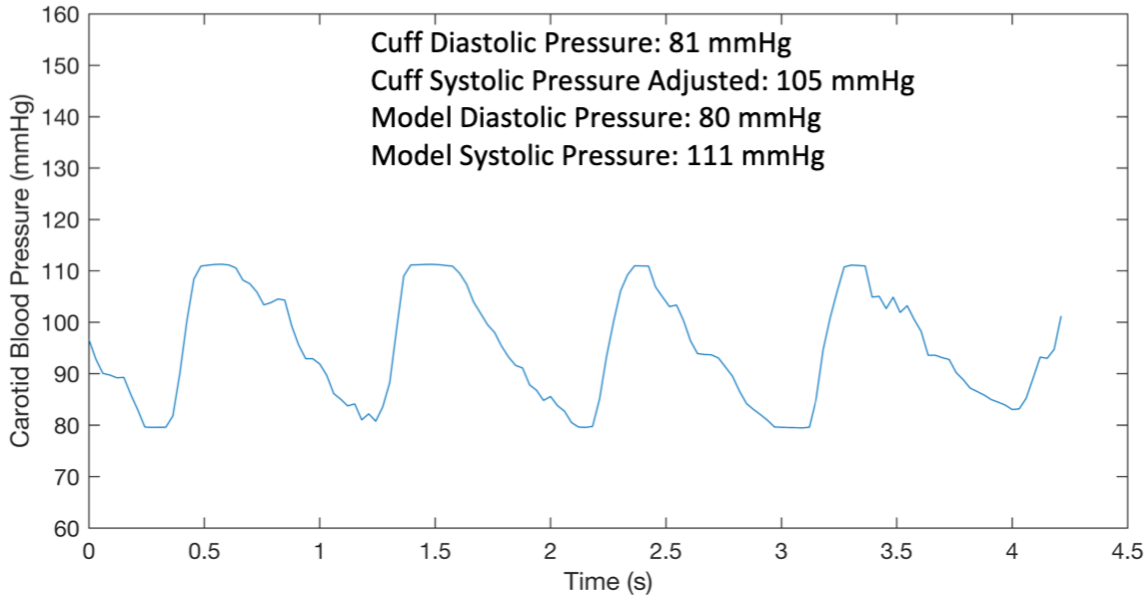

Figure 5-9: Reconstructed carotid blood pressure wave from the second optimization.

On average, each iterative inverse optimization takes about 10 hours to run on a Dell desktop computer running Windows 10 Enterprise with a 3.4 GHZ quad-core processor and 16 GB of RAM.

5.5 Discussion

We present a calibration-free, automated force-coupled ultrasound computational method to estimate carotid artery blood pressure along with less verifiable parameters such as carotid wall stiffness. Compared to previous versions of the method, the automation allows data processing to run without any monitoring or manual input, making it far more easily deployed, and the inverse model does not need blood pressure cuff calibration to provide an accurate estimate of blood pressure. We summarize the progress made with the current methodology compared to previous methodology of force-coupled ultrasound estimation of carotid blood pressure. We then consider limitations to our current methodology and examine how they propagate through subsequent modules to affect the result of carotid blood pressure estimation. We also examine ways to mitigate these limitations. Finally, we describe potential future application of our technology with emphasis on safety concerns.

The synchronization algorithm implemented by synchronizing a raw force signal with an optical flow signal derived from ultrasound images is automated and accurate. Most primary synchronization failures are automatically fixed through a secondary synchronization method. Our segmentation automatically initializes by means of a developed carotid detector. It has similar accuracy to past segmentation algorithms for B-mode images of the short-axis cross-section of the carotid and is without large segmentation errors [106], [120], whether the carotid is highly circular or compressed to be more of a horizontal oval. This segmentation is also able to segment more irregularly shaped veins at various levels of compression [110]. The region growing approach makes the segmentation quite generalizable to segment any short-axis image of a blood vessel of at least moderate size.

The iterative inverse finite element optimization approach takes segmentation data as inputs to estimate carotid blood pressure in addition to carotid wall stiffness and surrounding tissue stiffness parameters. A subsequent optimization of just blood pressure produces a sampled carotid blood pressure wave. In comparing the systolic and diastolic pressure outputs from the optimization with the brachial blood pressure cuff, we find similar, if not slightly smaller, error to past calibrated force-coupled ultrasound approaches [106], [111], here without any calibration from the blood pressure cuff.

5.5.1 Limitations

Although our approach yields strong positive correlation and average error of less than 10 percent when compared with the blood pressure cuff, we note that our average error is greater than 5 mmHg. Upon closer examination, there are multiple examples of error greater than 10 percent and other studies indicate that the blood pressure cuff is able to predict central blood pressure with a notably stronger correlation than ours [82], [141], [142]. To help our method achieve medical level accuracy, we now discuss various error sources to address.

The synchronization module is largely successful in that, given a standard commercial ultrasound probe and system, it correctly assigns forces to ultrasound images for virtually all force sweep datasets, providing reliable data to be segmented. Rare persisting synchronization errors occur largely because the operator of the device (the subject) provides low quality synchronization compressions before and after the force sweep. This problem could be mitigated in the future by providing automatic feedback to the operator when insufficient compression was applied. That said, the

synchronization procedure would be unnecessary if force measurement occurred within the ultrasound system such that the force signal and ultrasound images are subject to the same clock via a hardware connection, easing overall convenience of the methodology.

The carotid detection to initiate segmentation experiences very few errors, none of which are significantly consequential or result in the wrong object being segmented throughout the force sweep. The shortcomings of our segmentation algorithm lie in the noise seen in carotid vertical radius tracking during force sweeps and the manual carotid detection necessary at the beginning of a force sweep. Some ultrasound-based carotid measurements employ the radiofrequency (RF) signals upstream in the ultrasound signal processing from B-mode image formation [143], [144]. These methods track the strong deflections of the anterior and posterior walls of the carotid and can clearly see more subtle elements of the arterial pressure wave such as the dicrotic notch. Future work in force-coupled ultrasound carotid segmentation would benefit from combining the RF approach with the B-mode approach to track the anterior and posterior walls with a high sample rate and spatial resolution while also being able to trace the perimeter of the carotid for any ultrasound image obtained. These improvements should allow a blood pressure wave with more accuracy and a higher sample rate to be calculated after our inverse optimizations.

Several potential error sources in the finite element modeling must be explored before this approach can obtain accuracy up to the American Medical Association standard [141] as there is substantial variation in our measurement. A major assumption made in the finite element forward model is that the surrounding tissue of the carotid is a uniform Ogden hyperelastic material. The tissue surrounding the carotid is quite diverse, consisting of the sternocleidomastoid muscle, the thyroid, and internal jugular vein. This diversity causes observable asymmetric deformation of surrounding tissue despite a relatively uniform external compression executed by the force-coupled ultrasound probe, implying nonuniform elastic properties of the surrounding tissue. Not accounting for this nonuniformity of tissue and its variation across different subjects leads to error in our blood pressure estimation. A more detailed optical flow or speckle tracking approach could help inform the finite element model generation of nonuniform surrounding tissue [145], [146]. Nonuniform tissue in the finite element model would also allow for slight horizontal movement of the carotid within the center horizontal third, which is observed in segmentation data, to be reflected in the forward model. Additionally, 3-dimensional ultrasound imaging could provide more observation of surrounding tissue and its

interaction with the carotid artery, allowing one to discern the angle of incidence of the ultrasound probe and the long axis of the carotid artery while also observing the short axis compression [147].

Compared to the blood pressure cuff, it has the potential to be used on arteries, such as the carotid, for which a blood pressure cuff cannot safely or practically function. However, the blood pressure cuff has its own accuracy questions as it is often found to have errors of 5 mmHg or more [41], [82], [141], [148], [149]. There is also added uncertainty when estimating carotid systolic pressure from brachial systolic values with only the age demographic and without a cuff-generated pulse pressure waveform [138], [142], [144]. That said, using any model to convert from brachial blood pressure to carotid blood pressure is inferior to directly measuring carotid blood pressure. Perhaps a more practical invasive verification of the accuracy of our method would result from combined comparison to the invasive radial artery line [150] and noninvasive estimates of central blood pressure [90], [142].

Other sources of error for our carotid blood pressure estimation concern our method of data collection. First, having a subject sit upright introduces a significant hydrostatic pressure difference between the aortic valve and the carotid artery. This difference is accounted for by assuming a hydrostatic pressure difference in our calculations which is dependent on height of measurement above the aortic valve, which can vary among individuals. This orthostatic position could introduce motion artifacts of accidentally sliding the force-coupled ultrasound higher on the neck and shifting the carotid off center during the force sweep. These motion artifacts are not easily accounted for. Large movements of the carotid off center during the force sweep can be observed from carotid segmentation. Instruction to keep the ultrasound probe at the same height throughout the force sweep is provided while the sliding upward is possible but more difficult to observe in postprocessing. Second, error sources associated with brachial-cuff measurement, such as heavy respiration and inconsistent or dynamic orthostatic positioning, can occur despite instruction of best practices [151]. Hence, even normal breathing can slightly alter blood pressure [152], [153]. Third, true blood pressure could change in the time between the force-coupled ultrasound data capture and the cuff measurement [154].

When considering processing time, finite element iterative inverse optimization could be sped up from about 10 hours to about 3 seconds by running a Monte Carlo simulation across all input parameters to the model, storing all the converged outputs and interpolating a table-lookup method when introduced to new data. This rapid method is executed in a past version of this method with different data, different forward model, and different iterative inverse methodology [106].

5.5.2 Future Application Considerations

To be applied in practice in the future, our method will not only have to become more accurate, but also more simplified for the user. Specifically, synchronization of force and ultrasound should occur in real time via wire connection of force measurement electronics to an ultrasound system to remove the need to apply synchronization compressions before an after the force sweep. Also, guidance should be provided to the user in real time to ensure proper imaging of the carotid artery is occurring. Lastly, postprocessing should happen on the ultrasound system and produce a carotid pressure result in a similar time frame to an oscillometric cuff.

In considering the application of force-coupled ultrasound for other hemodynamic measurements, the approach has potential for noninvasive jugular venous pressure estimation, as one recent proof-of-concept study has shown [155], a measurement field in which noninvasive standards are less accurate than their arterial counterparts [92]. Furthermore, the carotid and jugular short-axis cross-sections are nearly always visible in the same ultrasound image, which allows for simultaneous and automated segmentation [156]. Thus, it is feasible for future simultaneous carotid arterial pressure and jugular venous pressure estimation.

5.5.3 Safety Considerations

In concert with thinking about future application of our methodology, the safety of this method should be considered, especially given a high-risk patient as opposed to the healthy subjects of this study. Carotid artery full occlusion reducing cerebral perfusion is virtually impossible given the high pressure and stiffness of the carotid preventing occlusion and the Circle of Willis providing alternate avenues for oxygen perfusion in the event of one common carotid occlusion [41]. Although the site over the carotid where we measure is not typically an atheroprone area, compressing the carotid poses the risk of dislodging plaque which could migrate to the brain and potentially cause a stroke. Despite low risk of this happening, it is nonzero in high-risk patients. Further reducing the maximum force applied by the ultrasound probe down from 15 N should reduce this risk by decreasing the amount of strain the inner walls of the carotid experience [41].

5.6 Summary

We develop an automated force-coupled ultrasound method to estimate carotid arterial blood pressure without calibration. We synchronize force and ultrasound by an optical flow-derived signal generation and a peak detection synchronization method. After detecting the carotid using a convolutional neural network trained detector, we segment it across the relevant frames of a force-sweep through a region growing approach. Finally, we use segmentation observations to solve an iterative inverse finite element optimization problem to estimate carotid blood pressure. We find strong correlation and low error when comparing diastolic and systolic estimates to those derived from blood pressure cuff measurements. Our method has the potential to be developed further for more accuracy and speed and applied to a wider range of cardiovascular health problems.

Chapter 6 – Force-coupled Ultrasound Imaging of Large Superficial Leg Veins

We quantitatively explore the compressibility of the thigh and calf great saphenous vein (GSV) and the femoral vein using force-coupled ultrasound imaging to sense the amount of force necessary to completely occlude each leg vein, the collapse force, in different orthostatic positions. Collapse force is measured by noting the lowest force at which the cross-sectional area of the vein is below the collapsed area threshold of 0.5 mm^2. In one healthy individual, we measure collapse force in supine and standing positions for the calf GSV, the thigh GSV, and the femoral vein. In ten healthy individuals we measure collapse force in supine position for the calf GSV, the thigh GSV, and the femoral vein and in the standing position for the thigh GSV. We find that cross-sectional area and hydrostatic pressure both correlate strongly with higher collapse force measurements with a lowest measured collapse force of about 1 N in the calf GSV while supine and a highest collapse force of over 45 N in the femoral vein while standing. Furthermore, through shear wave elastography, we deduce increases in stiffness from observed increases in shear wave speed in tissue surrounding the thigh GSV.

6.1 Introduction

Cardiovascular disease is presently the leading cause of death of Americans and the leading natural cause of death in American veterans [157], [158]. Within this large clinical classification is venous disease which covers pathologies of the veins which passively return deoxygenated blood to the heart [41]. Types of venous disease include, but are not limited to, venous insufficiency and thrombosis. Venous insufficiency causes veins to be unable to efficiently return blood to the heart most often causing pooling of blood in the leg veins. Thrombosis is the formation of blood clots in the veins which can potentially migrate into the heart and arterial system, resulting in obstruction of blood flow to vital areas [159]. Ultrasound imaging plays a large role in real-time detection of both venous insufficiency and thromboses [160], [161]. Force-coupled ultrasound imaging allows one to know the force applied by the ultrasound probe to the area being imaged. It has been applied to imaging the carotid and brachial arteries to estimate arterial blood pressure and the internal jugular vein to estimate venous pressure [109], [112], [155], [162]. Since veins are compressible, it is possible and often quite easy to completely occlude a vein of interest noninvasively with the imaging surface of the ultrasound probe and measure

the force necessary to do so – the collapse force. In the internal jugular vein, the collapse force has proven to be highly predictive of venous pressure for a wide range of venous pressures in several different individuals [163]. Furthermore, shear wave elastography yields stiffness estimates of tissue by measuring the speed of transverse shear waves traveling laterally in a defined area of an ultrasound image, providing a method of assessing stiffness of tissue surrounding blood vessels [25], [28].

In this study, we, for the first time, examine collapse force with force-coupled ultrasound imaging of leg veins. We focus specifically on the great saphenous vein (GSV) in the thigh and in the calf and on the femoral vein in the orthostatic positions of standing upright and lying supine. We also employ force-coupled ultrasound combined with shear wave elastography to assess the stiffness of tissue surrounding the leg veins as a function of force, which gives us a viewpoint from which to evaluate compressibility and elasticity assumptions often made for soft tissue.

6.2 Methods

Here we describe the data collection and data processing methods for finding the collapse force of different leg veins in different orthostatic positions. We collected data on 10 healthy subjects in a study approved by the MIT Institutional Review Board. For each subject, a relevant blood vessel is localized by an expert using ultrasound imaging. Three quick compressions are provided to the vessel, then between five and eight slower compressions ensuring full occlusion of the vessel occur, then three more quick compressions occur. The three quick compressions before and after the slow compressions are used to synchronize force and ultrasound, in that a force is assigned to each ultrasound image, with similar methodology to previous work [109]. The slower full compressions are used to estimate collapse force. Hence, the vein will collapse at some force within the slow full compression. The aim is for force to increase linear with time during a compression. When transitioning from standing to supine, we wait a minimum of 60 seconds before image capture begins and tell subjects to be still while standing. We divide the data capture into regions only useful for synchronization and regions useful for collapse force measurement in **Figure 6-1**. Depending on the vessel and the orthostatic position, the force application required to collapse the vein will vary greatly.

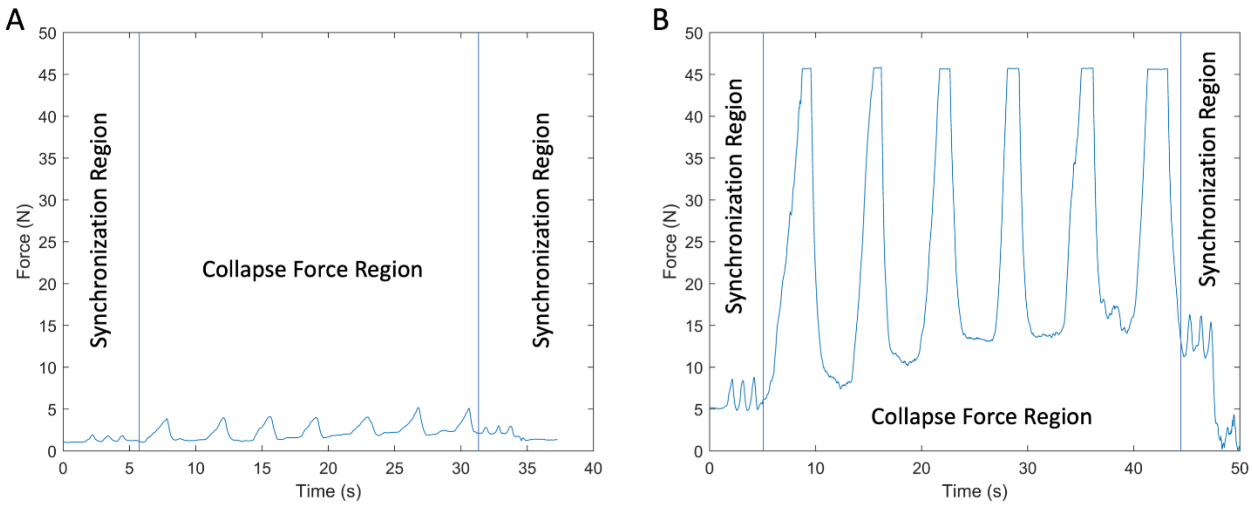

Figure 6-1: (A) Data capture force measurement from the thigh GSV of subject 1 in the supine position. (B) Data capture force measurement from the femoral vein of subject 1 in the standing position. Blue vertical lines divide synchronization regions from collapse force region.

The collapse force is found by noting the minimal force at which the cross-sectional area of the vein of interest, measured in segmentation, is less than 0.5 mm^2. The segmentation consists of a region growing step followed by an active contour based point optimization step. When the leg vein is close to complete occlusion, only the region growing step is performed to estimate area. This methodology is further explained in previous work [163].

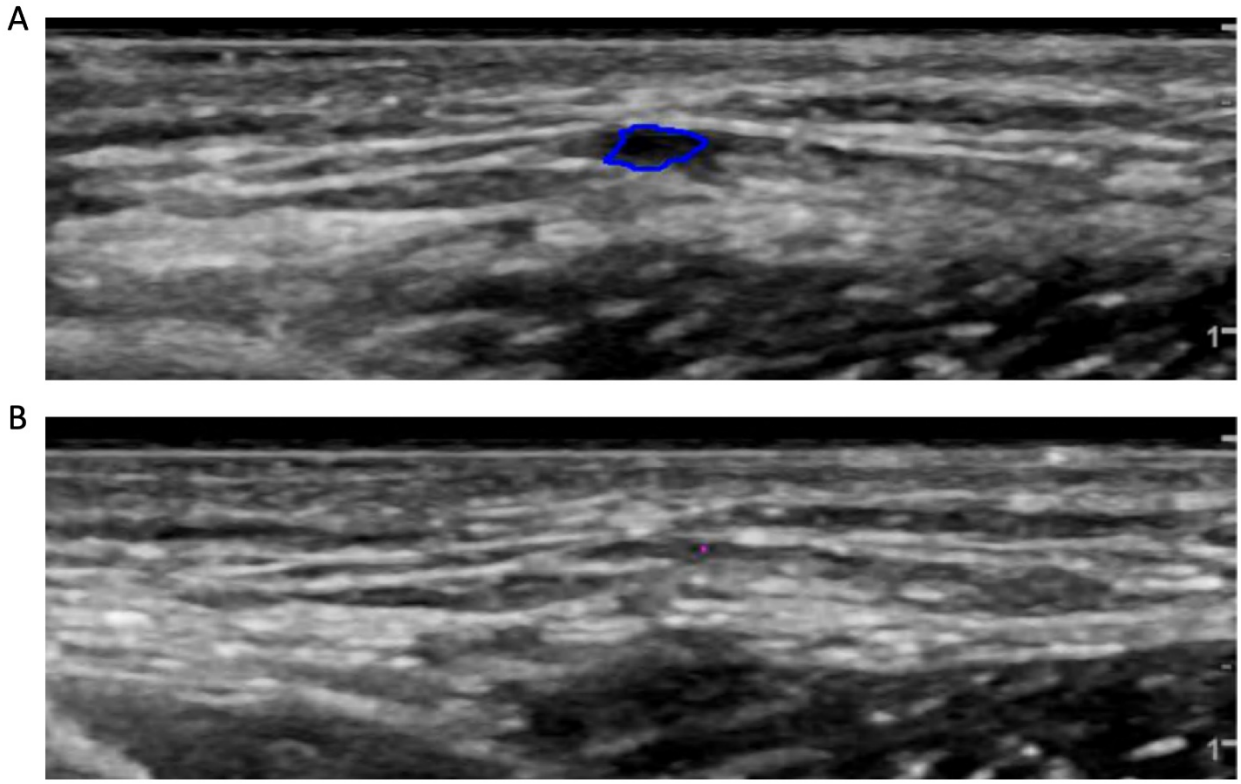

Figure 6-2: Calf GSV segmentation in subject 1. (A) Segmented calf GSV in open state. (B) Segmented calf GSV in collapsed state. The blue lines signifies region growing and active contour segmentation was performed and the magenta lines signify only region growing was performed. The numbers on the right side of each image signify depth in centimeters.

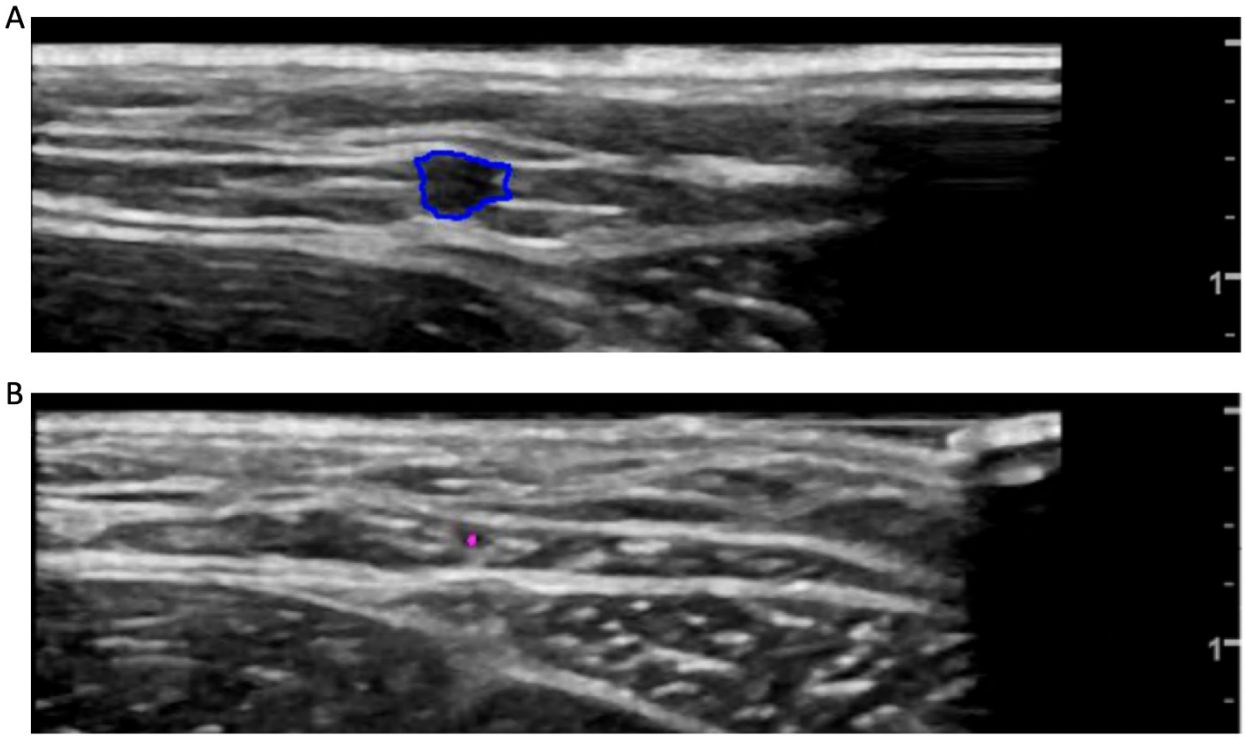

Figure 6-3: Thigh GSV segmentation in subject 1. (A) Segmented thigh GSV in open state. (B) Segmented thigh GSV in collapsed state. The blue lines signifies region growing and active contour segmentation was performed and the magenta lines signify only region growing was performed. The numbers on the right side of each image signify depth in centimeters.

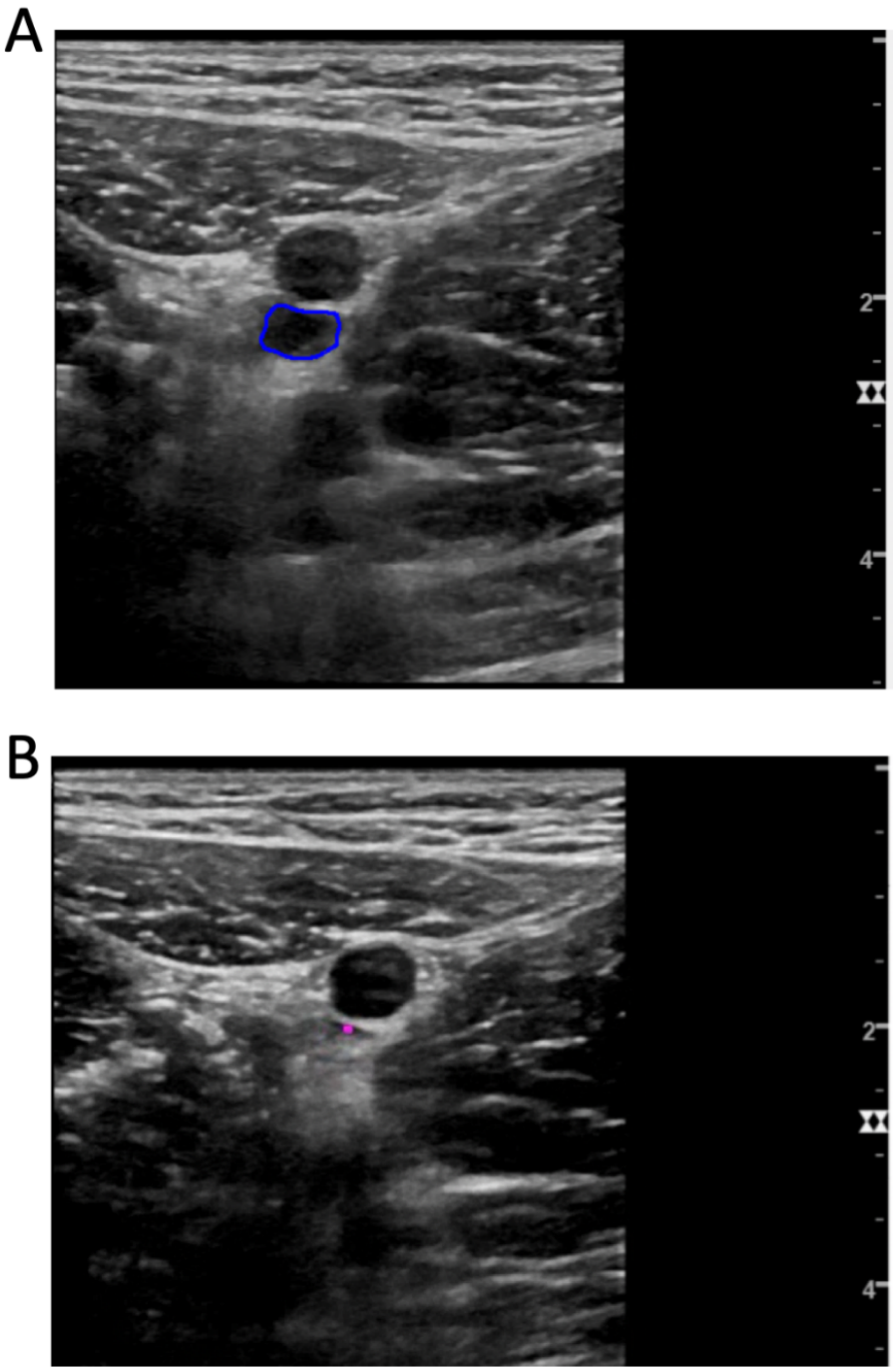

Figure 6-4: Femoral vein segmentation in subject 1. (A) Segmented femoral vein in open state. (B) Segmented femoral vein in collapsed state. The femoral artery is just above the femoral vein in the images. The blue lines signifies region growing and active contour segmentation was performed and the magenta lines signify only region growing was performed. The numbers on the right side of each image signify depth in centimeters.

Force-coupled shear speed images are generated by holding the force-coupled ultrasound probe at a relatively constant force while the shear speed image is being calculated (about 2 seconds) and then assigning the force to that image through synchronization [109].

6.3 Results

We first observe collapse forces in the calf GSV, thigh GSV, and femoral vein in the supine and standing positions. **Figure 6-5** contrasts distributions of standing and supine collapse forces in the calf GSV, thigh GSV, and femoral vein in the same subject. We note that the thigh GSV has a larger increase in average collapse force from supine to standing than the calf GSV. Furthermore, the femoral vein has the largest increase in collapse force from supine to standing. We also note that the mean collapse force for calf GSV in the supine position is lowest and the mean collapse force for the femoral vein in the supine position is highest among supine collapse force. We also note that the range of collapse forces for the standing thigh GSV is about 20 N within the same subject.

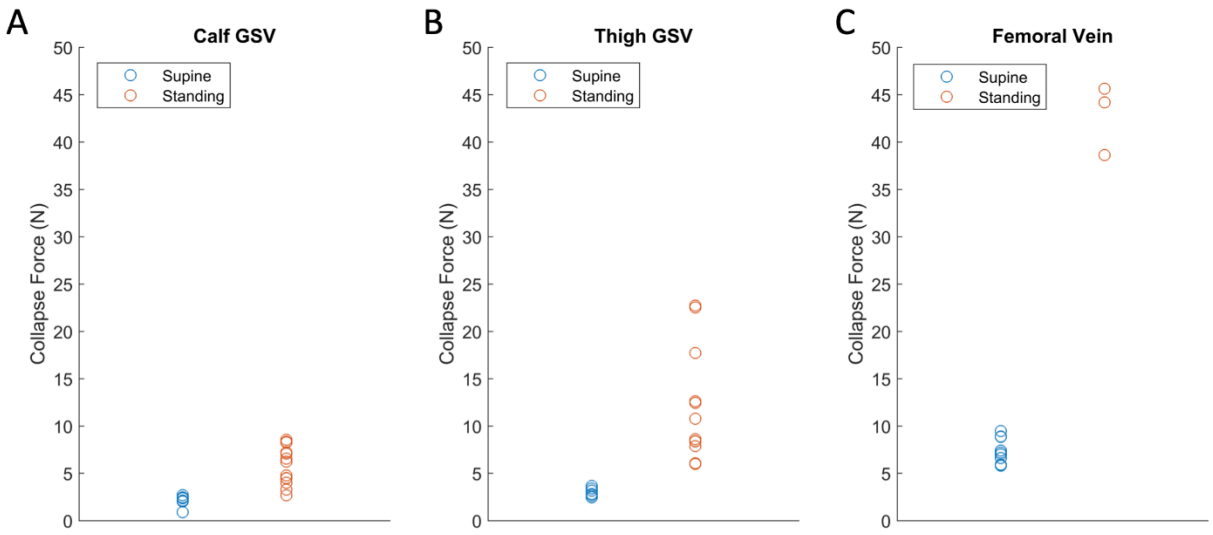

Figure 6-5: (A) Distribution of supine and standing collapse forces for the calf GSV of subject 1. (B) Distribution of supine and standing collapse forces for the thigh GSV of subject 1. (C) Distribution of supine and standing collapse forces for the femoral vein of subject 1.

In **Figure 6-6**, we confirm that most of these trends hold in a population of ten subjects but only use the thigh GSV for standing collapse force measurements. Furthermore, we note that the average

minimal compression force diameter of calf GSV, thigh GSV and femoral vein across the subjects was measured to be 0.25 cm, 0.40 cm, and 1.0 cm, respectively.

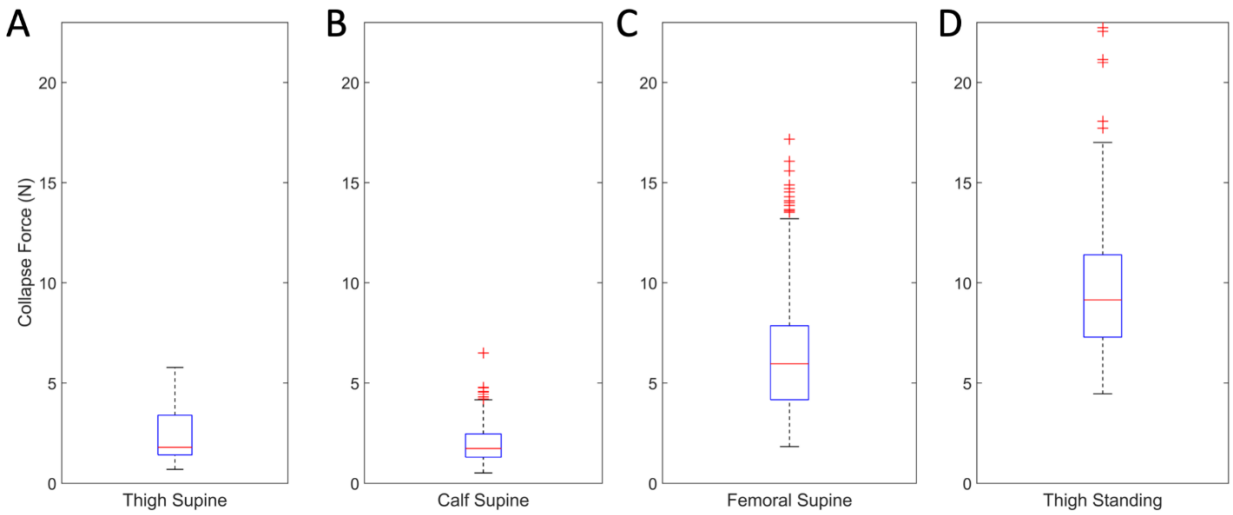

Figure 6-6: (A) Box and whisker plot of collapse force data on 10 subjects for the thigh GSV in the supine position. (B) Box and whisker plot of collapse force data on 10 subjects for the calf GSV in the supine position. (C) Box and whisker plot of collapse force data on 10 subjects for the femoral vein in the supine position. (D) Box and whisker plot of collapse force data on 10 subjects for the thigh GSV in the standing position. The red center line signifies the median collapse force. The top and bottom horizontal blue lines represent the 75th and 25th percentile collapse forces, respectively. The top and bottom black lines represent the maximum and minimum collapse forces which are not outliers. The red pluses represent outliers.

We next observe how shear speed in the tissue around the thigh GSV in subject 10 changes in response to increased external force. In **Figure 6-7**, we observe that the shear speed in the image is higher when the thigh GSV is collapsed than when it is open. The thigh GSV is collapsed at a higher external force than when it is open. We next calculate the average shear speed in each force-coupled shear-wave image.

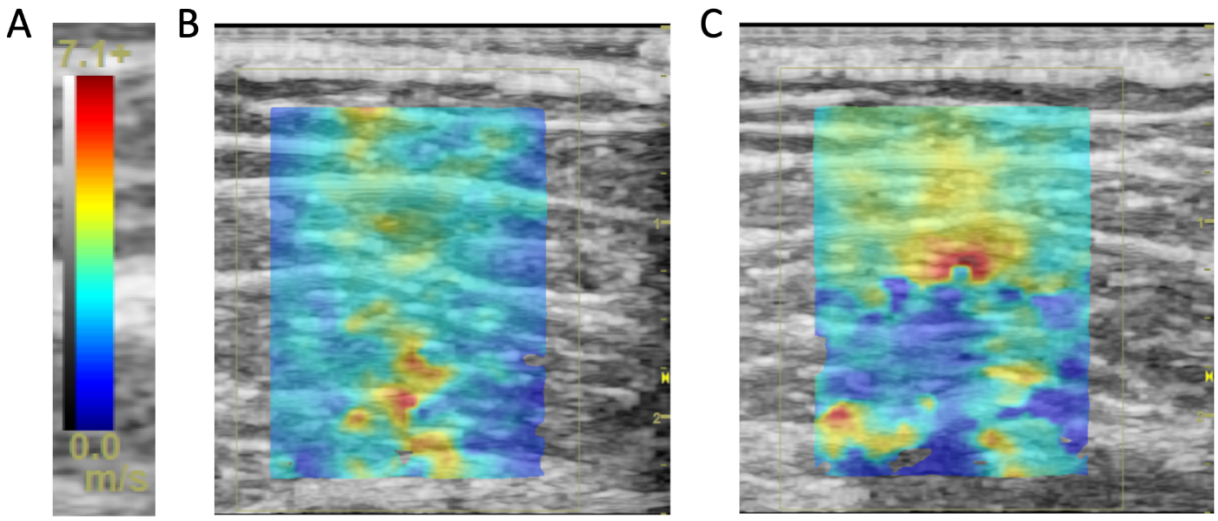

Figure 6-7: (A) Shear wave speed color map scale with a maximum measurable speed of 7.1 meters per second. (B) Shear wave speed image of the thigh GSV of subject 10 in the open state with low force. (C) Shear wave speed image of the thigh GSV of subject 10 in the collapsed state with high force.

We observe in **Figure 6-8** that the average shear speed increases with increasing external force. We find a second order polynomial is able to well-approximate the relationship between average shear speed and external force applied by the force-coupled ultrasound probe.

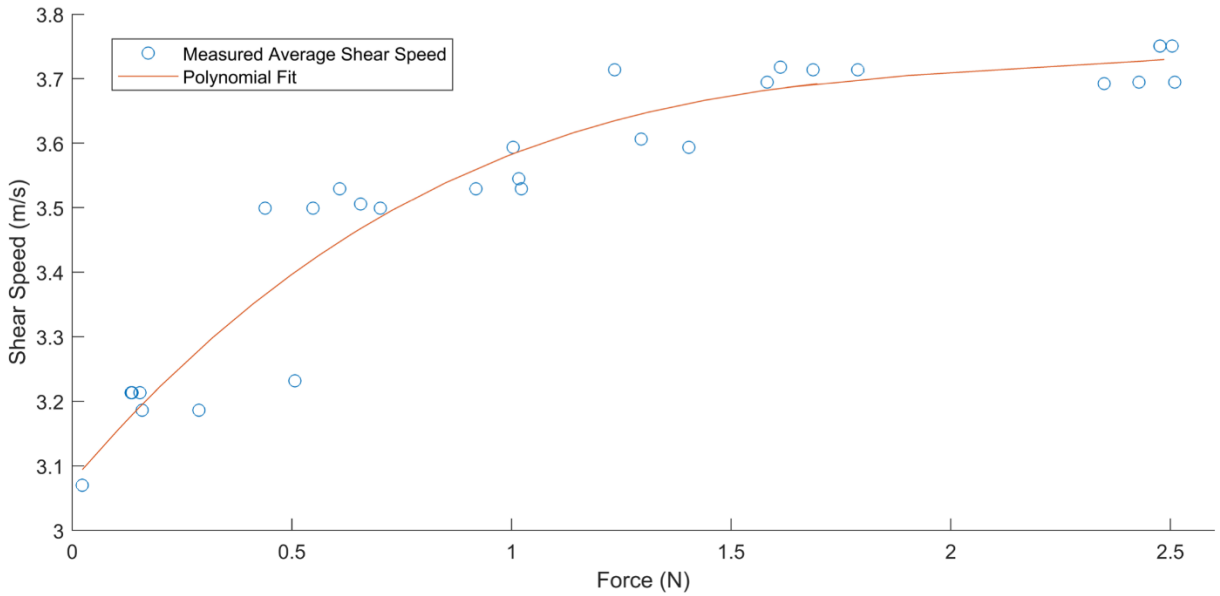

Figure 6-8: Average shear speed data as a function of force for subject 10 fit with a second order polynomial.

6.4 Discussion

In this study, we seek to investigate how collapse force is altered in different leg veins and in different orthostatic positions of supine and standing for a single healthy subject and a population of ten other healthy subjects. With respect to orthostatic positions, it is known that hydrostatic pressure in leg veins increases immensely when transitioning from supine to standing [41]. We see a concomitant increase in collapse force for each of the leg veins tested in every subject when transitioning from supine to standing, as observed elsewhere with respect to cuff occlusion pressure of the femoral artery [164].

Cross-sectional area also seems to correlate highly with collapse force as the femoral artery presents much higher collapse forces than the great saphenous vein in supine and standing positions. This is observed even though the thigh GSV and the femoral vein are measured at the same height. The calf GSV should have a higher hydrostatic pressure than both the femoral vein and thigh GSV given venous pumps are not activated through muscle activation around the leg veins. In fact, when considering **Figure 6-1**B and **Figure 6-5**C and noting that the maximum force measurement the load cell used is capable of is about 45 N, we can deduce that the true collapse force of the femoral artery in the standing position is likely higher than what is implied by these two figure panels. Yet, the lack of valves in the femoral vein as opposed to the presence of valves throughout the GSV present a confounding variable. It is also possible that the pressure is far higher in the femoral vein while standing than it is anywhere in the thigh or calf GSV. Vessel depth is another variable which likely correlates with collapse force, independent of lumen pressure, but like with cross-sectional area, there is not enough evidence to confirm this trend.

We also looked at shear speed estimates with force-coupled ultrasound imaging for the first time. The force measurement represents a stress applied to the tissue. Soft tissue stiffness has often been characterized using Young's modulus, implying a linear stress-strain relationship [165]. However, we show here that since shear speed correlates with shear modulus and shear modulus correlates with Young's modulus, soft tissue stiffness is observed to increase with increasing stress, implying a Poisson ratio less than 0.5 and compressibility. Therefore, linear elastic modeling may be a convenient and easy way to model soft tissue, but it is not the most accurate way, especially compared to hyperelastic tissue models [124], [136].

6.5 Summary

Here we utilize force-coupled ultrasound imaging of the great saphenous vein and the femoral vein to measure collapse force in healthy subjects in supine and standing positions. We note a marked increase in collapse force in relationship to leg vein hydrostatic pressure and suspected correlation of collapse force with cross-sectional area and depth from the surface of the skin. We also observe increases in shear speed when increasing force to compress the thigh GSV. We look to continue collapse force experiments of leg veins with hopes of providing key insights in the detection of venous insufficiencies and thromboses in a quantitative manner.

Chapter 7 – Central Venous Pressure Estimation from Force-coupled Ultrasound Imaging of the Internal Jugular Vein

We estimate central venous pressure (CVP) with force-coupled ultrasound imaging of the internal jugular vein (IJV). We acquire ultrasound images while measuring force applied over the IJV by the ultrasound probe imaging surface. We record collapse force, the force required to completely occlude the vein, in 27 healthy subjects. We find supine collapse force and jugular venous pulsation height (JVP), the clinical noninvasive standard, have a linear correlation coefficient of $r^2 = 0.89$ and an average absolute difference of 0.23 mmHg when estimating CVP. We perturb our estimate negatively by tilting 16 degrees above supine and observe decreases in collapse force for every subject which are predictable from our CVP estimates. We perturb venous pressure positively to values experienced in decompensated heart failure by having subjects perform the Valsalva maneuver while the IJV is being collapsed and observe an increase in collapse force for every subject. Finally, we derive a CVP waveform with an inverse three-dimensional finite element optimization that uses supine collapse force and segmented force-coupled ultrasound data at approximately constant force.

7.1 Introduction

Congestive Heart Failure (CHF) is a clinical syndrome in which the heart's pumping ability decreases, leading to fluid buildup in the circulatory system. It currently affects about 6.2 million people and is recorded on about 380,000 death certificates annually in the United States [157]. In heart failure progression, this fluid buildup, which increases venous pressure, begins as the circulatory system's way of compensating for a decreased pumping ability in order to maintain adequate cardiac output to perfuse the organs with oxygen [41]. Decompensated heart failure occurs when the increase in fluid volume is no longer able to maintain cardiac output, initiating a vicious cycle of continually increasing fluid volume despite eventually detrimental effects to cardiac output [41], [166]. At this point, venous pressure is high enough to release fluid from the circulatory system, causing peripheral and pulmonary edema, which can lead to death [41], [67], [167].

Treatment for elevated venous pressure in decompensated heart failure involves administration of diuretics informed by central venous pressure (CVP) measurement [75]. The gold standard for CVP assessment is direct measurement of pressure in the superior vena cava or right atrium with

catheterization [168], [169]. However, noninvasive assessment is often chosen unless the patient is already catheterized [75], [169]. The standard noninvasive venous pressure measurements are jugular venous pulsation height (JVP) measurement and inferior vena cava diameter measurement [92], [102]. Although rooted in physiological principles, these methods fall short of achieving a reliable noninvasive standard to guide treatment decisions compared to their arterial pressure counterpart, the brachial blood pressure cuff, which has a methodology not replicable in veins [82], [102], [170], [171]. There have been several attempts to improve venous pressure assessment in recent years, especially in the field of medical ultrasound [125], [172]–[175].

Force-coupled ultrasound is a technique which combines ultrasound imaging with simultaneous measurement of the force applied by the imaging surface of the ultrasound probe to the skin over the image plane [116], [162], [166]. This technique has had moderate success in the accurate estimation of blood pressure in the carotid artery in which the carotid artery is never close to being fully collapsed [106], [109], [111]. Additionally, a force-coupled single-element ultrasound study shows that changes in mean jugular venous pressure can be sensed by measuring the force necessary to completely occlude the internal jugular vein (IJV) [155]. A Korotkoff blood pressure cuff (sphygmomanometer) estimates systolic and diastolic brachial blood pressure by recording the maximum (systolic) and minimum (diastolic) cuff pressures at which the sound of artery wall opening-from-collapse action occurs [176]. While acknowledging that symmetric application of external pressure to the IJV is not feasible, we believe asymmetric compression of the IJV with force-coupled ultrasound imaging should be studied as a venous analog to the Korotkoff cuff [41]. The IJV is of lower pressure and stiffness than any of its surrounding anatomical landmarks, which should allow for its compression at a lower force than what would compress other surrounding tissue. Additionally, since there is no valve in between the IJV at the base of the neck and the right atrium, the pressure waveform of the right atrium should be reflected in that of the IJV [41].

Here we compare force-coupled ultrasound compression of the IJV to a quantitative version of the noninvasive standard JVP measurement in the same subjects in the supine position and when elevated to a small angle above supine. We have healthy subjects perform the Valsalva maneuver to artificially increase venous pressure to the range measured during decompensated heart failure [41], [177]. Finally, we use the correlation of supine collapse forces to JVP measurements and force-coupled

ultrasound IJV area measurements to derive a jugular venous pressure waveform in an effort to identify components of the right atrial pressure waveform.

7.2 Data Collection

Our study involves obtaining force-coupled ultrasound data on the left internal jugular veins of 27 healthy volunteers. The MIT Institutional Review Board approved this study under protocol number 2007000193. Informed consent was obtained for all subjects of the study. All data collection is noninvasive and is carried out in accordance with subject anonymity and minimal risk practices.

Table 7-1 includes deidentified subject population details. While ensuring that the long axis of the IJV is perpendicular to the compression of the short-axis seen in the ultrasound images, as diagrammed in **Figure 7-1**, each IJV is compressed to complete occlusion under various conditions: breathing normally while supine, breathing normally while elevated (negative venous pressure perturbation), and performing the Valsalva maneuver while supine (positive venous pressure perturbation).

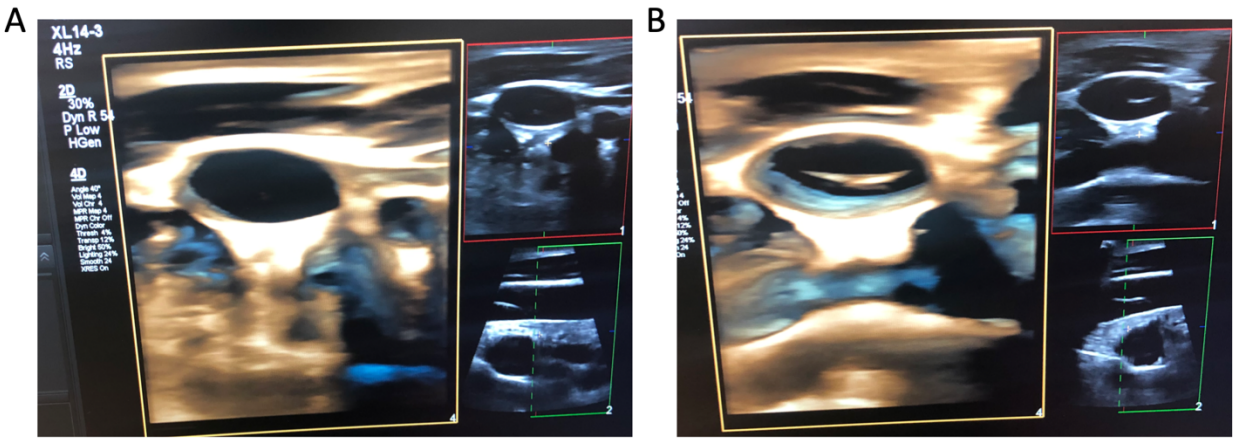

Figure 7-1: (A) 3-D rendering ultrasound image showing orthogonality of transverse image plane with the long-axis of the internal jugular vein. (B) 3-D rendering ultrasound image showing lack of orthogonality of transverse image plane with the long-axis of the internal jugular vein. Long-axis view imaging shows unevenness of long-axis indicating further lack of orthogonality.

Table 7-1: Subject data population and results. The sixth column is the noninvasive jugular venous pulsation height measurement while the last three columns are the experimental collapse force measurements. Dashes in the last three columns indicate no collapse force is obtained for the given condition and subject.

Subject Number	Age (years)	Sex (M/F)	Height (cm)	BMI (kg/m²)	JVP (mmHg)	Supine Collapse Force (N)	16-Deg Collapse Force (N)	Valsalva Collapse Force (N)
1	31	M	173	25.1	3.1	7.4	3.6	14.3
2	32	M	168	26.6	2.0	5.0	-	24.7
3	28	M	183	23.7	3.2	8.0	4.1	-
4	30	M	170	21.5	2.1	4.3	3.2	-
5	64	M	180	23.7	4.0	8.5	4.7	17.0
6	26	M	180	20.9	3.6	8.1	5.4	19.4
7	28	M	175	28.1	2.5	7.2	4.2	11.7
8	30	M	175	23.8	1.7	3.5	2.2	12.3
9	72	M	173	25.8	4.5	9.8	-	-
10	26	M	178	23.0	2.3	6.1	4.3	14.6
11	29	M	191	30.0	3.3	7.6	5.1	-
12	30	M	173	25.8	3.1	7.2	4.0	11.6
13	24	M	165	25.8	2.8	6.3	3.7	12.2
14	30	M	173	25.1	4.3	9.8	-	29.9
15	26	F	163	24.0	3.0	7.3	4.1	20.4
16	27	F	163	20.6	3.1	7.0	3.9	10.3
17	25	F	173	17.5	1.3	3.5	2.1	10.6
18	26	M	180	24.4	2.1	6.2	2.4	13.8
19	30	F	165	21.1	3.8	8.9	-	-
20	28	M	170	23.5	4.5	10.5	5.7	19.5
21	28	F	150	21.2	3.2	8.5	2.5	15.8
22	31	F	160	24.3	2.4	5.7	2.6	-
23	30	M	178	22.2	2.3	5.8	-	11.5
24	25	F	157	20.1	3.0	-	3.0	13.9
25	26	M	173	18.2	2.3	4.5	3.8	10.7
26	31	M	175	22.0	2.9	5.6	2.2	21.4
27	29	F	165	21.1	3.3	8.7	4.4	21.8

7.2.1 Jugular Venous Pulsation Measurement

A subject is slowly tilted downward on a tilt table starting from 60 degrees until the angle where IJV pulsations are visible at the base of the neck. This angle is recorded with an iPhone8 angle sensor app and converted to a hydrostatic pressure by assuming 10 cm between the right atrium and the base of the neck and converting cmH2O to mmHg.

The JVP is most conventionally estimated by measuring the height above the sternal angle. In this study, we aimed to make the method more quantitative by looking for pulsations just above the clavicle while reclining the subject and noting the angle at which pulsations first start to be visible. The precision of this angle is to the single degree, which corresponds to a JVP precision of about 0.1 mmHg after converting from cmH20 to mmHg. For every subject, 10 cm is assumed to be the distance from the

center of the right atrium to the pulsation viewing window just above the clavicle. The JVP is calculated from the following equation:

$$JVP = 0.7356 * 10 \sin\theta \quad (7.1)$$

where the four-digit decimal is the conversion from cmH20 to mmHg, 10 is the assumed distance in cm from the center of the right atrium to the base of the neck, and theta is the largest angle at which IJV pulsations can be seen at the base of the neck.

7.3 Collapse Force Measurement

An example of segmentation during normal breathing supine compression is shown in the force-coupled ultrasound images of **Figure 4-13**. When the IJV is near complete occlusion, the segmentation is simplified to only include the initial region-growing step (**Figure 4-13**C). We define the collapse force to be the force at which the cross-sectional area of the IJV is first below the collapse threshold of 0.5 mm^2, shown in **Figure 7-2**A with time on the x-axis and **Figure 7-3**C with force on the x-axis. In **Figure 7-2**A, we track both IJV area and external force as functions of time to add explanation for where the collapse force is sensed before any uncertainty in cardiac cycle or segmentation is quantified. The collapse force in our force-coupled ultrasound method is analogous to quantifying JVP, as both seek to estimate venous pressure.

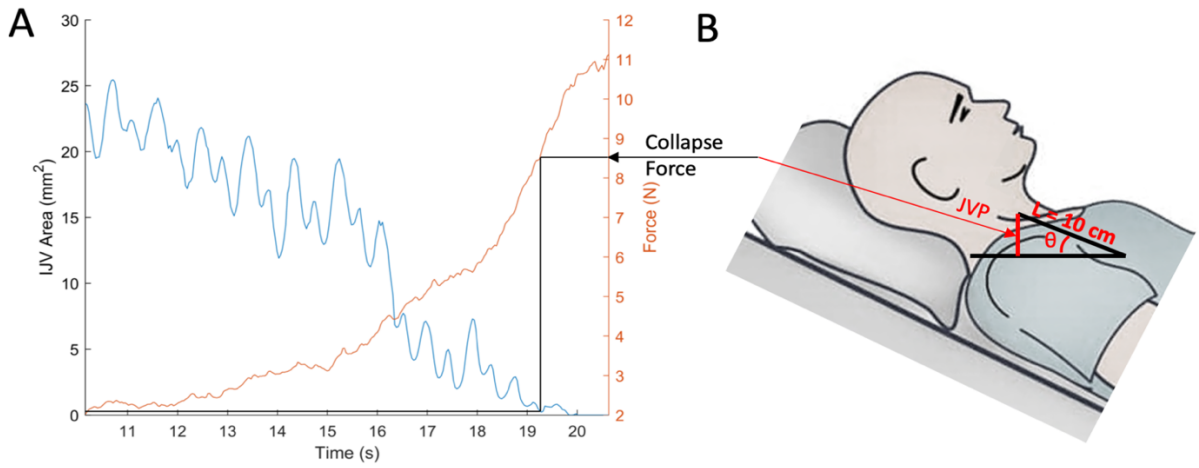

Figure 7-2: (A) Diagram of collapse force derivation. The collapse force threshold is denoted at 0.5 mm^2. A horizontal line is drawn from this area on the left y-axis to where the IJV area curve first intersects. Then a vertical line is drawn from there to the force curve where the collapse force is marked with a horizontal line to the right y-axis. (B) Adapted from https://nurseslabs.com/patient-positioning/. Diagram of the jugular venous pulsation (JVP) height derivation. We assume 10 cm between the center of the right atrium and the base of the neck and take the sine of the angle of the visible pulsation in the IJV at the base of the neck to get JVP.

7.3.1 Uncertainty Quantification

We quantify the uncertainty in collapse measurement from two sources: (1) variation in IJV area (pressure) based on the right atrium cardiac cycle (**Figure 7-3**C), and (2) segmentation uncertainty (**Figure 7-3**B). On the cardiac cycle uncertainty, when plotting force on the x-axis and IJV area on the y-axis, we do not see a purely monotonic decreasing area curve but rather a monotonic decreasing curve with variation superimposed. This variation stems from the contraction and relaxation of the right atrium during the cardiac cycle causing variation in right atrial pressure and central venous pressure [41]. The collapse force could occur at any point in the cardiac cycle. The segmentation uncertainty is derived from the possible range of pixel coordinates where the true wall could reside based on the region growing pixel intensity threshold and how much force is used to compress those pixels' area (0.25 mm^2 at the collapse force threshold). These pixels are highlighted in gold in **Figure 7-3**B. We compare our collapse force measurements in each subject to a quantitative version of the clinical noninvasive standard jugular venous pulsation height (JVP). We assume the distance from the right atrium to the clavicle to be 10 cm and measure the angle of recline when pulsations first start to be visible just above the clavicle. This method is illustrated in **Figure 7-2**B. Uncertainty here is quantified via a recent repeatability study at 0.1 mmHg [178]. These are the horizontal error bars in **Figure 7-4**A. The vertical error bars represent the sums of the cardiac cycle uncertainties and segmentation uncertainties for each subject.

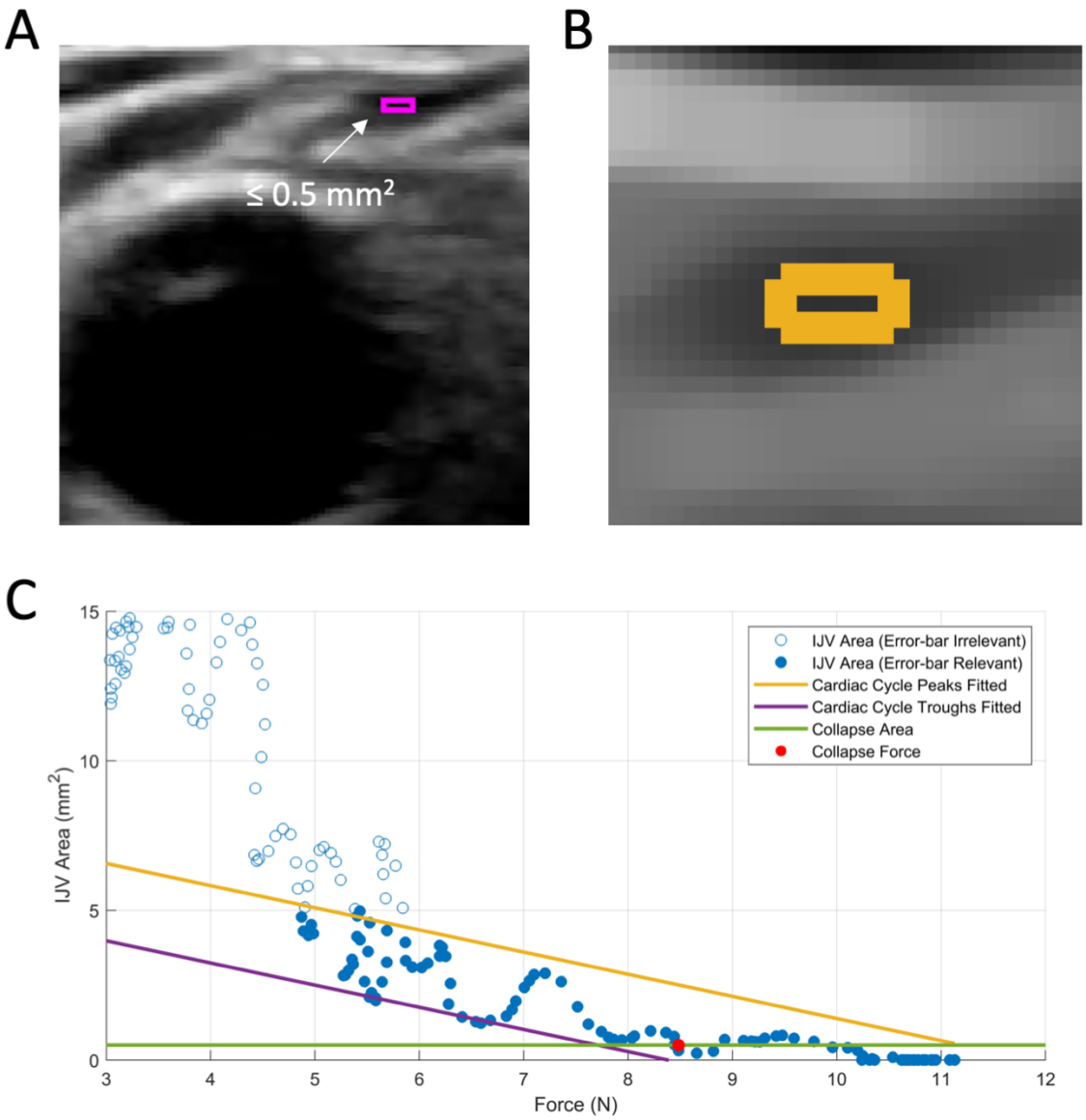

Figure 7-3: (A) Segmentation of a collapsed IJV in subject 21. (B) Collapse force uncertainty contribution due to segmentation. Uncertainty pixels are shaded in gold. (C) Collapse force uncertainty contribution due to cardiac cycle.

7.3.2 Supine and Normal Breathing

Figure 2F correlates the measured collapse forces of 26 subjects in the supine position breathing normally to their respective JVP measurements. The linear correlation coefficient is $r^2 = 0.89$. We can use the least squares correlation line of best fit to predict JVP from collapse force:

$$JVP = 0.416 * CF + 0.0539 \quad (7.2)$$

In **Figure 7-4**B, we measure the disagreement between the predicted JVP and the measured JVP with an average absolute disagreement of $\mathrm{mean}|\Delta| = 0.23\ \mathrm{mmHg}$.

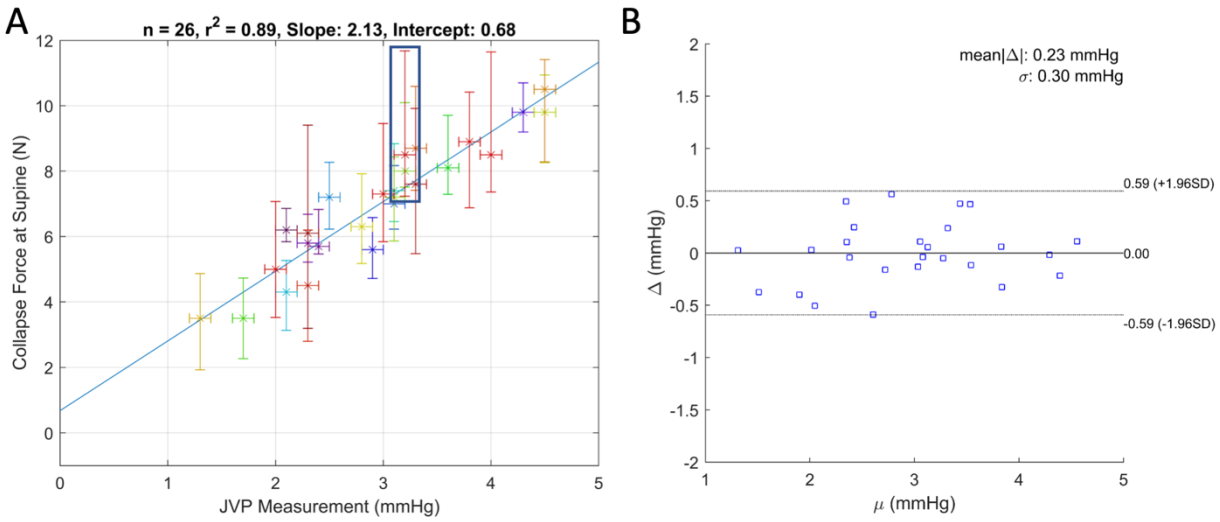

Figure 7-4: (A) Correlation with uncertainty of JVP height and supine collapse force. (B) Bland-Altman plot of predicted JVP based on collapse force compared to measured JVP.

7.3.3 16-degree Elevation and Normal Breathing

We next perturb venous pressure in the negative and positive direction. We decrease the pressure in the IJV for each subject by elevating on a tilt table to 16 degrees above supine to decrease hydrostatic pressure. We see in **Figure 7-5**A that the IJV is much more collapsed in the same subject at the same force when the subject is elevated to 16 degrees than when the subject is supine. We note the trend of increasing difference between supine and 16-degree elevated collapse forces when supine collapse force increases in **Figure 7-5**B. We also note that we cannot measure a collapse force less than 2 N because that is the minimum contact force required for clear images to be obtained.

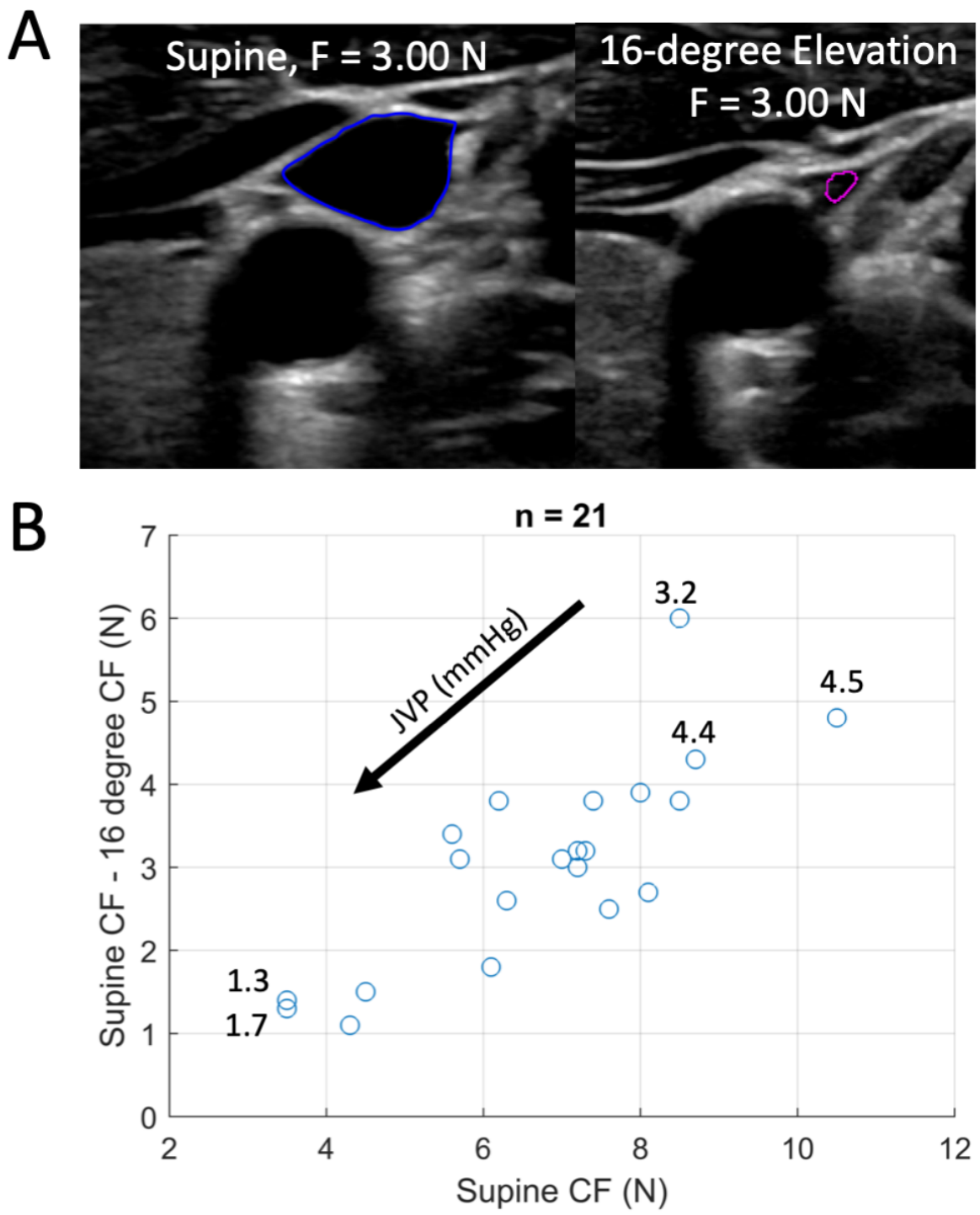

Figure 7-5: (A) Demonstration of hydrostatic effect when elevating a patient from supine to 16 degrees with images at the same force in subject 20. The blue outlines the IJV segmentation while the magenta dot signifies an IJV near collapse. (B) Differences between Supine CF and 16-degree CF in individual subjects. The solid black line signifies the expected effect on collapse force if only hydrostatic effect was present and our linear regression could perfectly predict collapse force from a perfect venous pressure measurement.

7.3.4 Supine and Valsalva Maneuver

To perturb venous pressure in the positive direction, simulating decompensated heart failure venous pressures in healthy subjects, we measure airway pressure during the Valsalva maneuver as a proxy for venous pressure [179]. **Figure 7-6**A shows the increase in IJV area as a result of increasing airway pressure during the Valsalva maneuver at relatively constant force. This increase in IJV area implies an increase in venous pressure. While measuring airway pressure, we compress the IJV during the Valsalva maneuver at an airway pressure between 10 and 20 mmHg. We consider the difference between Valsalva collapse force and supine collapse force in **Figure 7-6**B. We see that there is virtually no correlation between supine collapse force and this difference, yet there is a wide range of differences. The mean difference signified by the solid blue line is about 9.5 N.

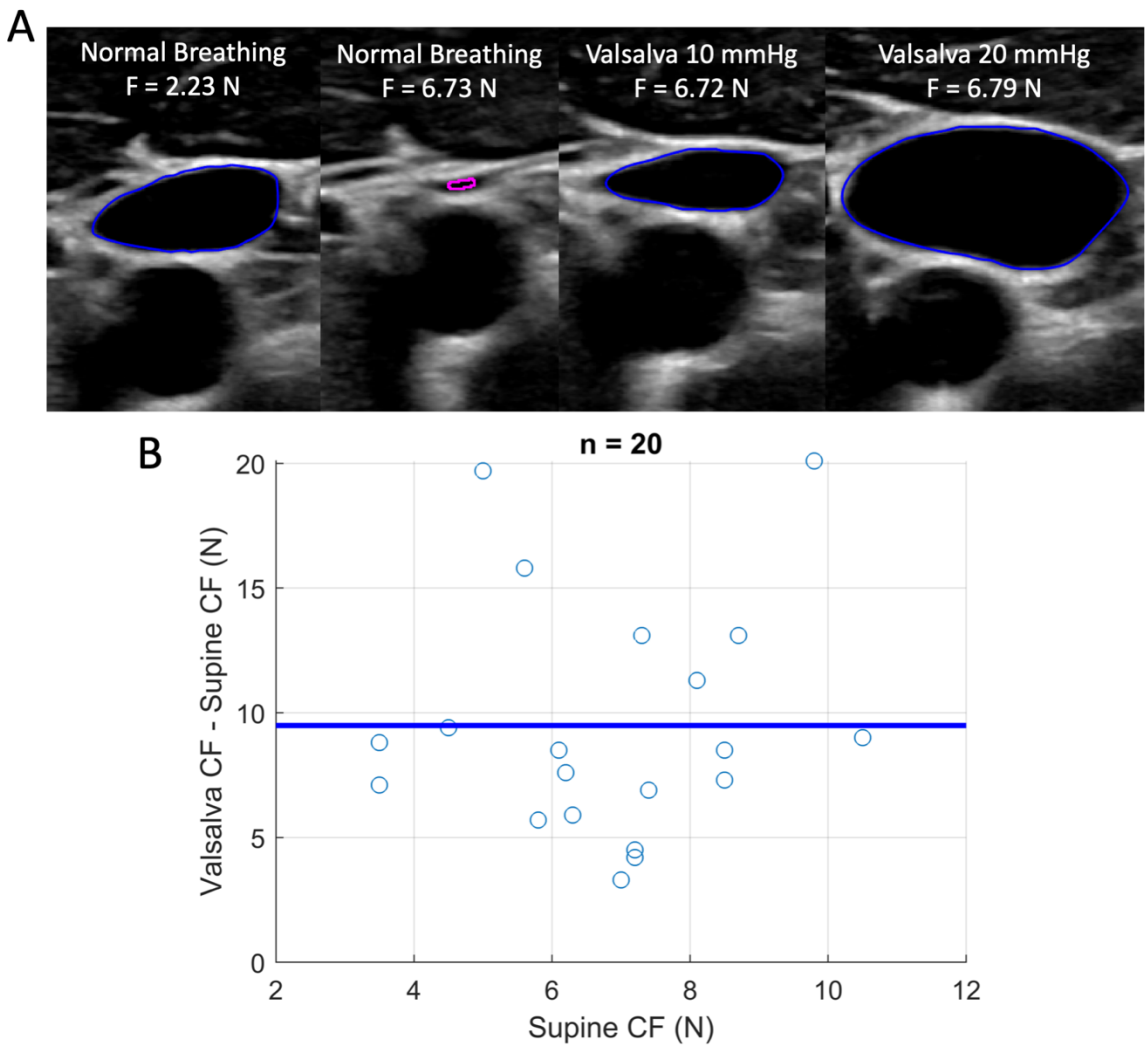

Figure 7-6: (A) Effects of Valsalva maneuver on increasing IJV area while under force in subject 20. The blue outlines the IJV segmentation while the magenta dot signifies an IJV near collapse. (B) Difference between Valsalva collapse force and supine collapse force in the same subjects. The solid blue line represents the mean difference.

7.3.5 Collapse Force Perturbation Analysis

We see in **Figure 7-7** that for each subject who had data recorded for the supine measurements and each of the two perturbations, the collapse forces during Valsalva while supine are larger than the collapse forces while breathing normally and supine. These supine collapse forces while breathing normally are larger than the collapse forces while breathing normally while elevated to 16 degrees above supine. We examine the relationships between the perturbed collapse force measurements and JVP in **Figure 7-9**.

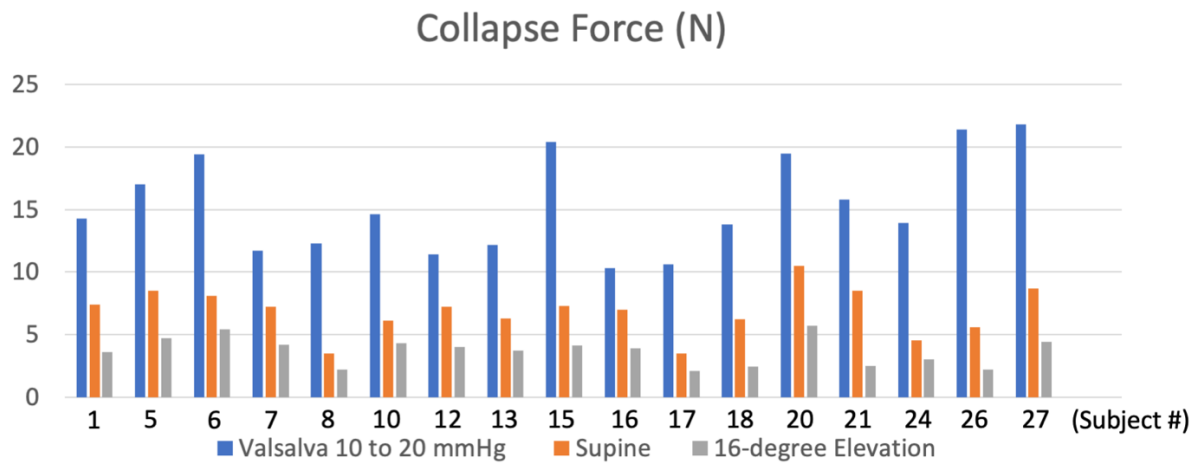

Figure 7-7: Collapse forces when subjects measure between 10 and 20 mmHg of airway pressure by the Valsalva maneuver compared to collapse forces when subjects are breathing normally while supine and while elevated by 16 degrees.

In **Figure 7-8**A, we see a combined plot of collapse forces while supine, while elevated to 16 degrees above supine, and while supine and performing the Valsalva maneuver along with their corresponding venous pressure measurements through JVP and airway pressure. We see a generally monotonic increasing trend in collapse force with respect to venous pressure. We can also observe asymptotic behavior of the 16-degree collapse force as it approaches zero as collapse force cannot be negative. One last observation which is apparent is that the linear regression described by equation 7.2 would underestimate the venous pressures measured during the Valsalva maneuver based off of the collapse force during Valsalva.

The perturbations of venous pressure allow us to examine collapse force at a wide range of venous pressures. In considering a Korotkoff blood pressure cuff, there is a symmetric compression of a limb such that the pressure outside the artery is equal to the pressure inside the artery when the artery collapses. This is essentially how blood pressure is measured with a cuff. With force-coupled ultrasound, there is an asymmetric compression. Therefore, we cannot make the same assumption that venous pressure is equal to external pressure provided at collapse. We can, however, note what the external pressure is which causes a collapse for a given collapse force:

$$P_{ext,c} = \frac{F_c}{A} \tag{7.3}$$

where F_c is the collapse force and A is the contact area of the force-coupled ultrasound probe. We can calculate what fraction the venous pressure is of that external pressure used to collapse, abbreviated by F_{EPC}:

$$F_{EPC} = \frac{P_v}{P_{ext,c}} \tag{7.4}$$

where P_v is the venous pressure measured with either JVP or the airway pressure during the Valsalva maneuver. We see in **Figure 7-8**B that for all venous pressures and collapse forces, this fraction is closer to zero than one. Additionally, we notice that the fraction tends to get larger as venous pressure increases. This trend and the corresponding observation with regard to collapse force as venous pressure increases in **Figure 7-8**A suggest a superlinear relationship between collapse force and venous pressure as venous pressure increases.

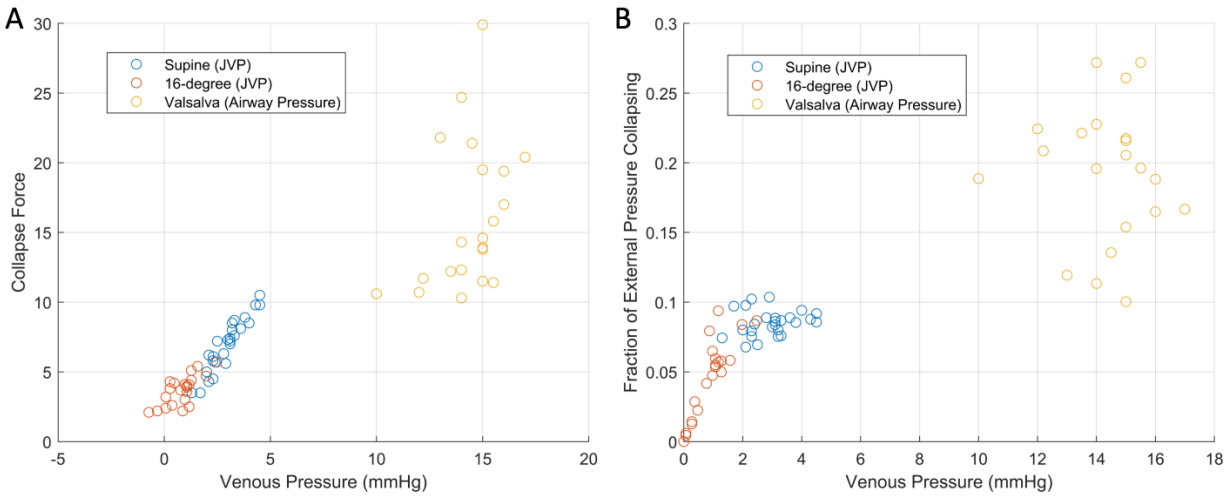

Figure 7-8: (A) Combined collapse force and venous pressure plot for all perturbations. The blue corresponds to the JVP measurement and the collapse force in the supine position. The orange corresponds to the JVP measurement by with a hydrostatic offset applied to account for the 16-degree elevation and the collapse force in the 16-degree elevation position. The yellow corresponds to the airway pressure measurement made when the Valsalva maneuver is performed to increase venous pressure and the collapse force measurement made during Valsalva. (B) Fraction of the external pressure applied to collapse equal to the venous pressure measured through JVP and Valsalva.

In **Figure 7-4**A, a linear least squares line of best fit, which only accounts for uncertainty in the dependent variable, is generated relating supine normal breathing collapse force and JVP measurement because the uncertainty in the collapse force is far greater than the repeatability uncertainty in JVP. However, in the negative and positive perturbations, the uncertainty in the JVP measurement is more equal in magnitude to the uncertainty in collapse force. When elevating the subject to 16 degrees, the

JVP measurement is adjusted assuming the distance from the right atrium to the base of the neck is 10 cm to account for the hydrostatic pressure decrease without allowing venous pressures below 0 mmHg. The population of subjects ranges in height, which adds uncertainty to the measurement. Regarding the Valsalva maneuver, a digital manometer measures airway pressure, which is used as a proxy for venous pressure. The uncertainty here stems from the imprecision of the manometer measurement and the indirectness of the airway pressure proxy, yielding an uncertainty of 3 mmHg on each side. Furthermore, the cardiac cycle variation of collapse force decreases because the right atrium is unable to expand and contract during Valsalva.

A Deming regression line accounts for uncertainty in both the dependent and independent variable and is used to produce lines of best fit for the supine normal breathing collapse force and JVP, the 16-degree elevation collapse force and hydrostatic offset adjusted JVP, and the Valsalva collapse force and airway pressure in **Figure 7-9**A, **Figure 7-9**B, and **Figure 7-9**C respectively. The r^2 correlation coefficient works to provide a certain level of confidence in the Deming regression lines in that low r^2 should yield low confidence and high r^2 should yield higher confidence. That said, the progressively steeper slopes of the Deming regression lines at higher venous pressures, shown in **Figure 7-9**D, lends credence to the theory that as venous pressure increases, a smaller percentage of the external force applied is dedicated to collapsing the IJV. Evidence against this theory is also present given the large gap in assumed venous pressure between the supine and Valsalva Deming regression lines.

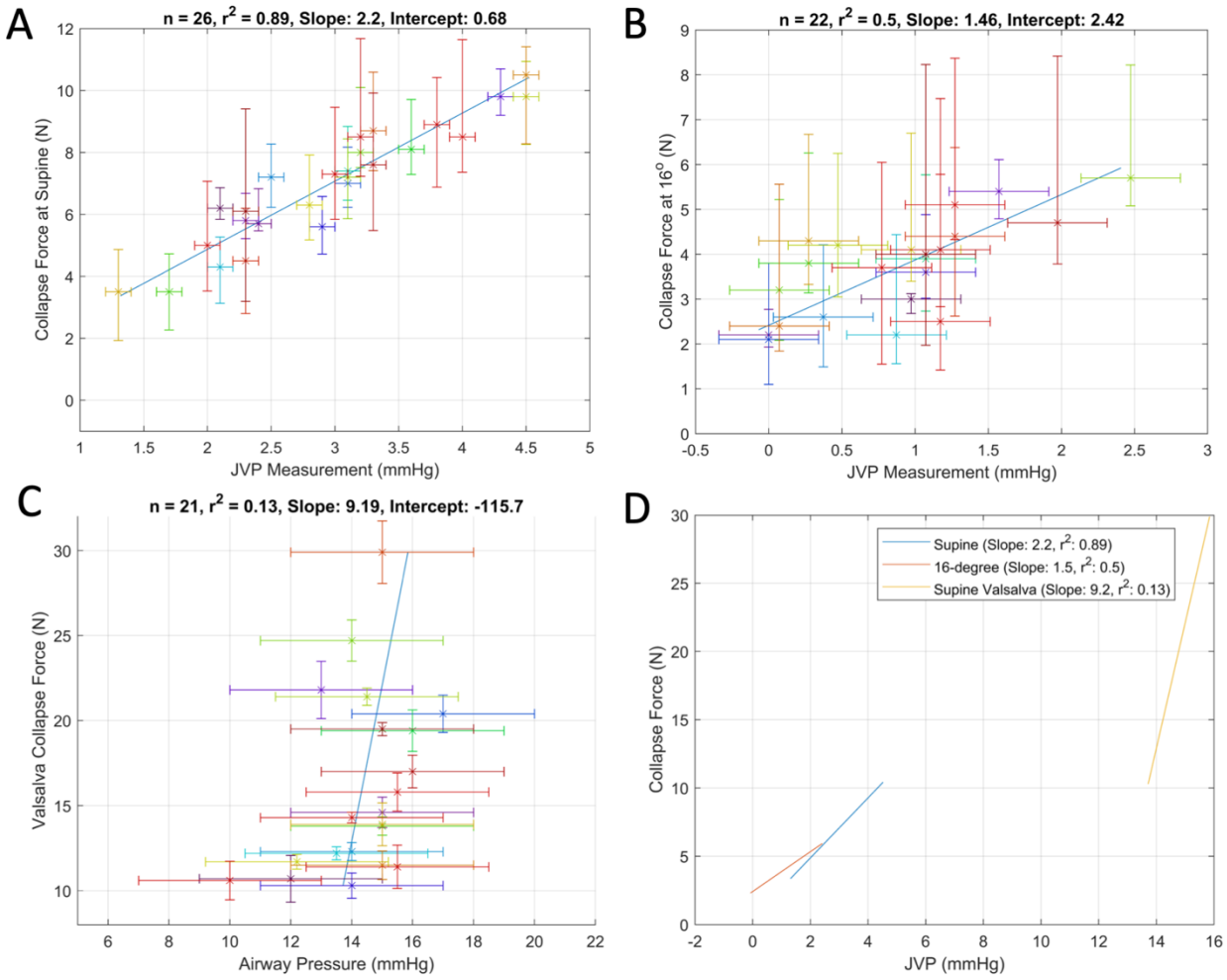

Figure 7-9: (A) Deming regression of supine collapse force with JVP height. (B) Deming regression of 16 degree collapse force with JVP height adjusted for hydrostatic offset. (C) Deming regression of Valsalva collapse force with airway pressure manometer measurements. (D) Combination of Deming regression lines at different collapse forces and inferred JVP measurements.

7.4 Central Venous Pressure Wave Construction

We utilize frame-by-frame constant force IJV segmentation data, our predicted venous pressure from collapse force, and three-dimensional inverse finite element modeling to produce a venous pressure waveform in the IJV. We first create a triangular prism meshed cylindrical three-dimensional finite element model for the internal jugular vein and surrounding tissue. The vein is modeled as a cylindrical hole in the otherwise uniform Ogden hyperelastic structure. We note a fixed boundary condition at the center of the model to signify the vertebral column, but there is no carotid artery present in the model. A force-coupled ultrasound probe is modeled as a stiff linear elastic material

compressing the top of the model over the IJV. In the center of the meshed cylinder is a fixed hole boundary condition to represent the vertebrae. The mesh is depicted in **Figure 7-10**A while the displacement upon compression is shown in **Figure 7-10**B,C. This model is fit to two-dimensional short-axis cross-section force-coupled ultrasound segmented data of the left IJV as it is compressed, as seen in **Figure 7-10**D and demarcated with the white dashed lines in **Figure 7-10**B,C. In our iterative inverse modeling, we set the venous pressure of the average IJV area frame to be the predicted venous pressure from the linear regression of measured collapse force from **Figure 7-4** by tuning forward finite element model parameters.

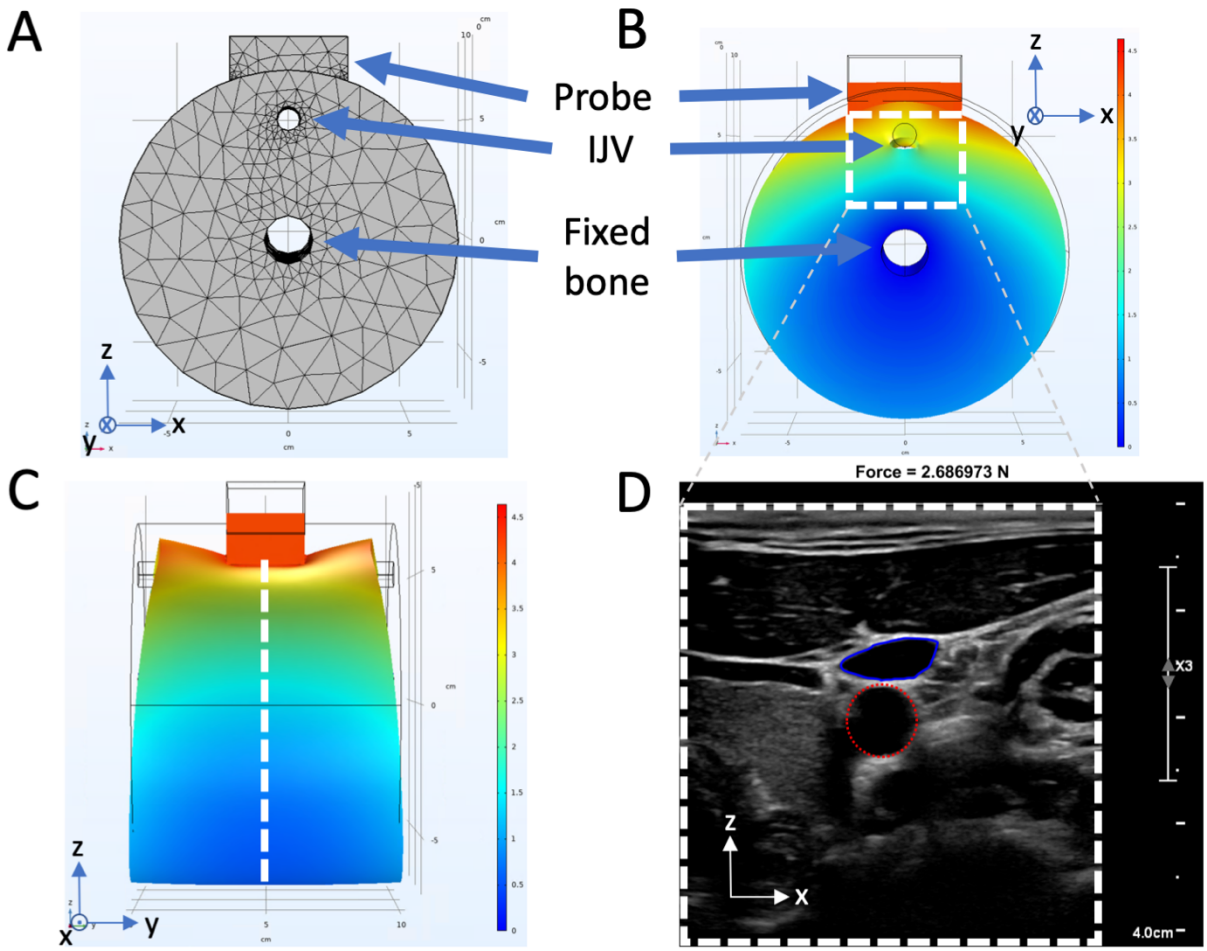

Figure 7-10: (A) 3-D finite element model mesh of the IJV passing through the neck and the force-coupled ultrasound probe contacting the surface of the skin above it. (B) 3-D finite element forward model Euclidean displacement (x-z view). The dashed white box is analogous to ultrasound imaging window. (C) 3-D finite element forward model Euclidean displacement (y-z view). The dashed white line signifies the ultrasound imaging x-z plane. (D) 2-D ultrasound image of segmented IJV (solid blue) and carotid artery (dashed red) short-axis cross-sections for subject 20.

We then arrive at a converged venous pressure for each frame in the sequence via a downhill simplex optimization. For each force-coupled ultrasound frame, venous pressure converges, and we use that pressure as the initial guess for the subsequent frame. We minimize the following cost equation:

$$Cost = \left\| A_{seg} - A_{mod} \right\|_2^2 \tag{7.5}$$

where A_{seg} is the observed IJV area from segmentation and A_{mod} is the IJV area found from running the forward finite element model for a given venous pressure guess. The superscript and subscript 2 indicate we are taking the square of the L2 norm. **Figure 7-11** shows the IJV area waveform, the carotid area waveform, the applied external force, the relevant linear regression results from collapse force measurement to predict CVP, and the venous pressure waveform. We note that the venous pressure waveform has nearly identical morphology to the IJV area waveform. **Figure 4-12** details the filtering of the carotid area waveform while the carotid waveform in **Figure 7-11** has an additional 3-point moving average filter applied to it. We note that in **Figure 7-10**D, the segmented carotid artery short-axis cross-section lies just below that of the IJV. Furthermore, in **Figure 7-11**, we note that when the carotid is in systole, the IJV waveform is depressed relative to the CVP waveform reference [180]. The labeled elements of the waveform (a, c, x, v, y) refer to filling and emptying of the right atrium and opening and closing of the tricuspid valve.

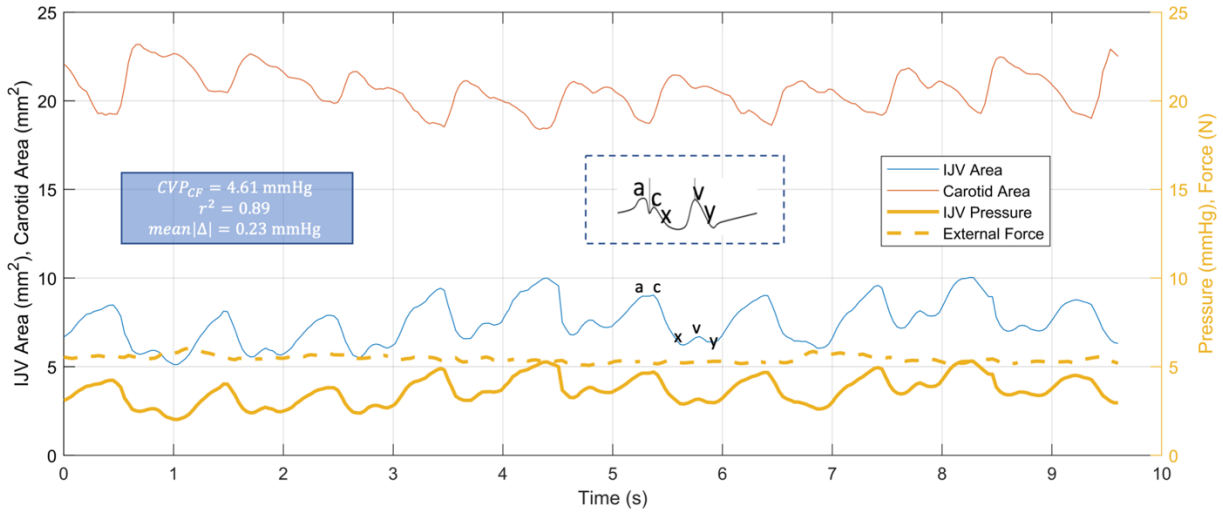

Figure 7-11: IJV area, carotid area, IJV pressure estimation, and force plot at an almost constant external force for subject 20. The scalar venous pressure estimate from collapse force is shown with correlation and error data of collapse force and JVP. Black vertical lines symbolize visually-assessed end-diastole from the ultrasound images. A reference central venous pressure waveform from catheterization is overlaid from Tansey et al (2019). In the dashed box and on the IJV area waveform, components of the right atrial pressure waveform reflected in the IJV area waveform are labeled. a: Right atrium (RA) pumps into right ventricle (RV). c: Tricuspid valve closes at systolic onset. x: RA relaxes. v: RA passively fills; tricuspid opens. y: RA passively empties before pumping.

Creation of the three-dimensional forward finite element model was done using COMSOL Multiphysics software version 5.6 (COMSOL Inc.; Burlington, Massachusetts, United States). Running an inverse optimization involved using COMSOL's LiveLink functionality with MATLAB (The MathWorks, Inc.; Natick, Massachusetts, United States), allowing MATLAB to run and adjust COMSOL models.

7.5 Discussion

Our goal in creating a force-coupled ultrasound methodology to estimate lumen pressure in the IJV is to provide a noninvasive, quantitative, and automated approach to venous pressure measurement. Given our high correlation of collapse force with subjects in the supine position breathing normally compared to JVP, we present a method with similar accuracy to JVP in healthy subjects. Like the Korotkoff blood pressure cuff's ability to measure arterial pressure by measuring the amount of external pressure necessary to collapse a major limb artery, our method yields a collapse force of the IJV proportional to CVP. Given the cuff wraps all the way around the arm, it is able to apply a uniform pressure around the artery of interest. In our case, the force-coupled ultrasound probe provides an external pressure subject to loss such that not all of the external pressure is dedicated towards compressing the IJV. In our narrow, healthy, venous pressure range with the same force-coupled ultrasound, the proportion of loss is predictable. This is likely due to the low pressure of the IJV relative to its anatomical surroundings. Given specifically the supine results, our hypothesis for force-coupled ultrasound collapse force measurement predicting CVP performs well in the relatively narrow range of healthy venous pressures.

When we perturb venous pressure, our experiments yield several noteworthy results. The simplest analysis is that each perturbation of venous pressure produced a concomitant change in collapse force for every subject. Regarding the negative perturbation, we observe a strong trend that as supine collapse force decreases, the difference between supine and 16-degree collapse force decreases to approach zero. This trend is actually quite intuitive. Collapse forces can only accurately be measured above 2 N while venous pressures around zero can be inferred from hydrostatic offset from supine position and JVP measurement. What's more, the IJV does not attain pressures below 0 mmHg because it is exposed to atmospheric pressure transmurally, unlike the sagittal sinus which is subdural, and will

collapse at 0 mmHg [41]. Thus, as supine venous pressures approach zero, one would expect less of a decrease in venous pressure when raised to 16 degrees above supine.

Regarding the positive perturbation of the Valsalva maneuver, on the one hand, the result gives us confidence that a collapse force will be able to be measured in patients with decompensated heart failure and high venous pressure with our current setup. Hence, none of the venous pressures reached with the Valsalva maneuver were high enough to require a collapse force of more than 30 N. The force-coupling has been shown to translate force entirely and linearly up to at least 45 N while the load cell capacity is 110 N, as addressed in the Supplementary Information. On the other hand, although an increase in collapse force is observed for each subject, the high variability of increase could mean that collapse force is a less reliable predictor of high venous pressures than of venous pressures in a normal healthy range. However, our highly noisy airway pressure measurement makes ascertaining a venous pressure measurement independent from what can be derived with collapse force quite challenging and unreliable. Other sources of variability in our Valsalva collapse force could be different levels of expansion of the IJV downstream toward the superior vena cava yielding variable compliances across the subject population where the IJV is being collapsed and poor Valsalva execution. A more accurate venous pressure measurement at high venous pressures could remove much of the variability observed. Further validation of this method at high venous pressures with a gold standard is of paramount importance to understand its potential impact on heart failure patients.

An additional takeaway from our venous pressure perturbation analysis on collapse force is the trend of an increasing fraction of external pressure causing IJV collapse being represented by the venous pressure as venous pressure increases. One can predict from this result that as CVP increases, although there should be a monotonic increase, the increase in collapse force should be sublinear. If this prediction is true, at higher CVP, CVP would be more sensitive to small changes in collapse force than it would be at lower CVP.

An assumption for our study is the validity of the JVP measurement which is also reliant on the hydrostatic pressure assumption. When calculating the JVP, one measures the height of the pulsations seen in the IJV in cmH20 and converts to mmHg. This models the IJV as a tube of water and the right atrium as the body of water below it. Our results indicate that the JVP is quite reliable in our healthy subjects given its high correlation to the different collapse force methodology. That said, difficulties in JVP measurement often have to do with the ability to see the IJV pulsations in patients with high BMI or

facial hair which includes part of the neck [92], [93]. Conversely, collapse force sensing should not be any more difficult in a high BMI patient than in a low BMI patient and facial hair does not obscure ultrasound image clarity given proper acoustic coupling of the probe to the skin. In addition, JVP methodology has poorer accuracy when estimating high venous pressures such as those observed in decompensated heart failure [92]. This is a major motivation for the development of our collapse force based force-coupled ultrasound method of estimating CVP.

Regarding our three-dimensional inverse finite element optimization to produce a venous pressure wave, we are able to produce a wave which is conceivably accurate, due to the collapse force's ability to predict JVP ($r^2 = 0.89, mean|\Delta| = 0.23\ mmHg$), but not verifiable. It is highly constrained in that the average venous pressure of the waveform is informed by what is predicted by the collapse force measurement. Additionally, there is a high dependence on the quality of segmentation of the IJV in a B-mode ultrasound image. Errors in segmentation area readily translate to venous pressure waveform errors. Given an accurate segmentation, elements of the right atrial pressure waveform are visible in the venous pressure waveform produced, but they seem to be altered due to the nearby pulsation of the carotid artery, for which our previous study provides a blood pressure estimate [109]. We do not account for the carotid artery in our optimization, which introduces unverifiable error in our IJV pressure waveform, but we can surmise that we are underestimating the v-wave peak in the venous pressure estimate as this occurs during systole. Further investigation with access to central venous pressure or right atrial pressure waveforms from an invasive catheterization is required to examine whether pathological conditions of the right atrium can be accurately inferred from this noninvasively obtained waveform.

In addition to the necessity for further study with comparison against gold standard invasive metrics for venous pressure, there is also reason to make our forward finite element model more accurately reflect observations from the force-coupled ultrasound images other than the IJV. An increase in complexity of the three-dimensional finite element model to include the carotid artery and a distributed tissue stiffness, informed by observed differential tissue compression in our force-coupled ultrasound images, could allow for our optimization to become significantly less constrained. These improvements could not only provide a more informed optimization for the venous pressure waveform, but also for a carotid artery pressure waveform to be measured simultaneously. Force-coupled ultrasound of the carotid artery has demonstrated potential to provide accurate, rapid, and automated

blood pressure measurements [109]. Furthermore, the IJV short-axis cross-section is always visible in the same frame as the carotid short-axis cross-section for all 27 subjects tested. If proven to be accurate and easy to use, force-coupled ultrasound has the potential to provide low cost, noninvasive, and rapid arterial blood pressure measurements while also providing venous pressure measurements.

7.6 Summary

Here we show that collapse force measurement of the left IJV can estimate venous pressure about as well as JVP in healthy individuals with relatively low venous pressures. We perturb our collapse force measurement to measure lower collapse forces when subjects are elevated to 16 degrees, demonstrating that a hydrostatic pressure decrease is reflected in collapse force. We measure higher collapse forces during the Valsalva maneuver to simulate venous pressures experienced during decompensated heart failure. Finally, we create a venous pressure waveform using force-coupled ultrasound segmentation, collapse force measurement, and three-dimensional finite element inverse optimization. We believe this initial study shows enough promise to merit future clinical studies which include comparison to invasive gold standard direct measurement of CVP via catheterization and further efficacy assessment in heart failure diagnostics and management.

Chapter 8 – Force-coupled Ultrasound Based Central Venous Pressure Estimation in Comparison with Invasive Catherization Measurement and Other Noninvasive Techniques

This chapter covers our venous pressure study at Massachusetts General Hospital, comparing our collapse force based method against the invasive gold standard CVP measurement from central lines and Swan Ganz catheter lines. This chapter arguably contains the most clinically comparable results of this thesis because they are the only results where an invasive gold standard is present for comparison. Here, we test our method for estimating venous pressure based on collapse force against this invasive gold standard while quantifying uncertainty inherent to the gold standard measurement and our methods under test. We first utilize a linear regression developed with data from MIT in chapter 7 to predict CVP with collapse force and hydrostatic offset. We then form linear regressions from the MGH collapse force data and hydrostatic offset data and evaluate accuracy compared to the invasive catheterization. We also assess JVP in this study and compare its accuracy with respect to the invasive measurement and usability compared to our metrics centrally based on the collapse force of the IJV.

8.1 Introduction

Congestive heart failure is currently affecting about 6 million people in the United States and is a central component to the leading cause of death which is cardiovascular disease. Venous pressure assessment in CHF is essential to determine optimal treatment. Careful invasive measurement of venous pressure and intravascular volume status in general allows a clinician to confidently determine treatment. However, invasive measurements are risky and costly. Hence, they are often reserved for heart failure patients who are in acute decompensated heart failure to effectively guide a dangerously high venous pressure down to more manageable levels. For other heart failure patients, noninvasive metrics, such as jugular venous pulsation height (JVP) and, more rarely, inferior vena cava diameter, are used. However, these techniques require high experience and skill to perform accurately and are not trusted by physicians who treat heart failure as a reliable substitute for the invasive CVP measurement.

In chapter 7, we develop a collapsed force based method to estimate central venous pressure in 27 healthy individuals. The results are promising but are limited due to two main reasons. The first is

that a slightly more quantitative form of jugular venous pulsation height (JVP) is used as the main standard of comparison. JVP is indeed the method we are trying to replace. Thus, we must use an actual gold standard measurement as the standard of comparison. The second is the limited range of assumed true central venous pressures we measure which was between 1.5 and 5 mmHg. In patients with congestive heart failure, depending on intravascular volume status, CVP could reach over 20 mmHg. We attempt to simulate high CVP by using the Valsalva maneuver, but it is not a reliable method to produce a precise and predictable CVP increase.

Here, we seek to validate and further develop our method based on force-coupled ultrasound imaging of the internal jugular vein in MGH Cardiac Intensive Care Unit (CICU) heart failure patients with a ground truth measurement of invasive CVP. We utilize CICU CVP waveform data to examine waveform morphology in terms of cardiac cycle variation and respiratory variation. We also compare our measurement to JVP in by means of various accuracy and uncertainty metrics

8.2 Data Acquisition

The acquisition of data at MGH is approved by the MGH institutional review board (IRB) under protocol number 2021P003587. Before data acquisition, a doctor on the study approaches eligible patients to inform about the study and answer any questions. Eligible patients must have an invasive CVP measurement at the time of collapse force measurement. Consent is obtained if an eligible patient wants to participate in the study. Data collection for the study can proceed once consent is obtained but can proceed days after consent is obtained.

Many of the patients in the CICU are very sick and have certain cardiovascular health issues which would not arise in healthy patients. Only one IJV is available as the catheter is threaded through the other one. Two of the eleven patients on which data is already collected have substantial clotting in the IJV where the catheter is not located. We refer to this as a thrombosed IJV which cannot be fully compressed. Therefore, we compress the external jugular vein (EJV) which has a smaller cross-sectional area. An ultrasound image of a patient with a thrombosed IJV is shown in **Figure 8-1**.

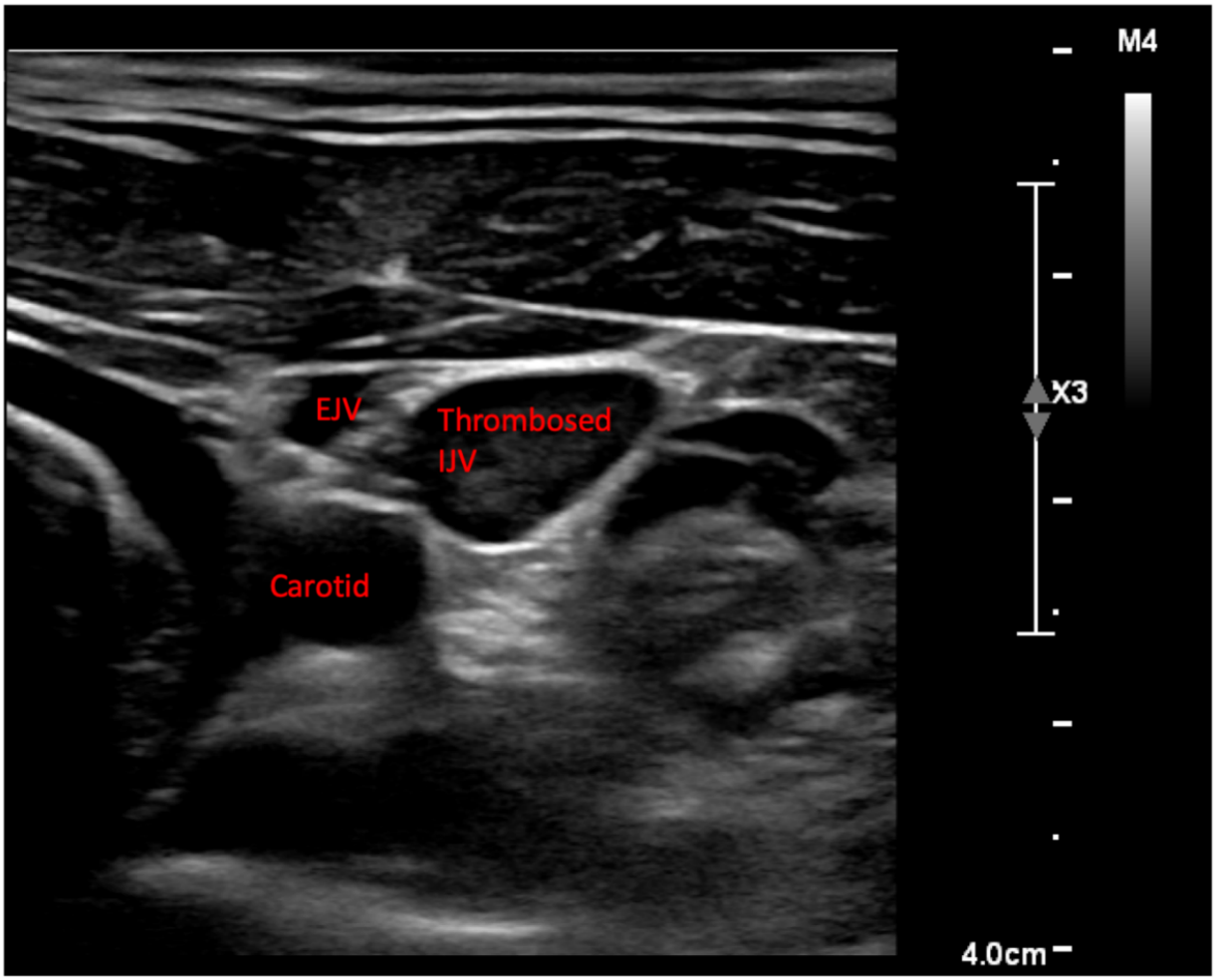

Figure 8-1: Ultrasound image of a thrombosed IJV, carotid artery, and EJV from the MGH cardiac ICU from subject 6.

8.2.1 Force-coupled Ultrasound Data

As observed in force-coupled ultrasound data is acquired in two stages. The first is a force ramp where a collapse force is obtained through complete occlusion of the IJV. The second is a constant low force where the IJV is partially compressed to obtain an IJV area waveform to be input into a finite element model to determine a venous pressure wave. Additionally, the LabVIEW graphical user interface (GUI) has been updated to be more user-friendly. Only what is necessary to capture a force recording along with directions and displays are present. **Figure 8-2** displays the GUI.

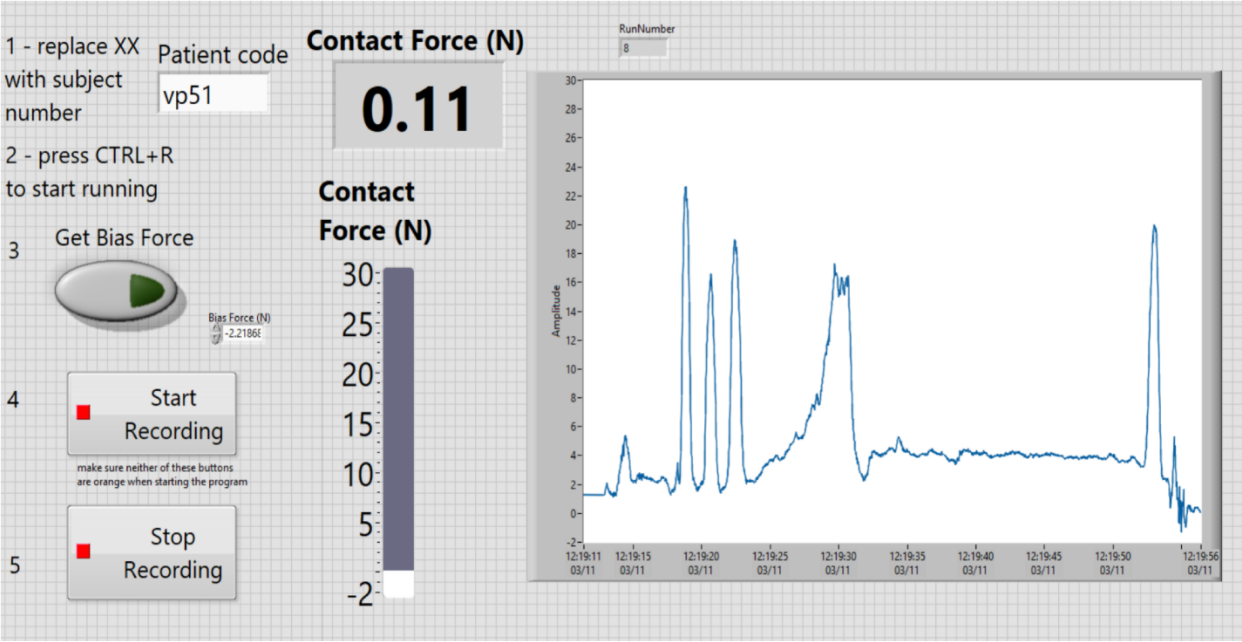

Figure 8-2: User-friendly LabVIEW front panel used for contact force data acquisition at MGH with a produced but realistic example of a data acquisition force profile.

8.2.2 Jugular Venous Pulsation Height

In most patients, JVP is captured by the typical method of estimating the height of the highest pulsation above the sternal angle, independent of angle of inclination, as described in section 3.4 and **Figure 3-17**A. In some patients the pulsation cannot be seen or there is no time to make a measurement in the study.

8.2.3 ICU Waveforms

In this study, we have access to all appropriate and relevant waveforms measured in the ICU. These waveforms always consist of a central venous pressure wave, presenting from either a central line or a pulmonary artery line, and one of the leads of a surface electrocardiogram (ECG). Some patients also have a pulmonary artery wave (most common), radial artery pressure wave, and/or a femoral artery pressure wave (least common). **Figure 8-3** shows a five-second segment of each subject's CVP waveform and ECG. The ECG morphologies are atypical in subjects 1, 2, 3, 5, 10 and 11 due to pacemakers. A wide range of respiratory variation is also visible among the subjects – subject 10 has a

respiratory variation of about 10 mmHg while subject 7 has almost no respiratory variation. Cardiac cycle variation ranges from about 3 mmHg in subject 11 to about 10 mmHg in subject 2.

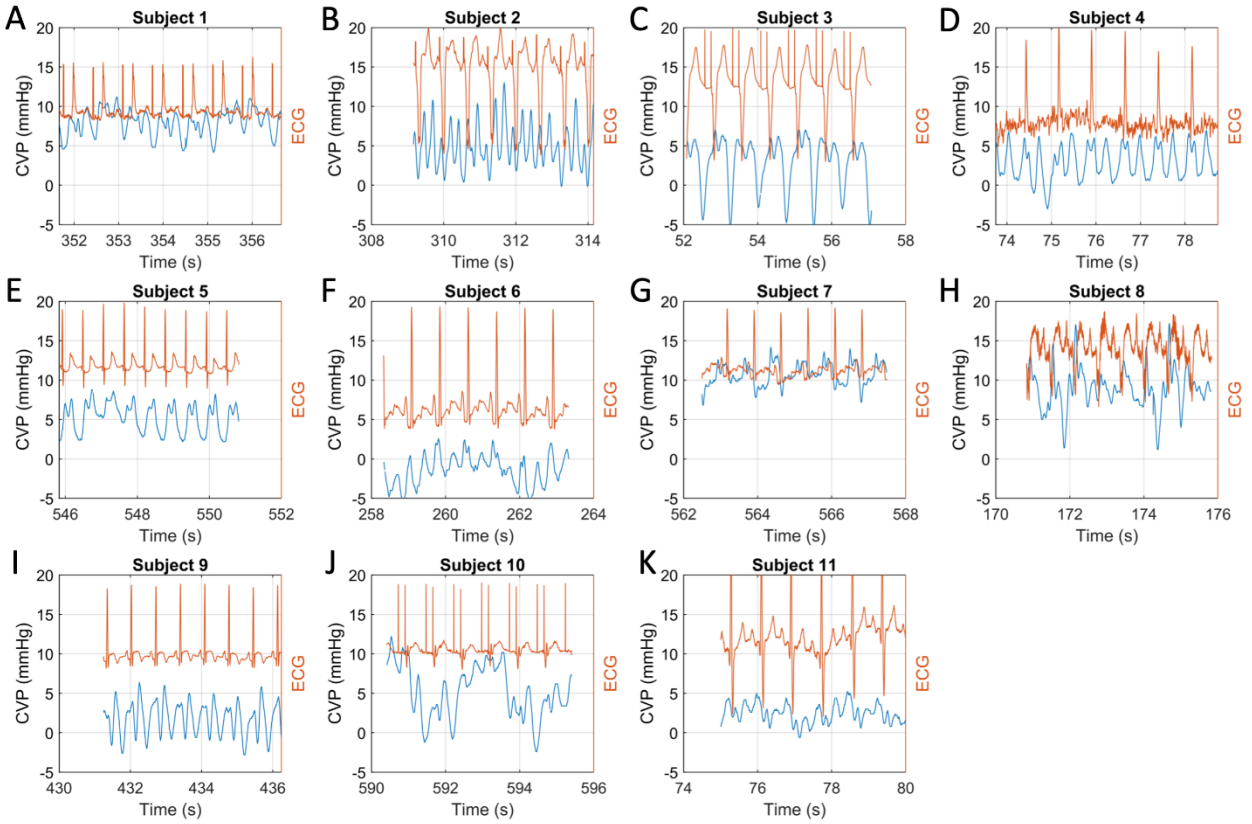

Figure 8-3: (A) Subject 1 invasive CVP and surface ECG waveforms. (B) Subject 2 invasive CVP and surface ECG waveforms. (C) Subject 3 invasive CVP and surface ECG waveforms. (D) Subject 4 invasive CVP and surface ECG waveforms. (E) Subject 5 invasive CVP and surface ECG waveforms. (F) Subject 6 invasive CVP and surface ECG waveforms. (G) Subject 7 invasive CVP and surface ECG waveforms. (H) Subject 8 invasive CVP and surface ECG waveforms. (I) Subject 9 invasive CVP and surface ECG waveforms. (J) Subject 10 invasive CVP and surface ECG waveforms. (K) Subject 11 invasive CVP and surface ECG waveforms.

8.3 CVP Predictor

In this section, we predict CVP using our collapse force based technique rooted in force-coupled ultrasound imaging of the IJV and compare our results to the invasive measurement for eleven patients. We also, when possible, measure the JVP in patients and compare those results to the invasive measurement. However, before discussing our results, we quantify uncertainty for each measurement we make as well as for the gold standard comparison in order to give our results proper context in terms of measurement sensitivity.

8.3.1 Uncertainty Quantification

The uncertainty quantification for collapse force is a simplified version of what is done in chapter 7 in that the method described in **Figure 7-3**C regarding cardiac cycle uncertainty is quantified. This method also quantifies uncertainty with respect to the respiratory cycle by principle of superposition as it extrapolates the maximum and minimum feasible collapse force based on the IJV area waveform variation as the IJV is near collapse. Segmentation uncertainty is not quantified as it is typically much smaller than the superposition of cardiac cycle uncertainty and respiratory cycle uncertainty.

Unlike in the MIT study, patients in the ICU are reclined to variable angles and are rarely completely supine. Therefore, any hydrostatic adjustments made to a predicted CVP are subject to uncertainty. We estimate that the combination of angle measurement uncertainty and deviation from our assumed 10 cm between where our measurement of the jugular takes place and the middle of the right atrium amounts to 0.3 mmHg and should be added to the collapse force uncertainty after it is also converted to pressure units.

Regarding the gold standard invasive CVP, it has relevant uncertainty for which to account. Looking at **Figure 8-3**, we notice that both cardiac cycle variation and respiratory variation can be significant in the CVP waveform, such as in subject 6 (**Figure 8-3**F). However, we notice cardiac cycle variation definitionally occurs within a fraction of a cardiac cycle while respiratory variation occurs over several cardiac cycles. We observe that the fast cardiac cycle variation is attenuated at the IJV and the slow respiratory variation is largely conserved in the IJV area. We see extreme respiratory variation with superimposed typical cardiac cycle variation in the unfiltered invasive CVP waveform in **Figure 8-4**. This subject is the only one out of the eleven with such a high respiratory variation and is the only one where the phenomenon shown in **Figure 8-4**A and **Figure 8-4**B occurs. No other subject demonstrated such high IJV area variation at similar force, despite other subjects having similar and even greater cardiac cycle variation than subject 10 (**Figure 8-3**J). Therefore, when quantifying uncertainty with respect to the invasive CVP measurement, we filter out the cardiac cycle variation, as observed in **Figure 8-4**C, and measure the standard deviation σ of the remaining respiratory variation. We quantify the uncertainty in the invasive signal to be 2σ and to be directionally symmetric.

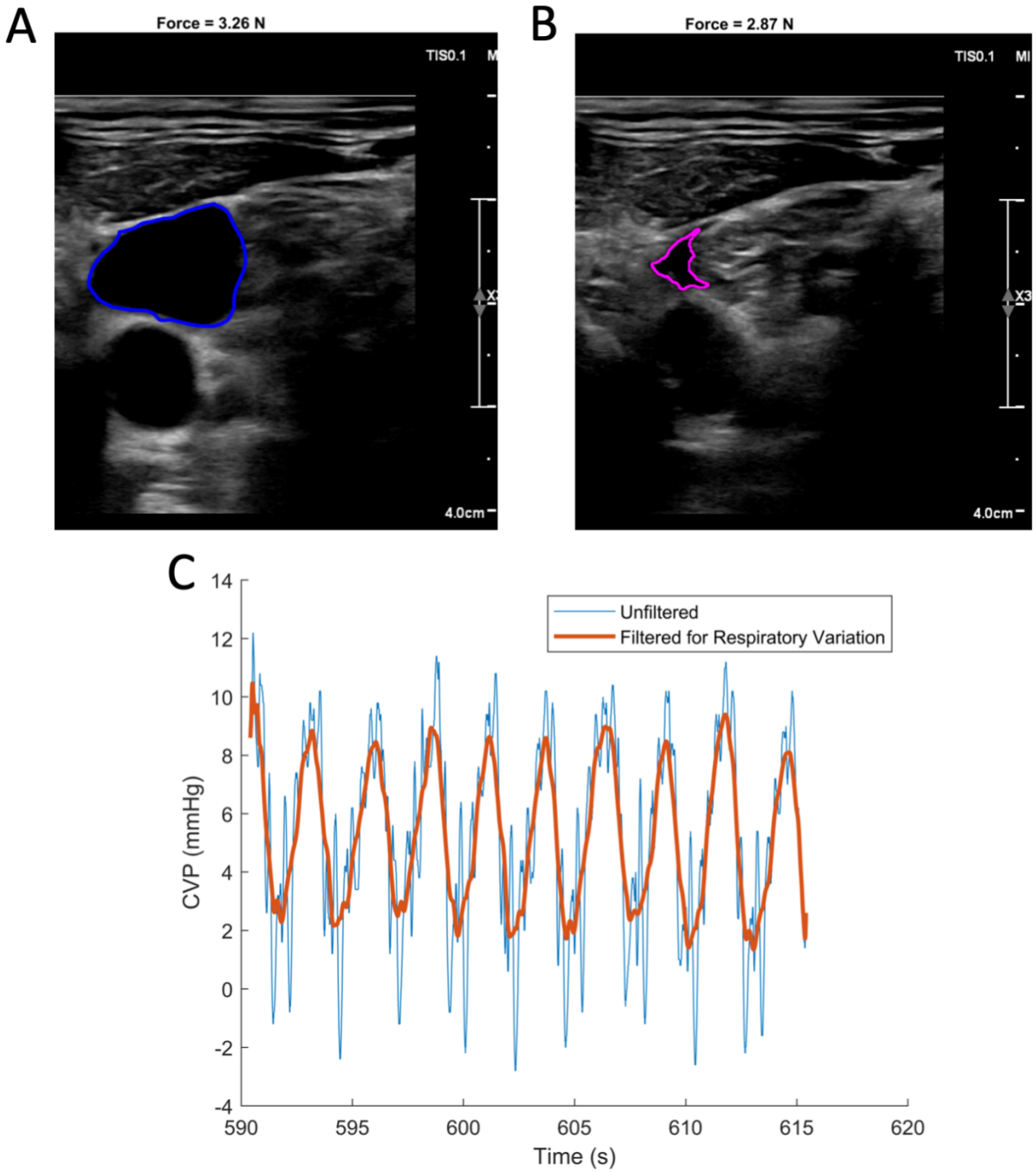

Figure 8-4: (A) Subject 10 segmented force-coupled ultrasound image of the IJV while exhaling. (B) Subject 10 segmented force-coupled ultrasound image of the IJV while inhaling. (C) Subject 10 unfiltered (blue) and filtered (orange) CVP waveform to highlight respiratory variation for about 25 seconds.

8.3.2 Trained MIT Regressor Results

Two to four force-coupled ultrasound data captures are executed on the IJV of each of the nine subjects. Each collapse force is combined with a hydrostatic pressure object based on the estimated height of the measurement above the middle of the right atrium to predict CVP using the linear regression developed in chapter 7.

$$CVP_{MIT} = CF * m + b + h \sin\theta \quad (8.1)$$

where m and b are the slope and intercept of the regressor from section 7.3.2, θ is the angle of inclination above supine, and h is 10 cmH_2O converted to mmHg which is about 7.356 mmHg. Hence, we assume 10 cm between the middle of the right atrium and the area of measurement for all subjects as we assumed in chapter 7. A predicted CVP_{CF} is calculated for each collapse force measurement and those predictions are averaged to produce a single CVP prediction for each subject.

We compare those CVP predictions to average invasive CVP measurements during the time the data is collected. We see that **Figure 8-5**A shows invasive CVP on the horizontal axis and predicted CVP based on collapse force on the vertical axis displaying a correlation coefficient of 0.46. Error bars are used to quantify uncertainty in both axes. We see that **Figure 8-5**B shows an error plot with the gold standard invasive measurement on the horizontal axis and their difference, or error of the collapse force based method on the vertical axis. This shows a mean absolute difference of 1.60 mmHg and a standard deviation of 2.17 mmHg. We note that higher CVPs tend to be underestimated by this model while lower CVPs tend to be accurate or slightly overestimated. We further note that the highest CVP estimated by this model is 6.92 mmHg which is yielded by the subject with the largest hydrostatic offset (θ = 40° → $h \sin\theta$ = 4.73 mmHg).

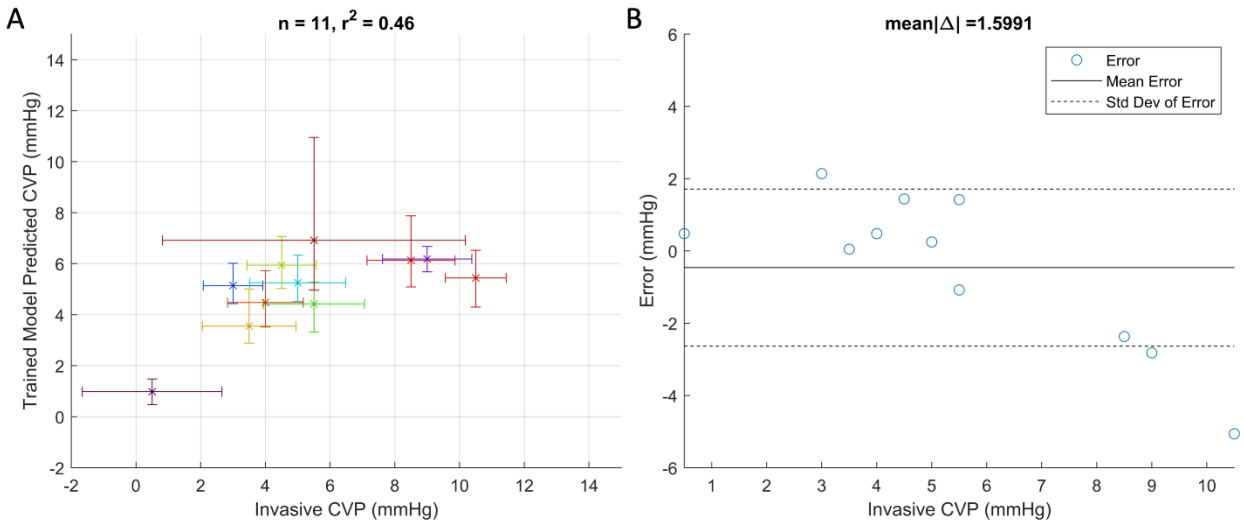

Figure 8-5: (A) CVP predictions from a previously trained linear regressor using collapse force measurements and hydrostatic pressure offset based on angle of inclination plotted against average invasive CVP measurement for 11 subjects. Error bars show quantified uncertainty in each measurement. (B) Error plot comparing average collapse force and hydrostatic pressure based measurement with average invasive CVP measurement for 11 subjects.

8.3.3 Collapse Force Results

If we ignore hydrostatic offset and the MIT-trained linear regressor, we are left with only collapse force as the force-coupled ultrasound output. In **Figure 8-6**A we plot collapse force against invasive CVP with uncertainties displayed in each axis in Newtons for collapse force and in mmHg for invasive CVP. When creating a linear least squares regression, we find a correlation coefficient of 0.82. We also find a mean absolute error of 1.08 mmHg, and a standard deviation of error of 1.24 mmHg, as displayed by the error plot in **Figure 8-6**B.

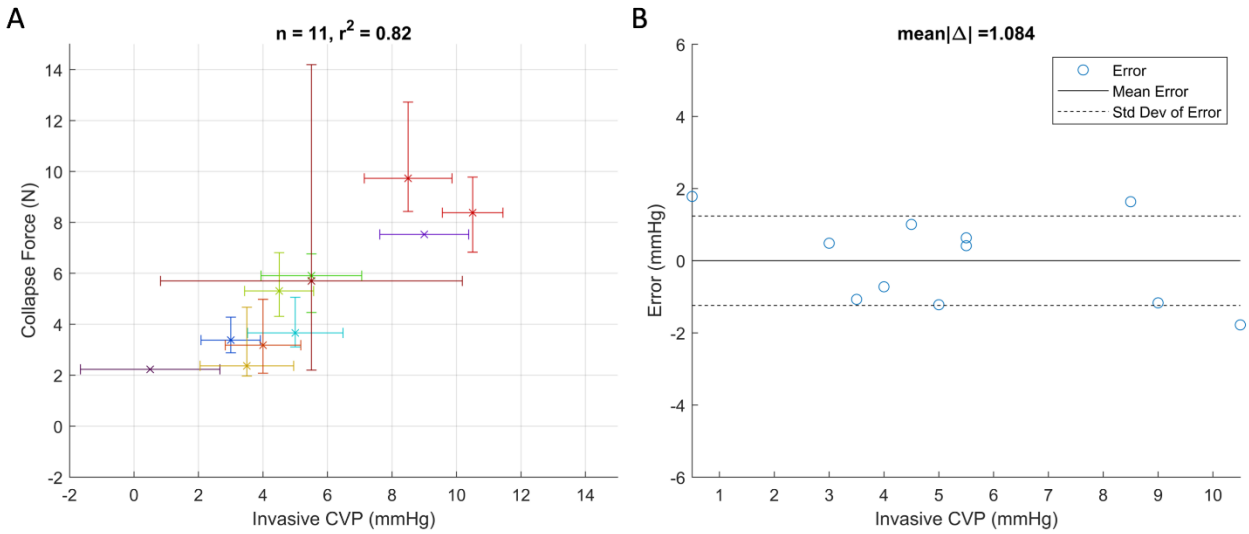

Figure 8-6: (A) Collapse force measurements plotted against average invasive CVP measurement for 11 subjects. Error bars show quantified uncertainty in each measurement. (B) Collapse force CVP prediction from linear regressor error plot against average invasive CVP measurement.

8.3.4 Multi-feature Regression Results

The model in the previous section does not consider hydrostatic offset whatsoever. The MIT trained model essentially assigns it a coefficient of 1 as it is directly added to the supine collapse force regressor CVP estimate. Here, we create another linear model but utilize collapse force and hydrostatic offset as features. A multi-linear least squares regression yields an equation of the following form:

$$CVP_{CF,HO} = CF * x_{CF} + h \sin\theta * x_{HO} + b \tag{8.2}$$

where x_{CF} is the coefficient for collapse force, x_{HO} is the coefficient for hydrostatic offset, and b is the intercept term. The collapse force coefficient converges to be 1.047 with a p-value of 0.000244. The hydrostatic offset coefficient converges to be 0.267 with a p-value of 0.44. The combination of the low p-value and relatively high collapse force coefficient highlight the importance of the collapse force term while the high p-value and coefficient far less than 1 diminish the importance of the hydrostatic offset term when estimating CVP. In **Figure 8-7**, we see that with the added term, there is a minuscule increase in model accuracy compared to the plain collapse force linear regression. The correlation coefficient increases by 0.01 to 0.83. The mean absolute error decreases by 0.02 mmHg to 1.06 mmHg and the standard deviation of the error decrease by 0.05 mmHg to 1.19 mmHg.

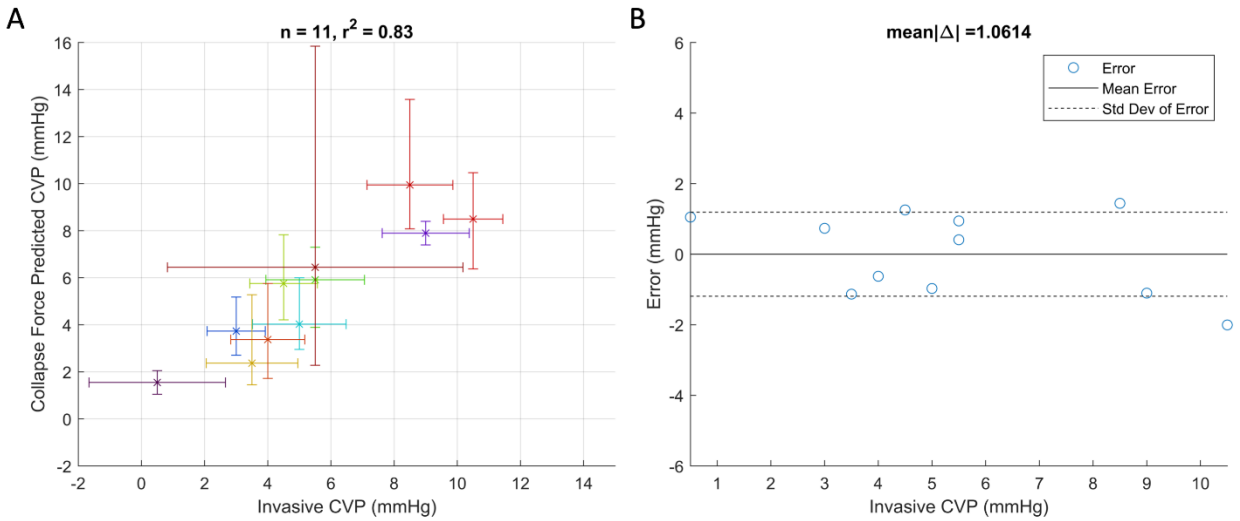

Figure 8-7: (A) CVP prediction from collapse force and hydrostatic offset linear regressor plotted against average invasive CVP measurement. Error bars show quantified uncertainty in each measurement. (B) Error plot of CVP prediction from collapse force and hydrostatic pressure linear regressor.

An additional quadratic regression is calculated. Justified by the increasing fraction of external pressure to collapse accounted for by the venous pressure, a quadratic regression allows for an offset, linear, and quadratic coefficient. This regression produces the most accurate results but runs the most risk of overfitting the data given the increase in coefficients for each feature.

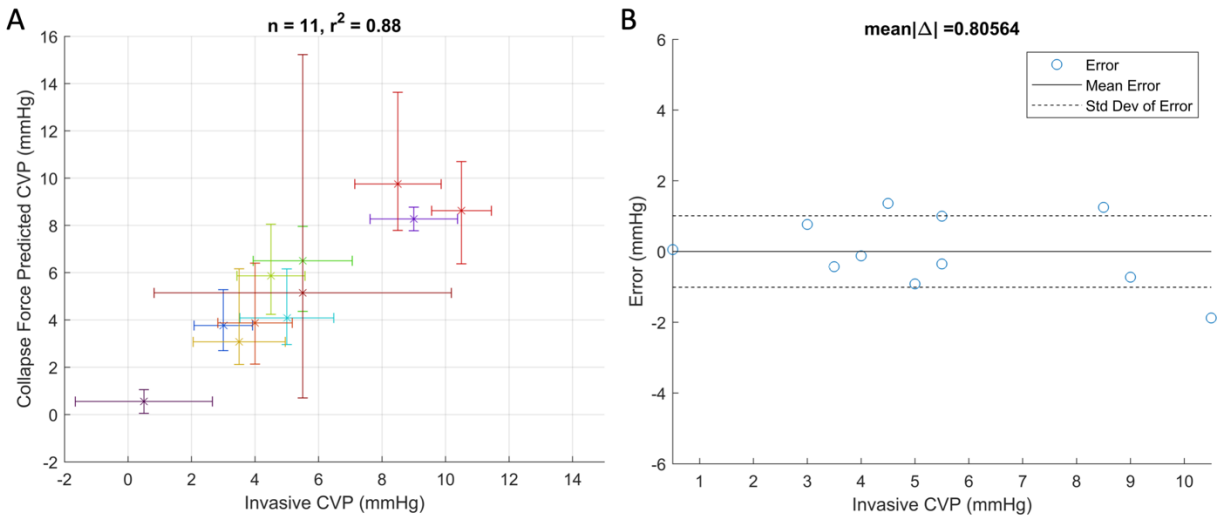

Figure 8-8: (A) CVP prediction from collapse force and hydrostatic offset quadratic regressor plotted against average invasive CVP measurement. Error bars show quantified uncertainty in each measurement. (B) Error plot of CVP prediction from collapse force and hydrostatic pressure quadratic regressor.

8.3.5 JVP Results

In a subset of patients, jugular venous pulsation height (JVP) is measured by a trained cardiologist visually estimating the height of the highest IJV pulsations above the sternal angle. Only five out of the eleven patients had their JVP measured. Three of the remaining six had no JVP measurement attempted. The other three had JVP attempted but could not produce an estimate. This failure to produce an estimate occurs if the height of the highest IJV pulsations is either too low to observe or too high to observe. The range of observable JVP shifts up and expands when a person is angled up.

The uncertainty with respect to JVP is the repeatability of the measurement which is found to be 0.1 in both directions. It is the same uncertainty as in chapter 7 when JVP is used as the standard of comparison. The JVP accuracy in comparison to the invasive gold standard CVP for this dataset is expressed by the correlation coefficient of 0.58, the mean absolute error of 1.29 mmHg, and the standard deviation of error of 1.69 mmHg. A subtler observation is that the range of the JVP measurement in terms of invasive CVP measurement is 3 mmHg while the range of the other aforementioned metrics in terms of invasive CVP measurement is 10 mmHg.

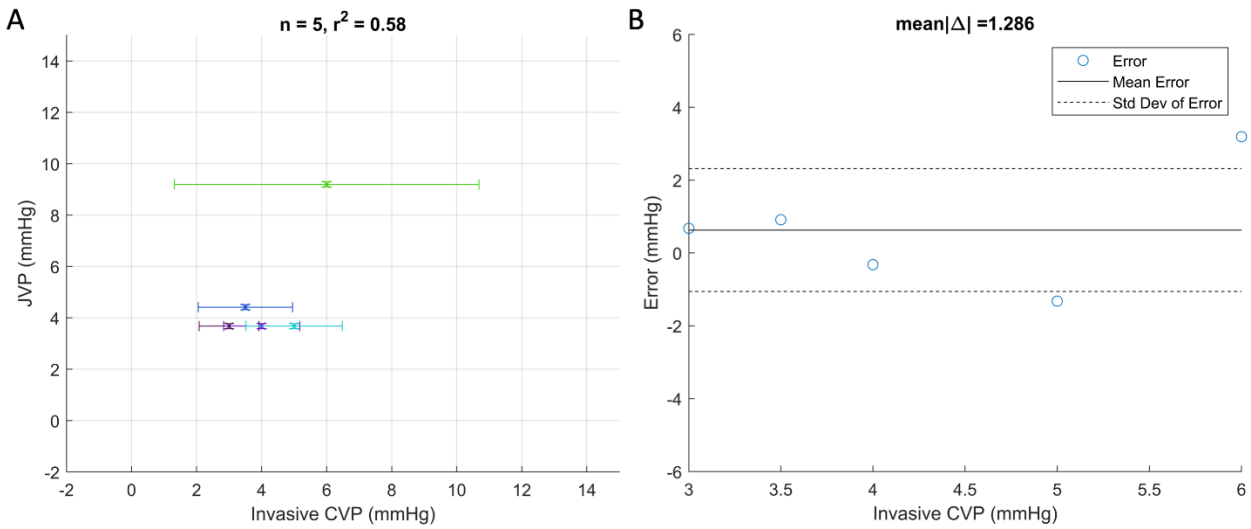

Figure 8-9: (A) JVP in mmHg plotted against average invasive CVP measurement. Error bars show quantified uncertainty in each measurement. (B) Error plot of JVP in mmHg compared to average invasive CVP measurement.

8.3.6. CVP Prediction Method Comparison

Now we strive to compare the three methods explored for CVP prediction in this chapter. These methods are the standard noninvasive JVP, our experimental noninvasive collapse force based technique, and the invasive CVP measurement.

Table 8-1 provides a summary of the gold standard invasive measurements along with the force-coupled ultrasound CVP estimations studied and the noninvasive standard JVP measurement. We note that all estimates are successfully made for all methods aside from the JVP. We also note that the external jugular vein (EJV) is compressed in two of the subjects due to thrombosed IJVs.

Table 8-1: Summary of CVP measurements and estimates made during the study for all subjects. Dashes symbolize JVP measurements not attempted. Exes symbolize JVP measurements attempted but unable to measure. The "Vein" column lists the vein measured for each subject. LIJV stands for left IJV. RIJV stands for right IJV. LEJV stands for left EJV. REJV stands for right EJV.

Subject Number	Average Invasive CVP (mmHg)	Vein	Collapse Force (N)	Hydrostatic Offset (mmHg)	Trained Model CVP (mmHg)	Collapse Force Predicted CVP (mmHg)	Multi-feature Predicted CVP (mmHg)	JVP (mmHg)
1	8.5	LIJV	9.73	2.03	6.13	10.14	9.94	-
2	5.0	LIJV	3.66	3.68	5.25	3.78	4.03	3.68
3	4.5	LIJV	5.31	3.68	5.94	5.51	5.76	-
4	4.0	LIJV	3.18	3.11	4.48	3.28	3.38	3.68
5	5.5	LIJV	5.91	1.90	4.42	6.14	5.91	X
6	0.5	LEJV	2.23	0.00	0.98	2.28	1.55	X
7	10.5	LIJV	8.38	1.90	5.44	8.72	8.50	X
8	9.0	REJV	7.53	2.99	6.18	7.83	7.90	-
9	3.0	LIJV	3.38	3.68	5.14	3.49	3.73	3.68
10	5.5	RIJV	5.70	4.73	6.92	5.92	6.44	9.19
11	3.5	LIJV	2.37	2.52	3.55	2.43	2.37	4.41

Factoring in uncertainty quantification for each of our methods, we compare each method's accuracy with respect to invasive CVP measurement. For each method, we examine the error bars and the estimates together in an effort to see if there is overlap with the CVP measurement with three distinct benchmarks for what qualifies as an overlap. We describe these benchmarks specifically in the caption of **Figure 8-10**. We further see from the figure that the multi-feature predicted CVP performs the best while the JVP performs the worst. Regarding the force-coupled ultrasound derived CVP estimates, the subjects where the EJV is compressed due to a thrombosed IJV are not considered. With respect to JVP, the three estimates which do not take place are not considered while the three estimates that took place but failed to make an estimate are considered to be a missed overlap.

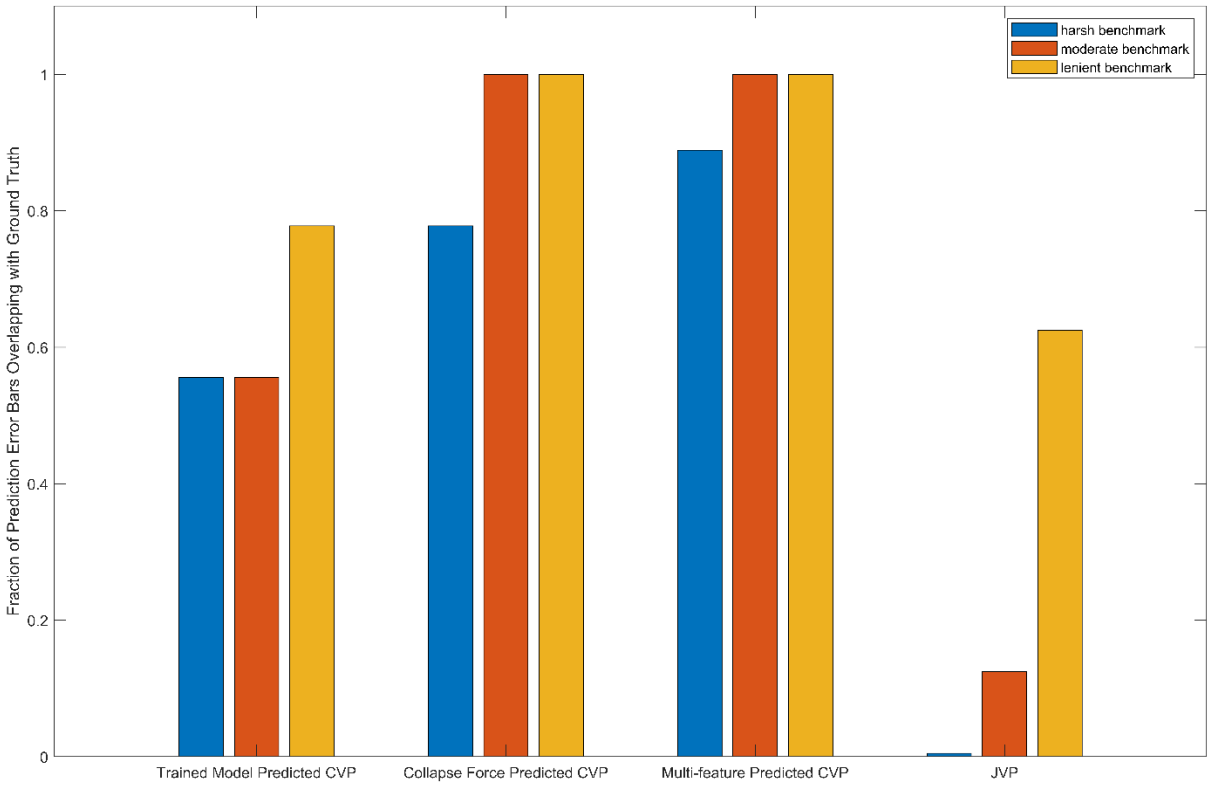

Figure 8-10: Bar graph showing overlap of predicted CVP including quantified uncertainty with gold standard average invasive CVP with three different benchmarks. The harsh benchmark (blue) includes no gold standard CVP uncertainty and assumes infinite precision. The moderate benchmark (orange) assumes a precision of 0.5 mmHg for the gold standard CVP. The lenient benchmark (yellow) assumes a precision of 0.5 mmHg and factors in invasive CVP uncertainty based on respiratory variation. The harsh benchmark fraction for the JVP is zero.

8.3.7 Uncertainty Comparison

We now turn to only uncertainty quantification comparison between collapse force derived uncertainty and invasive CVP derived uncertainty, keeping in mind that collapse force uncertainty quantifies respiratory variation and cardiac cycle variation. **Figure 8-11**A shows the scatter plot of invasive CVP uncertainty with the collapse force uncertainty transformed to reflect the collapse force predicted CVP regression and to make it symmetric in the positive and negative direction. The transformation is:

$$\overline{\varepsilon_{CVP,CF}} = \frac{(\varepsilon_{CF+} + \varepsilon_{CF-})}{2} x \tag{8.3}$$

where ε_{CF+} and ε_{CF-} are the positive and negative collapse force uncertainties, respectively, and x is the slope of the linear regressor used in section 8.3.3. We see that the correlation of the uncertainties is 0.92 while the mean absolute error is 0.52 mmHg and the standard deviation of the error is 0.66 mmHg, as seen in **Figure 8-11**B. We note that the two subjects with EJV compression are left out due to low collapse force uncertainty of the EJV in comparison to the IJV. Also, the highest uncertainty in invasive CVP is overestimated by the collapse force uncertainty model by over 1.5 mmHg.

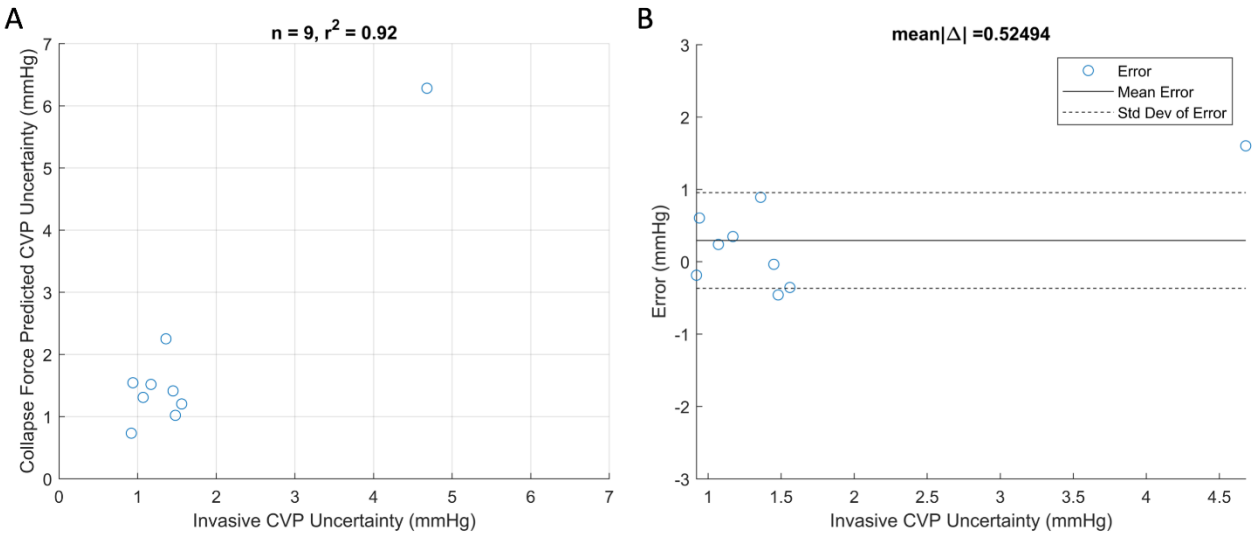

Figure 8-11: (A) Collapse force CVP prediction uncertainty plotted against invasive CVP uncertainty. (B) Error plot of collapse force predicted CVP uncertainty compared to invasive CVP uncertainty.

8.4 Discussion

This study at MGH is ongoing, yet there are several key takeaways from the analyzed data so far which can be utilized by themselves but also guide further data collection efforts as this study continues.

First, it is worth discussing the similarities and differences in data collection conditions with respect to force-coupled ultrasound at MGH compared to data collection at MIT. For the MIT study, all subjects are healthy and have their left IJV compressed. At MGH, subjects are CICU heart failure patients and eight out of eleven of them had their left IJV compressed while the other three and a right IJV, a left EJV, and a right EJV compressed. At MIT, I am the one to use the force-coupled ultrasound on subjects and collect data by myself. At MGH, Dr. Aaron Aguirre uses the force-coupled ultrasound on patients while I help collect data.

Perhaps the most significant difference in measurement between the MIT study and the MGH study is the fact that all MIT subjects are supine while only one out of eleven subjects at MGH are supine. Supine collapse force measurements allows one to assume no hydrostatic offset in venous pressure occurs between the right atrium, where CVP is invasively measured, and the IJV just above the clavicle. As seen by the current results, hydrostatic offset is very minorly predictive of what collapse force will be measured for a given invasive CVP measurement. Assuming hydrostatic offset, aside from its inherent uncertainty, is perfectly predictive is what is done when using the MIT linear regressor which is only trained on supine collapse force measurements.

Next, we discuss the two methods which use models which have not seen any MGH invasive CVP data, the trained MIT model and the JVP. These two models perform similarly in terms of correlation and the JVP performs slightly better than the trained MIT model in terms of error measurement. However, the range of ground truth CVPs tested under the trained MIT model is over three times the range tested with JVP. Furthermore, in this specific set of patients the MIT model is able to provide an estimate for CVP with minimal discomfort and no necessary movement from the patient. On the other hand, JVP would have required an increase in angle of inclination in order to measure CVPs which were too high and could not measure CVPs which provide a height below the sternal angle. Finally, the uncertainty quantification in the trained MIT model provides more insight into the invasive CVP waveform characteristics – specifically respiratory variation – than does the JVP visual assessment.

Perhaps the most encouraging result so far from the study is that collapse force by itself correlates highly with invasive CVP even with the confounding variable of different hydrostatic offsets for each patient. Collapse force is a measurement which can be made quickly and, in theory, can be inferred in real-time with current technology.

The result to examine the closest and try to examine in future data collection for the study is subject 7 which has an average invasive CVP of 10.5 mmHg. This subject has a lower collapse force than the invasive CVP would suggest even though the hydrostatic offset is on the lower side. Obtaining more force-coupled ultrasound measurements on the IJVs of patients with invasive CVP above 10 mmHg would lend more insight into the suggestion that a superlinear model for CVP as a function of collapse force could be useful at high CVP. This result is somewhat in line with what the combined plot in **Figure 7-11** suggests when showing the fraction of external pressure used to collapse represented by the

venous pressure rising when venous pressure rises to pressures obtained by means of the Valsalva maneuver.

Finally, the uncertainty quantification of invasive CVP with respect to only respiratory variation appears to tightly track the collapse force uncertainty which depends on respiratory variation and cardiac cycle variation of the IJV area waveform. This inference implies that the full cardiac cycle variation in the right atrium never reaches the IJV in terms of amplitude, although it reaches the IJV in terms of waveform morphology. Therefore, the cardiac cycle variation amplitude appears to drastically attenuate while the respiratory variation amplitude is largely preserved. Further data collection from patients with high respiratory variability in invasive CVP and more IJV area waveform analysis could provide more relevant information on this topic.

8.5 Summary

In this chapter, we cover the beginnings of the MGH-based study to validate our collapse force based venous pressure measurement against invasive catheterization. The results show a high correlation of collapse force with invasive CVP measurement. The results further suggest that a force-coupled ultrasound collapse force based technique for venous pressure assessment would far outperform JVP as a noninvasive quantitative metric. More data collection is merited for this promising technique.

Chapter 9 – Simultaneous Arterial and Venous Pressure Estimation from Force-coupled Ultrasound Imaging of the Common Carotid Artery and Internal Jugular Vein

Similar to last chapter, this chapter is focused on a study which is partially complete. Three subjects have been tested while the goal for the study is around 25 subjects. However, the analysis is in a complete form. Unlike last chapter which emphasized clinical verification of our collapse force based venous pressure method with gold standard invasive measurements, this chapter seeks to augment force-coupled ultrasound data acquisition and parameter estimation. Here we combine methodologies first discussed in chapter 5 (carotid blood pressure) and chapter 7 (central venous pressure) to simultaneously observe the carotid artery and internal jugular vein with force-coupled ultrasound imaging. In doing this, we simultaneously estimate carotid blood pressure and central venous pressure. We also look to improve the waveform estimation in each pressure wave. For the carotid, we use M-mode imaging, as described in section 4.1.1, to achieve a higher sample rate. For the IJV, we create a finite element model which has the carotid and IJV to account for the effects of the pulsation of the carotid on the IJV area waveform.

9.1 Introduction

A vital sign is considered to be an essential physiological measurement of a human; therefore, vital signs are often assessed [181], [182]. Arterial blood pressure, along with temperature, heart rate, and respiratory rate, is one of the four measurements widely considered to be vital signs [181]. The brachial blood pressure cuff is a noninvasive, convenient, and sometimes automated method of measuring blood pressure, making it by far the most common method [41]. However, as expressed earlier in chapter 5, the blood pressure cuff is known to be prone to errors in both systolic and diastolic measurements [82], [148]. Hence, there is motivation to improve on the blood pressure cuff assessment without sacrificing any of its strong suits.

Unlike, arterial blood pressure, central venous pressure is not currently a vital sign. It is rarely measured in patients who are not diagnosed with congestive heart failure and have not recently suffered a myocardial infarction [169], [178]. At the same time, congestive heart failure is quite common

in the United States – about 2% of people are currently living with congestive heart failure [183]. What's more, the pathophysiology of heart failure usually begins with a compensated stage where the kidneys compensate for lack of heart pumping ability by increasing blood volume [41], [71]. During this stage, increases in blood volume mean increases in central venous pressure (CVP), which has deleterious effects on one's physiology [70]. Angiotensin converting enzyme (ACE) inhibitors have been successful in preventing further blood volume increase in heart failure patients and improving outcomes [77]. Thus, it would be interesting to investigate the effects of ACE inhibitors on those with early heart failure, where central venous pressure has increased compared to its baseline minutely.

Investigating early heart failure in terms of CVP is only possible if CVP is measured. The incentive to measure CVP in patients who aren't very sick is quite low. When combining this reality with the desire for improved arterial blood pressure measurement, we are incentivized to try to combine arterial blood pressure measurement with central venous pressure measurement. In this chapter we focus on this simultaneous measurement through force-coupled ultrasound imaging of the short axes of the carotid artery and the internal jugular vein in the same viewing window. We also focus on producing carotid blood pressure waves, utilizing M-mode imaging for a higher sample rate, and central venous pressure waves through inverse finite element modeling, similar to chapters 5 and 7.

9.2 Data Acquisition and Processing

Force-coupled ultrasound data is acquired using the GE Logiq E6 system with the GE 9L ultrasound probe. It is essentially the same hardware setup as what is used in chapter 5. However, the ultrasound data acquisition differs because it records M-mode in addition to B-mode images. The frame rate becomes slower in B-mode – about 18.5 frames per second, down from 33 frames per second. The M-mode line rate, the amount of M-mode lines sampled per second, is 185.

The data acquisition has three stages which all occur while the subject is supine. The first is a ramp from low force to high force. This stage seeks to determine the collapse force of the IJV, yielding central venous pressure in scalar form, and compress the carotid to determine systolic and diastolic pressure by means of an iterative inverse finite element model. Just before the collapse of the IJV happens, the subject exhales lightly and holds breath until after collapse force occurs to minimize

respiratory variation in venous pressure. **Figure 9-1**A,B show how the IJV compresses entirely and the carotid compresses partially during the ramp.

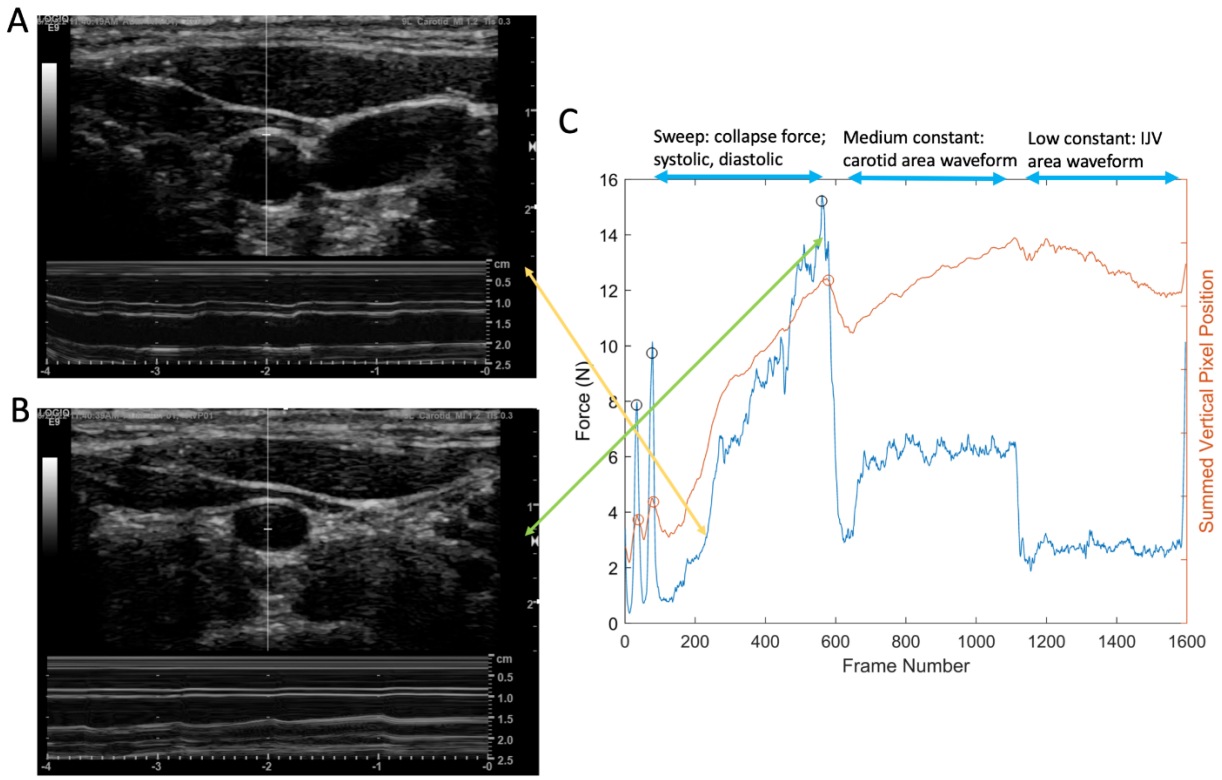

Figure 9-1: (A) Combined B-mode and M-mode image of the carotid and IJV at low force with the M-mode line going through the carotid. (B) Combined B-mode and M-mode image of the carotid at high force and the IJV completely collapsed with the M-mode line going through the carotid. (C) Force and optical flow synchronization plot subdividing into three distinct regions of analysis. The yellow double arrow points out the time and force of the low force signal while the green double arrow points out the time and force of the high force signal.

The second stage is a constant medium force where the M-mode line goes through the carotid, which provides an estimate of a carotid blood pressure waveform when combined with systolic and diastolic pressure estimates from the first stage. **Figure 9-2**A shows the carotid under medium force during this stage with the IJV fully collapsed. The third stage is a constant low force where the M-mode line goes through the IJV, which provides an estimate of a jugular venous pressure waveform when combined with CVP estimate from the first stage. **Figure 9-2**B shows the IJV and the carotid under low force with the M-mode line going through the IJV.

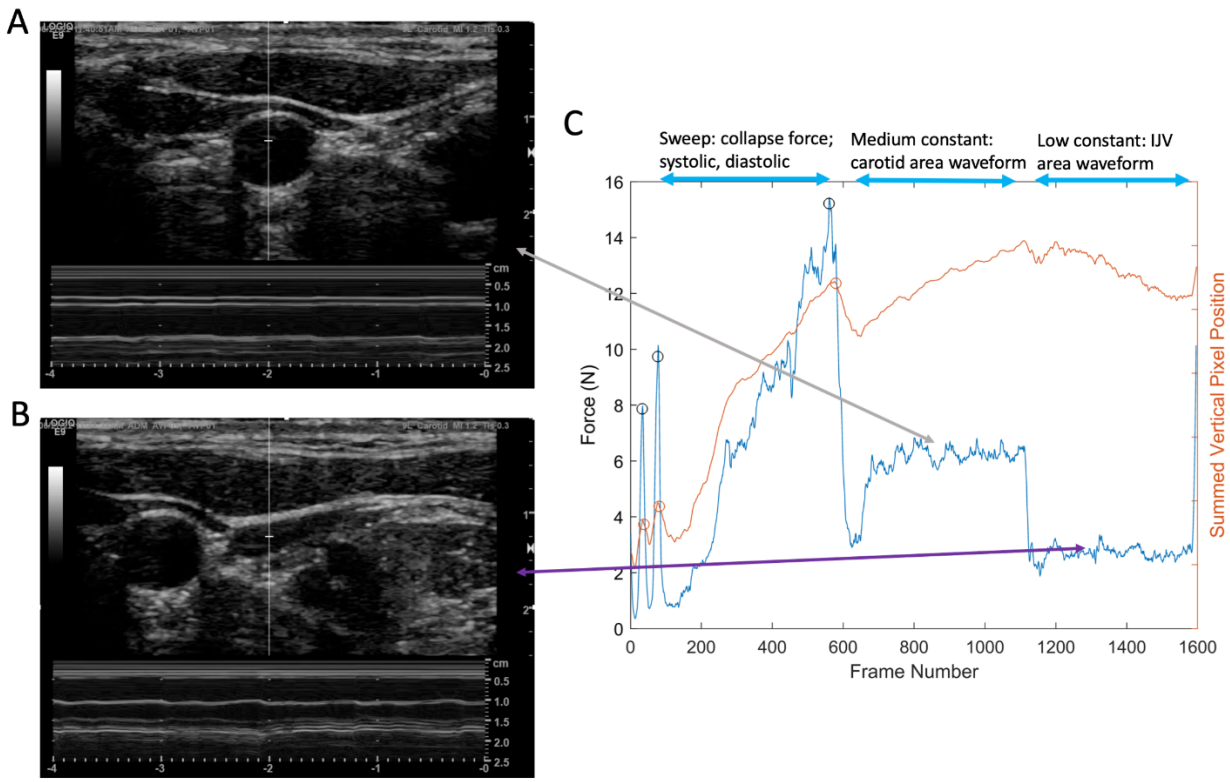

Figure 9-2: (A) Combined B-mode and M-mode image of the carotid under medium constant force with the IJV completely collapsed and the M-mode line going through the carotid. (B) Combined B-mode and M-mode image of the carotid and IJV under low constant force with the M-mode line going through the IJV. (C) Force and optical flow synchronization plot subdividing into three distinct regions of analysis. The gray double arrow points out the time and force of the constant medium force signal while the purple double arrow points out the time and force of the constant low force signal.

After synchronization, carotid detection takes place with the Faster R-CNN detector trained with segmented carotid images, and IJV detection takes place with the detector trained with segmented IJV images, both described in section 4.3. For all three-stages, B-mode segmentation takes place. In order for B-mode segmentation to proceed with minimal error, the M-mode line is detected and removed from each B-mode image prior to segmentation, as shown in **Figure 9-3**.

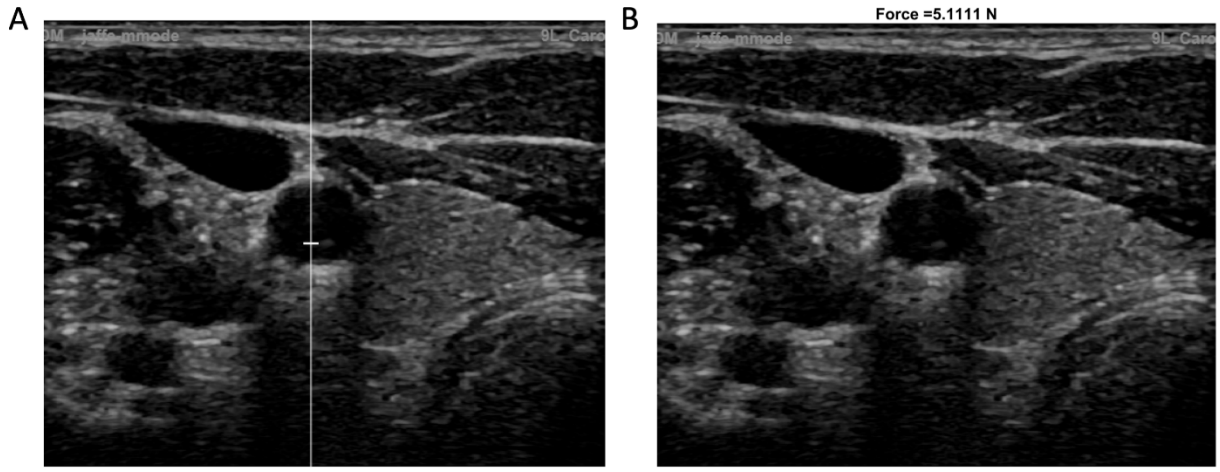

Figure 9-3: (A) B-mode image of the carotid and IJV with an M-mode line going through the carotid. (B) B-mode image of the carotid and IJV with the M-mode line removed.

M-mode segmentation takes place for only the second stage. The high sample rate isn't necessary for the first stage, and the IJV has too irregular a shape to utilize M-mode images without clever input from accompanying B-mode images, which has yet to take place. Each M-mode frame is 4 seconds long and consists of 740 lines into the past. The M-mode segmentation process is as follows:

1. Every 74 lines the B-mode segmentation and M-mode line is used to provide a guess reference for the M-mode segmentation.
2. For each line, an intensity gradient maximization is performed near the anterior and posterior walls on an interpolated and low-pass filtered M-mode line
3. The intensity gradient result for the previous line (one to the right) is the guess for the next line.

Figure 9-4 shows an M-mode image of the carotid segmented with the resultant anterior and posterior walls highlighted.

After carotid M-mode segmentation is accomplished, it is fed into a constrained iterative inverse finite element model, using the converged parameters from the optimization to determine systolic and diastolic pressure from the ramp stage. As mentioned in section 5.4, the systolic and diastolic pressure are used as regularization bounds while the unperturbed radius and carotid wall stiffness parameters are fed in as constants. An optimization is done for each point of the force-coupled ultrasound M-mode segmentation.

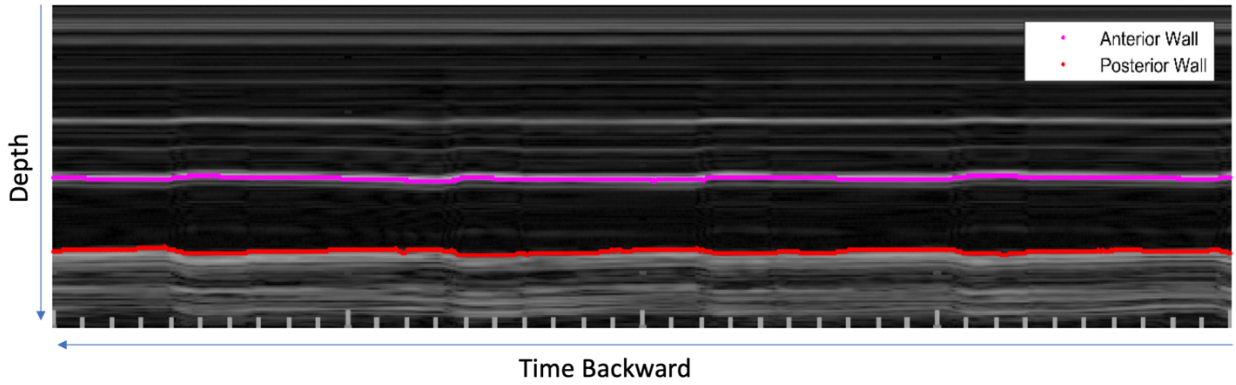

Figure 9-4: M-mode segmentation example of the carotid artery at constant medium force. The maximum depth of the image is 2.5 centimeters and each hashmark at the bottom of the image represents a tenth of a second back in time from right to left.

Nonexperimental data is acquired for comparison after the experimental data is acquired as described above for up to three acquisitions per subject. For venous pressure, jugular venous pulsation height (JVP) is measured in the same quantitative way as described in chapter 7.2. For arterial pressure, the Omron oscillometric brachial blood pressure cuff is used to acquire brachial systolic and diastolic pressure.

9.3 Simultaneous Carotid Blood Pressure and Central Venous Pressure Estimation

Figure 9-5A shows the results of our scalar venous pressure estimates for three subjects. For each subject, the displayed collapse force is the average of three data separate and sequential data captures. Uncertainty is quantified via identical methodology to that of section 7.3.1. These are the first collapse forces attained with the GE 9L force-coupled ultrasound probe, which has a lower cross-sectional area than the Philips XL14-3 force-coupled ultrasound probe and also does not have three-dimensional imaging capabilities. There is no correlation line attempted because of the small size of the dataset. The relationship between the three points appears to be monotonic increasing with respect to JVP.

Figure 9-5B shows the comparison of systolic and diastolic pressures estimated via the simultaneous force-coupled ultrasound method. This involves input of segmentation into an iterative inverse model to determine unperturbed carotid radius and carotid wall stiffness parameters in addition to systolic and diastolic estimates, as described in section 5.3.2. We make the same assumptions as

chapter 5 in adjusting the cuff systolic pressure down from the carotid to the brachial as a function of age. However, in this chapter, we account for the measurement uncertainty by adding horizontal error bars to the average disagreement between systolic and diastolic cuff estimates and systolic and diastolic model estimates. The systolic uncertainty in this cuff conversion is 3 mmHg. This yields an uncertainty of 1.5 when averaged with diastolic uncertainty which is zero.

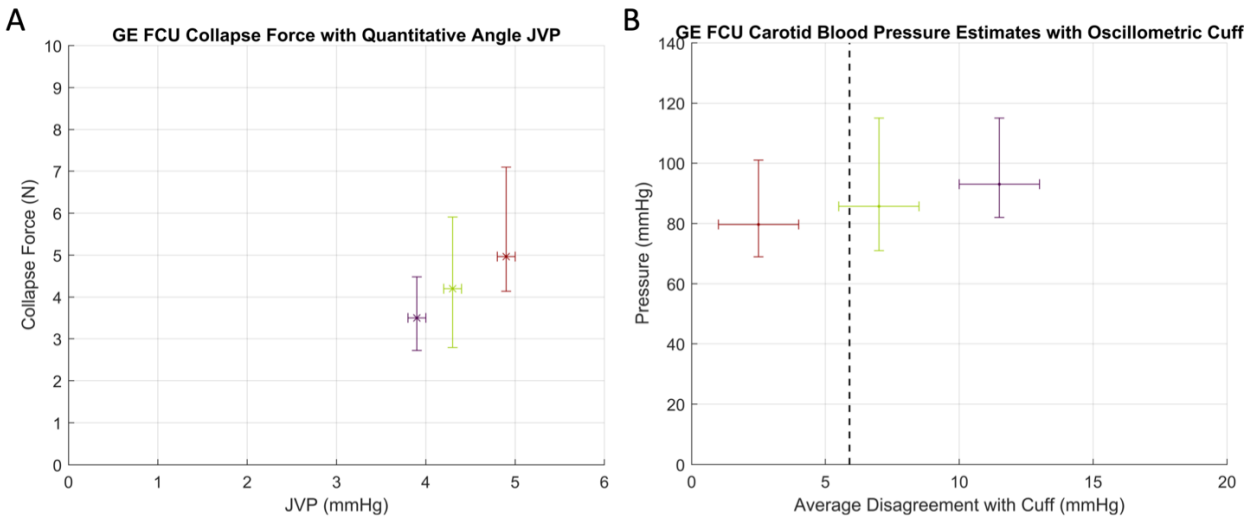

Figure 9-5: (A) Scatterplot of JVP measurement versus collapse force measurement for simultaneous venous pressure estimation for three subjects. (B) Comparison of brachial oscillometric cuff systolic and diastolic pressure measurements with force-coupled ultrasound inverse finite element model estimates for systolic and diastolic pressure for three subjects. The top and bottom of the vertical error bars represent systolic and diastolic pressure estimates, respectively. The black vertical dashed line is the average absolute error found in the carotid study from chapter 5.

9.4 Carotid Blood Pressure Waveform Using M-mode

Figure 9-6A shows the carotid M-mode vertical axis measurement with force for a span of about 25 seconds. The initial areas of segmentation where there is no force is due to force being below the range at which it is deemed to be constant. Some segmentation errors are visible here. Given a sample rate of 185 lines per second for M-mode, the sample rate of the carotid waveform is about six times that of the waveform measured in section 5.4 (33 samples per second). **Figure 9-6**B shows a zoomed in example of a carotid vertical diameter segmentation for slightly more than one cardiac cycle. The time points of the cardiac cycle for the carotid wave are as follows:

1. End-diastole (1): ~6.27 seconds
2. Systole: ~6.47 seconds
3. Dicrotic notch: ~6.69 seconds

4. End-diastole(2): ~7.19 seconds

These time points are in-line with those of a typical carotid blood pressure waveform [143], [184].

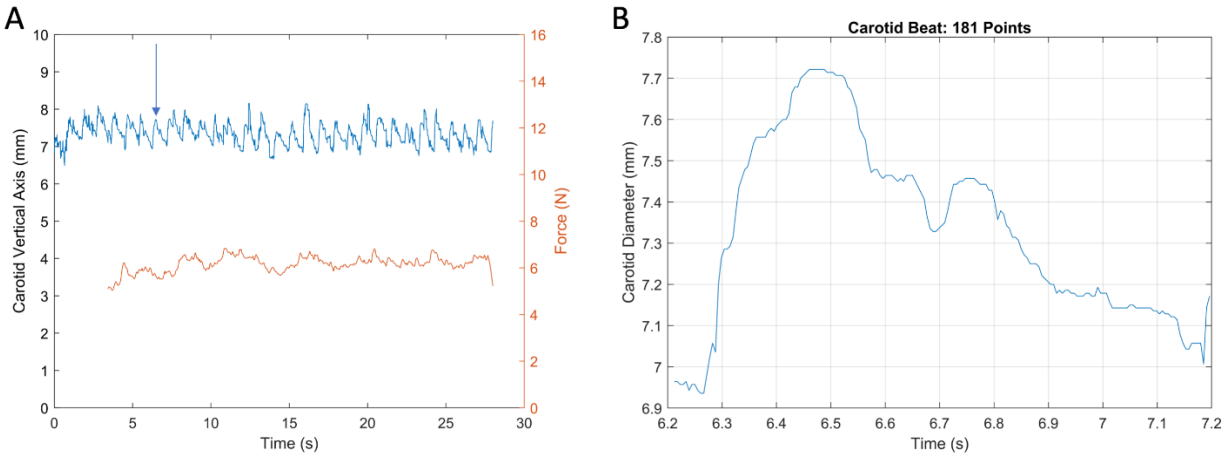

Figure 9-6: (A) Carotid M-mode vertical axis measurement in blue with force measurement in orange. The blue arrow points to the zoomed in carotid waveform in the second panel. (B) A zoomed in carotid vertical axis waveform for one cardiac cycle.

Figure 9-7 shows carotid pressure waveforms for three different subjects derived from the M-mode segmentation, which is also displayed. The top subject has four beats. The middle subject has five beats, and the bottom subject has eight beats. In comparison to the M-mode segmentation, the pressure waveforms occasionally get attenuated near the peak and trough. This is due to regularization penalties for exceeding the estimated systolic and diastolic estimates, respectively, from the first optimization. There is also a range of waveform morphologies for the different subjects, who are all healthy with no cardiovascular disease, which can be attributed to the M-mode segmentation. The subject shown in the middle panel has baseline wander in the third through fifth beat, which could be due to respiratory variation in blood pressure.

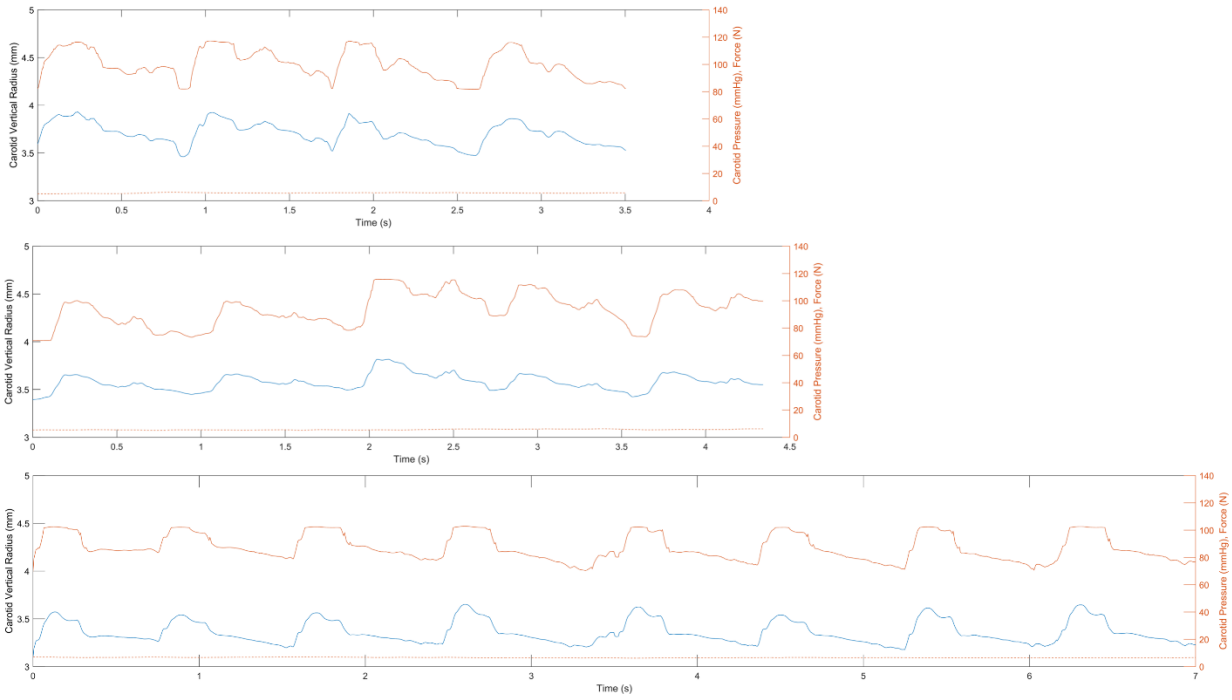

Figure 9-7: Carotid blood pressure waves in three different individuals. Carotid vertical radius is represented by the blue lines. Carotid pressure is represented by the orange solid lines. Force is displayed as the orange dashed lines.

9.5 Finite Element Model of Carotid and IJV

Regarding venous pressure estimation, accounting for the carotid artery pulsation did not occur in the initial finite element model of the IJV presented in section 7.4. This model is simpler than that of section 7.4 because it is only two-dimensional as opposed to three-dimensional. This model is more complicated because of its possession of the carotid artery. The carotid artery is positioned diagonal down from the IJV and pulses in rhythm with the cardiac cycle. Carotid pressure is not solved for in this inverse model. Rather it should be input using the results of the first and second optimization. A modified linear elastic shell, inversely dependent on venous pressure, is provided for the internal jugular vein which aids in its expansion and contraction in response to small changes in venous pressure, attempting to emulate what occurs under real observation. **Figure 9-8**A shows a forward model run where venous pressure is low while **Figure 9-8**B shows a run where venous pressure is quite high, displaying the difference 6 mmHg of pressure can make in cross-sectional area; all else equal.

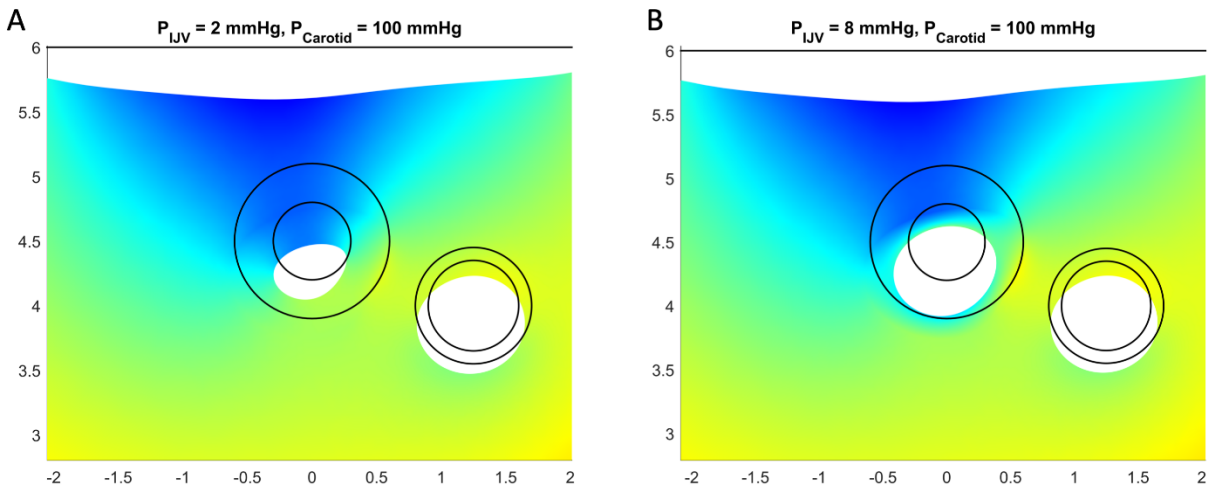

Figure 9-8: (A) Finite element model run with low IJV pressure. (B) Finite element model run with high IJV pressure and all else the same as the first panel.

9.5.1 Accounting for Carotid Pulsation

Since the carotid pressure in the forward model is already determined, the purpose for including it rests solely with its effect on the IJV area waveform. In **Figure 9-9**A, we see an observational example of a carotid segmentation and IJV segmentation displaying vertical radius and area, respectively. We can see that the v-wave in the IJV area is depressed relative to the more academic atrial pressure v-wave shown in **Figure 3-7**. We also see a c-wave, as defined in **Figure 7-11**, that is elevated relative to that same earlier waveform. We posit that these phenomena are due to the pulsation of the carotid adjacent to the IJV. Hence, the carotid compresses the IJV as it is near systole during the v-wave. It also lets the IJV expand as it is in end-diastole during the c-wave.

In **Figure 9-9**B, we create idealized carotid pressure and venous pressure waves in proper cardiac cycle synchronization and measure IJV area in response to a forward finite element model simulation. Here, we reproduce the depressed v-wave and elevated c-wave seen in the segmentation observation. We use these tuned model parameters in the inverse model when we seek to determine the venous pressure wave given the IJV area waveform and carotid waveform.

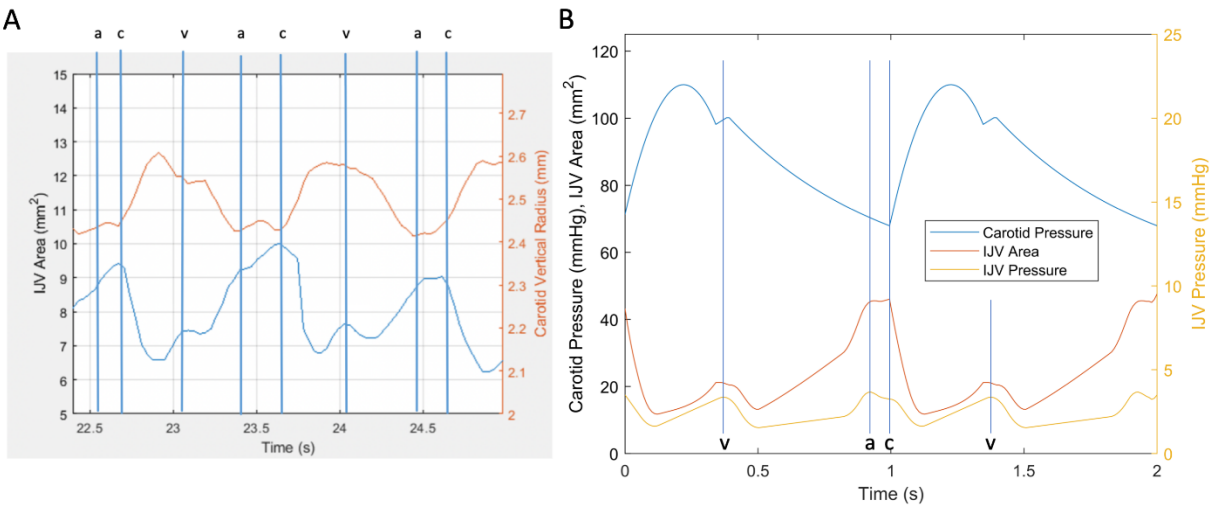

Figure 9-9: (A) Segmented carotid artery and IJV showing elements of right atrial pressure waveform with a compressed v-wave and expanded a-wave and c-wave compared to the right atrial pressure waveform. (B) Forward finite element model simulation of an input carotid pressure and an input jugular venous pressure showing intended suppression of v-wave and expansion of a-wave and c-wave in area waveform compared to venous pressure waveform.

9.5.2 Inverse Model for Venous Pressure Wave

Data from the MGH study is utilized to produce a jugular venous pressure wave for subject 9 and compare it to the invasive CVP waveform measured in the cardiac intensive care unit (CICU) at the same data force-coupled ultrasound data is recorded but not to the point that the data is synchronized. The mean venous pressure in the inverse finite element model waveform output is set to be the mean invasive CVP.

In **Figure 9-10**A, we observe the invasive CVP waveform from the right atrium along with a radial artery pressure waveform. These are both gold standard measurements. In **Figure 9-10**B, we see an IJV area waveform, a relatively constant force, a simplified carotid waveform formed from segmentation of the carotid, and the venous pressure estimate output from our inverse finite element model. We see that the radial artery waveform is delayed relative to the venous pressure in comparison to the carotid waveform because the radial artery is further down the arterial tree than the carotid and the IJV is a branch of the venous tree while the right atrium is the stem. The a-wave and c-wave morphology are not discernable from one another as observed in the invasive CVP waveform. Furthermore, the amplitude of the jugular venous pressure waveform is lower on average than that of the invasive CVP waveform.

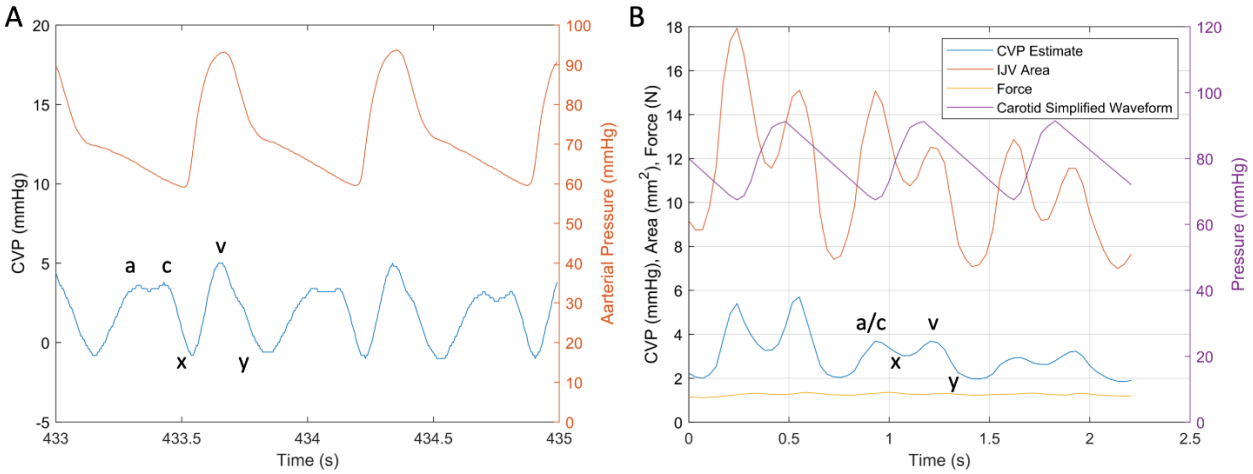

Figure 9-10: (A) Central venous pressure (CVP) measurement from a Swan Ganz catheter in the right atrium of subject 9 from the MGH study in blue. A radial arterial line from the same patient is shown in orange. The components of the CVP waveform is are labeled. (B) Inverse finite element model output of a jugular venous pressure wave in blue with waveform components labeled. IJV area is plotted in orange and a simplified carotid pressure waveform is plotted in orange.

9.6 Discussion

In this study, simultaneous carotid and IJV pressure estimates are achieved with carotid pressure waveforms produced for each subject and the feasibility of producing IJV pressure waveforms for each subject. As mentioned earlier, there are three stages to the data capture. We will now evaluate the performance of each of the data acquisitions and analyses with respect to each stage and suggest improvements.

The first stage involved joint B-mode and M-mode imaging. The B-mode segmentation of the carotid and IJV is used effectively for carotid systolic and diastolic pressure determination and IJV collapse force determination and CVP estimation in comparison to the study in chapter 5 for the carotid and the study in chapter 7 for the IJV. The carotid results are of slightly lower accuracy to the study in chapter 5. Aside from a very small dataset of only three, segmentation in B-mode tended to suffer due to poorer image resolution stemming from also having M-mode in the ultrasound image (pixel size about 1.3 times the size in the previous study) and a lower sample rate (18.5 Hz compared to 33 Hz). Future data captures should benefit from only running B-mode imaging for this stage.

The second stage involved joint B-mode and M-mode imaging of only the carotid at constant medium force. The B-mode segmentation is useful in that it provides a guide for the M-mode segmentation in terms of the vicinity of where to expect the anterior and posterior walls of the carotid.

The M-mode segmentation is used to acquire a carotid segmentation with high time resolution. This stage should continue to run joint B-mode and M-mode imaging.

The third stage involved joint B-mode and M-mode imaging of the carotid and IJV and constant low force. The M-mode line went through the IJV. However, M-mode was ineffective in segmentation of the IJV partially due to the irregular shape of the IJV and partially due to unreliable B-mode segmentation. B-mode segmentation at 33 frames per second would likely fare better than B-mode segmentation at 18.5 frames per second so changes in IJV area are less harsh from frame to frame and image resolution improves slightly. Therefore, future data captures would benefit from running only B-mode for this stage. This would mean stage one and stage three should be in the same data capture with only B-mode imaging while stage 2 should be its own data capture with joint B-mode and M-mode imaging.

Regarding the scalar estimates of arterial pressure and venous pressure, the methodology for carotid pressure is nearly identical to that of chapter 5, so one would expect similar results. When analyzing the results for carotid pressure, one must expect an undershoot of between 10 and 20 N for systolic pressure. This overshoot occurred in one of three subjects, although systolic pressure did overshoot in some respect in all three subjects. For diastolic pressure, one would expect similar estimates to the brachial cuff measurement if accuracy is achieved. Two of the three subjects were within 3 mmHg of the cuff measurement. Given the moderately accurate results noted in chapter 5, these results meet the expectations. With respect to the collapse force measurements, it appears the smaller cross-sectional area will, as expected, yield a lower collapse force for a given venous pressure. It also appears that collapse force is monotonic increasing with venous pressure. The breath hold after small exhalation acted valuably to control respiratory variation predictably in the IJV. For these scalar estimates, more subjects need to be studied for a more confident assessment to be made.

Regarding the waveforms, the carotid pressure waveform morphology would likely benefit from less regularization penalties for guessing outside the systolic and diastolic range. On the other hand, the systolic and diastolic pressures in some of the cardiac cycles may be too high and too low, respectively. The IJV pressure waveform was not produced from the IJV segmentation of stage three for any of the three subjects. Therefore, improvements must be made to the data acquisition to improve IJV segmentation as suggested earlier in this section. Additionally, the morphology of the calculated pressure wave looks discernably similar to its accompanying CVP waveform with an elevated v-wave

compared to its area waveform. Therefore, it appears the modeling of the carotid artery in the finite element model of the IJV has made the venous pressure waveform more accurate.

9.7 Summary

This chapter covers the first simultaneous arterial and venous pressure estimate using force-coupled ultrasound imaging. The carotid and IJV are imaged in three stages using B-mode and M-mode imaging. Stage one is a force ramp which yields scalar CVP and systolic and diastolic blood pressure estimates. Stage two is a constant medium force observing the carotid which yields a carotid pressure wave. Stage three is a constant low force observing the IJV and carotid which yields a venous pressure wave. Further data will be collected and further analysis will be executed for this study. Here, we stated the analysis and inferences at this midpoint of the study in terms of analysis and early point in terms of data collection. The largest takeaway is that simultaneous arterial and venous pressure estimation with force-coupled ultrasound imagining is feasible by viewing the compression of the carotid and IJV short axes.

Chapter 10 – Conclusions and Future Work

10.1 Conclusions

Force-coupled ultrasound imaging adds a quantifiable layer of dimensionality to one's observation. Here, we apply force-coupled ultrasound imaging to large superficial blood vessels including the carotid artery, the great saphenous vein, the femoral vein, and the IJV, while automating the post-processing analysis, allowing for analysis of large datasets without as much manpower. For the carotid artery, a calibration-aided methodology to estimate systolic and diastolic pressure is transformed into a stand-alone technique. This is achieved without loss of accuracy through more physiologically accurate inverse finite element modeling of the artery and its surrounding tissue. With this method, we estimate systolic and diastolic pressure but also a sampled carotid blood pressure waveform. For all veins, a new metric called *collapse force* is created which measures the amount of force needed to occlude the vein by using the force-coupled ultrasound imaging surface to compress it. When used on the IJV, this metric is shown to be a strong predictor of CVP when compared to noninvasive JVP at MIT and invasive CVP measurements at MGH. Hence, collapse force of the IJV appears to be the most accurate noninvasive point of care technique to determine CVP. Furthermore, inverse finite element modeling is utilized on the IJV to produce a venous pressure waveform. Finally, the carotid and IJV techniques are combined to provide a simultaneous estimate of carotid blood pressure and CVP by observing the compression of the carotid and IJV in the same viewing window. To build on the progress made during this research, further exploration of force-coupled ultrasound imaging is merited in the technical and clinical realms.

10.2 Future Work

There are three categories of future work I would suggest with respect to force-coupled ultrasound imaging of large superficial blood vessels: technical improvement, clinical testing, and product development. Given the current state of the research and recent results, there is sufficient motivation to pursue, or continue to pursue, all three of these categories in the immediate future.

10.2.1 Technical Improvement

The central area of technical improvement which is necessary is in the inverse finite element modeling. Currently, our forward finite element model assumes uniform Ogden hyperelastic tissue which leads to a carotid and/or IJV compression which is symmetric with respect to the horizontal axis. Using speckle tracking and/or optical flow to track how tissue deforms in response to a relatively uniform compressive force could better inform the forward finite element model, making the tissue more diverse and nonuniform and leading to a more precise compression compared to observation. The most physiologically accurate finite element model, in addition to having distributed tissue properties, should be three-dimensional and include both the carotid artery and the IJV, which have been accomplished separately in this thesis but will face forward model stability and runtime challenges when implemented together. A useful verification technique which has not been used before for the IJV, in the absence of gold standard data, is having a consistent venous pressure inverse finite element model output with varying force. I would start off by examining vertical and horizontal optical flow measurements in the surrounding tissue areas to see what would need to be replicated in a forward finite element model with diverse tissue.

A secondary area of technical improvement is higher sample rate and higher accuracy segmentation. In chapter 9, M-mode ultrasound is employed for the first time to segment the carotid artery at a constant medium force while guided by B-mode segmentation. However, the M-mode ultrasound used actually has lower spatial resolution than the B-mode ultrasound that is simultaneously recorded. Since the shape of the carotid is highly regular, elliptical if compressed, M-mode's high line rate can be utilized to provide intermediate B-mode segmentation estimations for at least the vertical axis if not also the horizontal axis. This approach should lead to a lower noise and higher sample rate carotid segmentation to be input into an inverse finite element model to determine a carotid pressure waveform. Another approach worth exploring is using an ultrasound research system, such as a Verasonics Vantage system, to collect force-coupled ultrasound images with the most flexibility. This specialization could lead to improved segmentation in terms of sample rate and resolution but will also require a high level of understanding of the ultrasound research system. I would start off by completing the simultaneous arterial and venous pressure study with the appropriate adjustments applied to the M-mode and B-mode data collection suggested here and in section 9.6.

On the computational side, an approach of statistical inference could take place in attempting to predict arterial and venous pressure in general through creating features to be fed into a neural network which would predict the clinical parameters. Although this approach could yield more accurate results, risk of overfitting is high and ample training data must be captured. To be clear, this is a powerful approach and merits effort put towards it. However, it veers away from actual physiology and physics in favor of statistical inference. Therefore, utmost caution should be exercised when pursuing this approach. I would start off with feature selection of derivable features from the fully processed force-coupled ultrasound images by means of regression analysis.

10.2.2 Clinical Testing

Although collapse force of the IJV is in the process of being validated at MGH and appears to be quite accurate when tested against invasive catheterization measurement of CVP, more validation is absolutely necessary to provide more confidence in the measurement. The current plan is to collect data on around 40 more patients at MGH and refine our CVP prediction models before the study is complete. After comprehensive validation against the gold standard of invasive CVP as compared to the noninvasive standard JVP, the proposed techniques could be utilized in patients (subjects) who are not severely ill. For instance, this sample could be composed of individuals diagnosed with CHF, but without a central line. Our method could be compared to JVP in terms of measurement and treatment decisions potentially informed by such measurements. Even further down the line, the measurement could be employed in primary care doctors' offices, obtaining longitudinal measurements in a large number of patients. This would help determine more precisely when congestive heart failure first presents in its early stages, as alluded to in **Figure 3-14**C, and potentially determine more optimal treatment of early stage heart failure to deter its progression.

10.2.3 Product Development

The farther from an academic lab force-coupled ultrasound travels, the more necessary it is to make techniques related to it as user-friendly as possible. Developing real-time localization of the vessel of interest and real-time collapse detection in the case of the IJV would make post-processing less necessary and provide an immediate estimate for CVP. Theoretically, by making segmentation of the

carotid and IJV real-time and using a large number of forward finite element model runs to create a table-lookup method for given segmentation measurements, we could measure arterial and venous pressure in a time similar to that of an oscillometric blood pressure cuff.

Concerning the force-coupling attachment, angle sensing accuracy could be improved and combined with real-time segmentation from ultrasound data in three-dimensions to reliably determine when the force-coupled ultrasound probe's angle is orthogonal to the long axis of a vessel, better ensuring that minimal force is used to provide a specific level of vessel compression. Additionally, the force-coupling attachment could be rendered obsolete if contact force-sensing is successfully incorporated into commercial ultrasound probes and systems.

Regarding form factor, ergonomics and contact area are important. Most people should be able to hold the force-coupled ultrasound probe comfortably with one hand, but some may need to use two hands. A smaller grip circumference would improve the ergonomics of the device. A smaller contact area would decrease the amount of force necessary to produce a given level of compression of a blood vessel. It could also help ensure efficient force transmission to compressing the blood vessel of interest. The sternocleidomastoid muscle (SCM), if flexed, can partially block the transmission of force to the IJV. This would occur if the imaging surface that is compressing is over the SCM. It is easier to avoid the SCM with a smaller contact area. Vascular ultrasound probes with small contact area should be explored.

The data capture methodology must also be standardized and further specified to minimize variability among different users. High variability in data capture methodology could lead to vastly difference blood vessel compression results. Testing compressions before recording and noting the angle of incidence which produces the most compression of a blood vessel given a specific force is a currently implemented idea. However, there may be a way to automate maximizing efficiency of compression by noting compression response to force with a simplified real-time segmentation (perhaps in just the vertical dimension).

10.3 Future Outlook

Given our arterial and venous pressure estimation capabilities now and our plans for the future, it is useful to predict the impact of our technology given assumed improvement which does not require a major technical breakthrough. Out of what is mentioned in the previous future work section, notable

improvement in arterial pressure scalar estimation is a major technical breakthrough and will not be assumed. Other ideas mentioned, such as further automation and straightforward hardware improvements are assumed.

In **Figure 10-1**, we generate a semi-quantitative plot, accounting for relevant metrics to likelihood of clinical adoption. The range for each axis is between zero and ten. The horizontal axis is safety and ease. For noninvasive standard methods, such as the blood pressure cuff and JVP, a ten is automatically given, citing high clinical adoption, noninvasive methodology, real-time capabilities, and high frequency of measurement. For other measurements, a rating is given between zero and ten for safety. Invasive measurements are given a zero while noninvasive measurements are given a ten. This rating is averaged with another zero to ten rating for ease of use. The ease of use rating concerns accessibility of the measurement, automation of analysis, and real-time capabilities of the measurement.

The vertical axis is accuracy. For invasive gold standard methods, such as an arterial line and a central line, a ten is automatically given. For other measurements, the following formula is applied for accuracy (ACC):

$$ACC = r^2 - \frac{|\bar{\Delta}|}{range} \tag{10.1}$$

where our experimental r^2, mean absolute error, and range measurements are used for force-coupled ultrasound and JVP and are estimated from literature values for the blood pressure cuff.

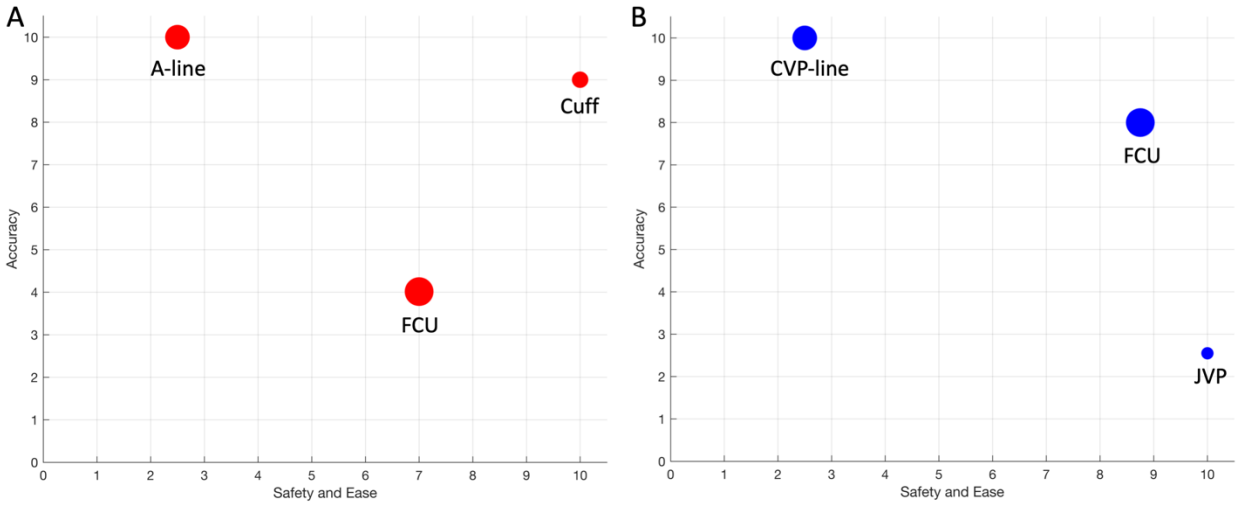

Figure 10-1: (A) Arterial pressure: safety and ease on the horizontal axis and accuracy on the vertical axis. Marker size indicates yield of relevant clinical information. A-line is the invasive gold standard arterial line cannulation pressure measurement. Cuff is the noninvasive standard blood pressure cuff. FCU is force-coupled ultrasound compression of the carotid artery. (B) Venous pressure: safety and ease on the horizontal axis and accuracy on the vertical axis. Marker size indicates yield of relevant clinical information. CVP-line is the invasive gold standard central line catheter or right-heart catheterization. JVP is the noninvasive standard jugular venous pulsation height measurement. FCU is force-coupled ultrasound compression of the internal jugular vein.

We note that the marker size for force-coupled ultrasound (FCU) is larger than the invasive gold standard and the invasive is larger than the noninvasive standard. The force-coupled ultrasound has been demonstrated to be able to estimate venous and arterial pressure with the same device at the same anatomical location and can yield pressure wave estimates for each. The invasive gold standards can yield pressure waves while the noninvasive standards just yield single scalars (venous pressure) or an ordered pair (arterial pressure).

Our semi-quantitative assessment of clinical adoption likelihood bodes well for our venous pressure methodology if the suggested straightforward improvements are made. The arterial pressure methodology will require both a major breakthrough in accuracy and a major breakthrough in ease to be clinically adopted.

This concludes the chapters of my thesis.

Appendix A: Using LabVIEW for Instantaneous CVP Estimation with Force-coupled Ultrasound

An instantaneous central venous pressure estimation is developed with the intention of being used during the compression of the internal jugular vein while a patient is supine. In the figure, we observe a collapsed IJV as well as an approximate indicator on the force profile of when the IJV is collapsed as determined by post-processing. However, since the operator of the force-coupled ultrasound is able to observe the ultrasound images (and with adept skill, force) as they are being acquired, the operator should notice when the collapse of the IJV occurs. Since an operator should have an idea of when the collapse will occur, this method should be better at determining the collapse force in real-time than just determining the peak of the force ramp without looking at the images in post-processing which should overshoot the collapse force.

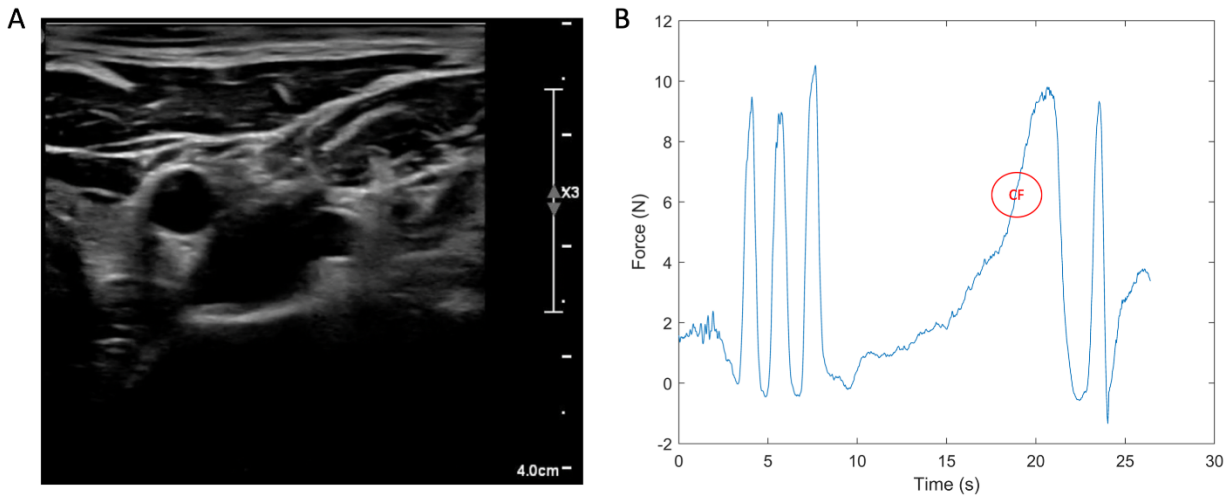

Figure A-1: (A) Ultrasound image of collapsed IJV diagonal up and right from the open carotid artery. (B) Force profile overlaying the collapse force at a specific time during the force ramp.

There is a linear regressor developed at MIT to estimate CVP from collapse force in the supine position described by equation 7.2 and modified by equation 8.1. The LabVIEW estimate, as shown by the block diagram in the following figure, simplifies the slope coefficient, rounding it to the tenths place and completely removes the bias coefficient. Thus, the formula for the conversion of collapse force to CVP in the estimate is simply:

$$CVP = 0.4 * CF \quad \text{(A.1)}$$

It is feasible to account for angle of inclination in the estimate if it is measured beforehand and LabVIEW code is written to incorporate a hydrostatic pressure offset into the CVP estimate.

If this method is to be used by a single operator, it would benefit from having a mechanical button located on the ultrasound probe as opposed to clicking a button on a computer or tablet screen as shown here. If this method is successfully implemented and produces similar CVP estimates to post-processing analysis, it would be a means to provide a real-time CVP estimate based on force-coupled ultrasound imaging and user observation. If force and ultrasound imaging are synchronized from the start instead of synchronized in post-processing, it would be possible to create an automated and instantaneous CVP estimate.

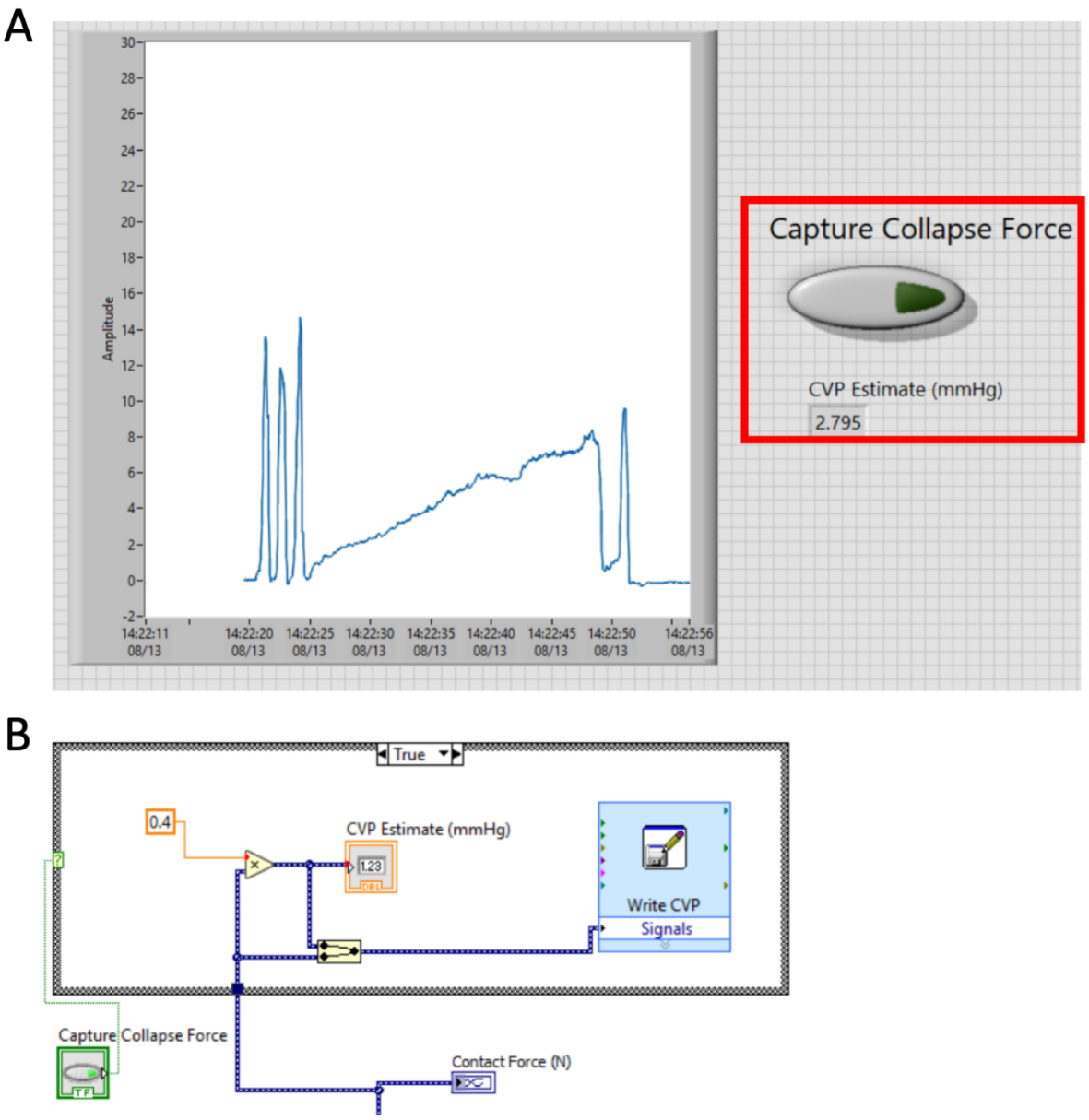

Figure A-2: (A) LabVIEW front panel showing the button to be pressed by the operator when IJV collapse is achieved and an instantaneous CVP estimate. (B) LabVIEW block diagram showing the simplified CVP estimation triggered by the front panel button to capture collapse force as well as the saving of the CVP estimate.

Appendix B: Observations on Carotid Blood Pressure with In-phase and Anti-phase Breathing

In-phase and anti-phase breathing is a breathing technique newly developed by MIT research scientist Praneeth Namburi to modulate heart rate at a specific and singular frequency, depending on the individual. In a short time frame of only a few seconds, increases and decreases in heart rate lead to increases and decreases in blood pressure because the body does not have time for compensatory effects to take place. Anecdotally, these breathing patterns may lead to positive mental and physical health outcomes. Therefore, changes to homeostasis resulting from these breathing patterns is worth understanding mechanistically.

Tracking the blood pressure in response to in-phase and anti-phase breathing is studied here with force-coupled ultrasound imaging. Like in chapter 5, the carotid artery is segmented under constant force and input into an inverse finite element model to determine a pressure wave. Unlike chapter 5, systolic and diastolic pressure are not determined beforehand so the model is less constrained in a regularization sense, allowing blood pressure estimation to fluctuate according to the breathing pattern implemented by the individual being imaged. We observe in the same individual, force-coupled ultrasound based carotid blood pressure waveform estimation when breathing normally, breathing in an in-phase pattern, and breathing in an anti-phase pattern.

The first figure shows the normal breathing pattern. This pattern is autonomic and unintentional and is executed while focusing on something else besides breathing. We see diastolic pressure remains relatively stable, while systolic pressure varies more. However, this could be due to segmentation error as morphologies of the carotid waveform seem to be quite imprecise. Furthermore, there is evidence of a slight offset between ECG and ultrasound.

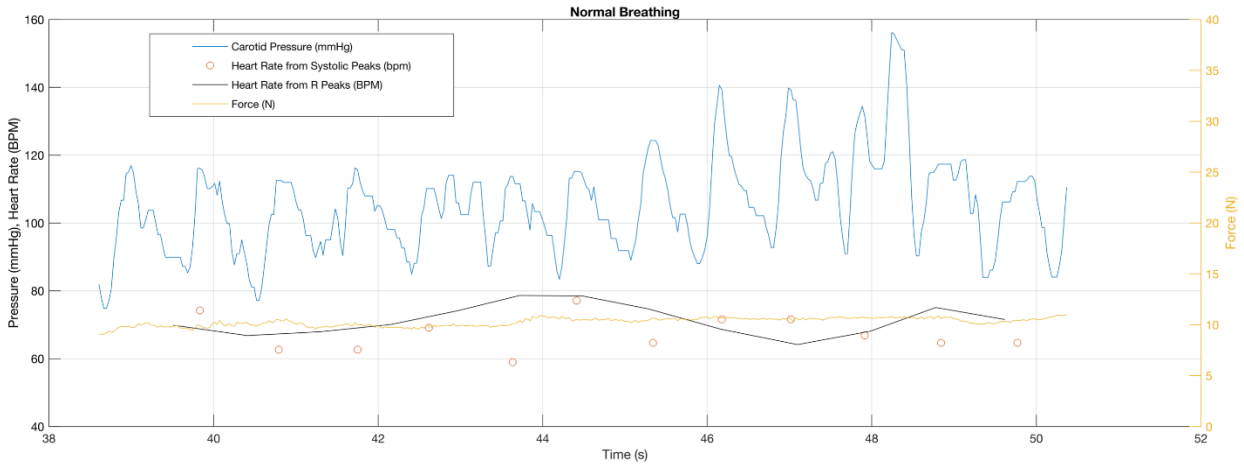

Figure B-1: Force-coupled ultrasound information of carotid blood pressure and heart rate during a normal breathing pattern and constant force at about 10 N. The black line represents RR interval heart rate estimates from surface ECG.

The second figure shows the in-phase breathing pattern. There is an identifiable frequency in heart rate and mean carotid arterial pressure fluctuation of about 0.1 Hz. Heart rate is not calculated where carotid segmentation is too inaccurate to discern where end-diastole is. Furthermore, there are two outlier samples in the R-R intervals which are low. This occurrence signals that an QRS-peak in the ECG is missed as the estimated heart rate is approximately halved.

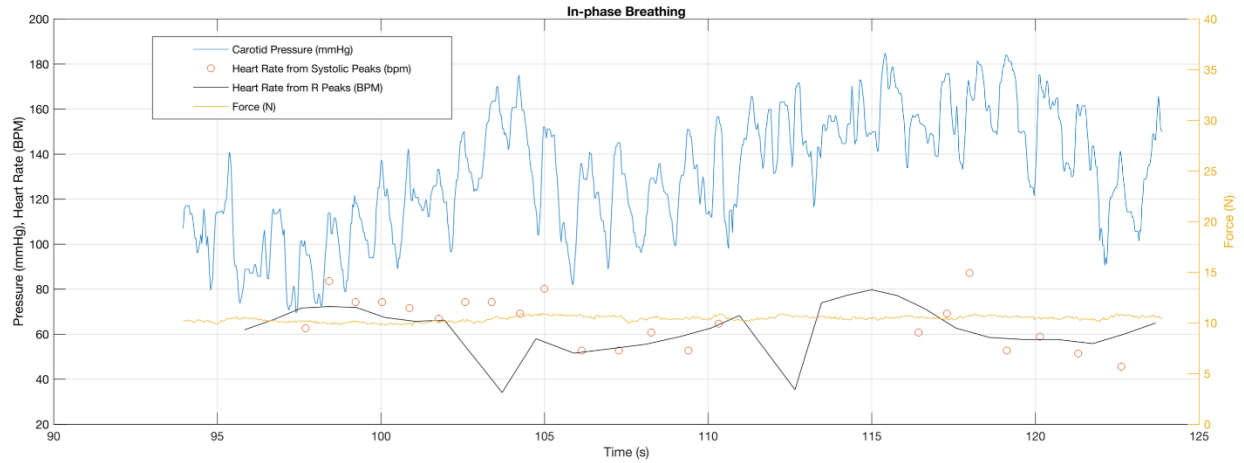

Figure B-2: Force-coupled ultrasound information of carotid blood pressure and heart rate during an in-phase breathing pattern and constant force at about 10 N. The black line represents RR interval heart rate estimates from surface ECG.

The third figure shows the anti-phase breathing pattern. There is an identifiable frequency of about 0.2 Hz for the fluctuation of heart rate and mean carotid blood pressure which is twice that of the in-phase breathing. The offset between ECG and ultrasound is most apparent here because the RR intervals appear to be anti-phasic with the mean blood pressure. There is also an increase in estimated carotid blood pressure as the anti-phase breathing extends for past 15 seconds.

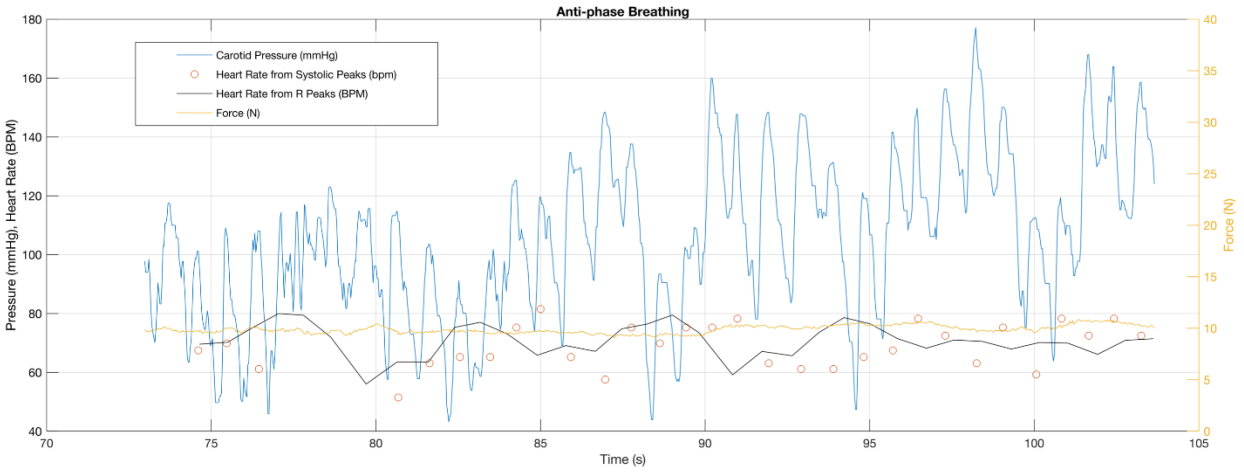

Figure B-3: Force-coupled ultrasound information of carotid blood pressure and heart rate during an anti-phase breathing pattern and constant force at about 10 N. The black line represents RR interval heart rate estimates from surface ECG.

Force-coupled ultrasound imaging presents a way to track blood pressure modulation in response to in-phase and anti-phase breathing. The estimation would be more precise with more accurate segmentation of the carotid as displayed in chapters 5 and 9. Still, further exploration of in-phase and anti-phase breathing should be explored with respect to force-coupled ultrasound imaging of the carotid artery.

Appendix C: Carotid Pressure Estimation with Long-axis Segmentation and Finite Difference Modeling

A finite difference model of the carotid artery using lump circuit components is constructed based on long-axis segmentation of the carotid. This first figure illustrates a reduced version of the finite difference model which actually has 169 nodes with most occurring in the middle of regions. The figure's model has five nodes which describe the boundary conditions of the model. The ϵ_w term describes a linear stress-strain relationship for the arterial walls which are assumed to be linear elastic. The a_t term describes a quadratic stress-strain relationship for the tissue anterior and posterior to the carotid artery. It is a simplified version of hyperelastic tissue. The p_l term describes a linear stress-strain relationship representing the pressure inside the artery, making it a passive component as opposed to an active component like in the finite element modeling run in previous chapters. Each node has a finite difference equation describing it over the form:

$$\frac{dx_i}{dt} = A(x_{i+1} - x_i)^p - B(x_i - x_{i-1})^p \tag{C.1}$$

where $A = B$ if within a region, $p = 2$ if in tissue, and $p = 1$ otherwise.

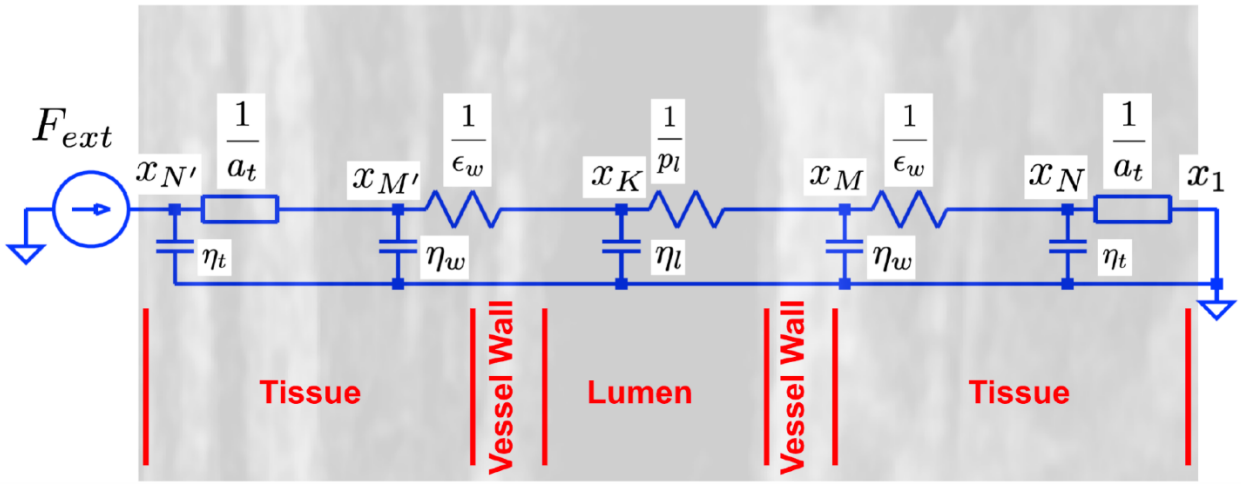

Figure C-1: A circuit based one-dimensional finite difference model for compression of the carotid artery overlaid on a rotated long-axis ultrasound image of the carotid. A diagrammed partition is also overlaid describing various regions around and within the long axis carotid artery.

Force-coupled ultrasound imaging of the long-axis of the carotid is used as observational data for the inverse finite difference model. The long-axis of the carotid artery provides easier viewing of the

carotid wall intima but it is more difficult to compress without a slip, causing it to fall out of frame. The short-axis case will still have the carotid in the image if a shift in angle or position of the ultrasound probe happens. This would manifest as a shift to the left or the right of the carotid artery in the image. A shift in angle or position in the long-axis case could remove the carotid artery from the viewing frame as the ultrasound imaging is only two-dimensional. The following figure shows the compression of the long-axis of the carotid with compression of anterior tissue quite evident, but also with visible compression of the carotid lumen.

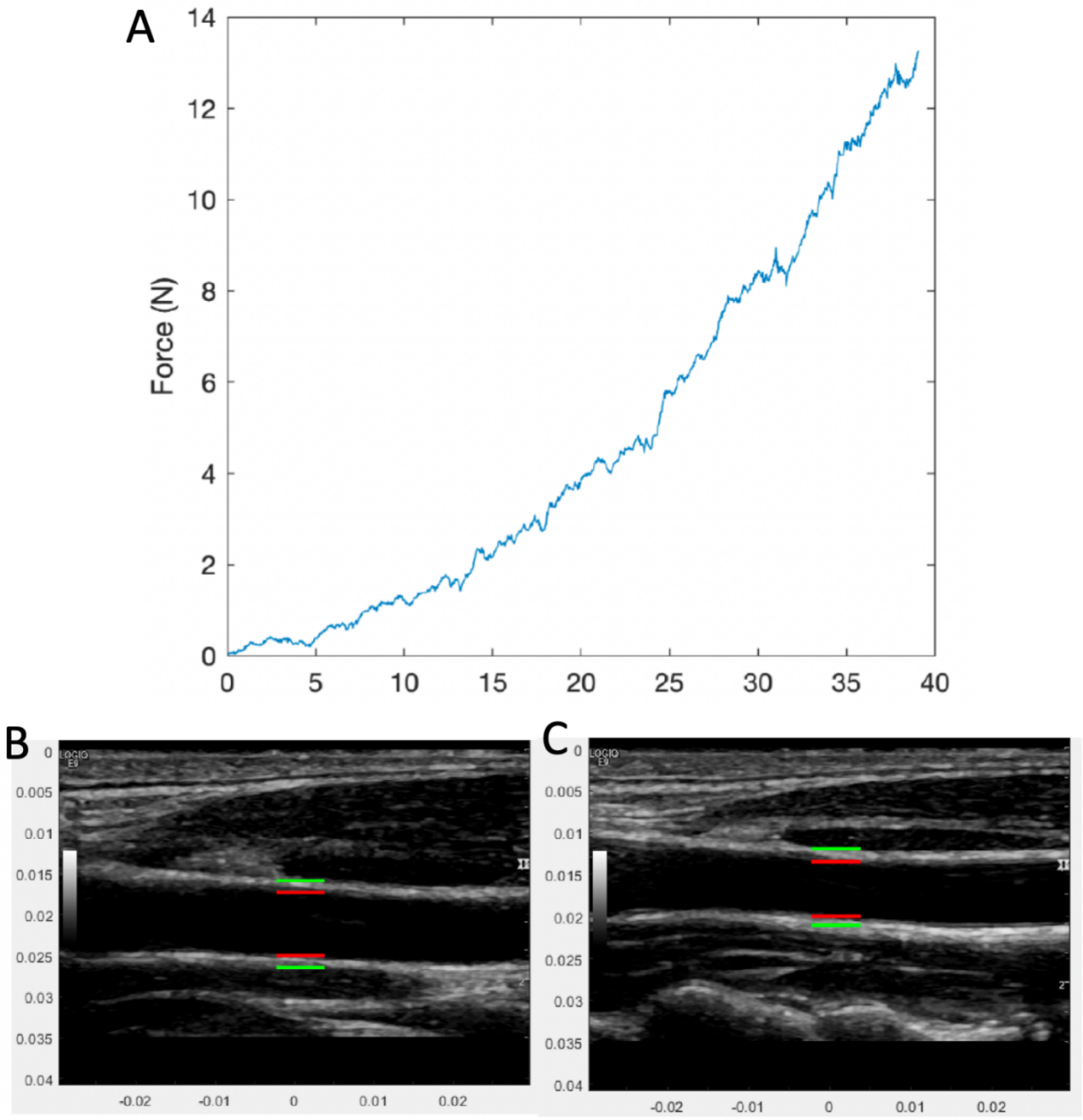

Figure C-2: (A) Force profile for a force ramp of the long-axis view of the carotid. (B) Long-axis carotid segmentation at low force. (C) Long-axis carotid segmentation at high force.

In running the inverse finite element model for each force-coupled ultrasound frame of the long-axis of the carotid artery, five separate parameters are converged. There are two arterial wall stiffness parameters for the anterior and posterior wall, two tissue quadratic stiffness parameters for the anterior and posterior tissue, and the lumen pressure parameter. However, the most impactful

parameter for each frame is the lumen pressure p_l. We see from the carotid pressure waveform produced that no dicrotic notch is sensed. Furthermore, while diastolic pressures are reasonably consistent, systolic pressures are quite inconsistent and average pulse pressures are higher than typical. That said, the advantage of the finite difference model over the finite element model is in runtime. Producing all of the 180 convergences for all five parameters only takes 5.4 seconds. In the case of a more complicated two-dimensional finite element model with tens of thousands of nodes, the same task would take several hours.

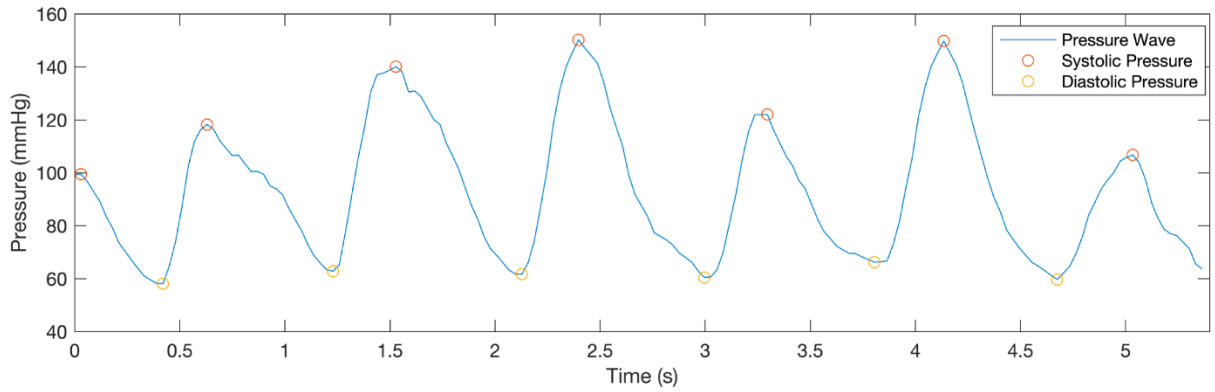

Figure C-3: Force-coupled ultrasound inverse finite difference model output of a carotid blood pressure wave estimation, identifying diastolic and systolic pressures.

Bibliography

[1] A. V. Oppenheim and R. W. Schafer, *Discrete-Time Signal Processing, Third Edition*. Upper Saddle River, NJ: Prentice-Hall, Inc., 2010.

[2] T. L. Szabo, *Diagnostic Ultrasound Imaging: Inside Out*. 2004.

[3] H. J. LANDAU, "Sampling, Data Transmission, and the Nyquist Rate," *Proc. IEEE*, vol. 55, no. 10, pp. 1701–1706, 1967, doi: 10.1109/PROC.1967.5962.

[4] "Series RC Circuit," 2016. https://electronics.stackexchange.com/questions/248882/series-rc-circuit (accessed Jul. 09, 2022).

[5] "Passive Low Pass Filter," 2020. https://www.electronics-tutorials.ws/filter/filter_2.html.

[6] All About Circuits, "Building a Differential Amplifier." https://www.allaboutcircuits.com/textbook/semiconductors/chpt-8/building-a-differential-amplifier/.

[7] CREx, "Filtering: The Basics." https://blricrex.hypotheses.org/filtering-introduction (accessed Jul. 11, 2022).

[8] MathWorks, "Find Local Maxima," 2022. https://www.mathworks.com/help/signal/ref/findpeaks.html (accessed Jul. 11, 2022).

[9] B. K. P. Horn and B. G. Schunck, "Determining optical flow," *Artif. Intell.*, vol. 17, no. 1–3, pp. 185–203, 1981, doi: 10.1016/0004-3702(81)90024-2.

[10] C. M. Bishop, "Neural Networks for Pattern Recognition CLARENDON PRESS • OXFORD 1995," pp. 116–146, 1995.

[11] S. Albawi, T. A. Mohammed, and S. Al-Zawi, "Understanding of a convolutional neural network," *Proc. 2017 Int. Conf. Eng. Technol. ICET 2017*, vol. 2018-Janua, pp. 1–6, 2018, doi: 10.1109/ICEngTechnol.2017.8308186.

[12] S. Ren, K. He, R. Girshick, and J. Sun, "Faster R-CNN: Towards Real-Time Object Detection with Region Proposal Networks," *IEEE Trans. Pattern Anal. Mach. Intell.*, vol. 39, no. 6, pp. 1137–1149, 2017, doi: 10.1109/TPAMI.2016.2577031.

[13] Q. Fan, L. Brown, and J. Smith, "A closer look at Faster R-CNN for vehicle detection," *IEEE Intell. Veh. Symp. Proc.*, vol. 2016-Augus, no. Iv, pp. 124–129, 2016, doi: 10.1109/IVS.2016.7535375.

[14] E. Williams, *Fourier acoustics: sound radiation and nearfield acoustical halography*. Academic Press, 1999.

[15] C. Vogt, K. Laihem, and C. Wiebusch, "Speed of sound in bubble-free ice," *J. Acoust. Soc. Am.*, vol. 124, no. 6, pp. 3613–3618, 2008, doi: 10.1121/1.2996304.

[16] K. Forinash and W. Christian, "Sound: An Interactive eBook," 2016, [Online]. Available: http://www.compadre.org/books/SoundBook.

[17] K. Ono, "A comprehensive report on ultrasonic attenuation of engineering materials, including metals, ceramics, polymers, fiber-reinforced composites, wood, and rocks," *Appl. Sci.*, vol. 10, no.

7, 2020, doi: 10.3390/app10072230.

[18] G. R. ter Haar, H. Meire, and P. Farrant, “Basic Ultrasound,” in *Radiation Research*, 1995, vol. 144, no. 3, p. 349, doi: 10.2307/3578957.

[19] J. Lochab and V. R. Singh, “Acoustic behaviour of plastics for medical applications,” *Indian J. Pure Appl. Phys.*, vol. 42, no. 8, pp. 595–599, 2004.

[20] IT’IS Foundation, “Speed of Sound,” 2022. https://itis.swiss/virtual-population/tissue-properties/database/acoustic-properties/speed-of-sound/.

[21] M. Feigin, D. Freedman, and B. W. Anthony, “A Deep Learning Framework for Single-Sided Sound Speed Inversion in Medical Ultrasound,” *IEEE Trans. Biomed. Eng.*, vol. 67, no. 4, pp. 1142–1151, 2020, doi: 10.1109/TBME.2019.2931195.

[22] M. Agarwal, A. Tomar, and N. Kumar, “An IEEE single-precision arithmetic based beamformer architecture for phased array ultrasound imaging system,” *Eng. Sci. Technol. an Int. J.*, vol. 24, no. 5, pp. 1080–1089, 2021, doi: 10.1016/j.jestch.2021.03.005.

[23] M. Toulemonde and C. Bernard -Lyon, “New beamforming strategy for improved ultrasound imaging : application to biological tissues nonlinear imaging,” *Acoustics*, no. November 2014, 2014, [Online]. Available: https://tel.archives-ouvertes.fr/tel-01127215.

[24] Y. Xiao, M. Boily, H. S. Hashemi, and H. Rivaz, “High-Dynamic-Range Ultrasound: Application for Imaging Tendon Pathology,” *Ultrasound Med. Biol.*, vol. 44, no. 7, pp. 1525–1532, 2018, doi: 10.1016/j.ultrasmedbio.2018.03.004.

[25] A. Ozturk *et al.*, “Variation of Shear Wave Elastography With Preload in the Thyroid: Quantitative Validation,” *J. Ultrasound Med.*, vol. 40, no. 4, pp. 779–786, 2020, doi: 10.1002/jum.15456.

[26] S. F. Eby, P. Song, S. Chen, Q. Chen, J. F. Greenleaf, and K. N. An, “Validation of shear wave elastography in skeletal muscle,” *J. Biomech.*, vol. 46, no. 14, pp. 2381–2387, 2013, doi: 10.1016/j.jbiomech.2013.07.033.

[27] R. Chimoriya, M. K. Piya, D. Simmons, G. Ahlenstiel, and V. Ho, “The use of two-dimensional shear wave elastography in people with obesity for the assessment of liver fibrosis in non-alcoholic fatty liver disease,” *J. Clin. Med.*, vol. 10, no. 1, pp. 1–13, 2021, doi: 10.3390/jcm10010095.

[28] A. Evans *et al.*, “Differentiating benign from malignant solid breast masses: Value of shear wave elastography according to lesion stiffness combined with greyscale ultrasound according to BI-RADS classification,” *Br. J. Cancer*, vol. 107, no. 2, pp. 224–229, 2012, doi: 10.1038/bjc.2012.253.

[29] U. Kleinevoß, H. Meyer, A. Schumacher, and S. Hartmann, “Absolute measurement of the Newtonian force and a determination of G,” *Meas. Sci. Technol.*, vol. 10, no. 6, pp. 492–494, 1999, doi: 10.1088/0957-0233/10/6/313.

[30] M. S. Jr and L. Cell, “Model LSB205,” pp. 1–2.

[31] D. Trent, “Load Cell and Strain Gauge Basics,” *Load Cell Central*, 2022. https://www.800loadcel.com/load-cell-and-strain-gauge-basics.html--.

[32] D. M. Stefanescu, “Strain gauges and Wheatstone bridges - Basic instrumentation and new

applications for electrical measurement of non-electrical quantities," in *Eight International Mulit-applications for electrical measurement of non-electrical quantities*, 2011, pp. 1–5.

[33] M. Pedley, "Tilt Sensing Using a Three-Axis Accelerometer," *Free. Semicond. Appl. notes*, pp. 1–22, 2013.

[34] R. Wasserstein, "George Box: A model statistician," *Significance*, vol. 7, no. 3, pp. 134–135, 2010, doi: 10.1111/j.1740-9713.2010.00442.x.

[35] O. . Zienkiewicz, R. . Taylor, and J. . Zhu, "Finite Element Method for Solid and Structural Mechanics," no. 1, pp. 6–8, 2005.

[36] M. Design, "Understanding Finite Element Analysis and Its Benefits for Your Medical Device." https://www.mindflowdesign.com/insights/finite-element-analysis-medical-product-benefits/ (accessed Mar. 08, 2022).

[37] D. P. Bertsekas, *Convex Optimization Theory*. Belmont, Massachusetts: Athena Scientific, 2009.

[38] I. Dabbura, "Gradient Descent Algorithm and Its Variants," *Towards Data Science*, 2017. https://towardsdatascience.com/gradient-descent-algorithm-and-its-variants-10f652806a3 (accessed Mar. 08, 2022).

[39] M. A. Luersen and R. Le Riche, "Globalized nelder-mead method for engineering optimization," *Comput. Struct.*, vol. 82, no. 23–26, pp. 2251–2260, 2004, doi: 10.1016/j.compstruc.2004.03.072.

[40] M. H. Wright, "Nelder, Mead, and the Other Simplex Method," *Doc. Math.*, vol. extra volu, no. August 2010, pp. 271–276, 2012.

[41] J. E. Hall, *Guyton and Hall Textbook of Medical Physiology, 13th Edition*. 2013.

[42] B. Folkow and E. Neil, *Circulation*. 1971.

[43] R. Mark and T. Heldt, "Functional Anatomy," 2018.

[44] A. P. Shepherd, H. J. Granger, E. E. Smith, and A. C. Guyton, "Local control of tissue oxygen delivery and its contribution to the regulation of cardiac output," *Am. J. Physiol.*, vol. 225, no. 3, pp. 747–755, 1973, doi: 10.1152/ajplegacy.1973.225.3.747.

[45] H. S. Badeer, "Hemodynamics for medical students," *Am. J. Physiol. - Adv. Physiol. Educ.*, vol. 25, no. 1–4, pp. 44–52, 2001, doi: 10.1152/advances.2001.25.1.44.

[46] V. Fuster *et al.*, *ACC/AHA/ESC guidelines for the management of patients with atrial fibrillation: Executive summary. A report of the American College of Cardiology/American Heart Association Task Force on Practice Guidelines and the European Society of Cardiology Committee*, vol. 104, no. 17. 2001.

[47] D. A. Kass, "Ventricular arterial stiffening: Integrating the pathophysiology," *Hypertension*, vol. 46, no. 1, pp. 185–193, 2005, doi: 10.1161/01.HYP.0000168053.34306.d4.

[48] A. C. Guyton, "Cardiac output and its regulation," *Circ. Physiol.*, pp. 353–371, 1973.

[49] A. C. GUYTON, "Determination of cardiac output by equating venous return curves with cardiac response curves," *Physiol. Rev.*, vol. 35, no. 1, pp. 123–129, 1955, doi:

10.1152/physrev.1955.35.1.123.

[50] G. A. Cooke *et al.*, “Physiological cardiac reserve: Development of a non-invasive method and first estimates in man,” *Heart*, vol. 79, no. 3, pp. 289–294, 1998, doi: 10.1136/hrt.79.3.289.

[51] S. Standring, *Gray’s anatomy e-book: the anatomical basis of clinical practice*. Elsevier Health Sciences.=, 2021.

[52] E. Bazigou and T. Makinen, “Flow control in our vessels: Vascular valves make sure there is no way back,” *Cell. Mol. Life Sci.*, vol. 70, no. 6, pp. 1055–1066, 2013, doi: 10.1007/s00018-012-1110-6.

[53] A. Fortier, V. Gullapalli, and R. A. Mirshams, “Review of biomechanical studies of arteries and their effect on stent performance,” *IJC Hear. Vessel.*, vol. 4, no. 1, pp. 12–18, 2014, doi: 10.1016/j.ijchv.2014.04.007.

[54] L. A. Bortolotto and M. E. Safar, “Blood pressure profile along the arterial tree and genetics of hypertension,” *Arq. Bras. Cardiol.*, vol. 86, no. 3, pp. 166–169, 2006.

[55] T. Khan, F. Farooqui, and K. Niazi, “Critical Review of the Ankle Brachial Index,” *Curr. Cardiol. Rev.*, vol. 4, no. 2, pp. 101–106, 2008, doi: 10.2174/157340308784245810.

[56] “New Jersey Vascular Center.” [Online]. Available: https://njvvc.com/the-anatomy-of-a-vein/.

[57] P. Howard, “Gravity and the circulation,” *Proc. R. Soc. London - Biol. Sci.*, vol. 199, no. 1137, pp. 485–491, 1977, doi: 10.1098/rspb.1977.0156.

[58] H. Hinghofer-Szalkay, “Gravity, the hydrostatic indifference concept and the cardiovascular system,” *Eur. J. Appl. Physiol.*, vol. 111, no. 2, pp. 163–174, 2011, doi: 10.1007/s00421-010-1646-9.

[59] G. Manley, M. M. Knudson, and D. Morabito, “Hypotension, Hypoxia, and Head Injury,” vol. 136, 2001.

[60] J. Stokes, W. B. Kannel, P. A. Wolf, R. B. D’Agostino, and L. Adrienne Cupples, “Blood pressure as a risk factor for cardiovascular disease the framingham study-30 years of follow-up,” *Hypertension*, vol. 13, no. 5, pp. I-13-I–18, 1989, doi: 10.1161/01.hyp.13.5_suppl.i13.

[61] P. Palatini, “Sympathetic overactivity in hypertension: A risk factor for cardiovascular disease,” *Curr. Hypertens. Rep.*, vol. 3, no. 1, pp. 3–9, 2001, doi: 10.1007/s11906-001-0065-z.

[62] W. Wang *et al.*, “A longitudinal study of hypertension risk factors and their relation to cardiovascular disease: The strong heart study,” *Hypertension*, vol. 47, no. 3, pp. 403–409, 2006, doi: 10.1161/01.HYP.0000200710.29498.80.

[63] J. P. Lea and S. B. Nicholas, “Diabetes mellitus and hypertension: key risk factors for kidney disease.,” *J. Natl. Med. Assoc.*, vol. 94, no. 8 Suppl, 2002.

[64] P. K. Whelton *et al.*, “2017 ACC/AHA/AAPA/ABC/ACPM/AGS/APhA/ASH/ASPC/NMA/PCNA Guideline for the Prevention, Detection, Evaluation, and Management of High Blood Pressure in Adults: A Report of the American College of Cardiology/American Heart Association Task Force on Clinical Pr,” *J. Am. Coll. Cardiol.*, vol. 71, no. 19, pp. e127–e248, 2018, doi:

10.1016/j.jacc.2017.11.006.

[65] N. I. Z. Saedon, M. P. Tan, and J. Frith, “The prevalence of orthostatic hypotension: A systematic review and meta-analysis,” *Journals Gerontol. - Ser. A Biol. Sci. Med. Sci.*, vol. 75, no. 1, pp. 117–122, 2020, doi: 10.1093/gerona/gly188.

[66] P. E. Owens, S. P. Lyons, and E. T. O’Brien, “Arterial hypotension: Prevalence of low blood pressure in the general population using ambulatory blood pressure monitoring,” *J. Hum. Hypertens.*, vol. 14, no. 4, pp. 243–247, 2000, doi: 10.1038/sj.jhh.1000973.

[67] R. H. G. Schwinger, *Pathophysiology of heart failure*, vol. 11, no. 1. 2021.

[68] S. J. Simmonds, I. Cuijpers, S. Heymans, and E. A. V. Jones, “Cellular and Molecular Differences between HFpEF and HFrEF: A Step Ahead in an Improved Pathological Understanding,” *Cells*, vol. 9, no. 1, 2020, doi: 10.3390/cells9010242.

[69] T. B. Abebe, E. A. Gebreyohannes, Y. G. Tefera, and T. M. Abegaz, “Patients with HFpEF and HFrEF have different clinical characteristics but similar prognosis: A retrospective cohort study,” *BMC Cardiovasc. Disord.*, vol. 16, no. 1, pp. 1–8, 2016, doi: 10.1186/s12872-016-0418-9.

[70] C. D. Kemp and J. V. Conte, “The pathophysiology of heart failure,” *Cardiovasc. Pathol.*, vol. 7, pp. 365–371, 2012, doi: 10.1080/10643389.2012.728825.

[71] K. T. Weber, “Aldosterone in congestive heart failure,” *N. Engl. J. Med.*, vol. 345, no. 23, pp. 1689–1697, 2001.

[72] S. H. Slight, J. Joseph, V. K. Ganjam, and K. T. Weber, “Extra-adrenal mineralocorticoids and cardiovascular tissue,” *J. Mol. Cell. Cardiol.*, vol. 31, no. 6, pp. 1175–1184, 1999, doi: 10.1006/jmcc.1999.0963.

[73] T. Langenickel, I. Pagel, K. Höhnel, R. Dietz, and R. Willenbrock, “Differential regulation of cardiac ANP and BNP mRNA in different stages of experimental heart failure,” *Am. J. Physiol. - Hear. Circ. Physiol.*, vol. 278, no. 5 47-5, pp. 1500–1506, 2000, doi: 10.1152/ajpheart.2000.278.5.h1500.

[74] G. M. Felker and M. Fudim, “Acute decompensated heart failure,” *Cardiol. Secrets*, vol. 36, no. 6, pp. 233–240, 2017, doi: 10.1016/B978-0-323-47870-0.00026-X.

[75] G. Albert Schweitzer Hospital, Lambarene, Gabon, and Institute of Tropical Medicine, University of Tübingen, Tübingen, “Diagnostic Strategies in Patients with Acute Decompensated Heart Failure,” *N. Engl. J. Med.*, vol. 365, pp. 687–696, 2011.

[76] N. J. Brown and D. E. Vaughan, “Angiotensin-Converting Enzyme Inhibitors,” *Circulation*, vol. 97, no. 14, pp. 1411–1420, 1998, doi: 10.1097/01.NURSE.0000524762.35753.23.

[77] M. D. Flather *et al.*, “Long-term ACE-inhibitor therapy in patients with heart failure or left-ventricular dysfunction: A systematic overview of data from individual patients,” *Lancet*, vol. 355, no. 9215, pp. 1575–1581, 2000, doi: 10.1016/S0140-6736(00)02212-1.

[78] W. B. Stason, P. J. Cannon, H. O. Heinemann, and J. H. Laragh, “Furosemide. A clinical evaluation of its diuretic action.,” *Circulation*, vol. 34, no. 5, pp. 910–920, 1966, doi: 10.1161/01.CIR.34.5.910.

[79] R. Greger and E. Schlatter, “Cellular mechanism of the action of loop diuretics on the thick ascending limb of Henle’s loop,” *Klin. Wochenschr.*, vol. 61, no. 20, pp. 1019–1027, 1983, doi: 10.1007/BF01537500.

[80] M. Bayeva, M. Gheorghiade, and H. Ardehali, “Mitochondria as a therapeutic target in heart failure,” *J. Am. Coll. Cardiol.*, vol. 61, no. 6, pp. 599–610, 2013, doi: 10.1016/j.jacc.2012.08.1021.

[81] A. C. Guyton, *Arterial Pressure and Hypertension*. Saunders WB Co, 1980.

[82] D. S. Picone *et al.*, “Accuracy of Cuff-Measured Blood Pressure: Systematic Reviews and Meta-Analyses,” *J. Am. Coll. Cardiol.*, vol. 70, no. 5, pp. 572–586, 2017, doi: 10.1016/j.jacc.2017.05.064.

[83] C. F. Babbs, “The origin of Korotkoff sounds and the accuracy of auscultatory blood pressure measurements,” *J. Am. Soc. Hypertens.*, vol. 9, no. 12, pp. 935-950.e3, 2015, doi: 10.1016/j.jash.2015.09.011.

[84] L. A. Geddes, M. Voelz, C. Combs, D. Reiner, and C. F. Babbs, “Characterization of the oscillometric method for measuring indirect blood pressure,” *Ann. Biomed. Eng.*, vol. 10, no. 6, pp. 271–280, 1982, doi: 10.1007/BF02367308.

[85] G. W. Mauck, C. R. Smith, L. A. Geddes, and J. D. Bourl, “The meaning of the point of maximum oscillations in cuff pressure in the indirect measurement of blood pressure-part II,” *J. Biomech. Eng.*, vol. 102, no. 1, pp. 28–33, 1980, doi: 10.1115/1.3138195.

[86] J. P. Loenneke *et al.*, “Blood flow restriction in the upper and lower limbs is predicted by limb circumference and systolic blood pressure,” *Eur. J. Appl. Physiol.*, vol. 115, no. 2, pp. 397–405, 2015, doi: 10.1007/s00421-014-3030-7.

[87] T. G. Pickering *et al.*, “Recommendations for blood pressure measurement in humans and experimental animals: Part 1: Blood pressure measurement in humans - A statement for professionals from the Subcommittee of Professional and Public Education of the American Heart Association Co,” *Circulation*, vol. 111, no. 5, pp. 697–716, 2005, doi: 10.1161/01.CIR.0000154900.76284.F6.

[88] K. Tegtmeyer, G. Brady, S. Lai, R. Hodo, and D. Braner, “Placement of an Arterial Line,” *N. Engl. J. Med.*, vol. 354, no. 15, p. e13, 2006, doi: 10.1056/nejmvcm044149.

[89] M. R. Nelson, J. Stepanek, M. Cevette, M. Covalciuc, R. T. Hurst, and A. J. Tajik, “Noninvasive measurement of central vascular pressures with arterial tonometry: Clinical revival of the pulse pressure waveform?,” *Mayo Clin. Proc.*, vol. 85, no. 5, pp. 460–472, 2010, doi: 10.4065/mcp.2009.0336.

[90] O. Narayan, J. Casan, M. Szarski, A. M. Dart, I. T. Meredith, and J. D. Cameron, “Estimation of central aortic blood pressure: A systematic meta-analysis of available techniques,” *J. Hypertens.*, vol. 32, no. 9, pp. 1727–1740, 2014, doi: 10.1097/HJH.0000000000000249.

[91] H. M. Cheng, D. Lang, C. Tufanaru, and A. Pearson, “Measurement accuracy of non-invasively obtained central blood pressure by applanation tonometry: A systematic review and meta-analysis,” *Int. J. Cardiol.*, vol. 167, no. 5, pp. 1867–1876, 2013.

[92] J. Rizkallah, M. Jack, M. Saeed, L. A. Shafer, M. Vo, and J. Tam, “Non-Invasive Bedside Assessment of Central Venous Pressure: Scanning into the Future,” *PLoS One*, vol. 9, no. 10, pp. 1–9, 2014,

doi: 10.1371/journal.pone.0109215.

[93] R. D. Conn and J. H. O'Keefe, "Simplified evaluation of the jugular venous pressure: significance of inspiratory collapse of jugular veins.," *Mo. Med.*, vol. 109, no. 2, pp. 150–152, 2012.

[94] R. Seth, P. Magner, F. Matzinger, and C. Van Walraven, "How far is the sternal angle from the mid-right atrium?," *J. Gen. Intern. Med.*, vol. 17, no. 11, pp. 861–865, 2002, doi: 10.1046/j.1525-1497.2002.20101.x.

[95] N. Sathish *et al.*, "Comparison between noninvasive measurement of central venous pressure using near infrared spectroscopy with an invasive central venous pressure monitoring in cardiac surgical Intensive Care Unit," *Ann. Card. Anaesth.*, vol. 19, no. 3, pp. 405–409, 2016, doi: 10.4103/0971-9784.185520.

[96] M. Ball, S. Falkson, and O. Adigun, "Anatomy, Angle of Louis," in *StatPearls*, StatPearls Publishing, 2021.

[97] N. Mehta, W. W. Valesky, A. Guy, and R. Sinert, "Systematic review: Is real-time ultrasonic-guided central line placement by ED physicians more successful than the traditional landmark approach?," *Emerg. Med. J.*, vol. 30, no. 5, pp. 355–359, 2013, doi: 10.1136/emermed-2012-201230.

[98] C. Kornbau, K. Lee, G. Hughes, and M. Firstenberg, "Central line complications," *Int. J. Crit. Illn. Inj. Sci.*, vol. 5, no. 3, p. 170, 2015, doi: 10.4103/2229-5151.164940.

[99] R. E. Gebhard, P. Szmuk, E. G. Pivalizza, V. Melnikov, C. Vogt, and R. D. Warters, "The accuracy of electrocardiogram-controlled central line placement," *Anesth. Analg.*, vol. 104, no. 1, pp. 65–70, 2007, doi: 10.1213/01.ane.0000250224.02440.fe.

[100] Epomedicine, "Jugular Venous Pulse and Pressure (JVP) Examination." 2013, [Online]. Available: https://epomedicine.com/clinical-medicine/clinical-examination-jugular-venous-pulse-pressure-jvp/.

[101] B. co. Staff, "Medical Gallery of Blausen Medical," 2014, [Online]. Available: https://en.wikiversity.org/wiki/WikiJournal_of_Medicine/Medical_gallery_of_Blausen_Medical_2014.

[102] R. A. De Lorenzo *et al.*, "Does a simple bedside sonographic measurement of the inferior vena cava correlate to central venous pressure?," *J. Emerg. Med.*, vol. 42, no. 4, pp. 429–436, 2012, doi: 10.1016/j.jemermed.2011.05.082.

[103] C. L. A. Erhardt, "Inferior Vena Caval Syndrome and the Sniff Test for Elevated Central Venous Pressure and Its Contributing Factors," *J. Diagnostic Med. Sonogr.*, vol. 12, no. 1, pp. 27–33, 1996.

[104] A. Weyman, "Right ventricular inflow tract," in *Principles of Echocardiography*, Philadelphia, PA: WB Saunders CO, 1994, pp. 852–857.

[105] L. G. Rudski *et al.*, "Guidelines for the Echocardiographic Assessment of the Right Heart in Adults: A Report from the American Society of Echocardiography. Endorsed by the European Association of Echocardiography, a registered branch of the European Society of Cardiology, and ," *J. Am. Soc. Echocardiogr.*, vol. 23, no. 7, pp. 685–713, 2010, doi: 10.1016/j.echo.2010.05.010.

[106] A. M. Zakrzewski and B. W. Anthony, “Noninvasive blood pressure estimation using ultrasound and simple finite element models,” *IEEE Trans. Biomed. Eng.*, vol. 65, no. 9, pp. 2011–2022, 2018, doi: 10.1109/TBME.2017.2714666.

[107] A. Y. Huang, “May the Force Be With You: A Medical Ultrasound System with Integrated Force Measurement,” pp. 0–110, 2017, [Online]. Available: https://dspace.mit.edu/handle/1721.1/85405.

[108] R. Girshick, J. Donahue, T. Darrell, J. Malik, U. C. Berkeley, and J. Malik, “Rich feature hierarchies for accurate object detection and semantic segmentation,” *Proc. IEEE Comput. Soc. Conf. Comput. Vis. Pattern Recognit.*, vol. 1, p. 5000, 2014, doi: 10.1109/CVPR.2014.81.

[109] A. T. Jaffe, R. E. Zubajlo, L. Daniel, and B. W. Anthony, “Automated force-coupled ultrasound method for calibration-free carotid artery blood pressure estimation,” *Ultrasound Med. Biol.*, vol. 48, no. 9, pp. 1806–1821, 2022.

[110] E. Karami, M. Shehata, P. McGuire, and A. Smith, “A semi-automated technique for internal jugular vein segmentation in ultrasound images using active contours,” in *3rd IEEE EMBS International Conference on Biomedical and Health Informatics, BHI 2016*, 2016, pp. 184–187, doi: 10.1109/BHI.2016.7455865.

[111] A. M. Zakrzewski and B. W. Anthony, “Arterial blood pressure estimation using ultrasound: Clinical results on healthy volunteers and a medicated hypertensive volunteer,” in *Proceedings of the Annual International Conference of the IEEE Engineering in Medicine and Biology Society, EMBS*, 2017, pp. 2154–2157, doi: 10.1109/EMBC.2017.8037281.

[112] A. M. Zakrzewski, A. Y. Huang, R. Zubajlo, and B. W. Anthony, “Real-time blood pressure estimation from force-measured ultrasound,” *IEEE Trans. Biomed. Eng.*, vol. 65, no. 11, pp. 2405–2416, 2018, doi: 10.1109/TBME.2018.2873297.

[113] R. Smith-Bindman, D. L. Miglioretti, and E. B. Larson, “Rising use of diagnostic medical imaging in a large integrated health system,” *Health Aff.*, vol. 27, no. 6, pp. 1491–1502, 2008, doi: 10.1377/hlthaff.27.6.1491.

[114] S. Campbell, “A short history of sonography in obstetrics and gynaecology.,” *Facts, views Vis. ObGyn*, vol. 5, no. 3, pp. 213–229, 2013.

[115] E. Picano, M. C. Scali, Q. Ciampi, and D. Lichtenstein, “Lung Ultrasound for the Cardiologist,” *JACC Cardiovasc. Imaging*, vol. 11, no. 11, pp. 1692–1705, 2018, doi: 10.1016/j.jcmg.2018.06.023.

[116] M. W. Gilbertson and B. W. Anthony, “Ergonomic control strategies for a handheld force-controlled ultrasound probe,” *IEEE Int. Conf. Intell. Robot. Syst.*, pp. 1284–1291, 2012, doi: 10.1109/IROS.2012.6385996.

[117] A. Kuzmin, A. M. Zakrzewski, B. W. Anthony, and V. Lempitsky, “Multi-frame elastography using a handheld force-controlled ultrasound probe,” *IEEE Trans. Ultrason. Ferroelectr. Freq. Control*, vol. 62, no. 8, pp. 1486–1500, 2015, doi: 10.1109/TUFFC.2015.007133.

[118] S. Koppaka, M. W. Gilbertson, J. S. Wu, S. B. Rutkove, and B. W. Anthony, “Assessing duchenne muscular dystrophy with force-controlled ultrasound,” 2014, doi: 10.1109/isbi.2014.6867965.

[119] A. J. Pigula, J. S. Wu, M. W. Gilbertson, B. T. Darras, S. B. Rutkove, and B. W. Anthony, “Force-

controlled ultrasound to measure passive mechanical properties of muscle in Duchenne muscular dystrophy," in *Proceedings of the Annual International Conference of the IEEE Engineering in Medicine and Biology Society, EMBS*, 2016, pp. 2865–2868, doi: 10.1109/EMBC.2016.7591327.

[120] A. M. Zakrzewski, "Arterial Blood Pressure Estimation Using Ultrasound," pp. 1–163, 2017, [Online]. Available: https://dspace.mit.edu/bitstream/handle/1721.1/111743/1004393248-MIT.pdf?sequence=1.

[121] L. A. Tomlinson and I. B. Wilkinson, "Does it matter where we measure blood pressure?," *Br. J. Clin. Pharmacol.*, vol. 74, no. 2, pp. 241–245, 2012, doi: 10.1111/j.1365-2125.2012.04203.x.

[122] X. Xing, Z. Ma, M. Zhang, Y. Zhou, W. Dong, and M. Song, "An Unobtrusive and Calibration-free Blood Pressure Estimation Method using Photoplethysmography and Biometrics," *Sci. Rep.*, vol. 9, no. 1, pp. 1–8, 2019, doi: 10.1038/s41598-019-45175-2.

[123] P. M. Nabeel, J. Joseph, S. Karthik, M. Sivaprakasam, and M. Chenniappan, "Bi-Modal arterial compliance probe for calibration-free cuffless blood pressure estimation," *IEEE Trans. Biomed. Eng.*, vol. 65, no. 11, pp. 2392–2404, 2018, doi: 10.1109/TBME.2018.2866332.

[124] K. M. Moerman, C. K. Simms, and T. Nagel, "Control of tension-compression asymmetry in Ogden hyperelasticity with application to soft tissue modelling," *J. Mech. Behav. Biomed. Mater.*, vol. 56, pp. 218–228, 2016, doi: 10.1016/j.jmbbm.2015.11.027.

[125] W. Ciozda, I. Kedan, D. W. Kehl, R. Zimmer, R. Khandwalla, and A. Kimchi, "The efficacy of sonographic measurement of inferior vena cava diameter as an estimate of central venous pressure," *Cardiovasc. Ultrasound*, vol. 14, no. 1, 2016, doi: 10.1186/s12947-016-0076-1.

[126] M. W. Gilbertson, "Electromechanical Systems to Enhance the Usability and Diagnostic Capabilities of Ultrasound Imaging," pp. 1–293, 2014, [Online]. Available: https://dspace.mit.edu/handle/1721.1/96459.

[127] A. Benjamin *et al.*, "Surgery for Obesity and Related Diseases: I. A Novel Approach to the Quantification of the Longitudinal Speed of Sound and Its Potential for Tissue Characterization," *Ultrasound Med. Biol.*, vol. 44, no. 12, pp. 2739–2748, 2018, doi: 10.1016/j.ultrasmedbio.2018.07.021.

[128] M. L. Eigenbrodt *et al.*, "Common carotid artery wall thickness and external diameter as predictors of prevalent and incident cardiac events in a large population study," *Cardiovasc. Ultrasound*, vol. 5, pp. 1–11, 2007, doi: 10.1186/1476-7120-5-11.

[129] L. Saba, R. Sanfilippo, R. Montisci, and G. Mallarini, "Carotid artery wall thickness: Comparison between sonography and multi-detector row CT angiography," *Neuroradiology*, vol. 52, no. 2, pp. 75–82, 2010, doi: 10.1007/s00234-009-0589-5.

[130] K. Kim, W. F. Weitzel, J. M. Rubin, H. Xie, X. Chen, and M. O'Donnell, "Vascular intramural strain imaging using arterial pressure equalization," *Ultrasound Med. Biol.*, vol. 30, no. 6, pp. 761–771, 2004, doi: 10.1016/j.ultrasmedbio.2004.04.003.

[131] E. J. F. Dickinson, H. Ekström, and E. Fontes, "COMSOL Multiphysics®: Finite element software for electrochemical analysis. A mini-review," *Electrochem. commun.*, vol. 40, pp. 71–74, 2014, doi: 10.1016/j.elecom.2013.12.020.

[132] S. S. Rao, *The finite element method in engineering*. 2017.

[133] A. R. Westervelt *et al.*, "A Parameterized Ultrasound-Based Finite Element Analysis of the Mechanical Environment of Pregnancy," *J. Biomech. Eng.*, vol. 139, no. 5, pp. 1–11, 2017, doi: 10.1115/1.4036259.

[134] A. P. C. Choi and Y. P. Zheng, "Estimation of Young's modulus and Poisson's ratio of soft tissue from indentation using two different-sized indentors: Finite element analysis of the finite deformation effect," *Med. Biol. Eng. Comput.*, vol. 43, no. 2, pp. 258–264, 2005, doi: 10.1007/BF02345964.

[135] E. M. H. Bosboom, M. K. C. Hesselink, C. W. J. Oomens, C. V. C. Bouten, M. R. Drost, and F. P. T. Baaijens, "Passive transverse mechanical properties of skeletal muscle under in vivo compression," *J. Biomech.*, vol. 34, no. 10, pp. 1365–1368, 2001, doi: 10.1016/S0021-9290(01)00083-5.

[136] L. A. Mihai, L. K. Chin, P. A. Janmey, and A. Goriely, "A comparison of hyperelastic constitutive models applicable to brain and fat tissues," *J. R. Soc. Interface*, vol. 12, pp. 1–12, 2015, doi: 10.1098/rsif.2015.0486.

[137] H. Hasegawa, H. Kanai, N. Chubachi, and Y. Koiwa, "Non-invasive evaluation of Poisson's ratio of arterial wall using ultrasound," *Electron. Lett.*, vol. 33, no. 4, pp. 340–342, 1997, doi: 10.1049/el:19970219.

[138] J. M. Meinders and A. P. G. Hoeks, "Simultaneous assessment of diameter and pressure waveforms in the carotid artery," *Ultrasound Med. Biol.*, vol. 30, no. 2, pp. 147–154, 2004, doi: 10.1016/j.ultrasmedbio.2003.10.014.

[139] S. Landahl, C. Bengtsson, J. A. Sigurdsson, A. Svanborg, and K. Svärdsudd, "Age-related changes in blood pressure," *Hypertension*, vol. 8, no. 11, pp. 1044–1049, 1986, doi: 10.1161/01.HYP.8.11.1044.

[140] W. E. Miall and H. G. Lovell, "Relation between Change of Blood Pressure and Age," *Br. Med. J.*, vol. 2, no. 5553, pp. 660–664, 1967, doi: 10.1136/bmj.2.5553.660.

[141] S. Berg, "4 big ways BP measurement goes wrong, and how to tackle them," *American Medical Association*, 2019. https://www.ama-assn.org/about#:~:text=Founded in 1847%2C the American,societies and other critical stakeholders.

[142] T. Weber *et al.*, "Validation of a brachial cuff-based method for estimating central systolic blood pressure," *Hypertension*, vol. 58, no. 5, pp. 825–832, 2011, doi: 10.1161/HYPERTENSIONAHA.111.176313.

[143] J. Seo, S. J. Pietrangelo, H. S. Lee, and C. G. Sodini, "Carotid arterial blood pressure waveform monitoring using a portable ultrasound system," in *Proceedings of the Annual International Conference of the IEEE Engineering in Medicine and Biology Society, EMBS*, 2015, pp. 5692–5695, doi: 10.1109/EMBC.2015.7319684.

[144] C. Wang *et al.*, "Monitoring of the central blood pressure waveform via a conformal ultrasonic device," *Nat. Biomed. Eng.*, vol. 2, pp. 687–695, 2018, doi: 10.1038/s41551-018-0287-x.

[145] A. Tarr *et al.*, "The impact of foreshortening on regional strain - A comparison of regional strain

evaluation between speckle tracking and tissue velocity imaging," *Ultraschall der Medizin*, vol. 34, no. 5, pp. 446–453, 2013, doi: 10.1055/s-0032-1330521.

[146] S. Charwat-Resl *et al.*, "Speckle-tracking-based evaluation of vascular strain at different sites of the arterial tree in healthy adults," *Ultraschall der Medizin*, vol. 37, no. 5, pp. 503–508, 2016, doi: 10.1055/s-0035-1553299.

[147] Q. Huang and Z. Zeng, "A Review on Real-Time 3D Ultrasound Imaging Technology," *Biomed Res. Int.*, vol. 2017, pp. 1–20, 2017, doi: 10.1155/2017/6027029.

[148] A. Bur *et al.*, "Accuracy of oscillometric blood pressure measurement according to the relation between cuff size and upper-arm circumference in critically ill patients," *Crit. Care Med.*, vol. 28, no. 2, pp. 371–376, 2000, doi: 10.1097/00003246-200002000-00014.

[149] D. W. Jones, L. J. Appel, S. G. Sheps, E. J. Roccella, and C. Lenfant, "Measuring Blood Pressure Accurately: New and Persistent Challenges," *J. Am. Med. Assoc.*, vol. 289, no. 8, pp. 1027–1030, 2003, doi: 10.1001/jama.289.8.1027.

[150] M. Brzezinski, T. Luisetti, and M. J. London, "Radial artery cannulation: A comprehensive review of recent anatomic and physiologic investigations," *Anesth. Analg.*, vol. 109, pp. 1763–1781, 2009, doi: 10.1213/ANE.0b013e3181bbd416.

[151] P. R. Steffen, T. Austin, A. DeBarros, and T. Brown, "The Impact of Resonance Frequency Breathing on Measures of Heart Rate Variability, Blood Pressure, and Mood," *Front. Public Heal.*, vol. 5, no. August, pp. 6–11, 2017, doi: 10.3389/fpubh.2017.00222.

[152] A. C. Dornhorst, P. Howard, and G. L. Landhart, "Respiratory Variations in Blood Pressure," *Circulation*, vol. 6, no. 4, pp. 553–558, 1952.

[153] D. Laude, M. Goldman, P. Escourrou, and J.-L. Elghozi, "Effect of breathing pattern on blood pressure and heart rate oscillations in humans," *Clin. Exp. Pharmacol. Physiol.*, vol. 20, no. 10, pp. 619–626, 1993.

[154] T. Pickering, D. Shimbo, and D. Haas, "Ambulatory Blood-Pressure Monitoring," *N. Engl. J. Med.*, vol. 354, no. 22, pp. 2368–2374, 2006.

[155] R. Singh *et al.*, "Noninvasive assessment of jugular venous pressure via force-coupled single crystal ultrasound," *IEEE Trans. Biomed. Eng.*, vol. 65, no. 8, pp. 1705–1710, 2018, doi: 10.1109/TBME.2017.2767828.

[156] L. A. Groves, B. VanBerlo, N. Veinberg, A. Alboog, T. M. Peters, and E. C. S. Chen, "Automatic segmentation of the carotid artery and internal jugular vein from 2D ultrasound images for 3D vascular reconstruction," *Int. J. Comput. Assist. Radiol. Surg.*, vol. 15, no. 11, pp. 1835–1846, 2020, doi: 10.1007/s11548-020-02248-2.

[157] S. S. Virani *et al.*, *Heart disease and stroke statistics—2020 update: A report from the American Heart Association*. 2020.

[158] J. Weiner, T. S. Richmond, J. Conigliaro, and D. J. Wiebe, "Military veteran mortality following a survived suicide attempt," *BMC Public Health*, vol. 11, no. 1, p. 374, 2011, doi: 10.1186/1471-2458-11-374.

[159] C. D. Wolinsky and H. Waldorf, “Chronic Venous Disease,” *Med. Clin. North Am.*, vol. 93, no. 6, pp. 1333–1346, 2009, doi: 10.1016/j.mcna.2009.08.001.

[160] A. W. Lensing and H. R. Prandoni, P., Brandjes, D., Huisman, P.M., Vigo, M., Tomasella, G., Krekt, J., ten Cate, J. W., Huisman, M.V., Buller, “Detection of deep vein thrombosis by real-time B-mode ultrasonography,” *N. Engl. J. Med.*, vol. 320, no. 6, pp. 342–345, 1989.

[161] P. Neglen and S. Raju, “Detection of outflow obstruction in chronic venous insufficiency,” *J. Vasc. Surg.*, vol. 17, no. 3, pp. 583–589, 1993.

[162] M. W. Gilbertson and B. W. Anthony, “An Ergonomic, Instrumented Ultrasound Probe for 6-Axis Force/torque Measurement,” in *35th Annual International Conference of the IEEE Engineering in Medicine and Biology Society (EMBC)*, 2013, pp. 140–143.

[163] A. Jaffe, I. Goryachev, C. Sodini, and B. Anthony, “Central Venous Pressure Estimation with Force-coupled Ultrasound of the Internal Jugular Vein,” pp. 1–21, 2022.

[164] N. D. Tafuna’i, I. Hunter, A. W. Johnson, G. W. Fellingham, and P. R. Vehrs, “Differences in femoral artery occlusion pressure between Sexes and dominant and non-dominant legs,” *Med.*, vol. 57, no. 9, pp. 1–11, 2021, doi: 10.3390/medicina57090863.

[165] R. Akhtar, M. J. Sherratt, J. K. Cruickshank, and B. Derby, “Characterizing the elastic properties of tissues,” *Materials Today*. 2011, doi: 10.1016/S1369-7021(11)70059-1.

[166] M. R. Zile *et al.*, “Transition from chronic compensated to acute d compensated heart failure: Pathophysiological insights obtained from continuous monitoring of intracardiac pressures,” *Circulation*, vol. 118, no. 14, pp. 1433–1441, 2008, doi: 10.1161/CIRCULATIONAHA.108.783910.

[167] D. Banerjee, J. Z. Ma, A. J. Collins, and C. A. Herzog, “Long-term survival of incident hemodialysis patients who are hospitalized for congestive heart failure, pulmonary edema, or fluid overload,” *Clin. J. Am. Soc. Nephrol.*, vol. 2, no. 6, pp. 1186–1190, 2007, doi: 10.2215/CJN.01110307.

[168] K. Chatterjee, “The Swan-Ganz catheters: Past, present, and future: A viewpoint,” *Circulation*, vol. 119, no. 1, pp. 147–152, 2009, doi: 10.1161/CIRCULATIONAHA.108.811141.

[169] S. Magder and F. Bafaqeeh, “The clinical role of central venous pressure measurements,” *J. Intensive Care Med.*, vol. 22, no. 1, pp. 44–51, 2007, doi: 10.1177/0885066606295303.

[170] J. M. S. Chua Chiaco, N. I. Parikh, and D. J. Fergusson, “The jugular venous pressure revisited,” *Cleve. Clin. J. Med.*, vol. 80, no. 10, pp. 638–644, 2013, doi: 10.3949/ccjm.80a.13039.

[171] P. J. Devine, L. E. Sullenberger, D. A. Bellin, and J. E. Atwood, “Jugular venous pulse: Window into the right heart,” *South. Med. J.*, vol. 100, no. 10, pp. 1022–1027, 2007, doi: 10.1097/SMJ.0b013e318073c89c.

[172] I. García-López and E. Rodriguez-Villegas, “Extracting the Jugular Venous Pulse from Anterior Neck Contact Photoplethysmography,” *Sci. Rep.*, vol. 10, no. 1, pp. 1–12, 2020, doi: 10.1038/s41598-020-60317-7.

[173] B. Lipton, “Estimation of central venous pressure by ultrasound of the internal jugular vein,” *Am. J. Emerg. Med.*, vol. 18, no. 4, pp. 432–434, 2000, doi: 10.1053/ajem.2000.7335.

[174] P. Zamboni *et al.*, “Central venous pressure estimation from ultrasound assessment of the jugular venous pulse,” *PLoS One*, vol. 15, no. 10 October, pp. 1–18, 2020, doi: 10.1371/journal.pone.0240057.

[175] A. Zaidi *et al.*, “Echocardiographic assessment of the tricuspid and pulmonary valves: A practical guideline from the British Society of Echocardiography,” *Echo Res. Pract.*, vol. 7, no. 4, pp. G95–G122, 2020, doi: 10.1530/ERP-20-0033.

[176] D. Perloff, C. Grim, J. Flack, and E. D. Frohlich, “AHA Medical / Scientific Statement Human Blood Pressure Determination by Sphygmomanometry,” *Library (Lond).*, pp. 2460–2470, 2012.

[177] H. Uthoff *et al.*, “Central venous pressure and impaired renal function in patients with acute heart failure,” *Eur. J. Heart Fail.*, vol. 13, no. 4, pp. 432–439, 2011, doi: 10.1093/eurjhf/hfq195.

[178] H. Mondal, S. Mondal, D. Das, N. Alam, and K. Saha, “Reliability of a jugular venous pressure scale in cardiovascular clinical examination,” *J. Clin. Prev. Cardiol.*, vol. 9, no. 2, p. 61, 2020, doi: 10.4103/jcpc.jcpc_4_20.

[179] P. A. Low, “Valsalva Maneuver,” *Encycl. Neurol. Sci.*, pp. 591–592, 2014, doi: 10.1016/B978-0-12-385157-4.00517-0.

[180] E. A. Tansey, L. E. A. Montgomery, J. G. Quinn, S. M. Roe, and C. D. Johnson, “Understanding basic vein physiology and venous blood pressure through simple physical assessments,” *Adv. Physiol. Educ.*, vol. 43, no. 3, pp. 423–429, 2019, doi: 10.1152/ADVAN.00182.2018.

[181] A. Sapra, A. Malik, and P. Bhandhari, *Vital Sign Assessment*. StatPearls Publishing, 2022.

[182] M. A. Cretikos, R. Bellomo, K. Hillman, J. Chen, S. Finfer, and A. Flabouris, “Respiratory rate: The neglected vital sign,” *Med. J. Aust.*, vol. 188, no. 11, pp. 657–659, 2008, doi: 10.5694/j.1326-5377.2008.tb01825.x.

[183] V. L. Roger, “Epidemiology of Heart Failure: A Contemporary Perspective,” *Circ. Res.*, vol. 128, no. 10, pp. 1421–1434, 2021, doi: 10.1161/CIRCRESAHA.121.318172.

[184] A. J. M. Lewis and D. Kotecha, “134 Peripheral Arterial Waveforms for the Prediction of Cardiovascular Events: Carotid Versus Radial Pulse Wave Analysis,” *Heart*, vol. 99, no. suppl 2, p. A79.2-A80, 2013, doi: 10.1136/heartjnl-2013-304019.134.